DECIPHERING 2D/3D PEROVSKITE HETEROJUNCTIONS FROM MICROSCOPIC PERSPECTIVE

LI ZHIMIN

PhD

The Hong Kong Polytechnic University

2025

The Hong Kong Polytechnic University
Department of Applied Physics

Deciphering 2D/3D Perovskite Heterojunctions from Microscopic Perspective

LI ZHIMIN

A thesis submitted in partial fulfilment of the requiremets for the degree of Doctor of Philosophy

August 2024

CERTIFICATE OF ORIGINALITY

I hereby declare that this thesis is my own work and that, to the best of my knowledge and belief, it reproduces no material previously published or written, nor material that has been accepted for the award of any other degree or diploma, except where due acknowledgement has been made in the text.

____________________________ (Signed)

______LI Zhimin__________ (Name of student)

Abstract

Perovskite solar cells (PSCs) that are composed of two-dimensional/three-dimensional (2D/3D) perovskite in structure combine the durability of 2D perovskites with the efficient movement of charge carries in 3D perovskites. This innovative approach improves the performance of PSCs in the fast-growing field of photovoltaic research. However, the transportation of charge carriers across the boundaries between 2D and 3D perovskite is impeded by the irregular distribution of the distinct fragments of 2D perovskite. This raises inquiries regarding the function of 2D perovskite in 2D/3D PSCs. Hence, this thesis intends to investigate the management of the 2D perovskite distribution and orientation and examine its influence on 3D grains. Additionally, electron microscopy will be used to provide feedback and verify the results obtained.

This thesis initially explores the impact of halide ions on structural issues and optoelectronic characteristics of 2D/3D perovskite heterojunctions. By manipulating the halide ion composition, including the incorporation of chloride (Cl^-) and bromide (Br^-) ions, the goal we have is to improve the dispersion, durability, and efficiency of perovskite films. Our approach involves varying concentrations of formamidinium chloride (FACl) in PEAI solutions and substituting phenethylammonium iodine (PEAI) with phenethylammonium bromine (PEABr) to assess their effects on 2D perovskite layer formation. The results demonstrate that chloride addition leads to more uniform 2D perovskite coverage and improved stability of the 2D/3D PSCs. However, while PEABr influences the ion exchange dynamics, achieving consistent layer thickness and orientation remains challenging. These findings highlight the critical role of halide ions in optimizing the microstructure and enhancing the optoelectronic performance of perovskite materials. This study provides valuable insights into the potential of tailored halide incorporation for advancing perovskite solar cell technologies, paving the way for the promotion of high-efficiency and durable PSCs.

The effectiveness of 2D surface passivation has been demonstrated in achieving cutting-edge perovskite optoelectronics, particularly in the field of solar cells, and the microstructural and phase heterogeneities of 2D perovskite passivators can strongly influence their effective roles. But synthesis of co-homogenized, stable microstructure and phase in such passivators remains a challenge because of uncontrolled surface reactions. Herein we leverage a [6,6]-phenyl-C_{61}-butyric acid methyl ester (PCBM) molecular interlayer to optimize the interaction between a 2D passivator and 3D perovskite, leading to a uniform, purer-phase 2D perovskite capping layer. This PCBM interlayer further mitigates the detrimental grain-boundary etching encountered in conventional approaches, creating a molecular passivation directly onto the perovskite surface. The inverted PSCs made as such feature a laminate-structured perovskite heterointerface at the electron-extracting side, which contributes to improved charge energetics and film stability, owing to regulated band alignment and laminate-layer protection, respectively. Power conversion efficiencies up to 26% are achieved, together with enhanced device stabilities under ISOS-standardized protocols, showing T_{90} lifetimes over 1,000 h in both the damp-heat test (85 ºC, 85% relative humidity) and maximum-power-point tracking under one-sun illumination. Lattice-resolved insights are provided to link the microstructure to device performance, shedding light on the significance of passivator-microstructure uniformity and reliability on the performance of perovskite optoelectronics.

List of Publications

1. **Zhimin Li**, Pengfei Guo, Yalan Zhang, Weizhen Wang, Songhua Cai*, Yuanyuan Zhou*, Synthesis of A Lattice-Resolved Laminate-Structured Perovskite Heterointerface, *Nature Synthesis*, https://doi.org/10.1038/s44160-025-00787-7 (2025).

2. Tamtaji, M. *, Kim, M. G., **Li, Z.**, Cai, S., Wang, J., Galligan, P. R., ... & Chen, G*. High-throughput screening of dual atom catalysts for oxygen reduction and evolution reactions and rechargeable zinc-air battery. *Nano Energy*, **126**, 109634 (2024).

3. Guo, S., Zhang, X., Hao, M., Duan, T., Wang, W., **Li, Z.**, ... & Cai, S. *, Zhou, Y*. Liquid-Phase Transfer of Organic–Inorganic Halide Perovskite Films for TEM Investigation and Planar Heterojunction Fabrication. *Advanced Optical Materials*, 12 (8), 2301255 (2024).

4. Tamtaji, M., Cai, S., Wu, W., Liu, T., **Li, Z.**, Chang, H. Y., ... & Luo, Z*. Single and dual metal atom catalysts for enhanced singlet oxygen generation and oxygen reduction reaction. *Journal of Materials Chemistry A*, 11(14), 7513-7525 (2023).

Acknowledgements

As I write this, I glance out the window at the faint light of dawn and reflect on the swift passage of time. Unwittingly, the three wonderful years of doctoral studies and research at The Hong Kong Polytechnic University are coming to an end, stirring a multitude of thoughts and emotions. Remain faithful to your original aspiration, and success will follow. When I first embarked on my postgraduate journey, my deepest desire was simply to see more—to venture into unfamiliar regions and interact with individuals that I had not previously experienced. I searched to discover what my heart genuinely desired: to experience, to grow, and to venture onward, observing wonders that remain hidden from others. To witness extraordinary sights, one must have ambition, strength, and resources. I am such a normal person who relies on the support and encouragement of those around me to take each step toward faraway goals. Therefore, I deeply cherish everything around me and my life. I take this opportunity to express my heartfelt gratitude.

I wish to convey my sincere appreciation to Professor Cai Songhua for his essential mentorship and assistance during my pursuit of a doctoral degree. His profound knowledge and perceptive observations have played a crucial role in influencing my research and significantly deepening my comprehension of the subject. Professor Cai's encouragement and guidance have been a constant source of inspiration, driving me to strive for excellence in my work. I am truly thankful for the opportunities he has provided and for his unwavering belief in my potential. His dedication and commitment to my academic and personal growth have left a deep impact, for which I am immensely grateful.

I express my gratitude to Professor Zhou Yuanyuan and Dr. Guo Pengfei from the Hong Kong University of Science and Technology. Professor Zhou supported the advancement of my research project and offered me numerous useful recommendations for my experimental design. Dr. Guo gave me a lot of help in the preparation, stability testing and related characterization of the solar cell device,

and discussions with him deepened my understanding of my research topic. Thanks to Zhang Yalan for her contribution to the illustrations and assistance in materials characterization.

I would also like to convey my gratitude to Professor Zhu Ye. The course AP617 has provided me with a deeper understanding of equipment and material analysis principles, which will be highly advantageous for my study. I also want to convey my gratitude to the students in their group for any valuable insights they provided during my experiment.

I would like to acknowledge the two postgraduates and other students in our group, Dr. Wang Weizhen and Dr. Guo Shuai, for their invaluable assistance with TEM, FIB operation, and data processing.

Lastly, I want to thank my family and friends. You are the driving force behind my progress and the unquenchable light in my life. Just thinking about them gives me hope and enthusiasm, and I intend to keep moving forward till the end of the world!

Table of Contents

Abstract .... Ⅰ

List of Publications .... Ⅲ

Acknowledgements IV

Table of Contents VI

List of Figures X

List of Tables XX

Chapter 1 Introduction 1

1.1 Background 1

1.2 Objectives of Research 4

1.3 Dissertation Scope and Organization 5

Chapter 2 Overview of 2D/3D PSCs and Characterization Methods for Heterojunctions 7

2.1 Introduction 7

2.2 Organic-inorganic Halide Perovskite Materials 7

2.3 Perovskite Solar Cells 9

2.4 Stability of Perovskite Solar Cells 13

2.5 2D/3D Perovskite Heterojunctions 15

2.5.1 2D Perovskite 16

2.5.2 2D Perovskite in 2D/3D Perovskite Heterojunctions 17

2.6 Interface Characterization Methods for Heterojunctions 31

2.6.1 Spectroscopic Probing 31

2.6.2 Electron Microscopy Characterizations 33

2.6.3 Low-dose S/TEM Characterizations of Halide Perovskites 36

2.6.4 Electrical and Optoelectronic Characterization 42

2.7 Summary 42

Chapter 3 Experimental and Characterization Methods 44

3.1 Materials 44

3.2 2D/3D Perovskite Heterojunctions Preparation 44

3.3 Cs-corrected TEM 46

3.4 FIB and Cross-sectional STEM Sample Preparation 47

3.5 Other Characterization 49

3.5.1 HAADF-STEM 49

3.5.2 EELS 50

3.5.3 4D-STEM 50

3.5.4 Morphology and Physical Property Characterizations 52

3.5.5 PSC Fabrication and Testing 53

Chapter 4 Effect of Halide Ion in 2D/3D Perovskite Heterojunctions 55

4.1 Introduction 55

4.2 FACl Addition on PEAI Solution 56

4.3 $FA_{0.9}Cs_{0.1}PbBr_3$ Treated with PEAI 62

4.4 $FA_{0.9}Cs_{0.1}PbI_3$ Treated with PEABr 66

4.5 Conclusions 68

Chapter 5 Synthesis of Lattice-Resolved Laminate-Structured Perovskite Heterointerface 70

5.1 Introduction 70

5.2 Synthesis and lattice-resolved STEM analysis 72

5.3 4D STEM of near-surface grain boundaries 94

5.4 Optoelectronic properties and chemical stability 97

5.5 Photovoltaic performance and device stability 102

5.6 Conclusion 121

Chapter 6 Conclusion and Outlook 123

6.1 Summary of Results 123

6.2 Prospects of Future Work 124

References 126

List of Figures

Figure 1.1 Best Research-Cell Efficiencies …………………………………………..……………… 2

Figure 2.1 Crystal structure of OIHP materials………………………………………………………...9

Figure 2.2 The structures of PSCs. (a), i) Meso-porous structure ii) conventional planar structure iii) Inverted planar. (b), Interfaces in a planar-structured PSC shown schematically………………………12

Figure 2.3 Advanced applications for integrated PSCs…………………………….……………….…13

Figure 2.4 Environmental and operational variables are used to illustrate the intrinsic and extrinsic stability of PSCs…………………………………..…………...……….…………………...………14

Figure 2.5 Illustration of the low-dimensional RP 2D perovskite structure…………………….……....16

Figure 2.6 The RP-, DJ-, and ACI-phase 2D perovskites structures……………….…………...……17

Figure 2.7 Schematic of 2D perovskite passivation effect in 2D/3D heterojunctions………...……...18

Figure 2.8 (a) The alignment of the energy levels. The 3D perovskite layer with $BA_2MA_{n-1}Pb_nI_{3n+1}$ for various n values ($n \leq 4$). (b) Effect of 2D perovskite layer thickness on PCE variation in *n-i-p* and *p-i-n* planar 3D/PP-2D PSCs. (c) Energy level scheme for films treated with OLAI and without. Schematic of the conventional 2D treatment (d) with $n \leq 2$ RDPs and the quasi-2D treatment (e) with $n \geq 2$ RDPs. (f) A typical cross-section 2D/3D heterostructure in the *p-i-n* configuration. Band alignment of PSCs after 2D or quasi-2D therapy (g, h) ……………………………………….………………………...….22

Figure 2.9 (a), *J-V* curves of the control, target-1, and target-2 champion cells. (b), PCE and V_{OC} of the corresponding devices. (c), The corresponding devices' Mott-Schottky plots. (d), EQE spectra and integrated J_{SC} of the corresponding devices. (e), V_{OC} versus light intensity for the corresponding devices. (f), TRPL spectra of the control, target-1, and target-2 films. (g−i), Time-resolved emission spectra (TRES) of the control (g), target-1 (h), and target-2 (i) films…………………………………….…….26

Figure 2.10 (a), (b), SCAG and TIAG process schematics. (c), (d), TOF-SIM depth profiles of $PhBA^+$ (green) in SCAG and TIAG perovskite film. (e), Illustration of the morphological alteration resulting from the bending test of several perovskite films applied to a flexible ITO-PET substrate. After bending for various cycles, the control and target perovskite films are shown in corresponding SEM images (f and g, respectively). Take note that the bending cycles were denoted by the numbers that followed the sample names……………………………………………………………………………………30

Figure 2.11 C-AFM images of (a) reference and (b) 2D/3D perovskite films…………………………33

Figure 2.12 High-angle annular dark-field STEM (HAADF-STEM) cross-sectional picture of a 2D perovskite material revealing its perpendicular orientation, zoomed in to the region close to the top C_{60} contact……………………………………………………………………………………34

Figure 2.13 SEM image of E1-doped $MAPbI_3$ film from (a) cross-sectional and (b) top-view. (c), The highly packed arrangement of E1 molecules on $MAPbI_3$ nanocrystals is illustrated in the scheme. (d), TEM image (e) HAADF-STEM image and (f) elemental mapping of the E1-$MAPbI_3$ nanocrystal……………………………………………………………………………………35

Figure 2.14 Chemical element distribution in the vertical direction can be revealed via EELS mapping. A HAADF-STEM image (a) and associated EELS mapping images of triple-layer TiO_2/$CH_3NH_3PbI_3$/Spiro-OMeTAD atomic areal densities for titanium (b), oxygen (c), and iodine (d)..35

Figure 2.15 Electron microscopy methods used to investigate nanomaterials. (a), Reciprocal-space diffraction in TEM mode offers information on the crystal structure, while real-space imaging allows for the observation of morphology. (b), In STEM mode, several imaging techniques have been used to examine the crystal structure (such as BF, ABF, (HA)ADF, iDPC, and 4D-STEM), composition (EDX and EELS), and electronic structure (EELS)……………………………………………………40

Figure 2.16 Damage mechanism of $FAPbI_3$ detected under a scanning electron beam in a 30 nm thick film produced with near-ideal stoichiometry…………………………………………………41

Figure 3.1 Preparation method of 2D/3D perovskite heterojunctions……………………………………45

Figure 3.2 Spherical Aberration Corrected Transmission Electron Microscope………………………47

Figure 3.3 Cross-sectional STEM sample preparation…………………………………………………49

Figure 3.4 Schematic of 4D-STEM experiment. Collected nano beam electron diffraction (NBED) can be employed to scrutinize the crystallinity and the orientation of the perovskite grains……………………………………………………………………………………..51

Figure 4.1 SEM images of perovskite film treated with different concentrations of PEAI. (a), Control $FA_{0.9}Cs_{0.1}PbI_3$ perovskite film; (b), treated with 5 mg/mL PEAI; (c), treated with 10 mg/mL PEAI……………………………………………………………………………………57

Figure 4.2 SEM images of perovskite film treated with 10 mg/mL PEAI and different amounts of FACl. (a), $FA_{0.9}Cs_{0.1}PbI_3$ perovskite film treated with 10 mg/mL PEAI; (b), 10 mg/mL PEAI with 0.0125% mmol/mL FACl addition; (c), 10 mg/mL PEAI with 0.05% mmol/mL FACl addition…………………………………………………………………………………...58

Figure 4.3 HAADF-STEM image (a) and magnified image (b) and line profile image (c) of yellow arrow area in the 2D/3D perovskite device, treated with 10 mg/mL PEAI…………………………..59

Figure 4.4 HAADF-STEM image (a) and (b) and line profile image (c) of yellow arrow area in the 2D/3D perovskite device, treated with 10 mg/mL PEAI with 0.05% mmol/mL FACl addition……………………………………………………………………………………..60

Figure 4.5 Stability test of perovskite films with different concentrations of Cl^- addition. (a), Initial sample; (b), Sample placed in RT RH~20℃ 30%-40% for 7 days. (c), Sample placed in ~ 85℃ 85% humidity for 1 min……………………………………………………………………61

Figure 4.6 Device performance of PSCs with different treatments. (a) Control sample $FA_{0.9}Cs_{0.1}PbI_3$; (b) treated with 5 mg/mL PEAI; (c), 5 mg/mL PEAI with 0.05% mmol/mL FACl addition……………62

Figure 4.7 Top-view SEM images of (a), $FA_{0.9}Cs_{0.1}PbBr_3$ perovskite film; (b), $FA_{0.9}Cs_{0.1}PbBr_3$ perovskite film treated with 10 mg/mL PEAI. (c), Magnified SEM images of $FA_{0.9}Cs_{0.1}PbBr_3$ perovskite film treated with 10 mg/mL PEAI. ……………………………………………………………63

Figure 4.8 HAADF-STEM image of (a) $FA_{0.9}Cs_{0.1}PbBr_3$ PSC treated with 10 mg/mL PEAI. (b), Magnified HAADF-STEM image of orange square in (a). ……………………………………………64

Figure 4.9 HAADF-STEM image of (a) $FA_{0.9}Cs_{0.1}PbBr_3$ PSC treated with 5 mg/mL PEAI. (b), Magnified HAADF-STEM image of orange square in (a). ……………………………….…………65

Figure 4.10 HAADF-STEM image of grain boundaries on (a) $FA_{0.9}Cs_{0.1}PbBr_3$ PSC treated with 5 mg/mL PEAI. (b), Magnified HAADF-STEM image of orange square in (a). ………………..………66

Figure 4.11 Top-view SEM images of (a), $FA_{0.9}Cs_{0.1}PbI_3$ perovskite film treated with 10 mg/mL PEABr. (b), Magnified SEM images of $FA_{0.9}Cs_{0.1}PbBr_3$ perovskite film treated with 10 mg/mL PEABr. …………………..…………………………………………………………………...……67

Figure 4.12 HAADF-STEM image of (a-d) $FA_{0.9}Cs_{0.1}PbI_3$ PSC treated with 10 mg/mL PEABr. ……………………………………………………………..……………………………..….68

Figure 5.1 Schematic illustration of 2D perovskite growth and distribution of LSS sample..................72

Figure 5.2 SEM images of $FA_{0.9}Cs_{0.1}PbI_3$ treated with PEAI with and without 5 mg/mL PCBM interlayer. (a), (c), SEM images of $FA_{0.9}Cs_{0.1}PbI_3$ treated with 10 mg/mL PEAI in IPA solution with and without 5 mg/mL PCBM interlayer. (b), (d), Magnified SEM images of the selected area as marked by the orange square in (a) and (c)…………………………….…………………………………………………73

Figure 5.3 HAADF-STEM images of the (a) LSS sample and (b) control sample. ……………...……75

Figure 5.4 SEM images of $FA_{0.9}Cs_{0.1}PbI_3$ treated with concentrations of (a-f) 0,1,3,5,10,15 mg/mL PEAI in IPA solution ……………………………………………………………….………….………75

Figure 5.5 HAADF-STEM images of 3D $FA_{0.9}Cs_{0.1}PbI_3$ films treated with concentrations of (a-f) 0,1,3,5,10,15 mg/mL PEAI in IPA solution……………………...……………………………………76

Figure 5.6 The morphology of 2D perovskite layers on 3D perovskite films prepared using dilute PEAI solutions and without the PCBM interlayer. **(a), (b),** SEM and cross-sectional STEM-HAADF image of the 2D perovskite layer (on top of the 3D perovskite film) prepared using 3 mg/mL PEAI, respectively. **(c), (d),** Top-view SEM and cross-sectional STEM-HAADF image of the 2D perovskite layer (on top of the 3D perovskite film) prepared using 5 mg/mL PEAI, respectively……………………………..……77

Figure 5.7 SEM images of FA0.9Cs0.1PbI3 with concentrations of (a-f) 0,1,2,3,5,10 mg/mL PCBM interlayer and treated with 10 mg/mL PEAI in IPA solution…………….……………...…………78

Figure 5.8 EELS STEM analysis. (a), (b), HAADF-STEM images of $FA_{0.9}Cs_{0.1}PbBr_3$ PSCs with 10 mg/mL PCBM interlayer and treated with 10 mg/mL PEAI in IPA solution. Green rectangle area in (b) is the survey region of EELS edge signal of $I(M_{4,5})$ and blue rectangle area in (b) is the survey region of EELS edge signal of $Br(L_{2,3})$. (c), (d), Corresponding EELS mapping images of iodine signal and bromine signal. (e), (f), Line profile of the signal intensity marked by yellow orange arrows in (c) and (d). ……………………………………………………………………………...…………77

Figure 5.9 (a), PEA^+ only contains C-N σ bond, while FA^+ contains both C-N σ bond and π bond. **(b),** N K-edge was signal extracted from regions I-V of the LSS structure. **(c),** Non-normalized N K-edge profiles of regions I-V in **(b)**, demonstrating evident σ bond dominant (PEA^+) characteristics in regions I-IV and π bond characteristics (FA^+) in region V. The N K-edge signal intensity in Region IV is higher than in Region I-III. Region I-V successively refers to the 2D perovskite layer, the top region of the PCBM interlayer, the middle region of the PCBM interlayer, the PCBM/3D perovskite interfacial region, and the 3D perovskite film bulk region…………………………………………………………...….81

Figure 5.10 EELS ELNES analysis of the LSS structure. **(a), (c),** N K-edge signal extracted from regions I-V of two different regions of the LSS structure. **(b), (d),** Non-normalized N K-edge profiles of regions I-V in **a**, **c**, respectively, demonstrating clear σ bond dominant (PEA^+) characteristics in regions I-IV and π bond characteristics (FA^+) in region V. ……………………………………………………………82

Figure 5.11 2D perovskite monolayers on 3D perovskite grains. (a), (b), HAADF-STEM images of $FA_{0.9}Cs_{0.1}PbI_3$ PSCs with 2 and 10 mg/mL PCBM interlayer and both treated with 10 mg/mL PEAI in IPA solution. (c), (d), Line profiles of the row of signal intensity marked by yellow arrows in (a) and (b). ……………………………………………………………………………...……………83

Figure 5.12 HAADF-STEM images of $FA_{0.9}Cs_{0.1}PbI_3$ PSCs with different concentration of PCBM interlayer and treated with 10 mg/mL PEAI. HAADF-STEM images of PSCs with (**a-f**) 0,1,2,3,5,10 mg/mL PCBM interlayer and treated with 10 mg/mL PEAI in IPA solution. Scale bar 100 nm……..…84

Figure 5.13 (a), (b), Magnified HAADF-STEM images of the control sample. (c), Signal intensity line profile of the row marked in (a). ……………………………………………………….…….……86

Figure 5.14 2D perovskite with varied orientations in the control device. HAADF-STEM image of the control device, treated with 10 mg/mL PEAI. Area 1 and area 2 Fast Fourier transform (FFT) shows the 2D $n = 2$ perovskite on 3D perovskite surface have different orientation. ……………………………...86

Figure 5.15 The *n*-value arrangement of 2D perovskite in control device. HAADF-STEM image and corresponding line profile of red arrow area in left image of control device, treated with 10 mg/mL PEAI. ………………………………………………………………………………………..87

Figure 5.16 2D perovskites distribution on 3D perovskite grains surface and grain boundaries in control device. (a), HAADF-STEM image of the control device, treated with 5 mg/mL PEAI. (b), (c), Magnified STEM-HAADF images of the selected area in (a). (d), (e), Corresponding line profiles of the row of signal intensity marked by yellow arrows in (b) and (c). ………………………………………….…88

Figure 5.17 The remaining PbI_2 in 3D perovskite of control device. HAADF-STEM image of the control device, treated with 10 mg/mL PEAI. (a), PbI_2 in 3D perovskite grains. (b), Magnification image of selected area in (a). …………………………………………...…………………...………89

Figure 5.18 $FA^+/Cs^+/I^-$ lost on the 3D perovskite surface in control device. Cross-sectional STEM image of 3D-2D device, treated with 10 mg/mL PEAI. (a), HAADF-STEM image of 3D perovskite grains. (b), Magnification image of selected area in (a). (c), Atomic-resolution integrated differential phase contrast (iDPC)-STEM image of area in (a). After PEAI solution treatment, some of the $FA^+/Cs^+/I^-$ will be lost on the surface of 3D grains. ……………………………………..……………..….………89

Figure 5.19 2D perovskites parallel and non-parallel to 3D grain surfaces in control device. HAADF-STEM images of the control device, treated with 10 mg/mL PEAI. (a), Horizontal and non-horizontal

2D perovskites simultaneously grow on the surface of 3D grains. (b), High-resolution image of non-horizontal 2D perovskite. (c), FFT of selected area in (b). ……………………………………………90

Figure 5.20 (a), (b), Magnified HAADF-STEM images of the LSS sample. (c), Signal intensity line profile of the row marked in (a). ……………………………………………………………………..91

Figure 5.21 The *n*-value arrangement of 2D perovskite in LSS device. HAADF-STEM image (left) and line profile image (right) of yellow arrow area in the LSS device (with 5 mg/mL PCBM interlayer), treated with 10 mg/mL PEAI. ……………………………………………………….………………92

Figure 5.22 The LSS samples prepared on the 3D perovskite with different [PbI_2] fractions. **(a), (b),** XRD results of 3D perovskites with different PbI_2 fraction (($(FAI)_{0.9}$·$(CsI)_{0.1}$·$(PbI_2)_{0.85}$, $(FAI)_{0.9}$·$(CsI)_{0.1}$·$(PbI_2)_1$ and $(FAI)_{0.9}$·$(CsI)_{0.1}$·$(PbI_2)_{1.15}$) and corresponding LSS samples prepared by 3D perovskites, respectively. **(c),** STEM-HAADF image of the LSS-0.85PbI_2 sample. **(d),** Magnified image of the squared region in c shows the $n = 2$ phase 2D perovskite. **(e),** STEM-HAADF image of the LSS-1.15PbI_2 sample. **(f),** Magnified image of the squared region in e shows the 2D perovskite with $n = 1$ and $n = 2$ phases……………………………………………………………………….…..92

Figure 5.23 Near-surface grain boundary microstructures. (a), HAADF-STEM image of 3D-2D device. (a_1)-(a_4), The NBED images of the corresponding region on the control device. The scale bar is 5 nm^{-1}. (b), Virtual DF-STEM image reconstructed from NBED signals of (a_3) and (a_4). (c), HAADF-STEM image of the LSS sample. (c_1)-(c_4), The NBED images of the corresponding region on the LSS sample. The scale bar is 5 nm^{-1}. (d), Virtual DF-STEM image reconstructed from NBED signals of (c_2), (c_3) and (c_4). ………………………………………………………………………………….………95

Figure 5.24 Dark-field STEM images reconstructed from selected nano-beam diffraction signal of 3D-2D sample. Scale bar, 50 nm. ……………………………………………………………..………96

Figure 5.25 Dark-field STEM images reconstructed from selected nano-beam diffraction signal of the LSS sample. Scale bar, 50 nm. ……………………………………...………………..……96

Figure 5.26 XRD patterns of the neat 3D, control, and LSS films.. …………………..……………..…99

Figure 5.27 Optoelectronic properties and stability of perovskite films. (a), GIWAX patterns of pristine 3D, control, and LSS films. (b), Normalized PL spectra of pristine 3D, control, and LSS films. (c), PL images of control and LSS films at wavelength ~510 nm, 570 nm, and ~780 nm, which correspond to *n* = 1 and 2 layers and 3D layers, respectively. The scale bar is 1 μm. Steady-state PL spectra of pristine 3D, control, and LSS films deposited on bare glass with excitation from glass (d) and perovskite (e) sides. Time-resolved PL spectra of pristine 3D, control, and LSS films deposited on bare glass with excitation from glass (f) and perovskite (g) sides. (h), Evolution of 2D peak and 3D bandgap of control and LSS films by tracking UV-vis spectra under RH of 40%. (LSS: 3D perovskite sample with the PCBM-mediated 2D surface passivation treatment; Control: 3D perovskite sample with conventional 2D surface passivation treatment; Pristine 3D: 3D perovskite sample with no 2D surface passivation treatment.)……………………………………...………………………………………………100

Figure 5.28 Humidity stability of different films. UV-vis spectra of control **(a)** and LSS **(b)** films exposed under RH of 75 ± 10% for 55 days. The insets show the evolution of the 3D bandgap during the aging time…………………………………………………………………………..…………102

Figure 5.29 Schematic illustration of device configuration for LSS-based inverted PSCs. (b), *J*-*V* curves of the best-performing pristine-3D, control, and LSS PSCs (at both reverse and forward scans). (c), Energy level scheme for pristine-3D, control, and LSS PSCs extracted from UPS data ([2-(3,6-Dimethoxy-9H-carbazol-9-yl)ethyl]phosphonic acid, MeO-2PACz; bathocuproine, BCP)...……..…103

Figure 5.30 UV-vis absorption spectra of pristine-3D, control, and LSS films with the 3D perovskite composition of $Cs_{0.05}(MA_{0.05}FA_{0.95})_{0.95}Pb(I_{0.95}Br_{0.05})_3$.. ………………………..……………………..…104

Figure 5.31 Concentration optimization of PEAI and PCBM for *p-i-n* PSCs. *J-V* curves of 3D-2D PSCs with different concentrations of PEAI (**a**) and PCBM (**b**). The pure 3D device is used as a reference………………………………………………………………………………………...…104

Figure 5.32 Hysteresis analyses of *J-V* curves for different *p-i-n* PSCs. *J-V* curves of PSCs for pure 3D (a), control (b), and LSS (c-g) with different concentrations of PCBM under forward and reverse scanning. h, The evolution of HI with the PCBM concentration increases……………………..………108

Figure 5.33 Statistical distributions of the photovoltaic parameters (V_{OC}, J_{SC}, FF, and PCE) for 50 individual *n-i-p* 3D-2D devices with or without PCBM interlayer. The 3D device is utilized as a reference. Both the concentrations of PEAI and PCBM are 5 mg/mL. ……………………………..……109

Figure 5.34 Hysteresis analyses of *J-V* curves for different *p-i-n* PSCs. *J-V* curves of PSCs for pure 3D (a), control (b), and LSS (c-g) with different concentrations of PCBM under forward and reverse scanning. h, The evolution of HI with the PCBM concentration increases. ……………………...…110

Figure 5.35 Summary of the reported V_{OC} values for the representative PSCs with different bandgaps…………………………………………………………………………... ………...…111

Figure 5.36 Helium La (21.22 eV) spectra of secondary electron cutoff (a) and valence band (b) for different films. Helium La (21.22 eV) spectra of secondary electron cutoff (c) and valence band (d) for PCBM ETL……………………...…………………………………………………………….…112

Figure 5.37 Mott-Schottky (*M-S*) plots of pure 3D, control, and LSS devices ………………..………113

Figure 5.38 Evolution of normalized photovoltaic parameters (PCE, V_{OC}, J_{SC}, and FF) for control and LSS PSCs in N_2 under continuous one-sun illumination. The error bars represent the standard deviation for five devices…………………………………………………………………..…………………114

Figure 5.39 Evolution of the series resistance (*R*s) and shunt resistance (*R*sh) for control and LSS PSCs in N2 under continuous one-sun illumination.……………………………..………………………115

Figure 5.40 (a), Operational stability measured at maximum-power-point tracking in N_2 under continuous one-sun illumination for control and LSS PSCs. The initial PCEs of devices with and without LSS in (a) were typically 21.69% and 23.72%, respectively. (b), Evolution of PCEs of control and LSS PSCs under 85% RH and 85°C. The error bars represent the standard deviation for 13 devices. (c), (d), HAADF-STEM images of control and LSS films after the identical damp-heat aging. (LSS: 3D perovskite sample with the PCBM-mediated 2D surface passivation treatment; Control: 3D perovskite sample with conventional 2D surface passivation treatment; Pristine 3D: 3D perovskite sample with no 2D surface passivation treatment.)…………………………………………………………….…116

Figure 5.41 Initial PCEs of control and LSS PSCs. ……………………………..……………………117

Figure 5.42 STEM-HAADF characterization of the control and LSS device samples before the MPP stability tests. (a), STEM-HAADF image of pristine control devices without PCBM interlayer. (b), Magnified STEM-HAADF image of the squared region in (a) shows the 2D and 3D perovskite structure. (c), STEM-HAADF image of pristine LSS devices. (d), Magnified STEM-HAADF image of the squared region in c shows the LSS structure. ……..…………………………………………………………118

Figure 5.43 STEM-HAADF characterization of control and LSS devices after 15 days of MPP operation. (a), The grain-boundary regions of the control device exhibit serious damage. (b), Magnified STEM-HAADF image of the squared region in (a) showing the existence of PbI_2. (c), Only minor damage occurs in the LSS device, mainly at the buried interface. (d), The LSS structure remains intact………..……..119

Figure 5.44 SEM characterization for the ambient degradation of control and LSS samples. (a), (b), SEM images of the control sample stored at 50-60% relative humidity for 0 and 15 days, respectively. (c), (d), SEM images of the LSS sample stored at 50-60% relative humidity for 0 and 15 days, respectively…..120

Figure 5.45 STEM-HAADF characterization for the ambient degradation of control and LSS devices. (a), STEM-HAADF image of the control device stored at 50-60% relative humidity for 15 days. (b), Magnified image of the squared region showing the prominent existence of PbI_2. (c), STEM-HAADF image of the LSS device exhibiting little change after the ambient storage. (d), Magnified image of the squared region in (c) showing the retention of the complete LSS structure……………………………………………...121

List of Tables

Table 2.1. Summary of several causes of PSC deterioration and related strategies for enhancing device stability……………………………………………………………………………………15

Table 5.1 Summaries of fitting parameters in TRPL spectra for different samples under different detection ……………………………………………………..…………………………..……101

Table 5.2 The photovoltaic parameters of 3D *n-i-p* devices with different concentrations of PEAI under reverse scanning. ……………………………….……………………………...……105

Table 5.3 The photovoltaic parameters of 3D-2D *n-i-p* devices with different concentrations of PCBM under reverse scanning. ……………………………………...……………..………105

Table1 5.4 The photovoltaic parameters of champion *p-i-n* 3D-2D devices with or without the PCBM interlayer under forward and reverse scanning. ……………………………..……..107

Chapter 1 Introduction

As civilization advances, the need for energy is also growing, and our reliance on energy can be witnessed in our apparel, food, lodging, and transportation. While enjoying the conveniences of modern life, the extraction, transportation and processing of traditional fossil energy sources have caused serious damage and pollution to the natural environment, triggering a series of environmental problems[1-3]. To address the increasing energy demand while ensuring environmental protection, a wide range of non-conventional and conventional renewable energy is necessary to be incorporated[4,5]. Solar energy is a secure, environmentally friendly, limitless, and highly significant form of renewable and sustainable energy[6,7]. The utilization of solar energy also helps to stabilize energy prices and brings many social, environmental and economic benefits[8,9]. Thus, the subject of how to utilize solar energy more efficiently has emerged as a pressing scientific issue in both industry and scientific study. At this point, solar cells have progressed from silicon solar cells to include many types of thin film solar cells, quantum dot cells, dye-sensitized solar cells, perovskite solar cells (PSCs), and other revolutionary solar cell technologies. Among these, PSCs have shown the most rapid development. In just a dozen years, their efficiency has become comparable to the highest efficiency of single crystalline silicon cells, which can demonstrate their significant potential[10].

1.1 Background

Organic-inorganic halide perovskite (OIHP) materials have been utilized in photovoltaic cells, which have many advantages over other solar cell technologies. Under controlled laboratory circumstances, the power conversion efficiency (PCE) of PSCs has been demonstrated to exceed 26.7%

in less than twenty years. This level of efficiency is comparable to the highest PCE of conventional silicon solar cells. (Figure 1.1)[10-12]. Perovskite solar cells are an affordable option for batch production due to their use of inexpensive components along with simple manufacturing procedures like solution processing and printing technologies. Moreover, the versatility of these materials is another advantage, given that they can be produced on diverse substrates, such as flexible and transparent materials, enabling their integration into a broad spectrum of devices[13-15]. One notable feature of perovskite materials is their capacity to modify their electrical and optical characteristics by chemical composition adjustments. Moreover, it is worth noting that perovskite materials possess a substantial absorption coefficient, enabling them to effectively capture solar energy despite their significantly reduced thickness compared to silicon solar cells.

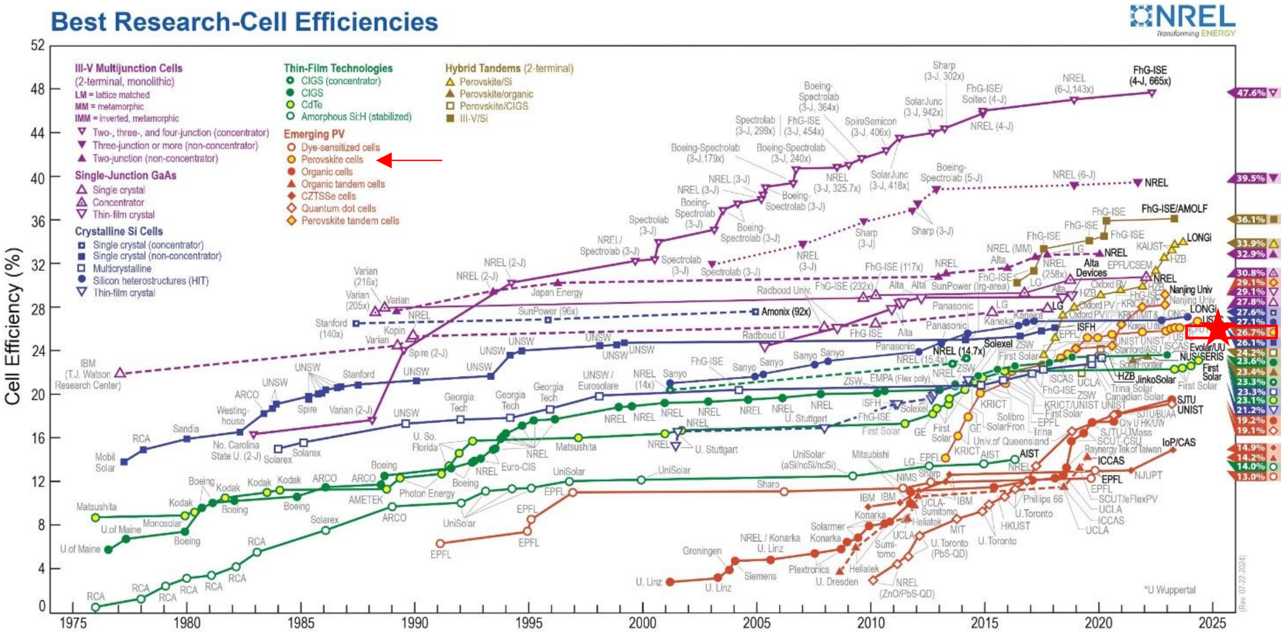

Figure 1.1 Best Research-Cell Efficiencies[10].

The stability problem of OIHP materials and devices is a key issue limiting the further development and application of them. Under the premise of ensuring the PCE, how to improve the stability of PSCs in different environments has become a critical issue in recent years. When OIHP is exposed to elevated temperature and humidity, it suffers rapid decomposition due to the destruction of its lattice structure. In the case of methylammonium lead iodide ($MAPbI_3$), the main reaction that occurs is the destruction and decomposition of $MAPbI_3$ into methylammonium iodide (CH_3NH_3I) and lead iodide (PbI_2)[16]. This process renders the perovskite inactive, and PbI_2 is non-conductive, which further diminishes the device's performance. By altering the cation in the perovskite, the researchers, Park et al., were able to enhance the material's thermal stability. They achieved this by substituting methylammonium $CH_3NH_3^+$ (MA^+) iodide with formamidine $HN{=}CH(NH_3)^+$ iodide in the creation of $HN{=}CH(NH_3)PbI_3$ ($FAPbI_3$) devices. Their results showed that $FAPbI_3$ exhibited superior thermal stability compared to $MAPbI_3$[16]. Through the replacement of methylammonium with the more stable formamidine and the incorporation of the inorganic cations Rb^+ and Cs^+, Saliba's group successfully synthesized $RbCsFAPbI_3$ perovskite. Subsequently, they fabricated devices without methylammonium (MA-free) and observed a significant enhancement in their stability[17]. Karunadasa et al. chose $C_6H_5(CH_2)_2NH_3^+$ phenylethylamine (PEA^+) as a substitute for $CH_3NH_3^+$ in order to produce $(PEA)_2(CH_3NH_3)_2Pb_3I_{10}$ perovskite as the absorbing layer[18]. They figured out that this particular kind of two-dimensional (2D) perovskite film exhibited improved stability in humid conditions. These kinds of larger organic cations were further applied to the preparation of OIHP, and the researchers also prepared two-dimensional/three-dimensional (2D/3D) PSCs whose excellent stability was further verified[19-22].

In order to attain precise manipulation of the distribution of 2D perovskites and understand its interaction with 3D perovskites, an extensive comprehension of the heterojunction structure formed by 2D/3D perovskites is essential. Conventional diffraction-based structure analysis has challenges in precisely identifying interface defects because of their localized and non-repetitive characteristics. On the other hand, transmission electron microscopy (TEM) can provide high-resolution real-space images of perovskite crystal structure. However, the use of high-energy electron beams for imaging can easily alter the unstable structure of perovskites and result in their decomposition. Recent promising developments in low-dose high-resolution scanning transmission electron microscope (HR-STEM) characterization are significant in their capability to identify structures of perovskite materials or nanomaterial samples without the requirement of special cryogenic conditions or detectors[19,20,23,24].

1.2 Objectives of Research

This thesis aims to explore the utilization of low-dose STEM to analyze and understand the structure and functions of 2D/3D PSCs. It is important to carefully consider the process of preparing samples using a focused ion beam (FIB) to acquire a suitable thickness for STEM observation. Additionally, efforts should be made to minimize any potential damage to the sample caused by the electron beam. The optimal level of electron radiation can be determined by regulating the beam current and exposure duration while observing the condition of the sample.

Another goal of this thesis is to investigate the formation and distribution of 2D perovskite layers on 3D perovskite grains with halide ions Br^-, I^- and Cl^- participation, based on organic spacer cation solutions containing PEA^+ via a spin-coating method. The formation of 2D perovskite layers was initially observed by applying a phenethylammonium iodide (PEAI) solution onto 3D perovskite $Cs_{0.1}FA_{0.9}PbI_3$ surface. Subsequently, formamidinium chloride (FACl) was introduced into the PEAI solution to find out its impact on the production and dispersion of 2D perovskite. Then, PEAI was substituted with PEABr for the purpose of treating $Cs_{0.1}FA_{0.9}PbI_3$. The variations in the structure of the 2D/3D heterojunctions were analyzed afterward. In addition, the composition of 3D perovskite was adjusted to produce films of $Cs_{0.1}FA_{0.9}PbBr_3$. The films were subsequently subjected to treatment with a PEAI solution to investigate the existence of 2D perovskite layer on 3D grains.

In addition, this thesis is intended to construct a stable 2D/3D heterojunction with improved efficiency by utilizing a comprehensive understanding of the structure of 2D/3D perovskites. In this thesis, a layered perovskite heterojunction is prepared by employing [6,6]-phenyl-C_{61}-butyric acid methyl ester (PCBM) molecules as an intermediary layer. Distinguishing the structure of conventional

2D/3D perovskite, the PCBM layer mediated surface reaction, leading to a uniform, purer phase 2D perovskite capping over the entire 3D perovskite absorber surface. In addition, this method also prevents the detrimental grain-boundary etching encountered in conventional approaches. Compared with the 2D/3D heterojunctions formed by directly spin-coating 2D organic salt solutions, PSCs with this structure demonstrate higher PCE, and their exceptional stability is further verified.

Finally, based on the above experimental results, this thesis will analyze the process of fabricating 2D/3D perovskite heterojunctions through the spin-coating method. It will also outline the characteristics and factors that need to be considered when manufacturing these heterojunctions. Additionally, this thesis will include practical recommendations for boosting the performance as well as the durability of 2D/3D PSCs.

1.3 Dissertation Scope and Organization

This thesis focuses on evaluating the effectiveness of the formation of 2D/3D perovskite heterojunctions through electron microscopy. Low-dose STEM is used to analyze the distribution and effect of 2D perovskite layer on 3D perovskite grains, which can provide valuable suggestions for improving both the efficiency and lifespan of PSCs. The thesis is structured into six chapters, which are outlined below:

Chapter 1: This chapter gives background information and describes the purpose of related study in this thesis. The dissertation scope and arrangement of this thesis are also laid out.

Chapter 2: This chapter provides a comprehensive introduction to the fundamental aspects of 2D/3D PSCs. This chapter will cover major issues and concepts pertaining to the thesis, including the structure of OIHPs and PSCs. This chapter will also discuss the causes of the inadequate stability of PSCs and propose methods to enhance their stability. Finally, the key subject of this thesis, 2D/3D perovskite heterojunctions and interface characterization methods for them will be addressed in detail.

Chapter 3: This chapter highlights significant characterization methods utilized in the thesis, including FIB and aberration-corrected TEM. It also covers the characterization of perovskite films and measurement of device performance.

Chapter 4: This chapter involved analyzing the impact of the halide ion on the arrangement of 2D perovskite within 2D/3D perovskite heterojunctions. This study focused on examining the dispersion of 2D perovskite and its impact on 3D perovskite through modifying the constituents of 2D organic spacer solutions and 3D perovskite, while incorporating various halide ions.

Chapter 5: This chapter aimed at the construction of a lattice-resolved laminate-structured perovskite heterointerface. This chapter will introduce the process for developing a novel 2D/3D perovskite heterojunction by utilizing the PCBM interlayer. Then, an analysis is conducted on the dispersion and impact of 2D perovskite with a unique structure on a 3D grain. We conducted more research on the optical properties and durability of 3D-2D perovskite films, the performance and durability of 3D-2D PSCs.

Chapter 6: The conclusions based on the above experiments will be concisely summarized in this chapter. Additionally, suggestions will be provided on how to design a stronger and more efficient heterojunction of 2D/3D perovskite.

Chapter 2 Overview of 2D/3D PSCs and Characterization Methods for Heterojunctions

2.1 Introduction

OIHP materials offer enormous opportunities for constructing efficient, low-cost optoelectronic devices[12,25-27]. The unique photovoltaic properties of PSCs, such as the ability to adjust the bandgap, low exciton binding energy, long carrier diffusion length, and efficient carrier transport, contribute to their exceptional PCE, which has reached a historic high in recent years[12,25,28-30]. Despite the excellent performance of PSCs, the main concern has always been how to enhance their efficiency and stability. Researchers have made attempts to broaden and enhance the materials used in the electron transport layer (ETL)[31-34] and hole transport layer (HTL)[35-38]. In addition, they participate in the process of controlling the constituents of the perovskite active layer[39-42] and studying the interface engineering on PSCs[43-46]. Among these methods, the technique of constructing 2D/3D perovskite heterojunctions in PSCs has been extensively validated as a very efficient approach[47-54]. Because 2D/3D PSCs can merge the durability of 2D perovskites with the superior ability of 3D perovskites to transport charges.

This chapter will provide an introduction to the structure and properties of OIHPs, as well as PSCs. Discussions will also focus on the factors that influence the stability of PSCs, and potential methods to enhance their stability will be proposed. Some topics relevant to 2D/3D heterojunction will be further explored, such as the structure of different types of 2D perovskites and functions for appropriate 2D perovskites in PSCs, and some important interface characterization methods of heterojunction.

2.2 Organic-inorganic Halide Perovskite Materials

During a scientific expedition to Russia in 1839, German scientist Gustav Rose made the discovery of $CaTiO_3$ in the Ural Mountains. In recognition of the Russian geologist with the same name, Rose termed this compound "perovskite". Nowadays, compounds having the general formula ABX_3 structure are referred to as perovskites. A and B represent metallic elements, whereas X represents a non-metallic element. The chemical ratio between them is 1 part to 1 part to 3 parts. Perovskite oxides typically consist of divalent cations (Mg^{2+}, Ca^{2+}, Sr^{2+}, Ba^{2+}, Pb^{2+}) and tetravalent cations (Ti^{4+}, Si^{4+}, Fe^{4+}), together with oxygen anions. Perovskites utilized in solar cells often exhibit cubic or octahedral structures. The cation A, which is normally a larger organic cation that occupies the unit cell angle and has a coordination number of 12. In OIHP materials, as Figure 2.1 shows, the typical ones are methylammonium ($CH_3NH_3^+$, MA^+, the radius is $R_A = 0.18$ nm), formamidine ($NH_2CH{=}NH_2^+$, FA^+, $R_A = 0.19$-0.22 nm), and ethylammonium ($CH_3CH_2NH_3^+$, EA^+, $R_A = 0.23$ nm); B represents a diminutive metal cation situated within the body-centered position with a coordination number of 6, such as lead (Pb^{2+}, $R_B = 0.119$ nm), tin (Sn^{2+}, $R_B = 0.110$ nm), respectively. X is a halide anion, including iodine (I^-, $R_X = 0.220$ nm), bromine (Br^-, $R_X = 0.196$ nm), and chlorine (Cl^-, $R_X = 0.181$ nm)[55]. The most important property of the perovskite structure is its ability to accommodate stable coexistence of ions with significant variances in radius within the same structure. The variety of arrangements also allows for an assortment of functional possibilities.

OIHPs have outstanding semiconducting properties and can absorb light across a wide spectrum of solar radiation. As a result, they have high efficiency in converting solar power into energy for electricity. OIHPs demonstrate a variety of positive traits that make them well-suited for use in photovoltaic (PV) technology. These properties include elevated charge carrier mobilities, extended carrier lifetimes, and reduced trap densities. Moreover, these materials have exhibited promising capabilities for implementation in diverse applications, including but not limited to light-emitting diodes (LEDs), photodetectors, and X-ray detectors[56-58].

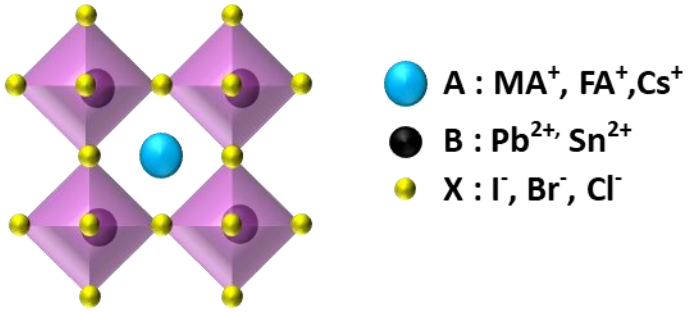

Figure 2.1 Crystal structure of OIHP materials.

2.3 Perovskite Solar Cells

The PSCs can be basically classified into two types of structures: the *n-i-p* structure and the *p-i-n* structure[59]. The *n-i-p* structure may be further classified into meso-porous and conventional planar structures based on the utilization of meso-porous metal oxides as ETL, as seen in Figure 2.2a(i) and (ii). Another structure is the *p-i-n* structure, depicted in Figure 2.2 a(iii). The main distinction between the *n-i-p* and *p-i-n* structures is in the orientation of their current flow.

Substrates, transparent conductive electrodes (TCEs), electron transport layers (ETLs), photoactive layers (PLTs), hole transport layers (HTLs), and metal electrodes make up PSCs.

The initial part is the substrate, which serves as a foundation for the subsequent layers. Typically, the substrate is transparent and can be either stiff or flexible, depending on the specific needs of the device. Glass often serves as a rigid substrate because it is inexpensive and can resist high heat. However, to accomplish the mass production of solar cells, the necessity should be met without delay for cost reduction in manufacturing and the development of appropriate procedures. The prevalent "roll-to-roll" processing technique necessitates a flexible and sufficiently thin substrate, thereby limiting the use of glass in large-scale industrial manufacture[60,61]. Organic polymers, such as polyethylnaphthoate (PEN) and polyethylene terephthalate (PET), are favorable substitutes for glass substrates due to their affordability, transparency, and widespread usage. Currently, PSCs may achieve an efficiency of 25.05% when applied to flexible substrates[62,63].

Indium tin oxide (ITO) or fluorine-doped tin oxide (FTO) is frequently employed as a transparent conductive electrode (TCE) on a transparent substrate. Typical requirements for this electrode are low surface square resistance, high light transmittance, large area coverage, lightweight, ease of processing, and impact resistance.

The ETL works by extracting and transmitting photogenerated electrons that are produced in perovskite materials. The typical electron transport layer consists of a compact inorganic metal oxide layer, such as titanium dioxide (TiO_2), zinc oxide (ZnO), tin dioxide (SnO_2) and others. Examples of organic polymer compounds are PCBM and fullerene (C_{60}). Furthermore, in the case of meso-porous PSCs, the ETL is composed of mesoporous metal oxides, specifically meso-porous titanium dioxide (mp-TiO_2) and meso-porous aluminum oxide (mp-Al_2O_3). Meso-porous materials function as support, while the top layer of perovskite nanocrystals fills the pores and forms a linked layer that absorbs light.

The layer of absorber typically consists of metal halide perovskite materials, such as $MAPbI_3$ and $FAPbI_3$, as well as mixed metal halide perovskite compounds, like $FA_{1-x}MA_xPb(I_{1-y}Br_y)_3$, or inorganic perovskite, for example $CsPbI_3$. Perovskite can also be divided into three types based on its structure: 3D perovskite, 2D perovskite, and quasi-2D perovskite.

The HTL can be classified into two types: inorganic HTL and organic HTL. The inorganic HTL includes materials such as nickel oxide (NiO), copper cyanide (CuSCN), copper iodide (CuI), and others. The organic hole transport layer includes polytriarylamine (PTAA), poly(3-hexylthiophene)

(P3HT), 2,2′ ,7,7′ -tetrakis(N,N-di-p-ethoxyphenylamine)-9,9′ -spirobifluorene (spiro-OMeTAD), poly(3,4-ethylenedioxythiophene): poly(styrenesulfonate) (PEDOT:PSS), and other materials.

The metal electrodes used in PSCs are silver (Ag), gold (Au), aluminum (Al), and copper (Cu). The most common electrode materials are the precious metals Au and Ag. The availability of Au reserves is constrained and high-cost. Besides, the Ag electrode is susceptible to corrosion by the perovskite decomposition product hydroiodic acid (HI), which adversely impacts the PSC's stability. As a result, developing a more suitable electrode is an important task that needs to be considered in the future.

The operation of PSCs can be separated into the subsequent steps: Initially, as the sunlight enters, the perovskite material is photoexcited, creating holes in the valence band (VB) and causing electrons to transition to the conduction band (CB). To reach the cathode, electrons go from the perovskite's conduction band (CBM) to the ETL's lowest unoccupied molecular level (LUMO) in organic materials or the inorganic materials' CBM. A hole travels from the perovskite's valence band maximum (VBM) to the anode via organic materials' highest occupied molecular level (HOMO) or inorganic materials' VBM of the HTL. Finally, as revealed in Figure 2.2b[59], a full circuit is formed when electrons and holes are united in the external circuit, resulting in the production of an electric current.

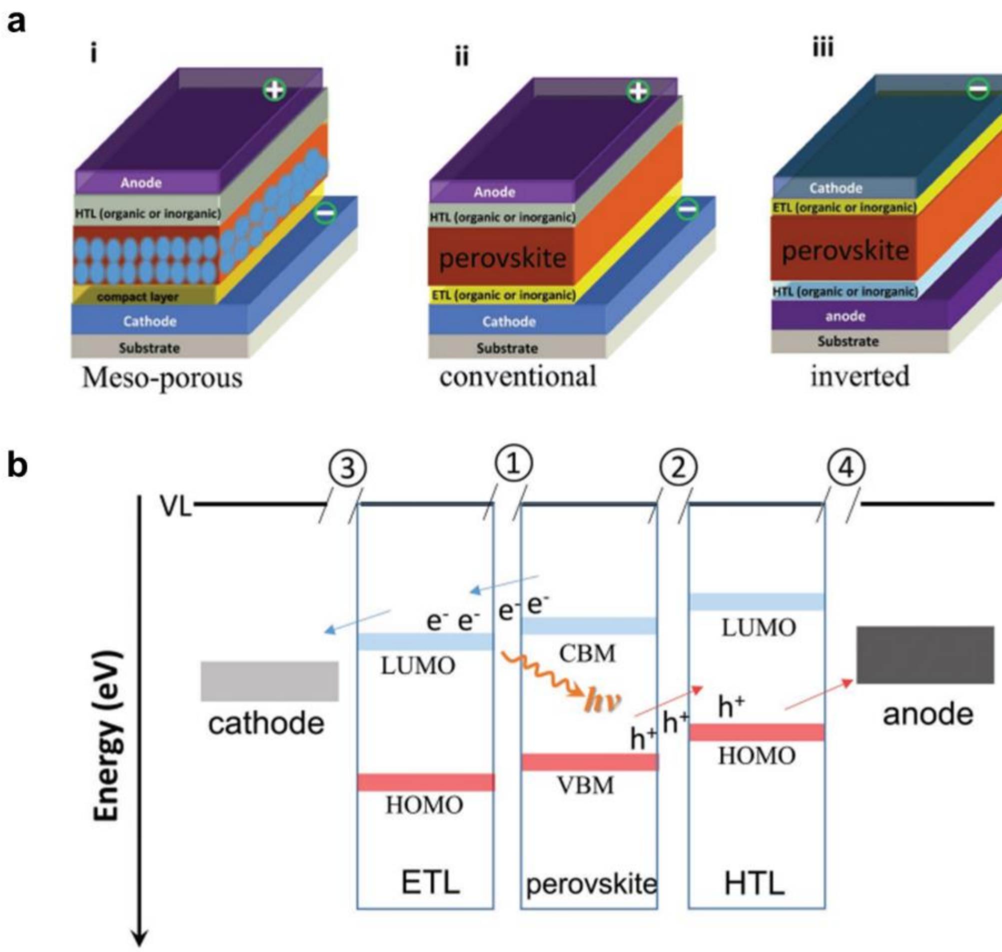

Figure 2.2 The structures of PSCs. **(a),** i) Meso-porous structure ii) conventional planar structure iii) Inverted planar. **(b),** Interfaces in a planar-structured PSC shown schematically[59].

Perovskites possess distinct characteristics and have experienced significant progress in enhancing solar cell performance. As a result, they have been successfully incorporated into various practical applications such as tandem solar cells, building-integrated photovoltaics, space applications, photovoltaic-driven catalysis, integration with batteries and supercapacitors for energy storage systems[64,65]. Notwithstanding the benefits, perovskite solar cells encounter certain obstacles that necessitate resolution, including concerns regarding stability and operation longevity. Despite any limitations, the potential advantages of PSCs render them a highly promising technology for achieving a sustainable future.

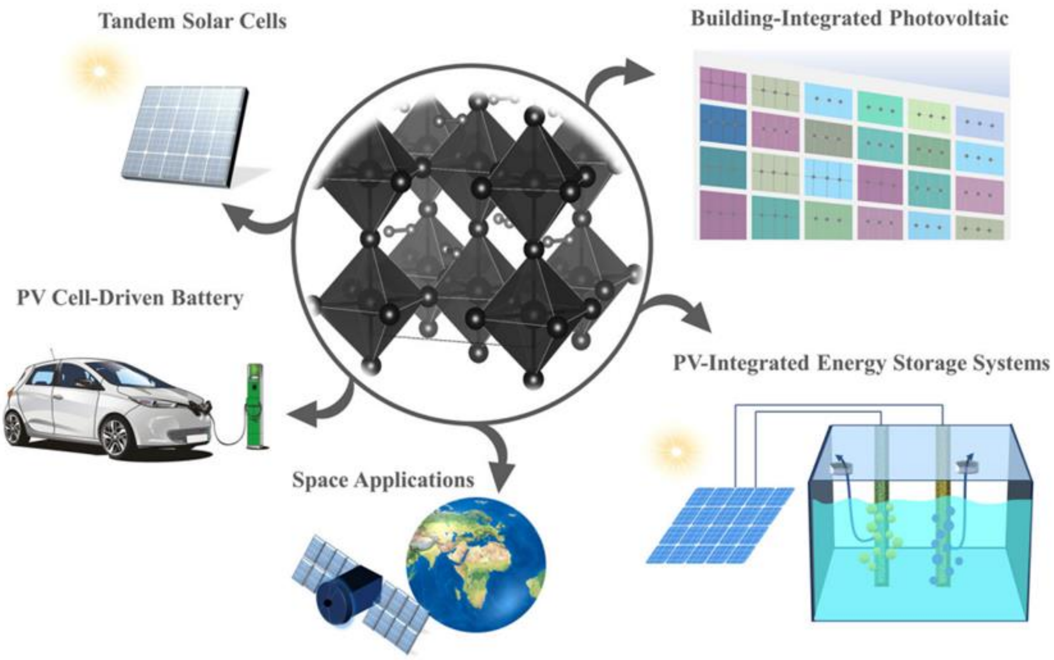

Figure 2.3 Advanced applications for integrated PSCs[65].

2.4 Stability of Perovskite Solar Cells

Instability can occur in PSCs for several reasons[66,67]. Figure 2.4 demonstrates that the chemical instability of perovskite materials is a significant factor that negatively impacts their long-term stability[67]. Moreover, the inherent defects in the perovskite lattice, such as vacancies, interstitials, and anti-sites, can lead to non-radiative recombination, charge trapping, and degradation of the material’s optoelectronic properties. Undesirable byproducts such as lead hydroxide and lead oxide could appear because of the high sensitivity of PSCs to oxygen and moisture. These products may lead to the degradation of the device. In addition, the perovskite material is sensitive to ion migration when subjected to external stimuli such as temperature, humidity, and electric fields because of the weak ionic connection between the inorganic and organic parts. This instability severely impedes the development of PSCs. Besides, PSCs have the potential to degenerate because of mechanical stress, leading to the formation of cracks and separation of layers. This phenomenon occurs due to a disparity between the coefficients of thermal expansion between the device's perovskite layer and its other parts. It is important to point out that PSCs are highly responsive to these factors, emphasizing the significance of effective encapsulation strategies and enhanced material design. Strengthening the stability of PSCs for longer operations is crucial to maximize their potential benefits and ensure their extended durability.

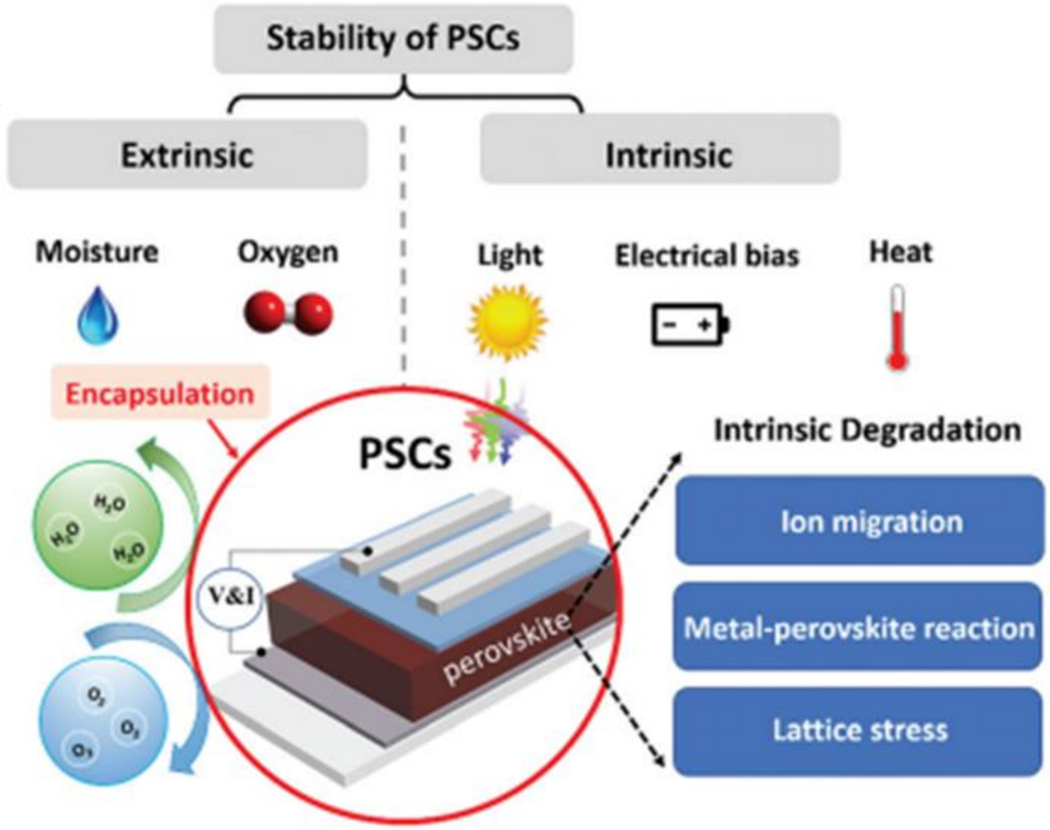

Figure 2.4. Environmental and operational variables are used to illustrate the intrinsic and extrinsic stability of PSCs[67].

Table 2.1 exhibits that the development of low-dimensional Ruddlesden-Popper (RP) perovskites provides an additional approach to stabilize 3D perovskites[67-70]. For example, 2D perovskites containing sizable aliphatic or aromatic alkylammonium cations such as PEA^+ and *n*-butylammonium (n-BA^+) have been synthesized as space cations between inorganic Pb-I octahedrons[71-74]. Because of the hydrophobic properties of organic space cations, they effectively exclude moisture from entering perovskites. Additionally, these cations create strong van der Waals forces with surrounding layers, resulting in enhanced stability of 2D RP perovskites. Because of their high exciton binding energy, PSCs that use low-dimensional RP perovskites operate inadequately[50,75-79]. For devices to attain optimal performance and excellent stability, researchers have synthesized and studied various 2D/3D perovskites.

Table 2.1. Summary of several causes of PSC deterioration and related strategies for enhancing device stability [67].

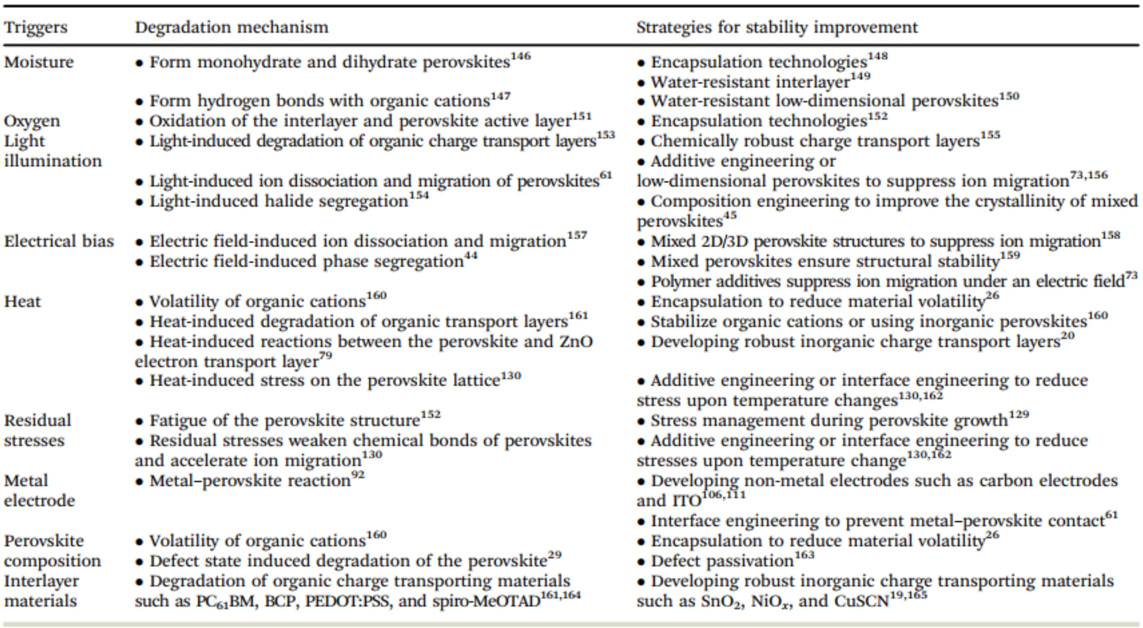

Triggers	Degradation mechanism	Strategies for stability improvement
Moisture	• Form monohydrate and dihydrate perovskites[146] • Form hydrogen bonds with organic cations[147]	• Encapsulation technologies[148] • Water-resistant interlayer[149] • Water-resistant low-dimensional perovskites[150]
Oxygen	• Oxidation of the interlayer and perovskite active layer[151]	• Encapsulation technologies[152]
Light illumination	• Light-induced degradation of organic charge transport layers[153] • Light-induced ion dissociation and migration of perovskites[61] • Light-induced halide segregation[154]	• Chemically robust charge transport layers[155] • Additive engineering or low-dimensional perovskites to suppress ion migration[73,156] • Composition engineering to improve the crystallinity of mixed perovskites[45]
Electrical bias	• Electric field-induced ion dissociation and migration[157] • Electric field-induced phase segregation[44]	• Mixed 2D/3D perovskite structures to suppress ion migration[158] • Mixed perovskites ensure structural stability[159] • Polymer additives suppress ion migration under an electric field[73]
Heat	• Volatility of organic cations[160] • Heat-induced degradation of organic transport layers[161] • Heat-induced reactions between the perovskite and ZnO electron transport layer[79] • Heat-induced stress on the perovskite lattice[130]	• Encapsulation to reduce material volatility[26] • Stabilize organic cations or using inorganic perovskites[160] • Developing robust inorganic charge transport layers[20] • Additive engineering or interface engineering to reduce stress upon temperature changes[130,162]
Residual stresses	• Fatigue of the perovskite structure[152] • Residual stresses weaken chemical bonds of perovskites and accelerate ion migration[130]	• Stress management during perovskite growth[129] • Additive engineering or interface engineering to reduce stresses upon temperature change[130,162]
Metal electrode	• Metal–perovskite reaction[92]	• Developing non-metal electrodes such as carbon electrodes and ITO[106,111] • Interface engineering to prevent metal–perovskite contact[61]
Perovskite composition	• Volatility of organic cations[160] • Defect state induced degradation of the perovskite[29]	• Encapsulation to reduce material volatility[26] • Defect passivation[163]
Interlayer materials	• Degradation of organic charge transporting materials such as $PC_{61}BM$, BCP, PEDOT:PSS, and spiro-MeOTAD[161,164]	• Developing robust inorganic charge transporting materials such as SnO_2, NiO_x, and CuSCN[19,165]

2.5 2D/3D Perovskite Heterojunctions

2.5.1 2D Perovskite

In 2D OIHPs, the inorganic perovskite layers have been separated by organic cations to form the low-dimensional RP perovskite structure, as shown in Figure 2.5. A typical RP 2D perovskite has the formula $(A')_2(A)_{n-1}M_nX_{3n+1}$, where A' for a small organic cation, A stands for a larger one, M for a metal cation, X for a halide anion, and *n* for the quantity of inorganic perovskite layers. The collaboration between the metal cation (M) and the halide anions (X) leads to the formation of inorganic layers. These layers are stabilized by the presence of organic cations (A and A') located between them. Unlike 3D perovskites, the layers in this case are connected by relatively weak van der Waals forces, which enable them to be flexed and stacked mechanically[80,81]. 2D perovskites are categorized according to the amount of coordinated amino tails in the spacer cations. This classification includes the RP phase, the Dion–Jacobson (DJ) phase, and the alternating cations in the interlayer space (ACI) phase, as depicted in Figure 2.6.

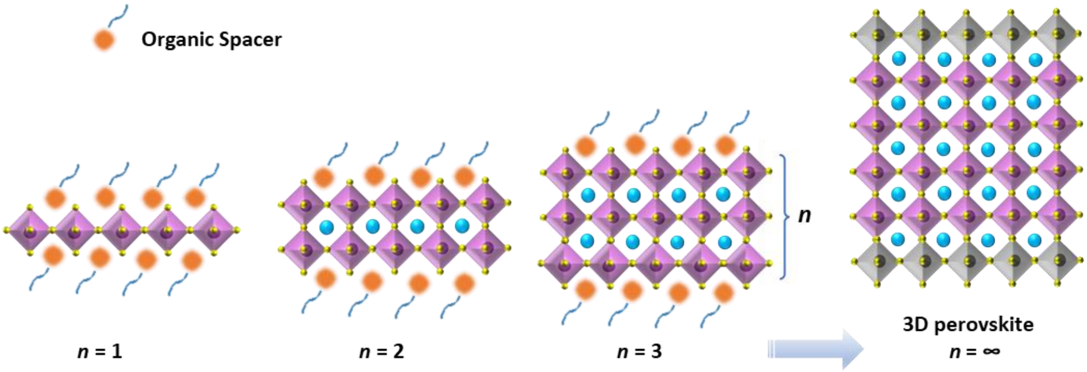

Figure 2.5 Illustration of the low-dimensional RP 2D perovskite structure.

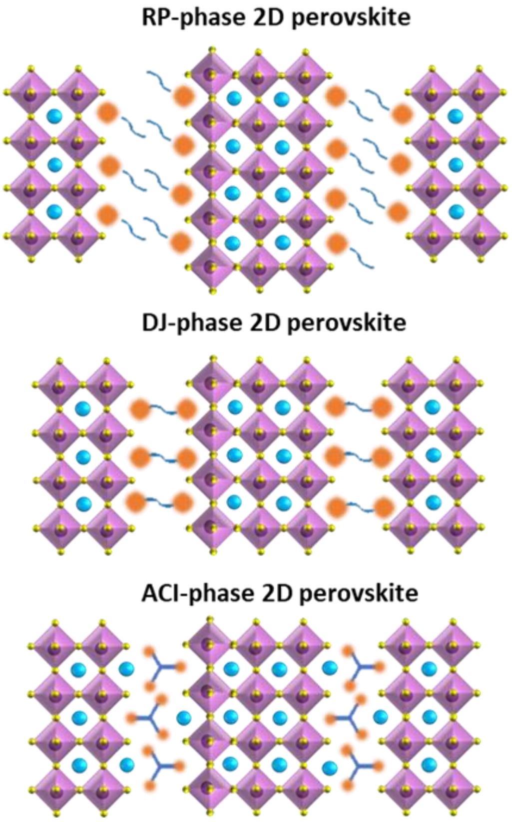

Figure 2.6 The RP-, DJ-, and ACI-phase 2D perovskites structures.

Compared to 3D perovskites, 2D perovskites exhibit inherent multi-quantum well architecture, resulting in distinct optical and electrical characteristics. The high fluorescence efficiency of the 2D perovskite is owing to the strong quantum limiting effect caused by the sandwiching of the single-layer lead halogen octahedral layer between the insulating organic layer. Furthermore, this natural 2D layered structure exhibits the properties of spontaneous anisotropic development, thus facilitating the production of a range of 2D crystals with extremely thin atomic sizes[82]. The exceptional optical characteristics and extremely thin nature of 2D perovskites offer significant possibilities for a variety of uses in transverse and vertical heterostructure optoelectronic devices.

2.5.2 2D Perovskite in 2D/3D Perovskite Heterojunctions

Building a 2D/3D perovskite heterojunction offers several benefits in improving the stability and efficiency of PSCs. As depicted in Figure 2.7, the 2D layer can act as a layer that prevents corrosion, safeguarding the underlying 3D perovskites from moisture and other environmental influences. In addition, the performance of the device can be improved by reaching a higher level of charge transfer efficiency through the 2D layer, which has the ability to reduce surface defects. Thus, the 2D/3D interface enhances charge separation and extraction, leading to a more efficient power conversion. Furthermore, the bandgaps of 2D/3D perovskite heterojunctions can be adjusted, which assists in developing highly efficient tandem solar cells.

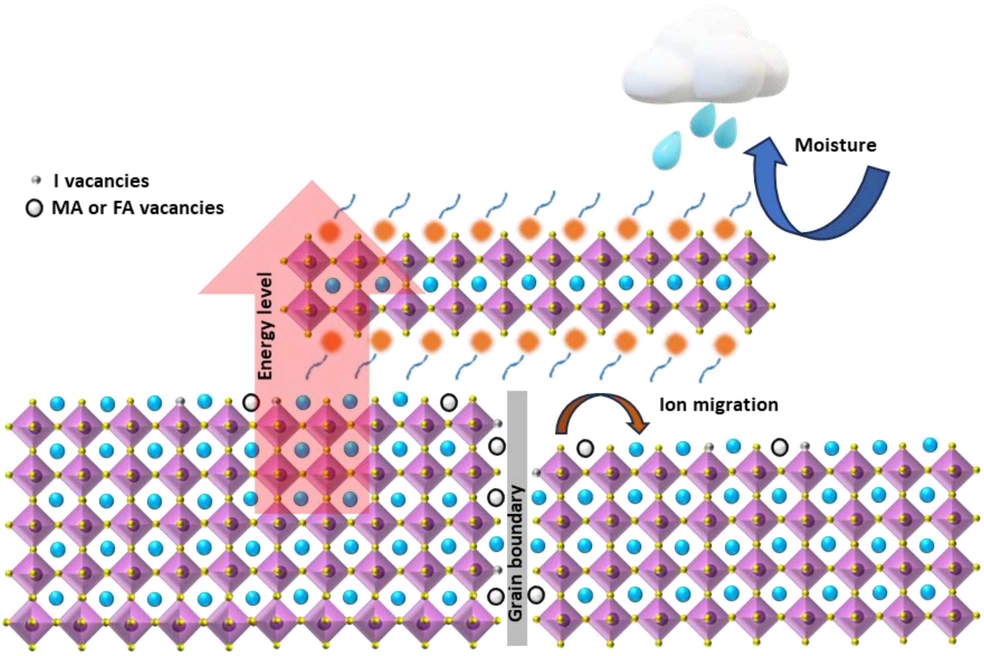

Figure 2.7 Schematic of 2D perovskite passivation effect in 2D/3D heterojunctions.

The corner-sharing PbI_6 octahedra in 2D perovskites provide them optoelectronic characteristics similar to those of 3D halide perovskites[83,84]. Like 3D halide perovskites, 2D perovskites exhibit the same atomic orbital character in their VBM and CBM. The organic spacer layers prevent out-of-plane electron migration in 2D halide perovskites, therefore increasing their bandgap significantly under quantum confinement. The organic spacer's type and length (e.g., aliphatic versus aromatic molecules), the composition of the metal halides, as well as the perovskite layer thickness clearly determine the 2D perovskite optical bandgap and exciton properties. To be more specific, 2D perovskites have an advantage over multi quantum wells (MQW) systems and other 2D semiconductors in terms of applications since the exciton binding energy and decreased mass may be continually adjusted between 3D perovskites ($E_b \approx 0.01$ eV, $m_X \approx 0.1$ m_0) and $n = 1$ 2D perovskites ($E_b \approx 0.5$ eV, $m_X \approx 0.1$-0.2 m_0) by simple material design[85-88].

Sidhik et al. have shown a diagram of energy-level (Figure 2.8a) for the RP type 2D perovskite. Based on the values anticipated from first-principles calculations and confirmed by photoemission yield spectroscopy (PES) and absorption measurements, the 3D perovskite $Cs_{0.05}(MA_{0.10}FA_{0.85})Pb(I_{0.90}Br_{0.10})_3$ is used in the $BA_2MA_{n-1}Pb_nI_{3n+1}$ structure, where n ranges from 1 to 4[22,89]. The 3D and $n = 3$ 2D perovskites were found to be aligned in a type II band. In this alignment, the valence band boundaries of the 3D and 2D perovskite are nearly perfectly aligned, which is great for hole extraction but creates a high energy barrier for electrons. The type I alignment of the 3D/PP-2D perovskite bilayer stack was further validated by the fabrication of solar cells with a charge extraction barrier employing thicker 2D layers. The PCE of PSCs in an *n-i-p* structure initially rose with increasing 2D perovskite layers but dropped after the thickness exceeded 50 nm, as shown in Figure 2.8b. They reasoned that the 3D–2D charge carrier transport was hindered by the diffusion length for a 2D $n = 3$ RP perovskite sheet with mixed orientation, which is less than 100 nm, and led to a drop in PCE[90,91]. In contrast, the *p-i-n* devices showed a 2D perovskite thickness of 5 nm, leading to an increase in PCE. Previous research on 2D/3D interfaces utilizing ultrathin 2D layer passivation has shown a substantial decrease with increasing 2D perovskite thickness, which is consistent with this finding[92]. The above energy band diagram demonstrated a significant difficulty in collecting electrons in the *p-i-n* type, which was compatible with the reduction in PCE. Moreover, the bandgap of 2D perovskite layers can be tuned via adjustment of the annealing temperature and treatment techniques, besides changing the organic spacer. Azmi et al. applied oleylammonium iodide (OLAI) molecules to address the defects of 3D perovskites in the surface, resulting in the formation of 2D perovskite (RP-phase) layers[20]. Afterward, they figured out that 2D perovskite layers with $n = 1$ were most likely created by annealing with heat (2D-TA), while 2D perovskite structure with increased dimensionality ($n \geqslant 2$) were more prominently formed following a room-temperature post-treatment (2D-RT), due to a reduced formation energy of the higher-n layers[93] . A rise in the secondary electron cutoff (E_{cutoff}), and a fall in the Fermi level (E_F) of perovskite films treated with OLAI resulted in a 3D to 2D perovskite phase transition, as shown in the energy-level diagrams in Figure 2.8c. Their 2D perovskite passivation approach was successful since the energetic gap between E_F and VBM was greater in the 2D-RT sample, indicating that the 3D perovskite films treated afterward are more *n*-type. Because the 2D-RT films' CBM is closer to the CBM of C_{60} at the *n*-type contact, the charge transfer efficiency at the 2D/3D perovskite interface and the C_{60} electron transport layer would be increased. On the other hand, the electron-selective contact at the interface of 2D/3D perovskite was less efficient according to the 2D-TA films' substantially larger CBM compared to C_{60}'s lower *n*-type character. To improve the performance of PSCs through passivation and improved electron blocking, a heterostructure can be formed by spin coating reduced-dimensional perovskites (RDPs) or 2D ligands onto 3D perovskite surfaces[94-97]. Overlying a bulk 3D perovskite, this heterostructure will have a thin layer of $n = 1$ and/or $n = 2$ 2D perovskite. However, it has been found by Chen et al. that 2D perovskite layers with $n \geqslant 3$ RDP layers could be formed by adding a tiny quantity of dimethylformamide (DMF) (DMF: isopropanol (IPA) = 1:200 by volume) and a proportion of methylammonium iodide to the 2D ligands in solution of 1:2 by weight. In this case, Pb is introduced directly from the 3D perovskite surface by DMF, and MAI is needed to lower the 2D ligand to cation ratio at the A-site[21,98]. Reducing confinement in the 2D layer could lead to less electron blocking and exceptionally performing inverted PSCs, according to their speculation, as illustrated in Figure 2.8d-e. Figure 2.8f-h displays the band alignment of 2D/3D heterostructures, which reveals that the CBM values of 2D-treated surfaces are higher than the controls. In contrast, the 2D/3D CBM offset is significantly reduced for the quasi-2D treatment films compared to their $n = 1$ (and/or 2) analogues. Changing the RDP width has minimal influence on the VBM, and decreasing confinement only moves the conduction band deeper, nearer to the 3D perovskite, according to surface-sensitive ultraviolet photoelectron spectroscopy (UPS) tests conducted on control, 2D, and quasi-2D-treated films[21,97,99].

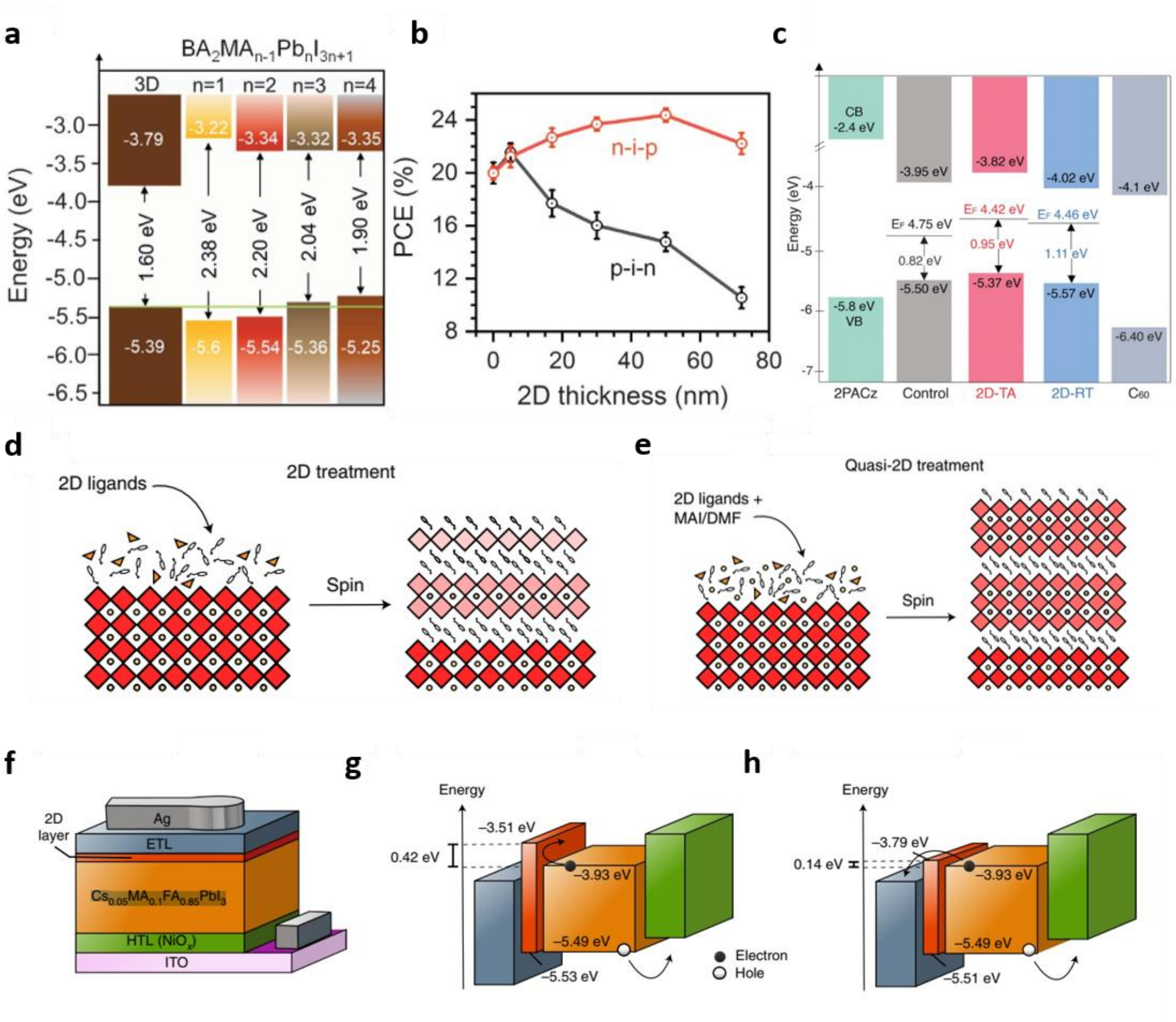

Figure 2.8 (a), The alignment of the energy levels. The 3D perovskite layer with $BA_2MA_{n-1}Pb_nI_{3n+1}$ for various n values ($n \leqslant 4$). **(b),** Effect of 2D perovskite layer thickness on PCE variation in *n-i-p* and *p-i-n* planar 3D/PP-2D PSCs[22]. **(c),** Energy level scheme for films treated with OLAI and without[20]. Schematic of the conventional 2D treatment **(d)** with $n \leqslant 2$ RDPs and the quasi-2D treatment **(e)** with $n \geqslant 2$ RDPs. **(f),** A typical cross-section 2D/3D heterostructure in the *p-i-n* configuration. Band alignment of PSCs after 2D or quasi-2D therapy **(g, h)**[100].

When the interface passivation layers are not adjusted carefully, the charge extraction across the perovskite/charge transport layer interface can be compromised due to the weak conductivity of the organic spacers employed to generate 2D perovskites[101,102]. In addition, the charge transfer efficiency can be even worse in mixed-dimensional PSCs with unaltered or negative energy band alignment[76,103]. On the other hand, there are still some explanations for why carrier transport can be improved. Gong et al. found that the modified perovskite films with long chain organic spacers exhibited enhanced carrier transport, better crystallization, and more effective defect passivation, resulting in a longer average carrier lifetime as compared to the control sample[104]. According to their research, it is expected that the primary causes of increased hole extraction are the better alignment of energy bands, reduced density of traps, and higher mobility of carriers. Furthermore, the improved charge extraction in these studies can be explained by the 2D perovskite's vertical crystal orientation, which takes advantage of the good conductivity along the inorganic planes, in contrast to other studies that demonstrate 2D perovskite layers reducing charge extraction owing to their poor conductivity[105]. Additionally, charge transfer at the perovskite/HTL interface can be improved by the advantageous orientation of the HTL film[106].

The $(DFP)_2PbI_4$ single crystal was synthesized by Song et al. through the use of the 4,4-difluoropiperidine (DFP) spacer as its fundamental component[107]. After that, they produced the target-1 films by incorporating the $(DFP)_2PbI_4$ single crystal into the $FA_{0.95}MA_{0.05}PbI_3$ precursor as seeds. As for target-2, they coated the target-1 film surface with an acetonitrile solution of the $(DFP)_2PbI_4$ single crystal to passivate defects in the surface and adjust energy level alignment. The *J-V* curves of *n-i-p* type PSCs are displayed in Figure 2.9a. With an open-circuit voltage (V_{OC}) of 1.129 V, a short-circuit current density (J_{SC}) of 24.88 mA cm^{-2}, and a fill factor (FF) of 79.84%, the control device exhibits a low PCE of 22.43%. Improved film quality and decreased non-radiative recombination loss led to a 23.16% improvement in the PCE of the target-1 devices. After adjusting the annealing time to 5 minutes for perovskite films covered with a passivation layer, target-2 devices were able to obtain a PCE of 24.87% with a significantly enhanced V_{OC} of 1.185 V. Figure 2.9c shows the results of the capacitance-voltage (C-V) characterization according to the Mott-Schottky relationship, which further confirmed the better V_{OC} of the target-1 and target-2 devices in contrast to the control device (Figure 2.9b)[108]. Corresponding to the rising trend of V_{OC} in the *J-V* curves, the built-in potential (V_{bi}) for control, target-1, and target-2 devices are 1.06 V, 1.10 V, and 1.14 V, respectively. Target-2 devices have a higher V_{OC} due to the increased driving force for more effective charge transfer and capture, as evidenced by the elevated V_{bi}. The results from the *J-V* analysis are in good agreement with the integrated current densities derived from the external quantum efficiency (EQE) in Figure 2.9d, which are 24.36 mA cm^{-2} for the control, 24.61 mA cm^{-2} for target-1, and 24.95 mA cm^{-2} for target-2 devices. The results from the *J*−*V* analysis are in good agreement with the integrated current densities derived from the external quantum efficiency (EQE) in Figure 2.9d, which are 24.36 mA cm^{-2} for the control, 24.61 mA cm^{-2} for target-1, and 24.95 mA cm^{-2} for target-2 devices. Figure 2.9e shows the devices' V_{OC} as a function of light intensity using seminatural logarithmic curves with slopes calculated by linearly fitting the data. The trap-induced recombination is reflected by the slope of the function *kT/q*, where *k* is Boltzmann's constant, *T* is the absolute temperature, and *q* is the elementary charge. Compared to the control device's slope of 2.41 *kT/q*, the perovskites for targets 1 and 2 have lower slopes of 1.95 and 1.05 *kT/q*, respectively. According to the space-charge-limited current (SCLC) technique, the lowered trap density results in a significantly smaller slope for target-2 devices, which in turn suppresses charge carrier recombination[109-111]. The results of their mobility (μ) and trap density

(N_t) experiments show that the combined effects of seed-induced growth and surface gradient passivation successfully decrease bulk and surface defects, leading to an increase in the V_{OC} of the related devices[112]. To understand how the 2D $(DFP)_2PbI_4$ perovskite affected the carrier lifetime of the associated perovskite films, the steady-state photoluminescence (PL) spectra and time resolved PL decay curves have been used. Because the $(DFP)_2PbI_4$ seeds produce a higher quality 3D perovskite film, the researchers found that the target-1 film exhibited a greater PL intensity. Surface gradient passivation significantly inhibits nonradiative recombination, as evidenced by the further enhancement of the target-2 film's PL intensity. The target-1 film exhibits a substantially extended bulk carrier lifetime of 4.26 μs, as shown in the time-resolved PL (TRPL) spectra presented in Figure 2.9f. This indicates that there were considerably fewer bulk defects in the target-1 film with the 2D $(DFP)_2PbI_4$ seed, as it is approximately eight times larger than the control film's 0.56 μs[113]. Additionally, the 2D perovskite $(DFP)_2PbI_4$ treatment increased the carrier lifetime of the target-2 film to 5.91 μs, demonstrating that vertically distributed 2D passivation layers can reduce surface defects and thereby interfacial nonradiative recombination. Figure 2.9g-i shows that the target-1 and target-2 films had extended PL lifetimes in the 775–825 nm light-emitting range compared to control samples, which corresponds with the previous examination results.

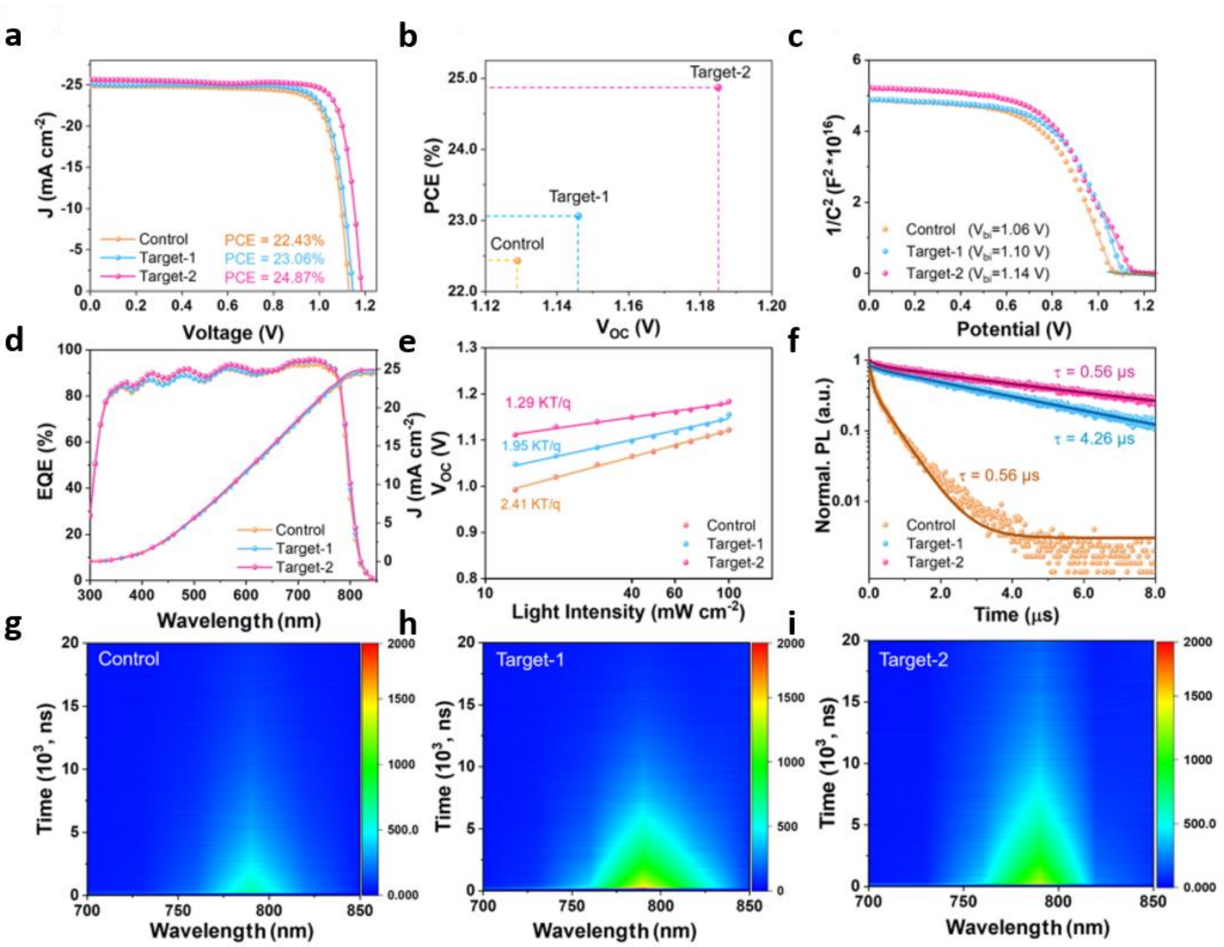

Figure 2.9 (a), *J*-*V* curves of the control, target-1, and target-2 champion cells. **(b),** PCE and V_{OC} of the corresponding devices. **(c),** The corresponding devices' Mott-Schottky plots. **(d),** EQE spectra and integrated J_{SC} of the corresponding devices. **(e),** V_{OC} versus light intensity for the corresponding devices. **(f),** TRPL spectra of the control, target-1, and target-2 films. **(g–i)** Time-resolved emission spectra (TRES) of the control **(g)**, target-1 **(h)**, and target-2 **(i)** films[107].

Degradation caused by moisture is a major issue for 3D perovskite films, as it can lead to a loss of structural integrity and decreased performance over time. Mixed 2D/3D PSCs have been shown to have improved moisture stability, which is thought to be caused by the hydrophobic feature of long-chain spacer cations in 2D perovskite[114]. It is demonstrated that the 2D surface layer may function as a moisture barrier since the surface free energy of a 3D perovskite surface treated with 2D perovskite is substantially lower than that of the pure 3D perovskite film[115]. In addition, the 2D perovskite can serve as an encapsulating layer and prevent moisture intrusion into the 3D perovskite by employing surface passivation with hydrophobic chemicals such as alkylammonium compounds[116].

The existence of volatile small organic ions like MA^+, which induce perovskite decomposition at high temperatures, has been identified as a possible reason for the structural instability of 3D perovskite[117]. Though increasing the perovskite tolerance factor by substituting FA^+ or Cs^+ cations for MA^+ ions might improve the structural stability of perovskite films, MA^+ ions are still preferred for device performance in most high efficiency PSCs[118]. The structural resilience of 3D perovskite films may be enhanced by extra molecular bonding when 2D perovskite is included, which can lead to better thermal and operational stability of PSCs, especially in the case of MA-based films. The formation energy of 2D perovskite is significantly greater than that of 3D perovskite because of the difficult breakdown of the layered structure caused by strong intermolecular interactions, such as hydrogen bonds and van der Waals forces, between the large organic cations[119].

Despite their high PCE, organic-inorganic perovskites are often considered unstable because of their vulnerable lattice structure, weak chemical interactions, and low defect formation energy. The ABX_3 perovskites have a low activation barrier and a high diffusion coefficient for the A-site ions (MA^+ and FA^+), B-site ions (Pb^{2+} and Sn^{2+}), and X-site ions (I^-, Br^-, Cl^-, and other halogen ions)[120,121]. Extrinsic factors have the potential to cause ionic defects inside the perovskite films, leading to substantial ion migration[122]. Ion migration prompted by electric fields was considered to have the greatest impact on photocurrent hysteresis. In addition, the intrinsic electric field of the perovskite films can be impacted by ion migration and accumulation, which in turn may change the localized crystal structure and produce stability and degradation problems with PSCs[123]. By incorporating robust 2D perovskite layers at either the top or bottom interface, PSCs made of bilayer 2D-3D perovskite heterostructures are able to protect the 3D perovskite films from oxygen and moisture while also reducing the infamous ion migration[124]. This results in improved photo- or thermal robustness of the 3D perovskite crystals under operating conditions, leading to significantly longer device lifespans compared to bare 3D devices.

By solid-state transfer of a spacer cation layer onto the 3D perovskites, Zhu et. al. design a transfer-imprinting-assisted growth (TIAG) technique to construct the 2D/3D perovskite heterojunctions in-situ, as seen in Figure 2.10b[125]. They built the 2D/3D perovskites using the organic salt of benzenebutanammonium iodide (PhBAI) as the spacer molecule. To further compare, the 2D/3D perovskites are also grown using the traditional solution approach, spin-coating-assisted growth (SCAG). As shown in Figure 2.10a, the organic salt solution is spin coated onto the 3D perovskite layer directly. A nonuniform two-dimensional film is formed when solution and cation diffusion into perovskite films, which are inherently rough and uneven, damage the 3D perovskite grains. Avoiding solution and cation diffusion into the perovskite film is achieved in the solution-free TIAG method by coating the poly-di-methyl-siloxane (PDMS) substrate with the solid-state organic salt film and then overlapping it on top of the 3D perovskite. A uniform 2D perovskite layer can be created on the surface once the organic salt and perovskites come into close contact through the chemical reaction and pressure induced by the TIAG process. Through the use of time-of-flight secondary ion mass spectrometry (TOF-SIMS), the spatial distribution of $PhBA^+$ in the perovskite film can be identified. As demonstrated in Figure 2.10c, the SCAG perovskites show a deep penetration of $PhBA^+$ into the perovskite absorber, indicating that the organic salts and solvent have diffused into the grain boundaries and holes. An obvious junction may be grown in 2D/3D perovskites because the solid-state-transferred $PhBA^+$ is uniformly distributed and tightly bound to the surface of the TIAG perovskites (Figure 2.10d). In addition, the TIAG PSCs exhibit extremely little hysteresis, which may be because the uniform 2D perovskites grown over the 3D perovskites reduce ion migration and enhance charge carrier transportation.

The group led by Wu was able to achieve a fine-tuned 2D/3D heterostructure with a gradient distribution of perovskite compositions along the vertical bottom-to-top direction of the perovskite film, ranging from 1 to $n = \infty$, by carefully modifying the perovskite ink formulation with a small amount of 2D PEA_2PbCl_4 component and PEACl additive[126]. After fabricating the control and target films on flexible ITO/PET (ITO films on polyethylene terephthalate) substrates, they treated them to 100 cycles of bending to reach a 1 cm radius. Figure 2.10e and f show that after 20 bending cycles, the control perovskite film developed cracks at the grain boundary areas, which are called intergranular fractures. A significant change in morphology was seen after 100 bending cycles, with fissures shown to have grown and spread throughout the grain's interior, a phenomenon commonly referred to as trans-granular fracture[126]. On the contrary, the target perovskite film retained its compact and intact shape even after 100 bending cycles, and there was no apparent delamination on the perovskite-substate interface, as shown in Figure 2.10e and g. The target perovskite films could have their mechanical strength improved, lattice distortion reduced, and residual stress released by using the stretchable 2D perovskite components as a "band-aid" to adhere to the 3D perovskite surface and the perovskite substrate interface.

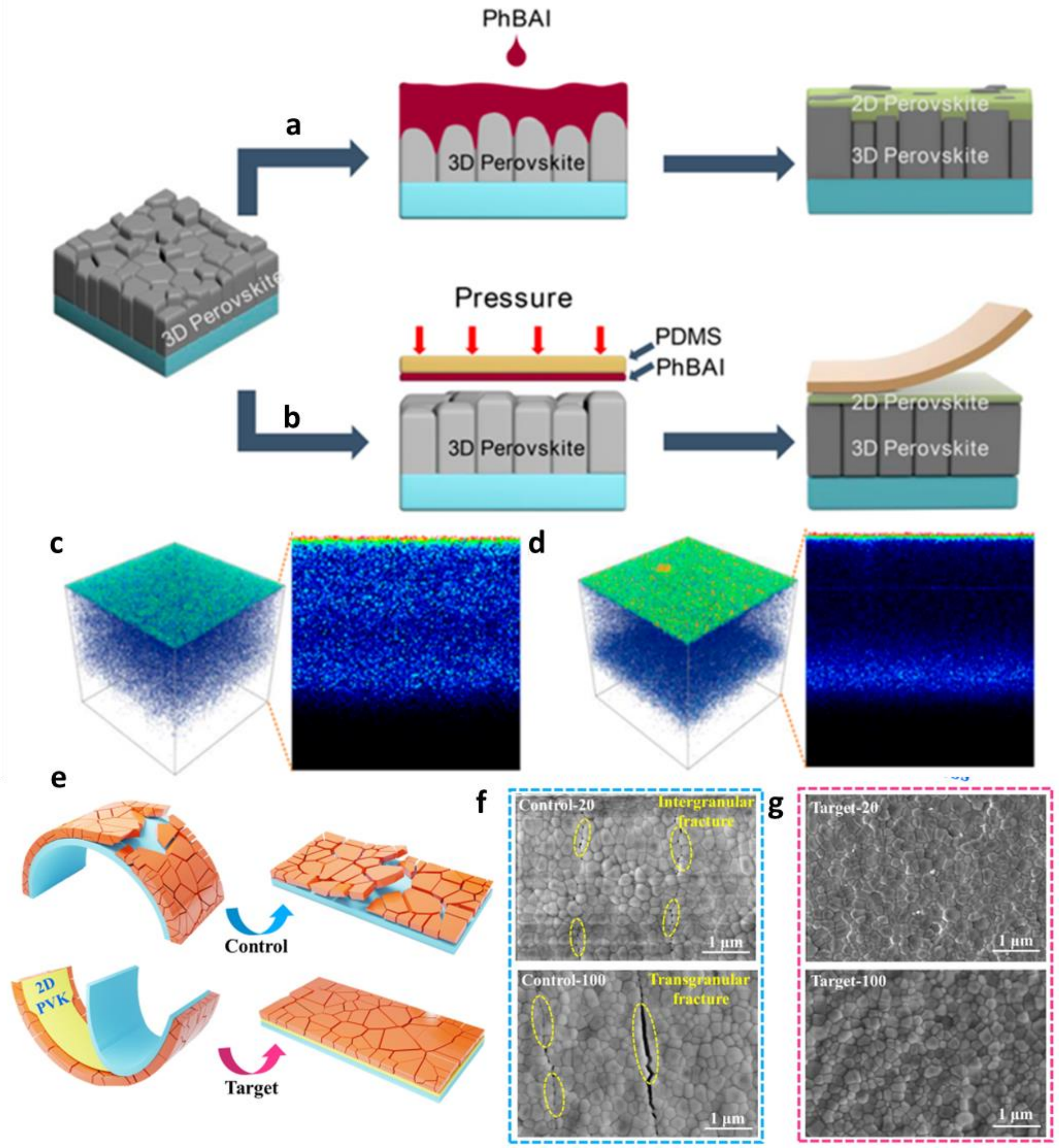

Figure 2.10 (a), (b), SCAG and TIAG process schematics. **(c), (d),** TOF-SIM depth profiles of $PhBA^+$ (green) in SCAG and TIAG perovskite films[125]. **(e),** Illustration of the morphological alteration resulting from the bending test of several perovskite films applied to a flexible ITO-PET substrate. After bending for various cycles, the control and target perovskite films are shown in corresponding (scanning electron microscopy) SEM images (**f** and **g**, respectively). Take note that the bending cycles were denoted by the numbers that followed the sample names[126].

2.6 Interface Characterization Methods for Heterojunctions

In order to improve the stability and performance of 2D/3D PSCs, the interface structure and quality are crucial and need to be carefully observed. Solar cells' carrier dynamics, recombination suppression, environmental stability, and energy alignment are all profoundly affected by the interface between 2D and 3D perovskites. Thus, in an effort to increase the efficiency and stability of PSCs, interface engineering is a primary area of study. More efficient and stable perovskite solar systems will definitely be developed as a result of further understanding of interfacial phenomena through theoretical modeling and better characterization techniques.

2.6.1 Spectroscopic Probing

When investigating the heterojunctions interface, X-ray photoelectron spectroscopy (XPS) is an effective method for determining the elemental composition and oxidation states. Chemical environments, the possibility of interfacial dipole generation, and defect states can be better understood with the use of XPS, which analyzes the binding energy of core electrons. Surface roughness and morphology can be revealed by topographical maps produced using atomic force microscopy (AFM), which uses a small tip to "touch" the material's surface. Chen et. al. discovered that the organic substance they utilized is efficiently adsorbed on the perovskite surface when a new peak at 533.0 eV, associated with C−O, emerged in the XPS spectra of O 1s[127]. Investigation of the structure of the valence band and the work function at the perovskite interface is carried out via ultraviolet photoelectron spectroscopy (UPS). Charge carrier injection or extraction obstacles and energy level alignment can be better understood through this method. As for Fourier-Transform infrared spectroscopy (FTIR), by analyzing the vibrational modes at the interface, it can provide a non-destructive way to learn about molecule orientations, bond forms, and potential interactions between the 2D and 3D perovskite. After absorbing photons, perovskite materials can cause the emission of light. Charge carrier recombination can be detected via photoluminescence spectroscopy (PL), which can indicate the existence of trap states and the heterointerface quality. Furthermore, distinct PL characteristic peaks can be used to further confirm the compositions of the two-dimensional perovskites with varying *n* values[107].

Conductive Atomic Force Microscopy (C-AFM) is utilized to directly measure the local electrical conductivity and to identify conductive or insulating regions at the interface, which is essential for assessing the efficiency of charge transport across the junction. According to C-AFM investigations illustrated in Figure 2.11a and b, where the yellow and black regions represent high and low conductivity, respectively, the electric current was reduced due to the presence of 2D perovskite organic layers on the surface[128]. Kelvin Probe Force Microscopy (KPFM) is a non-contact AFM method that measures the surface potential to reveal information on the potential landscape and work function of the interface. In order to detect electrostatic forces, KPFM brings a conducting AFM tip extremely close to the sample’s surface. An alternating current (AC) voltage is applied to the tip, which interacts with the surface potential, generating an oscillating electrostatic force. By superimposing a direct current (DC) voltage to nullify this force, KPFM can measure the difference in work function between the tip and the sample, thus determining the local contact potential difference with high spatial resolution. The carrier dynamics, including charge transfer and recombination processes at the interface, can be studied via TRPL measurements. The interface quality and its impact on device performance can be revealed by the lifetime and quenching of photoluminescence.

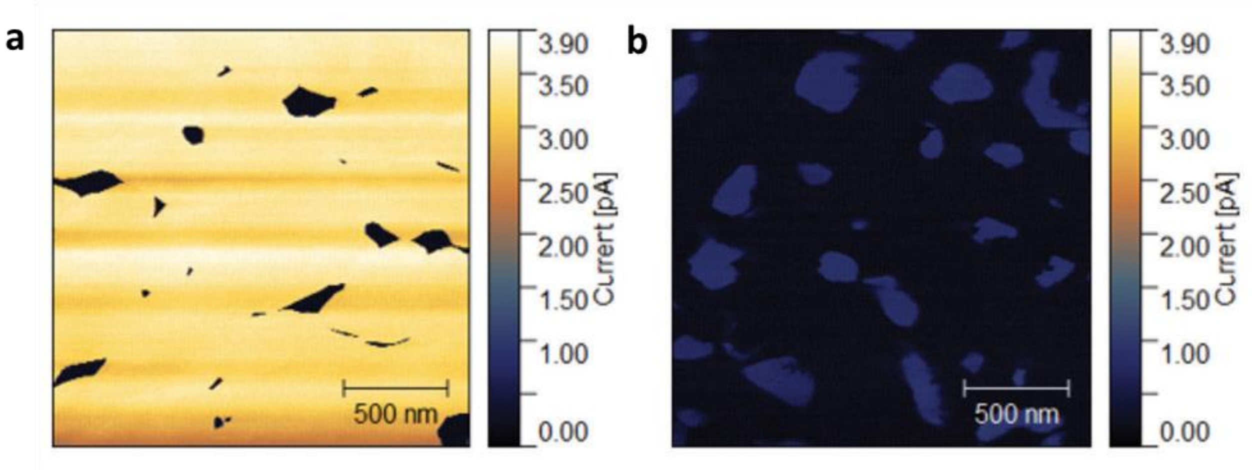

Figure 2.11 C-AFM images of **(a)** reference and **(b)** 2D/3D perovskite films[128].

2.6.2 Electron Microscopy Characterizations

Surface and cross-sectional morphological properties, including layer thickness, uniformity, and interfacial defect, can be studied with SEM. However, SEM can only provide a spatial resolution up to several nanometers, which is insufficient for revealing detailed crystal structures. Therefore, aberration-corrected high-resolution TEM becomes the promising solution to provide the real-space atomic arrangements and crystalline structures at the 2D/3D perovskite interface. Due to the electron sensitivity of halide perovskites, a low-dose condition is necessary for TEM observations to avoid beam-induced damage. Besides, a cross-sectional view is also crucial to provide in-depth insights into the 2D/3D junction's characteristics, such as the interlayer spacing, orientation of 2D or 3D perovskite, and possible interdiffusion of materials, which requires a special sample preparation approach involving FIB processing. Compared with TEM, the STEM image is more interpretable with contrast related to atomic numbers (Z-contrast). By employing high-resolution STEM (HR-STEM), Azmi et. al. were able to observe the 2D perovskite structure and orientation, which were found to be mostly perpendicular at the top contact, as shown in Figure 2.12[19].

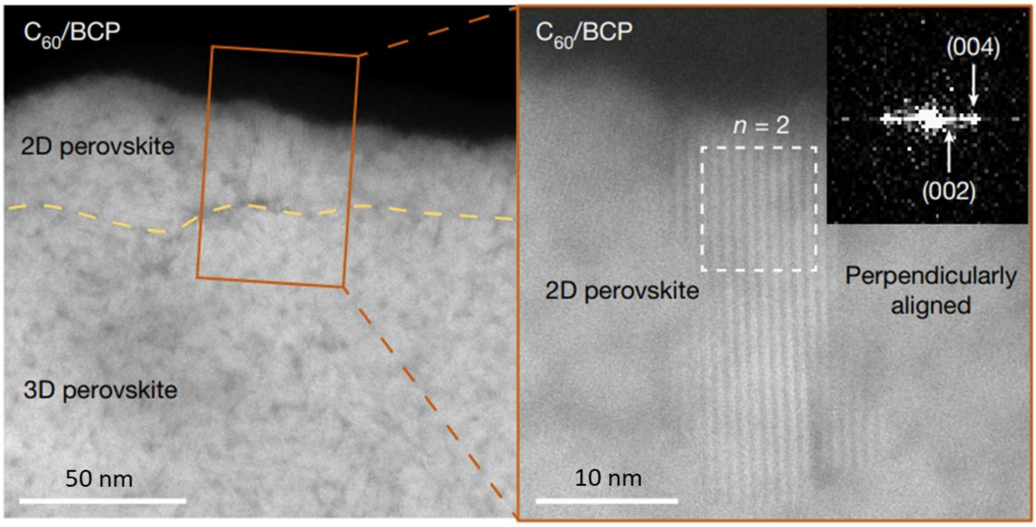

Figure 2.12 High-angle annular dark-field STEM (HAADF-STEM) cross-sectional picture of a 2D perovskite material revealing its perpendicular orientation, zoomed in to the region close to the top C_{60} contact[19].

Material releases X-rays when excited by high-energy electrons and those signals within a particular solid angle can be detected by a silicon detector. Energy-dispersive X-ray spectroscopy (EDX) allows for elemental analysis and mapping at the material's interface, which is typically used in conjunction with SEM and TEM[107]. Priya's group developed an emulsion-based self-assembly approach using natural lipid biomolecules in a nonionic solution system to form a 0D/3D bilayer structure[129]. A crystalline $MAPbI_3$ nanoparticle covered with a shell of E1 molecules is indicated by the elemental distribution of iodine (I) and carbon (C) in Figure 2.13f. The $CH_3NH_3PbI_3$ is a representation of the inner lattice that includes I and C components. It is possible to attribute the carbon-based E1 molecules to the outer amorphous layer, which is denoted by the gray dashed line, since it contains just carbon, as shown in Figure 2.13. In combination with TEM, electron energy loss spectroscopy (EELS) can provide information regarding the interface layers' thickness, electrical structure, and elemental composition[79,86]. Through EESL mapping, Yang et al. revealed that, in ambient air, O probably destroys the organic component $CH_3NH_3^+$ of perovskites, Figure 2.14[130]. However, damage to the sample is quite possible when using EDS and EELS due to the high electron dose needed to achieve a high signal-to-noise ratio.

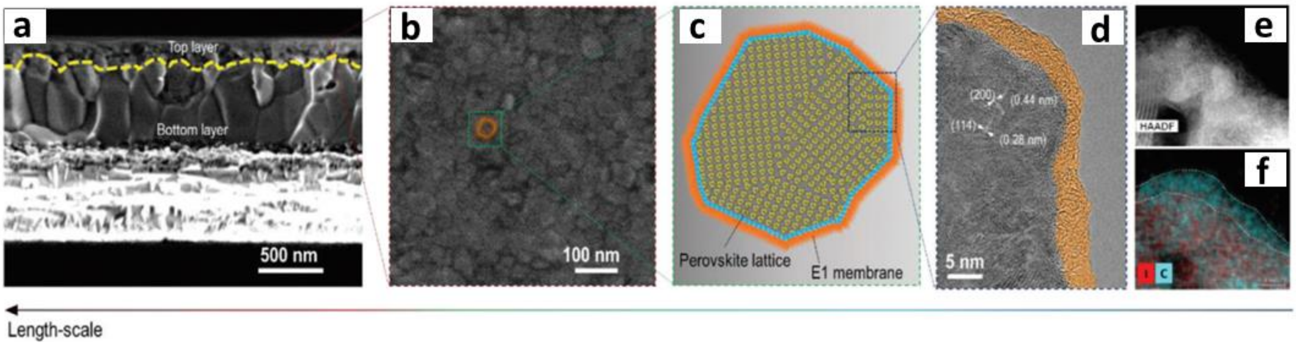

Figure 2.13 SEM image of E1-doped $MAPbI_3$ film from **(a)** cross-sectional and **(b)** top-view. **(c),** The highly packed arrangement of E1 molecules on $MAPbI_3$ nanocrystals is illustrated in the scheme. **(d),** TEM image **(e),** HAADF-STEM image and **(f),** elemental mapping of the E1-$MAPbI_3$ nanocrystal[129].

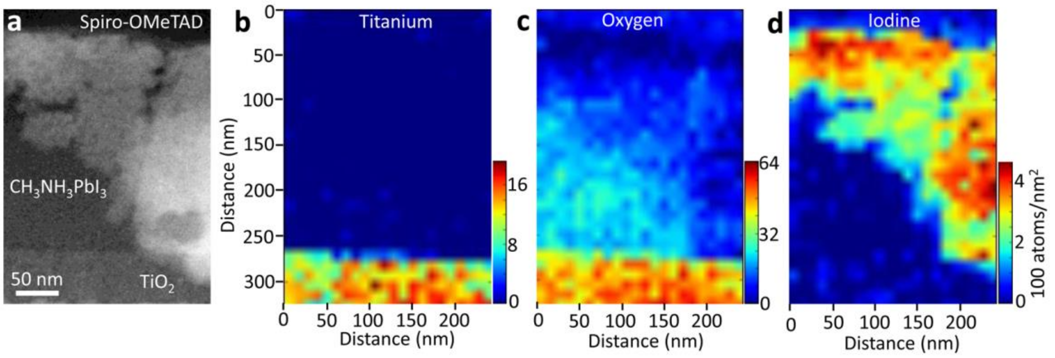

Figure 2.14 Chemical element distribution in the vertical direction can be revealed via EELS mapping. A HAADF-STEM image **(a)** and associated EELS mapping images of triple-layer $TiO_2/CH_3NH_3PbI_3$/Spiro-OMeTAD atomic areal densities for titanium **(b)**, oxygen **(c)**, and iodine **(d)**[130].

2.6.3 Low-dose S/TEM Characterizations of Halide Perovskites

Figure 2.15 illustrates the distinct operational principles of TEM mode and STEM mode. TEM has two main tasks: one is collecting the reciprocal-space diffraction information of materials, and another is imaging the real-space structure of materials. For reciprocal-space diffraction, when an electron beam interacts with a crystalline sample, it is diffracted according to Bragg's law. This diffraction pattern is recorded in reciprocal space, which is the Fourier transform space of the real lattice. These patterns provide information about the crystal structure, lattice parameters, and symmetry. The spots in a diffraction pattern correspond to the different planes in the crystal lattice. By analyzing diffraction patterns, researchers can determine the crystallographic orientation, identify phases, and study defects such as dislocations or stacking faults that are particularly useful for characterizing polycrystalline and single-crystal materials. Selected Area Electron Diffraction (SAED) allows for the selection of a specific region of the sample to obtain diffraction information, which is essential for analyzing heterogeneous materials. Real-space imaging in TEM involves forming an image of the sample by focusing transmitted electrons after they pass through the specimen. The contrast in these images is related to variations in thickness, composition, and crystallographic structure. TEM can achieve atomic resolution, allowing for direct visualization of the arrangement of atoms, defects, and interfaces within a material. Techniques such as bright-field (BF) and dark-field (DF) imaging enable the differentiation of features based on differences in mass, thickness, and diffraction conditions. Real-space imaging is used to study the morphology, size distribution, and internal structure of nanoparticles, thin films, and biological specimens. It provides direct visual evidence of phenomena like grain boundaries, phase transitions, and compositional inhomogeneities.

STEM combines elements of both TEM and SEM. In STEM, a focused electron beam is scanned over the sample, and transmitted electrons are detected to create an image. STEM offers various imaging modes such as bright field, dark field, and HAADF, each providing different types of contrast and information about the sample. STEM is often combined with spectroscopic techniques like EDS and EELS, allowing for elemental and chemical analysis at the nanoscale. STEM can achieve atomic resolution similar to TEM but offers the advantage of enhanced contrast and sensitivity, especially for heavier elements using HAADF imaging. Besides, STEM is particularly useful for studying the structure and composition of complex materials, interfaces, and heterostructures, making it ideal for research in fields like semiconductor technology and nanotechnology.

DPC (Differential Phase Contrast) technology achieves imaging by measuring the phase shift of the electron beam after it passes through the sample. When the electron beam traverses the sample, the internal potential distribution of the sample causes a phase shift in the electron wave. DPC technology utilizes a segmented detector to measure the deflection of the electron beam in both the X and Y directions, thereby obtaining information about the internal potential gradient of the sample. IDPC technology (Integrated Differential Phase Contrast) represents a further advancement of DPC technology. By performing a two-dimensional integration of the differential phase signals acquired through DPC, it reconstructs a projected image of the internal potential distribution of the sample.

Since the internal potential distribution is directly related to the types and positions of atoms within the sample, iDPC technology can provide images with atomic-level resolution. The distinction between DPC and iDPC lies in the fact that DPC measures the deflection of the electron beam (i.e., the potential gradient), providing differential phase signals, whereas iDPC reconstructs the internal potential distribution of the sample through integration of the DPC signals, offering more intuitive images with atomic-level resolution. IDPC is particularly advantageous in mapping electric potential at interfaces and within semiconductor devices and is crucial for studying ferroelectric and piezoelectric materials by visualizing domain structures and polarization fields. Its application extends to nanotechnology, aiding in the characterization of nanoscale devices through electric field analysis. The method's non-destructive nature, coupled with the high spatial resolution of STEM, makes it suitable for analyzing sensitive materials at the atomic scale, providing quantitative data on electric fields essential for advancing electronic materials and optimizing devices. The iDPC imaging technique demonstrates dual advantages in electron microscopy: exceptional signal-to-noise ratio under low-dose conditions ($\leqslant 100$ $e^-/\text{Å}^2$), achieved through phase-gradient signal amplification, and atomic-number contrast sensitivity down to Z=3 (lithium) with 0.8 Å resolution, enabled by its intrinsic sensitivity to electrostatic potential gradients[131].

4D-STEM is a sophisticated technique that extends the capabilities of conventional STEM by capturing a two-dimensional diffraction pattern at each probe position across a scanned area, resulting in a four-dimensional dataset comprising spatial and momentum information. This method allows for comprehensive analysis of crystallographic, electronic, and magnetic properties with unprecedented detail. By utilizing pixelated detectors, 4D-STEM provides enhanced sensitivity and resolution in mapping local structural variations, strain fields, and electric or magnetic fields within a sample. The technique enables researchers to perform quantitative phase imaging, orientation mapping, and strain analysis, offering insights into the material's microstructure and functional properties at the atomic scale. 4D-STEM is particularly valuable in studying complex materials and interfaces, where conventional methods may fall short, as it captures the intricate interplay of local structural and electronic phenomena. This capability makes it indispensable for advancing research in materials science, nanotechnology, and condensed matter physics, facilitating the development of next-generation materials and devices.

OIHPs exhibit a significant sensitivity to electron beams. As Figure 2.16 illustrates, Rothmann et al. observed a gradual decomposition of $FAPbI_3$ perovskite films under continuous electron beam irradiation. Following a single scan with the electron beam, the cumulative dose amounts to roughly 66 e $Å^{-2}$. After three scans (around 200 e $Å^{-2}$), notable changes in the contrast of the pristine perovskite structure are observed. Following nine scans (around 600 e $Å^{-2}$), the perovskite structure is entirely depleted, substituted by a crystal structure exhibiting uniform column intensity. Further exposure (around 1333 e Å-2) results in the sample being remarkably similar to 2H-hexagonal PbI_2. This suggests that to accurately observe the real structure of OIHPs in TEM, it is essential to utilize certain low-dose imaging techniques.

In this thesis, a combination of low-dose HAADF-STEM, iDPC, and 4D-STEM was employed to characterize OIHPs. Recognizing that halide perovskites are susceptible to degradation under high electron doses, which can significantly alter their crystal structure and intrinsic properties, low-dose techniques are critical for preserving these materials' original characteristics during analysis. Low-dose S/TEM facilitates high-resolution imaging that allows for the detailed visualization of crystal structures, grain boundaries, lattice fringes, and phase interfaces. When combined with energy-dispersive EDS and electron energy loss spectroscopy EELS, low-dose S/TEM enables comprehensive analysis of the elemental composition and electronic structure of halide perovskites, aiding in phase identification and atomic-level compositional understanding. This approach is particularly valuable for investigating defects and interfaces, which are pivotal to understanding the performance and efficiency of perovskite solar cells, by revealing defect densities, types, and distributions. Moreover, advanced low-dose S/TEM techniques allow for the in situ observation of dynamic processes, such as ion migration and phase transitions under external stimuli, offering significant insights into the operational mechanisms of perovskite-based devices.

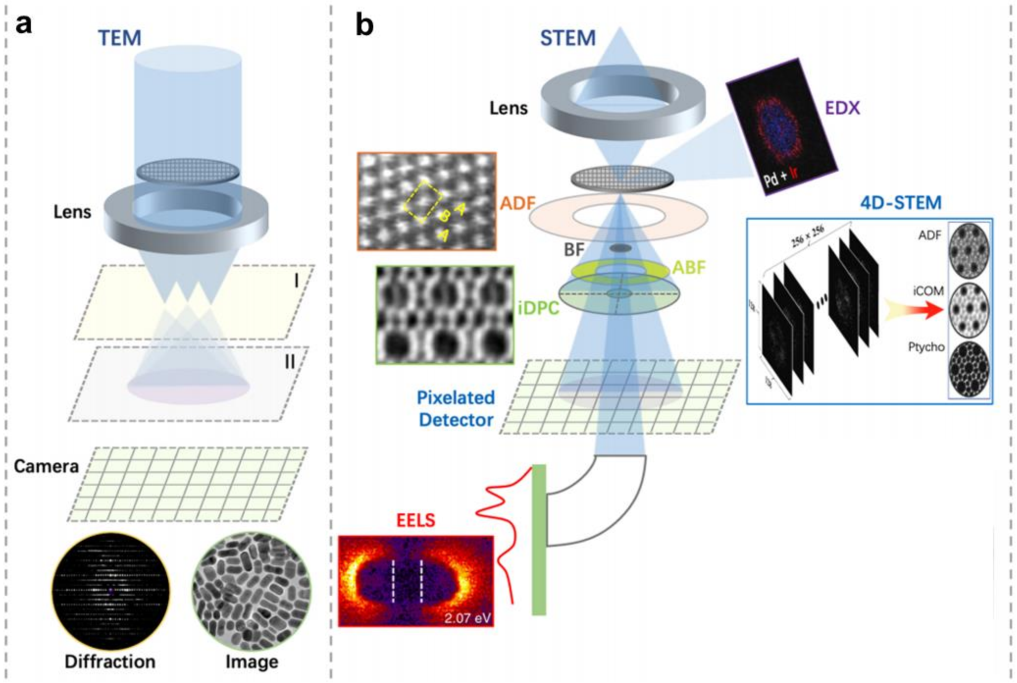

Figure 2.15 Electron microscopy methods used to investigate nanomaterials. **(a),** Reciprocal-space diffraction in TEM mode offers information on the crystal structure, while real-space imaging allows for the observation of morphology. **(b),** In STEM mode, several imaging techniques have been used to examine the crystal structure (such as BF, ABF, (HA)ADF, iDPC, and 4D-STEM), composition (EDX and EELS), and electronic structure (EELS)[131].

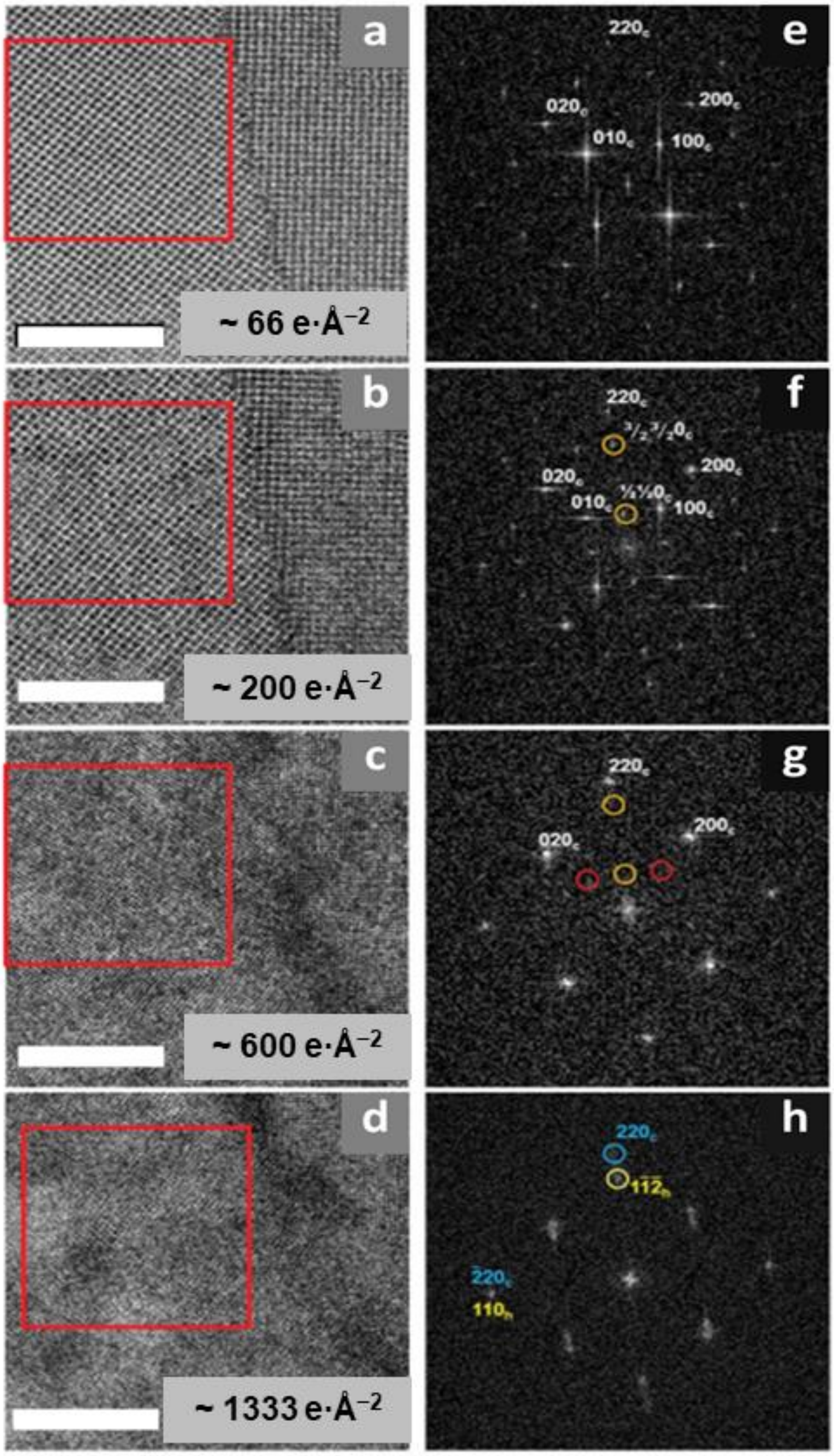

Figure 2.16 Damage mechanism of FAPbI$_3$ detected under a scanning electron beam in a 30 nm thick film produced with near-ideal stoichiometry[141]. **(a)-(d)**, scale bar, 10 nm.

2.6.4 Electrical and Optoelectronic Characterization

From the perspective of solar cell devices, electrochemical impedance spectroscopy (EIS), an enchanting plot of the real versus imaginary components of impedance, typically unfurls into a series of semicircles known as Nyquist plots. The frequency range of each semicircle suggests the spatial domain of the corresponding process within the device, whether that activity is occurring at the interfaces or in the bulk material.

2.7 Summary

Constructing a perovskite heterojunction in 2D/3D form presents multiple advantages in enhancing the stability and performance of perovskite solar cells. Firstly, the 2D layer can function as a passivation layer that safeguards the underlying 3D perovskite from moisture and other environmental factors. Additionally, the 2D layer has the ability to diminish surface defects, which ultimately leads to improved charge transport properties and device performance. The 2D/3D interface also can enhance charge separation and extraction, leading to greater power conversion efficiency. In addition, the tunable bandgaps of 2D/3D perovskite heterojunctions can be engineered, making them advantageous for the development of highly efficient tandem solar cells. Ultimately, constructing 2D/3D perovskite heterojunctions holds immense potential for enhancing the stability and performance of perovskite solar cells.

Although 2D/3D perovskite structures have many advantages, some issues still need to be resolved. The stability of perovskite films is still one of the main issues among these. Compared to their 3D counterparts, 2D perovskites have shown improved stability, but they are still susceptible to heat and moisture. The overall performance and stability of the device may also be affected by the interactions between the 2D and 3D layers. Charge separation and recombination are significantly influenced by the band alignment at the interface. Additionally, defects or traps at the interface may result in non-radiative recombination, which eventually lowers the device's effectiveness. Controlling the composition and thickness of the layers is also a difficult issue because these factors have a significant impact on the device's characteristics. Last but not least, the substantial exciton binding energy in 2D perovskites may limit their utility in solar systems. As a result, it is necessary to investigate methods that can lower the binding energy while maintaining stability and other important features.

This thesis will concentrate on a deeper understanding of 2D/3D perovskite heterojunctions through electron microscopy. The low-dose STEM technique was employed to directly evaluate the distribution of 2D perovskite on 3D grain and its impact on the device. The observation results are subsequently utilized to assess the techniques and factors involved in constructing 2D/3D perovskite heterojunctions. Then, it is possible to further optimize and obtain more stable and efficient 2D/3D PSCs.

Chapter 3 Experimental and Characterization Methods

3.1 Materials

Lead iodide and lead bromide (PbI_2 and $PbBr_2$, >99.99%) were acquired from TCI (Japan). Formamidinium iodide and Methylammonium chloride (FAI and MACl, >99.99%) were purchased from Greatcell Solar (Australia). 4-tert-butylpyridine (4-TBP, 96%), Bis(trifluoromethane) sulfonimide lithium salt (Li-TFSI, 99.95%), N, N-Dimethylaniline (DMF) and dimethyl sulfoxide (DMSO), acetonitrile (ACN), chlorobenzene (CB), ethyl acetate (EA), isopropyl alcohol (IPA) were purchased from Merck (USA). Phenyl-C_{61}-butyric acid methyl ester (PCBM), C_{60}, Bathocuproine (BCP) and PEAI, chloroformamidine (FACl), phenethylammonium bromine (PEABr) were purchased from Xi'an Polymer Light Technology Corp. Tin (IV) oxide (15 wt.% in H_2O colloidal dispersion) and cesium iodide (CsI, >99.998%) and cesium bromide (CsBr, >99.998%) were acquired from Alfa Aesar (USA). Spiro-OMeTAD (99.8%) was purchased from Borun Chemical Co., Ltd. (China). MeO-2PACz was acquired from the Tokyo Chemical Industry. All materials were utilized without further purification.

3.2 2D/3D Perovskite Heterojunctions Preparation

The ITO substrates underwent a cleaning process involving ultrasonic treatment with deionized water, acetone, and isopropanol for a duration of 20 minutes each, followed by UV ozonation. The tin (IV) oxide colloid was diluted with deionized water at a volume ratio of 1:5, followed by filtration and uniform spin-coating at 3000 rpm for 30 seconds. Subsequently, the sample was annealed at a temperature of 180 degrees for a duration of 30 minutes. A mixture comprising of 461 mg of PbI_2, 154.8 mg of FAI, and 26 mg of CsI was dissolved in a solvent mixture of anhydrous DMF and DMSO with a volume ratio of 4:1. The solution was subjected to shaking until complete dissolution was achieved. Then, the solution containing the perovskite precursor underwent spin-coating at an acceleration rate of 1000 revolutions per minute for a duration of 20 seconds, while being subjected to a rotational speed of 5000 rpm. Subsequently, 200 µl of CB was gradually introduced into the solution as an anti-solvent at the 10-second after the beginning of spin-coating, followed by a heating process at 150 °C for a duration of 10 minutes. Various concentrations of PEAI (or PEABr) were dissolved in an IPA solution. The perovskite film was subjected to spin-coating at 3000 rpm for 30 seconds with an organic spacer cation solution after being cooled. To form 2D perovskite, the film was annealed on a hot table at 100 ° C for 10 min after spinning the IPA solution, as shown in Figure 3.1 below. The HTL solution was formulated through the dissolution of 72.3 mg of Spiro-OMeTAD, 17.5 µL of a stock solution containing 520 mg/mL LiTFSI/acetonitrile, and 28.8 µL of 4-TBP in 1 mL of CB. Subsequently, a metal electrode was produced through thermal evaporation of a gold film with a thickness of 80 nm.

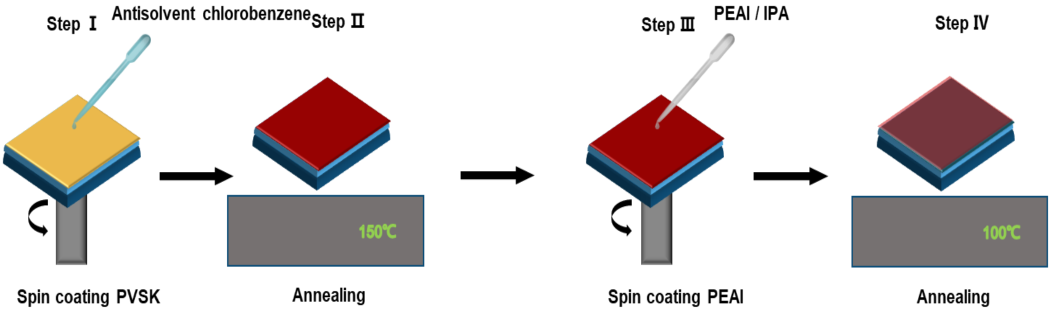

Figure 3.1 Preparation method of 2D/3D perovskite heterojunctions.

3.3 Cs-corrected TEM

The “Cs corrector” generates a negative coefficient (Cs) of spherical aberration to counterbalance the positive Cs of the objective and condenser lenses, which are magnetic field lenses with axial symmetry. The Cs-corrected TEM is a highly sophisticated variant of the transmission electron microscope that has been developed to address the issue of spherical aberration. This type of aberration is a fundamental constraint of electron lenses in traditional TEM. Spherical aberration is a phenomenon that arises when electrons traverse a lens and converge at disparate focal points, leading to the production of an indistinct image. The correction of Cs-induced aberration in TEM is achieved through the utilization of electron lenses that are specifically designed to produce an image with enhanced sharpness and focus. This results in the acquisition of images with higher resolution and increased sample detail. The foremost benefit of Cs-corrected TEM lies in its capability to capture images of materials at the atomic level. This feature is crucial in comprehending the characteristics and actions of materials at the nanoscale. The instrument possesses the ability to generate high-quality images of both crystalline and amorphous substances and can capture images of specimens subjected to diverse conditions, including elevated temperatures and reactive surroundings. The utilization of Cs-corrected TEM is prevalent in the fields of materials science, nanotechnology, and biology, where it serves a multitude of purposes. These include the examination of nanoparticle structure and characteristics, the comprehension of catalyst behavior, and the visualization of biological structures such as viruses and proteins. The low-dose imaging properties of this technique enable high-resolution imaging of electron beam-sensitive materials, including perovskite.

As Figure 3.2 shows, the Thermo Scientific™ Spectra 300 Scanning/Transmission Electron Microscope (S/TEM) is a highly efficient and dependable instrument that offers exceptional performance for the examination of semiconductor materials and semiconductor failure analysis, making it the fastest and most reliable tool in its category. The combination of a high-brightness field emission gun (X-FEG) and user-friendly software enables access to knowledge pertaining to sophisticated products, including those with 7 nm or smaller node devices. This high-end S/TEM is well-suited for industrial applications due to its capacity to produce rapid energy-dispersive X-ray spectroscopy (EDS) maps while maintaining spatial resolution, as well as its capability for EELS and low-kV analysis. The utilization of this potent instrument enables us to achieve high-resolution imaging of perovskite materials while employing a low beam dose.

Figure 3.2 Spherical Aberration Corrected Transmission Electron Microscope.

3.4 FIB and Cross-sectional STEM Sample Preparation

The FIB technique is a form of microscopy that employs a concentrated beam of ions to generate images, ablate and manipulate samples at a nanometer scale. The ion beam is composed of gallium ions that are accelerated to high energies and subsequently concentrated onto a limited region of the sample surface. The utilization of this method presents multiple benefits in the context of sample preparation for STEM visualization. The FIB technique is capable of achieving high precision and accuracy in the milling and shaping of samples to meet specific requirements in terms of thickness, size, and shape. This facilitates the generation of extremely thin specimens for achieving high-resolution imaging and the construction of intricate configurations for conducting in situ experiments. Furthermore, FIB has the capability to selectively eliminate undesired regions of a specimen, thereby enabling the isolation of particular regions of interest for STEM imaging. The utilization of FIB enables the direct extraction of cross-sectional samples from perovskite solar cell devices with a high degree of precision and reliable reproducibility, rendering it an optimal technique for conducting STEM experiments.

The cross-sectional TEM specimens were prepared through a dual-beam FIB nanofabrication platform (Helios 5CX, Thermofisher, USA). A 0.3 μm thick platinum (Pt) protection layer was first deposited on the top of the device's metal electrode surface by electron deposition. Then, a 3 μm thick Pt protection layer was deposited by an ion beam to further protect the sample area. The operation voltage of the gallium ion beam is 30 kV and the working current is 0.1–47 nA for lamella processing. Subsequently, the lamella was extracted from the substrate and directly transported to a TEM half grid in FIB chamber. The lamella's observation area was thinned to less than 50 nm using a gallium ion beam with a current ranging from 40 to 790 pA, followed by precise milling and polishing using an ion beam with an accelerating voltage as low as 1 kV and a working current of 72 pA. Furthermore, as shown in Figure 3.2, subsequent to acquiring the STEM sample from FIB, we applied a layer of amorphous carbon with a thickness of approximately 10 nm onto the sample by a high-vacuum coater

(Leica ACE 600) at a pressure of 1 × 10^{-4} mbar. The protective function of the amorphous carbon coating is attributed to its ability to absorb the energy of incoming electrons, thereby preventing their penetration and subsequent damage to the underlying sample. The application of this coating results in a reduction of electron radiation that reaches the sample, thereby mitigating the deleterious effects of the electron beam. Furthermore, the application of an amorphous carbon coating has the potential to enhance image contrast and resolution in electron microscopy through the mitigation of charging and beam-induced contamination[23,24,132].

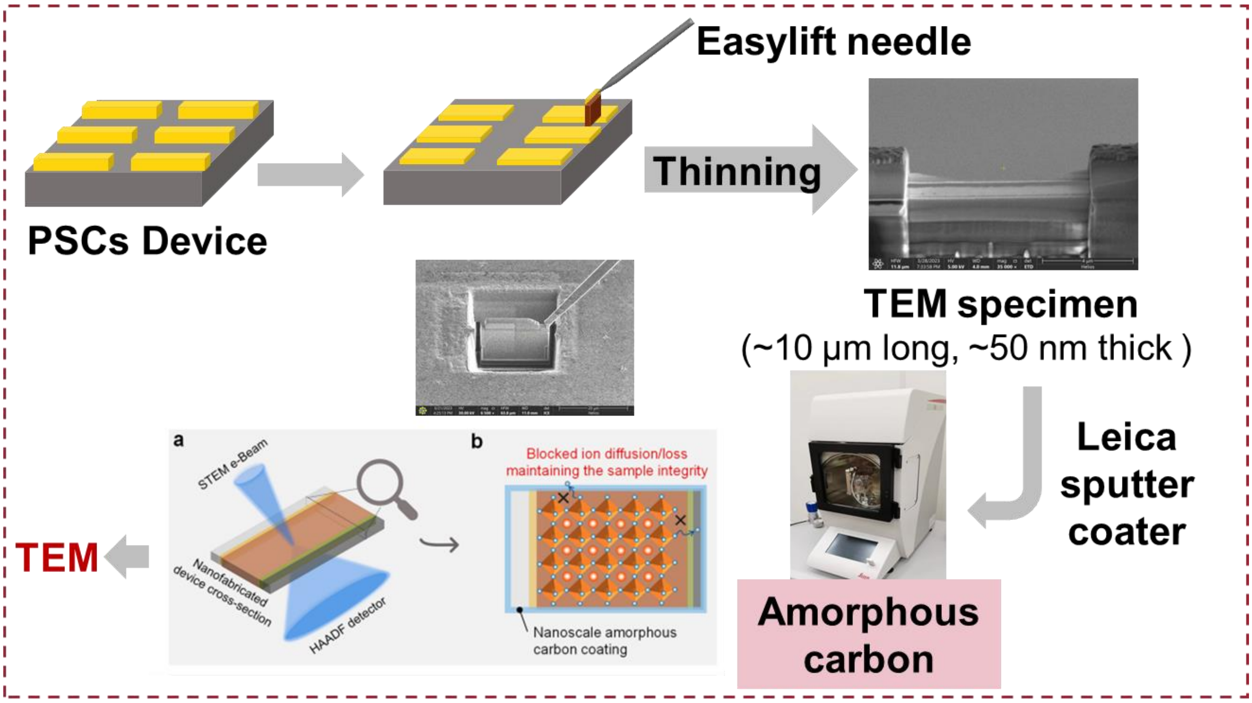

Figure 3.3 Cross-sectional STEM sample preparation[23].

3.5 Other Characterization

3.5.1 HAADF-STEM

The device cross-section specimens were observed using an aberration-corrected S/TEM (Spectra-300, Thermofisher, USA; equipped with a field emission gun) operating at an accelerating voltage of 300 kV. The probe convergence angle is 24.5 mrad, whereas the angular range of the HAADF detector extended from 79.5 to 200 mrad. The duration that each pixel is exposed during the acquisition of HAADF-STEM images is 6 μs for image acquisition area is larger than 200×200 nm^2 (4 μs for image acquisition area is smaller than 200×200 nm^2), and the dimensions of all STEM images in this study are 2048×2048 pixel^2. The frame size for the high-resolution STEM images is around 200×200 nm^2. The beam current was around 1 pA and the cumulative electron dose was approximately 39.3 e·Å^{-2} (< 50 e·Å^{-2}), which was confirmed to be maintained at a low level to minimize beam-induced damage.

3.5.2 EELS

The EELS datasets were acquired with an electron beam current of 25 pA using Gatan's K3 single-electron counting direct detection camera in Spectra 300 S/TEM. Dual-EELS mode with a dispersion of 0.18 eV/ch, covering a 622 eV energy range was used to capture the N K-edge, I M-edge and Br L-edge signals. In order to obtain a better signal-to-noise ratio (SNR), the I and Br signals were detected separately with different acquisition energy ranges (for I M-edge, 380 eV to 1002 eV, for Br L-edge, 1200 eV to 1822 eV) at the same location.

3.5.3 4D-STEM

The utilization of 4D-STEM (four-dimensional scanning transmission electron microscopy) presents various benefits in comparison to traditional STEM methodologies[133-136]. The foremost advantage of this technique is its ability to provide atomic resolution images and diffraction patterns concurrently, thereby facilitating comprehensive structural and physical analysis of materials. Then, it facilitates the swift accumulation of extensive datasets, which can be subjected to analysis through machine learning and other sophisticated methodologies to extract comprehensive insights about the characteristics of the substance. Besides that, it has the potential to be utilized for in-situ and operando investigations, thereby facilitating the examination of dynamic phenomena in real-time. As depicted in Figure 3.3, 4D-STEM has the ability to rectify aberrations and other imaging distortions, thereby yielding measurements of material properties that are highly accurate and precise[137-140].

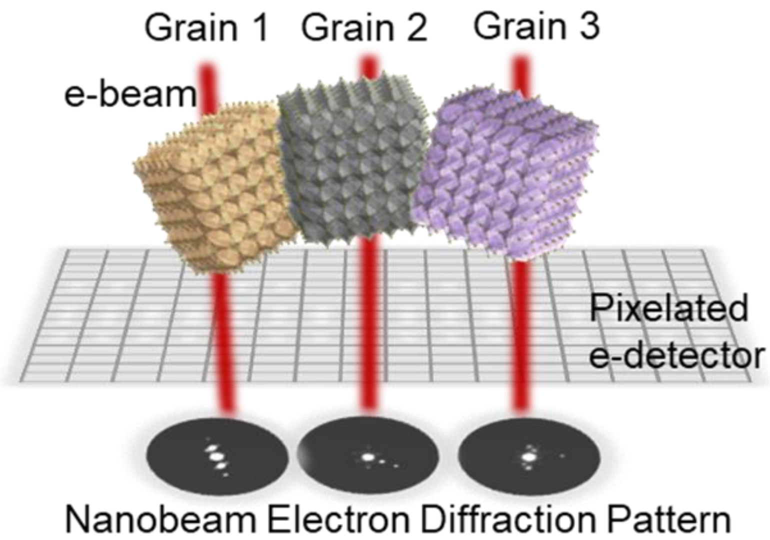

Figure 3.4 Schematic of 4D-STEM experiment. Collected nano beam electron diffraction (NBED) can be employed to scrutinize the crystallinity and the orientation of the perovskite grains.

For the 4D STEM measurements, an electron probe with a convergence angle of 1 mrad was used and the beam current was reduced below 1pA (~0.2pA), thus reducing the electron dose below the threshold values for radiation damage. The 4D STEM datasets were acquired by a pixelated e-detector (EMPAD, the pixel number of the EMPAD detector is 128 × 128 pixels) with a single exposure of 1 ms and the summed intensities of 512 × 512 diffraction patterns were collected. Therefore, the cumulative electron dose for a 300 nm × 300 nm acquisition region is approximately 36 $e \cdot Å^{-2}$, which is significantly lower than the 50 $e \cdot Å^{-2}$ critical electron dose that has been documented as causing beam damage in organic and inorganic hybrid perovskite samples[141,142].

3.5.4 Morphology and Physical Property Characterizations

SEM images were taken by a Helios 5CX with a 3 kV, 86 pA e-beam. The absorption was characterized by the ultraviolet-visible (UV-vis) spectrophotometer (Perkin-Elmer Lambda 35 UV-vis-NIR). Glancing-incident X-ray diffraction (XRD) was performed on a Rigaku Smartlab 3kw at an incident angle of 1°. Ultraviolet photoelectron spectroscopy (UPS) was characterized by a VG Scienta R4000 analyzer and the HeI (21.22eV) emission line was employed for excitation at a bias of -5 V. The steady-state photoluminescence spectra were obtained using a pulse laser as an optical excitation source (wavelength: 470 nm, Horiba FluorologFL-3), and a time-resolved photoluminescence (TRPL) experiment was carried out by excitation at 470 nm. Mott-Schottky was measured by a CHI660E at a frequency of 1 kHz with an applied bias voltage of 0 V~1.4 V. The fluorescence confocal images were obtained by the laser scanning fluorescence confocal microscope (Leica TCS SP8) with 488 nm laser excitation.

3.5.5 PSC Fabrication and Testing

The MeO-2PACz layer (1 mg/mL in IPA) was deposited on the ITO glass at 3000 rpm for 30 s in a nitrogen-filled glove box, then annealed at 100 °C for 10 min. For the preparation of $Cs_{0.05}(MA_{0.05}FA_{0.95})_{0.95}Pb(I_{0.95}Br_{0.05})_3$ perovskite layers, a 1.5 M precursor solution was prepared by dissolving PbI_2 (676.8 mg), FAI (232.8 mg), CsI (19.5 mg), $PbBr_2$ (41.3 mg), and MACl (35.2 mg) in 1 mL of a DMF/DMSO solvent mixture (4:1 volume ratio). The mixture was stirred overnight at room temperature and filtered through a 0.22 μm syringe filter before use. The resultant perovskite precursor solution was then spin-coated at 4000 rpm for 40 s, using 200 μl of EA as the antisolvent at the 30th second. The film was annealed at 120 °C for 20 min. For the control device, the PEAI solution (PEAI with different concentrations in IPA) was spin-coated at 3000 rpm for 30 s and annealed at 100 °C for 10 min. For the LSS device, 3D perovskite films were first subjected to spin-coating at 3000 rpm for 30 seconds with different concentrations of PCBM in CB solution to form an interlayer, then processed the same way as control samples. After forming the control films, the $PC_{61}M$ (20 mg/mL in CB) layer and the BCP (0.7 mg/mL in IPA) film were spin-coated at 2000 rpm and 4000 rpm for the 20s, respectively, then annealed at 70 °C for 10 min. Finally, a 100 nm thick layer of Ag was evaporated onto the active area through a mask ($0.09\ cm^2$). Under standard AM 1.5 G illumination using a xenon-lamp-based solar simulator (Enlitech, IVS-KA5000), the current-voltage (*J*-*V*) characteristic and steady-state power output of solar cells were measured by a Keithley 2420 sourcemeter in the nitrogen-filled glovebox. The light intensity was calibrated by a silicon (Si) diode (Hamamatsu S1133) equipped with a Schott visible-color glass filter (KG5 color filter). The step voltage and scan speeds were 20 mV and $0.2\ V\ s^{-1}$. The reference cell for further calibrating the solar simulator before *J*-*V* measurements was an Oriel® reference solar cell accredited by NIST to the ISO-17025 standard. The area of the metal aperture used during the test is 0.069 cm^2. EQE was recorded at a chopping frequency of 165 Hz in AC mode on a solar cell quantum efficiency measurement system (QE-R3011, Enlitech). The *p-i-n* PSCs with the configuration of ITO/MeO-2PACz/perovskite/C60/BCP/Ag were fabricated for all stability tests. For the light-soaking stability, the unencapsulated PSCs were tested periodically on continuous one-sun illumination in a nitrogen atmosphere. For the damp heat test, the PSCs were all encapsulated using UV-curing adhesive with a cover glass. Then, the edge of the cover glass was further protected by epoxy and cured at room temperature for >48 hours. The encapsulated devices were placed in an environmental chamber at 85 °C and 85% RH, and the PCEs were measured periodically after the devices cooled to room temperature. Experiments were conducted to determine the unencapsulated devices' long-term operational stability in a flowing nitrogen atmosphere upon MPP tracking and continuous light irradiation with a white LED lamp (100 mW cm^{-2}).

Chapter 4 Effect of Halide Ion in 2D/3D Perovskite Heterojunctions

4.1 Introduction

Halide ions play a crucial role in tuning the properties of OIHPs. First of all, bandgap adjustment can be achieved by using different halide ions such as chloride, bromide, and iodide, hence impacting the range of light absorption[143-146]. Besides, by selecting specific halide ions, the ability of OHIPs to withstand moisture and heat stress can be improved, thereby extending the longevity of the PSCs[147-150]. Furthermore, optimal halide selection may reduce defects and trap states, resulting in improved movement of charges and decreased losses due to recombination[149,151-154]. The optoelectronic properties of solar cells can be optimized by the presence of halide ions, which have a significant impact on the optical and electrical characteristics, leading to improved efficiency and performance[155-160].

In addition, different halide ions also have significant effects on the optical properties of 2D perovskite. The bandgap of perovskite is directly influenced by the specific type of halide ion present. Typically, the presence of chlorides, bromides, and iodides can progressively elevate the bandgap, resulting in a modification of the material's absorption spectra. The alteration of the bandgap will result in a corresponding modification in the material's ability to absorb various wavelengths of light. This can be utilized to modify the optical reaction of the device to accommodate a particular application. Besides, a particular choice of halide ions also impacts the fluorescence emission properties of the material, altering its luminosity and color[161-165].

Researchers have recently discovered that precise manipulation of the crystal orientation in 2D layered perovskite (LP) films is a crucial factor in the attainment of optimal optoelectronic device functionality, including but not limited to solar cells and photodetectors[72]. The successful preparation of 2D LP films with diverse crystal orientations, such as random, vertical, mixed, and parallel, has been achieved through the manipulation of chlorine ion concentration. The findings of their research indicate that the incorporation of chlorine can serve as a viable means of controlling the crystallization mechanisms of 2D LP films, as evidenced by their synchrotron-based in situ grazing-incidence X-ray diffraction experiments. This is attributed to the creation of intermediates that are associated with chlorine[72].

The study in this chapter involved the incorporation of a different quantity of FACl into PEAI to treat 3D perovskite with the aim of investigating its potential impact on the dispersion of 2D perovskite. Additionally, we will analyze the impact of introducing a specific quantity of Cl^- on the performance of PSCs and the durability of OIHP films. Next, we modified the composition of the 3D perovskite to $FA_{0.9}Cs_{0.1}PbBr_3$ and kept employing a PEAI solution as a substrate to form 2D perovskite. Our objective is to examine the potential changes in the structure and distribution of the resulting 2D perovskite. Finally, PEAI will be substituted with PEABr to examine the impact of halide ions in 2D organic salt solutions on the configuration of 2D/3D heterojunctions.

4.2 FACl Addition on PEAI Solution

The grain distribution on the perovskite film of $FA_{0.9}Cs_{0.1}PbI_3$ appears to be relatively uniform, as depicted in the SEM presented in Figure 4.1a. Notably, there is no apparent variation in brightness. However, it is worth noting that some nanosheets are observed to be present between the grains that may be attributed to excess PbI_2 (Figure 4.1a). Upon exposure to a concentration of 5 mg/mL of PEAI, the grain boundaries exhibited significant blurring, and the surface of the film displayed dark-colored regions, as evidenced by the white circles (Figure 4.1b). Upon further augmentation of the PEAI concentration, an expansion in the coverage of regions exhibiting dark hues was observed[96,166], concomitant with the generation of broad strips of two-dimensional grains (Figure 4.1c).

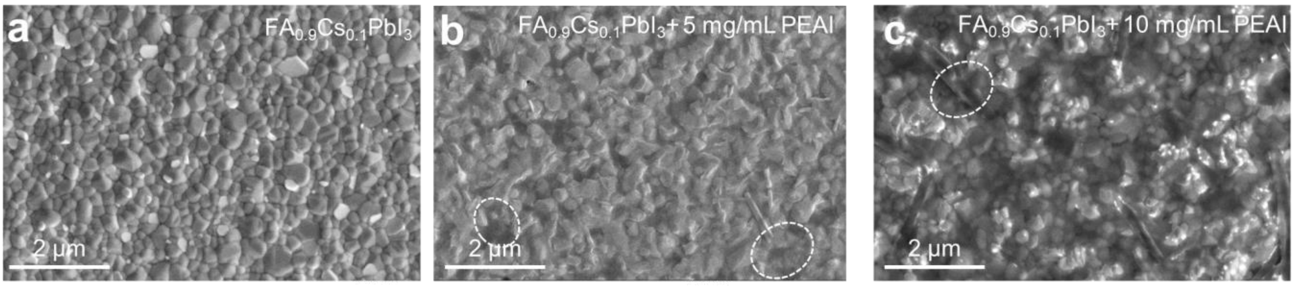

Figure 4.1 SEM images of perovskite film treated with different concentrations of PEAI. **(a),** Control $FA_{0.9}Cs_{0.1}PbI_3$ perovskite film; **(b),** treated with 5 mg/mL PEAI; **(c),** treated with 10 mg/mL PEAI.

The SEM image presented in Figure 4.2a reveals that the application of 10 mg of PEAI treatment on the pristine perovskite film resulted in the formation of a non-uniform thickness of 2D perovskite. The surface of the film exhibited numerous strips of 2D perovskite that displayed a significantly higher thickness compared to the non-stripped regions, as evidenced by the deeper contrast observed. Furthermore, it is evident that a majority of the 3D perovskite grains remain uncovered by the 2D perovskite. The inclusion of 0.0125% mmol/mL (by weight ratio) FACl in 10 mg/mL PEAI solution resulted in a notable reduction in the striped pattern of 2D perovskite, accompanied by a substantial increase in the surface area covered by these materials. Upon increasing the FACl concentration to 0.05% mmol/mL, the striped 2D perovskite became nearly imperceptible, while the 2D perovskite effectively enveloped the entirety of the 3D perovskite grains.

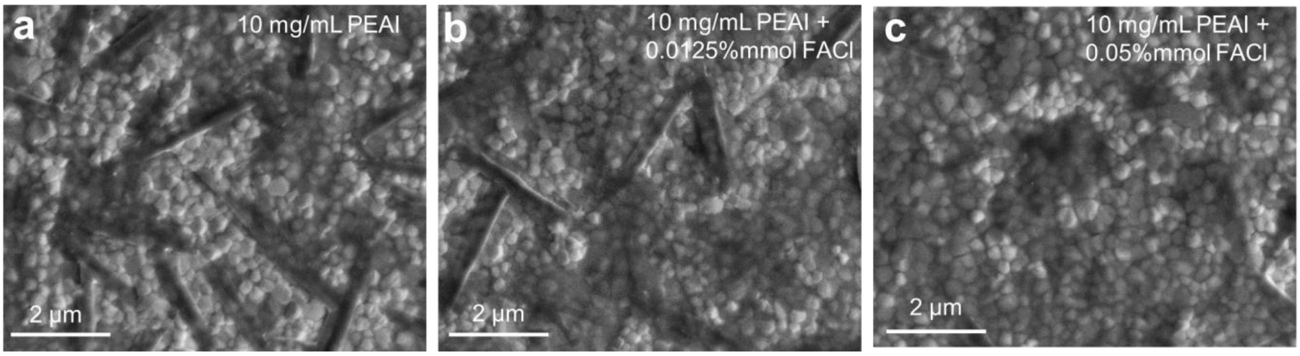

Figure 4.2 SEM images of perovskite film treated with 10 mg/mL PEAI and different amounts of FACl. **(a)**, $FA_{0.9}Cs_{0.1}PbI_3$ perovskite film treated with 10 mg/mL PEAI; **(b),** 10 mg/mL PEAI with 0.0125% mmol/mL FACl addition; **(c),** 10 mg/mL PEAI with 0.05% mmol/mL FACl addition.

Figure 4.3a illustrated that the grain surface of $FA_{0.9}Cs_{0.1}PbI_3$ became uneven and exhibited significant variations in height after being treated with a concentration of 10 mg/mL PEAI. The challenging task of preserving the original structure of the 3D perovskite near the surface arises due to the vigorous ion exchange occurring between PEAI and the 3D grain surface. The thickness of the 2D perovskite produced through ion exchange reaction ranges from 15 to 50 nm, with the primary distribution of n values being $n = 1$ ($d = 1.71$ nm), $n = 2$ ($d = 2.20$ nm), and $n = 4$ ($d = 3.60$ nm), measured from Figure 4.3b and Figure 4.3b. The unorganized mixture of these 2D perovskites with varying n values will result in hindered charge transport, hence causing a substantial decrease in the energy conversion efficiency of PSCs[71,72,167,168]. During the experimental process, we observed that severe ion beam damage during FIB sample preparation may lead to the emergence of large-area bright spot-like features in HAADF-STEM images. In contrast, electron beam irradiation damage induced by STEM observations typically manifests as newly formed darkened regions within the imaging area.

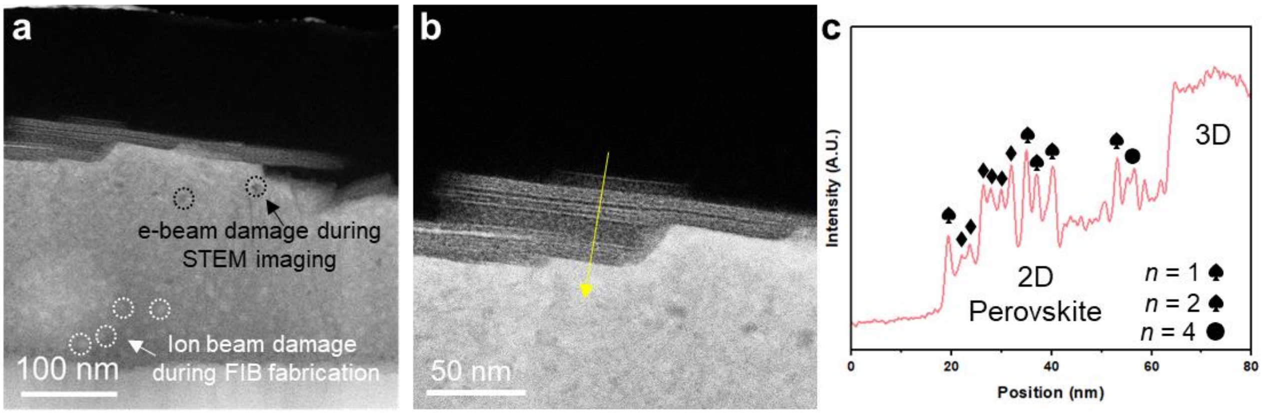

Figure 4.3 HAADF-STEM image **(a)** and magnified image **(b)** and line profile image **(c)** of yellow arrow area in the 2D/3D perovskite device, treated with 10 mg/mL PEAI. The bright contrast features are likely attributed to gallium ion implantation or platinum redeposition during FIB sample preparation (typical beam current: 40 pA, acceleration voltage: 30 kV), whereas the dark-contrast regions predominantly result from localized amorphization caused by electron beam irradiation.

When 0.05% mmol FACl was added to the PEAI solution, as depicted in Figure 4.4a, the thickness of the resulting 2D perovskite fell dramatically to around 3-15 nm. Additionally, the coverage of the 3D grain surfaces increased, resulting in a smooth surface without noticeable damage. Figure 3.4b and c demonstrate that there is only one thin layer of 2D perovskite present on the surface of 3D perovskite. The layer’s thickness, as measured, is approximately 2.99 nm, contributing to a 2D perovskite with *n* value of 3. The presence of FACl in these extremely thin 2D structures demonstrates that it may minimize the adverse effects caused by PEA^+ to 3D grains. This inclusion also promotes the formation of 2D perovskite with a single *n* value, consequently enhancing the stability of 2D/3D PSCs without sacrificing efficiency.

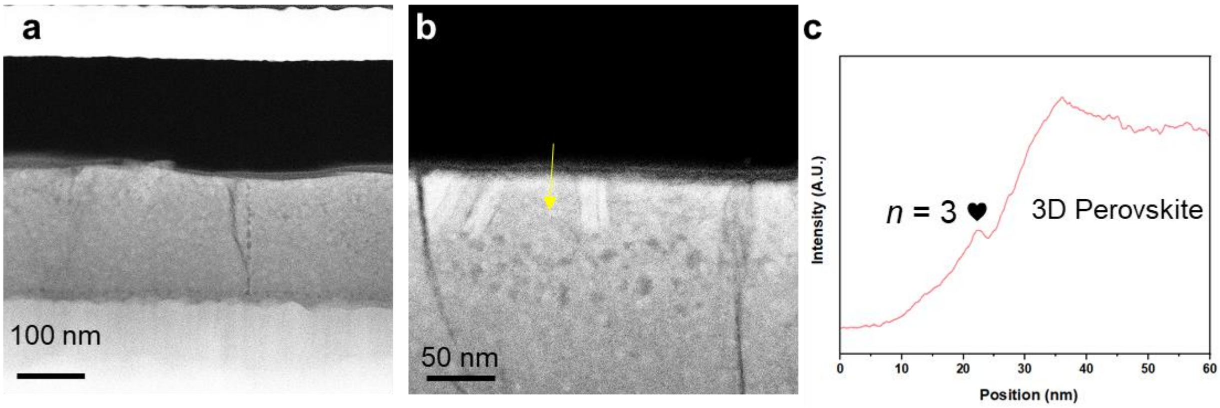

Figure 4.4 HAADF-STEM image **(a)** and **(b)** and line profile image **(c)** of yellow arrow area in the 2D/3D perovskite device, treated with 10 mg/mL PEAI with 0.05% mmol/mL FACl addition. The bright contrast features are likely attributed to gallium ion implantation or platinum redeposition during FIB sample preparation (typical beam current: 40 pA, acceleration voltage: 30 kV), whereas the dark-contrast regions predominantly result from localized amorphization caused by electron beam irradiation.

Subsequently, an investigation was conducted to assess the stability of the films under varying concentrations of the Cl^- mixture in perovskite. After being kept at room temperature (RT) and humidity levels of approximately 20°C and 30%-40%, respectively, for a period of 7 days, the unencapsulated initial films did not exhibit any notable alterations (Figure 4.5a and Figure 4.5b). Upon elevating the temperature and humidity levels, notable alterations were detected in select films, as depicted in Figure 4.5c. Specifically, the 3D perovskite films exhibited near-complete transparency, which suggests a considerable deterioration of the perovskite material. A discernible reddening of the 3D perovskite film has been observed after the application of 5 mg PEAI. This suggests that the 2D perovskite layer has been effectively conserved, while a certain proportion of the 3D perovskite has undergone degradation. The stability of the perovskite phase of 2D/3D material remained unaffected after chlorine doping, as evidenced by the insignificant change in its color. This suggests that the material's perovskite phase is stable and did not undergo any significant degradation.

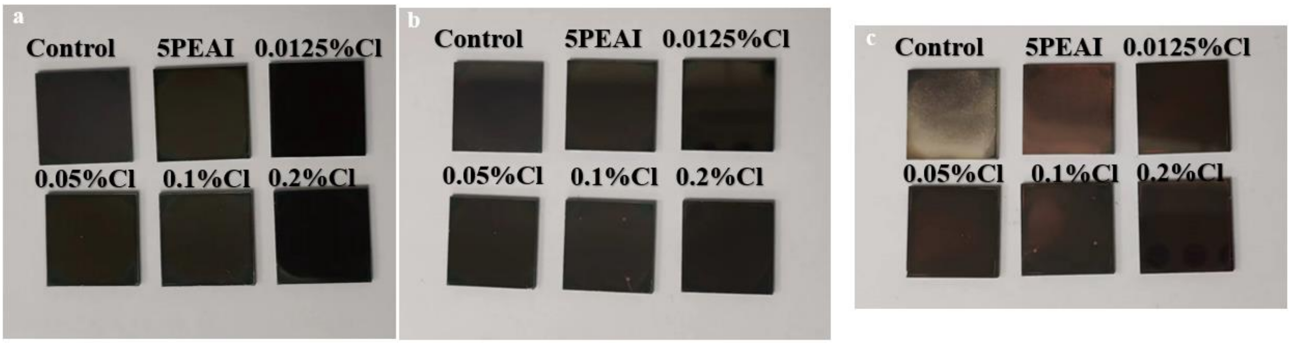

Figure 4.5 Stability test of perovskite films with different concentrations of Cl$^-$ addition. **(a),** Initial sample; **(b),** Sample placed in RT RH~20℃ 30%-40% for 7 days. **(c),** Sample placed in ~ 85℃ 85% humidity for 1 min.

The *J-V* plot of the perovskite solar cell device is depicted in Figure 4.6. The V_{OC} of the device exhibits a noteworthy enhancement of 1.12 V with the application of 5 mg of PEAI treatment, in contrast to the reference value of 1.07 V. There exist multiple factors that may contribute to the augmentation of V_{OC} in perovskite-based photovoltaic devices. The mitigation of non-radiative recombination within the apparatus is a primary contributing element. Enhancement of the perovskite film's quality can be attained through defect reduction or surface passivation improvement. An additional aspect to consider is the enhancement of charge carrier mobility, which may be attained through the optimization of the perovskite film's morphology or the incorporation of additives into the device. Furthermore, augmenting the energy offset amid the perovskite and the charge transport layers has the potential to enhance the V_{OC}. Ultimately, the enhancement of V_{OC} can be achieved through the mitigation of parasitic absorption in the charge transport layers. However, the J_{SC} experiences a minor reduction. The above observation suggests that the implementation of a 2D perovskite layer serves to passivate the surface of 3D perovskite, thereby mitigating the occurrence of defects and non-radiative recombination. The introduction of Cl$^-$ doping has resulted in an enhanced efficiency of the device from 15.26% to 18.10%, with a slight increase in J_{SC} and a higher V_{OC} being maintained. Cl$^-$ doping has adjusted the distribution of the 2D perovskite layer, which is more conducive to improving the device's performance.

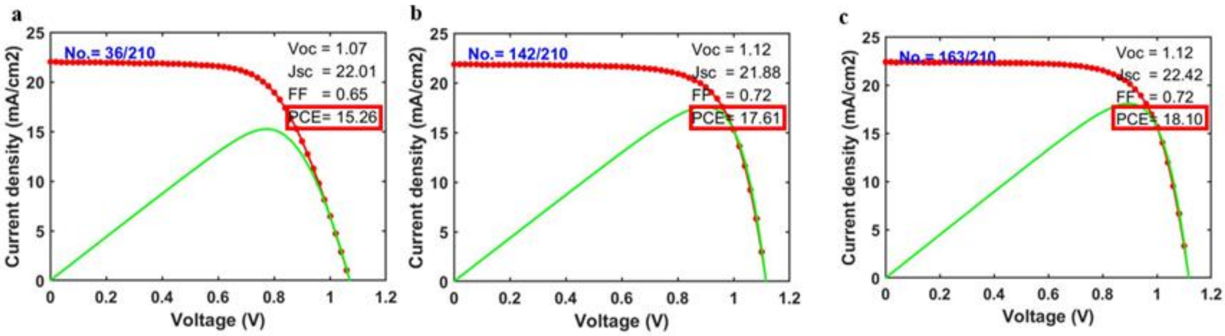

Figure 4.6 Device performance of PSCs with different treatments. **(a),** Control sample $FA_{0.9}Cs_{0.1}PbI_3$; **(b),** treated with 5 mg/mL PEAI; **(c),** 5 mg/mL PEAI with 0.05% mmol/mL FACl addition.

4.3 $FA_{0.9}Cs_{0.1}PbBr_3$ Treated with PEAI

$FAPbBr_3$ is a kind of perovskite that possesses a broad energy gap, making it well-suited for applications in LEDs and displays[169-173]. Perovskite containing bromide has superior resistance to moisture when compared to iodide[174,175]. Instead of using $FA_{0.9}Cs_{0.1}PbI_3$, we constructed $FA_{0.9}Cs_{0.1}PbBr_3$ via a two-step procedure. To provide a mixed solution with a concentration of 1 mmol/mL, 0.9 mmol $PbBr_2$ and 0.1 mmol CsBr were put into a 1 mL mixed solvent of DMF:DMSO (4:1 at volume ratio). Subsequently, the above solution was applied onto the substrate via spin-coating and then subjected to annealing on a heating plate at a temperature of 70 °C for a duration of 1 minute. Next, a solution of FAI (in IPA) with a concentration of 1 mmol per milliliter was applied onto the prepared films via spin-coating. The coated films were then subjected to annealing on a heating plate at a temperature of 150 °C for a duration of 15 minutes. This process resulted in the formation of

$FA_{0.9}Cs_{0.1}PbBr_3$. To conduct a comparison with $FA_{0.9}Cs_{0.1}PbI_3$, we utilized the same concentration of 10 mg/mL PEAI to treat those 3D grains of $FA_{0.9}Cs_{0.1}PbBr_3$.

Figure 4.7a reveals that the grain size of $FA_{0.9}Cs_{0.1}PbBr_3$ is larger than that of $FA_{0.9}Cs_{0.1}PbI_3$. A 2D perovskite film with non-uniform thickness was formed when a concentration of 10 mg/mL of PEAI was applied (Figure 4.7b). Additionally, there were areas where 3D grains were not fully coated by the 2D perovskite. Figure 4.7c clearly illustrates that the exposed surface of three-dimensional grains still exhibits remnants of damage despite not being fully covered by two-dimensional material.

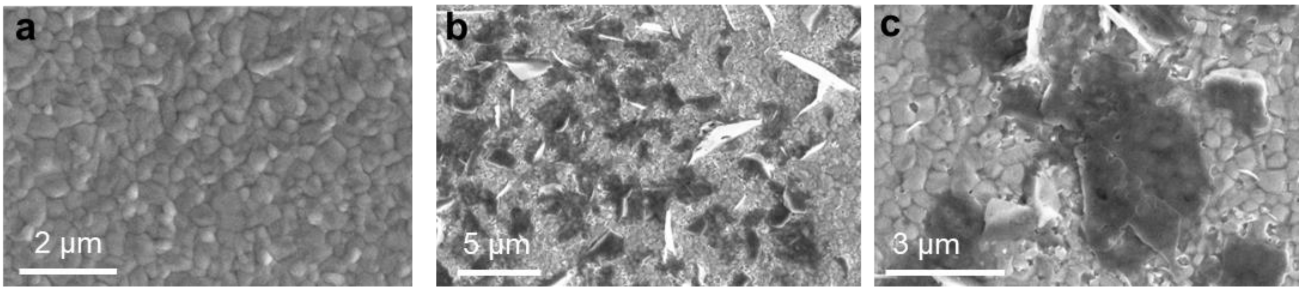

Figure 4.7 Top-view SEM images of **(a)**, $FA_{0.9}Cs_{0.1}PbBr_3$ perovskite film; **(b)** $FA_{0.9}Cs_{0.1}PbBr_3$ perovskite film treated with 10 mg/mL PEAI. **(c),** Magnified SEM images of $FA_{0.9}Cs_{0.1}PbBr_3$ perovskite film treated with 10 mg/mL PEAI.

Figure 4.8a illustrates a perovskite heterojunction with a damaged 3D surface and a thick, uneven 2D perovskite layer. The 2D perovskite has a thickness of roughly 100 nm when measured parallel to the 3D grain, whereas its vertical growth measures over 800 nm in thickness. The excessive thickness and unevenness of 2D perovskite suggested that the surface of the 3D grain has a very strong ion exchange with PEAI, possibly exacerbated by the presence of Br in the 3D perovskite. Furthermore, Figure 4.8b illustrates the presence of a 2D perovskite layer with $n = 2$ on the surface of the 3D grain, followed by many stacked layers of 2D perovskite with $n = 1$. The existence of several layers of $n = 1$ perovskite placed horizontally on 3D perovskite grains will significantly impede the movement of carriers.

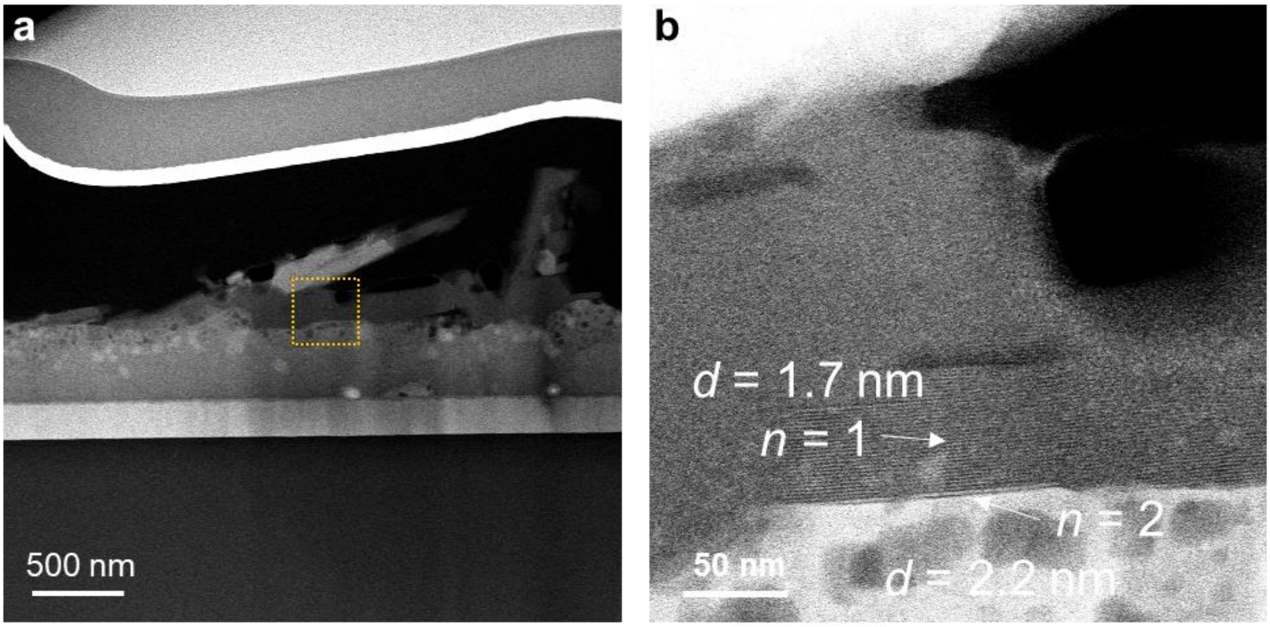

Figure 4.8 HAADF-STEM image of **(a)** $FA_{0.9}Cs_{0.1}PbBr_3$ PSC treated with 10 mg/mL PEAI. **(b),** Magnified HAADF-STEM image of orange square in **(a)**.

After that, we lowered the concentration of PEAI to 5 mg/mL. As a result, we observed a decrease in the thickness of the 2D perovskite layer formed by it, as well as a reduction in the growth of the vertical 2D perovskite on the 3D grain surface. However, the thickness of the 2D layer remained relatively thick, measuring approximately 50–100 nm, as depicted in Figure 4.9a. Furthermore, after conducting a more detailed analysis of the orange box in Figure 4.9a, it is observed that the distribution of *N*-values in 2D perovskites consists of alternating layers of 2D perovskites with $n = 2$ and 1-4 layers of 2D perovskites with $n = 1$. This would indicate that as the concentration of PEAI decreases, the proportion of 2D perovskites with $n = 2$ increases while the number of 2D perovskites with $n = 1$ decreases (Figure 4.9b).

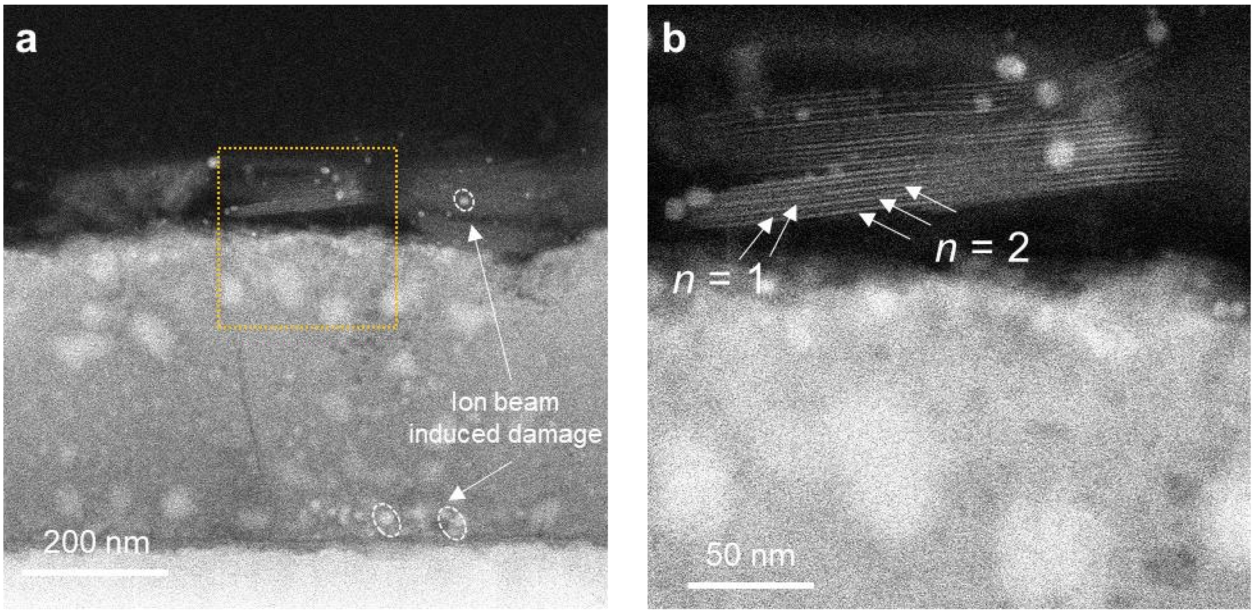

Figure 4.9 HAADF-STEM image of **(a)** $FA_{0.9}Cs_{0.1}PbBr_3$ PSC treated with 5 mg/mL PEAI. **(b),** Magnified HAADF-STEM image of orange square in **(a)**. The bright contrast features are likely attributed to gallium ion implantation or platinum redeposition during FIB sample preparation (typical beam current: 40 pA, acceleration voltage: 30 kV), whereas the dark-contrast regions predominantly result from localized amorphization caused by electron beam irradiation.

Aside from 2D/3D interfaces, there has consistently been a significant interest in studying 3D grain boundaries[176-179]. We chose an instance of the grain boundary, as depicted in Figure 4.10a. While there was no apparent presence of 2D perovskite on the surface of the 3D grains, it was shown to exist near the grain boundary. Three layers of 2D perovskites with a value of $n = 2$ were discovered after carrying out an investigation (Figure 4.10b). The penetration depth of these two-dimensional perovskites into three-dimensional structures is around 180 nanometers.

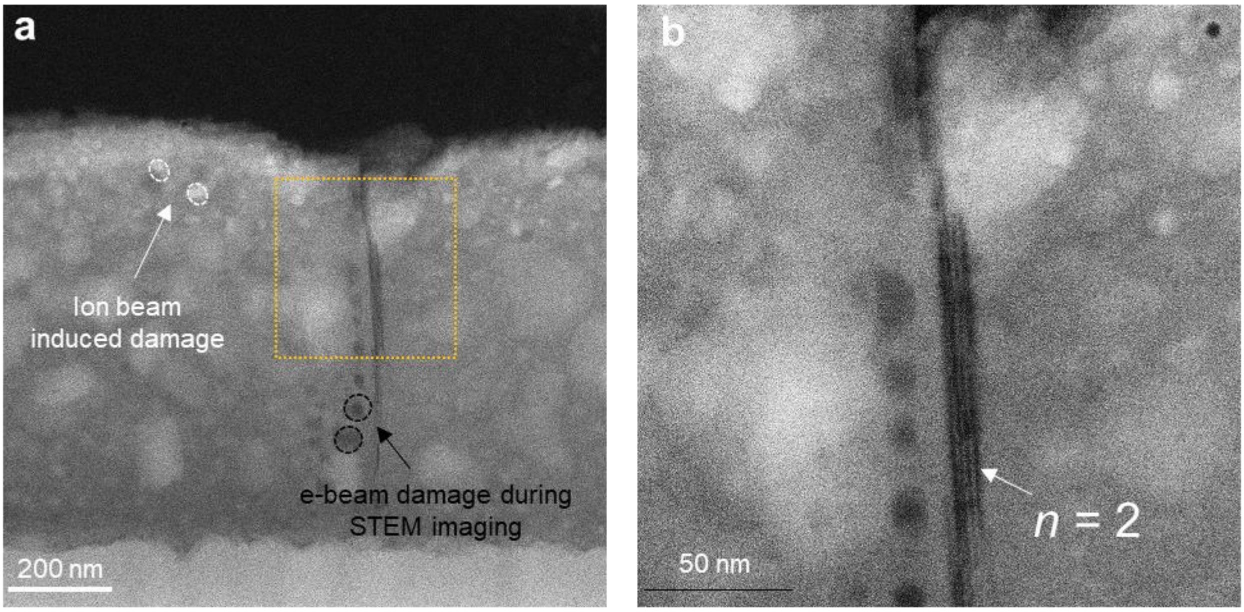

Figure 4.10 HAADF-STEM image of grain boundaries on **(a)** $FA_{0.9}Cs_{0.1}PbBr_3$ PSC treated with 5 mg/mL PEAI. **(b),** Magnified HAADF-STEM image of orange square in **(a)**. The bright contrast features are likely attributed to gallium ion implantation or platinum redeposition during FIB sample preparation (typical beam current: 40 pA, acceleration voltage: 30 kV), whereas the dark-contrast regions predominantly result from localized amorphization caused by electron beam irradiation.

4.4 $FA_{0.9}Cs_{0.1}PbI_3$ Treated with PEABr

The distribution of 2D perovskite exhibits a dramatic change when the I^- in 3D perovskite is replaced with Br^-. Hence, our intention is to exchange PEAI with PEABr to carry out a more detailed investigation on the potential of Br^- to improve ion exchange at the interface between 2D and 3D perovskite, as well as their impact on the formation and distribution of 2D perovskite. As depicted in Figure 4.11a and b, the 3D perovskite grains received surface treatment with a concentration of 10 mg/mL PEABr. This resulted in the formation of non-uniform 2D perovskite on the surface, which featured considerable variations in all directions.

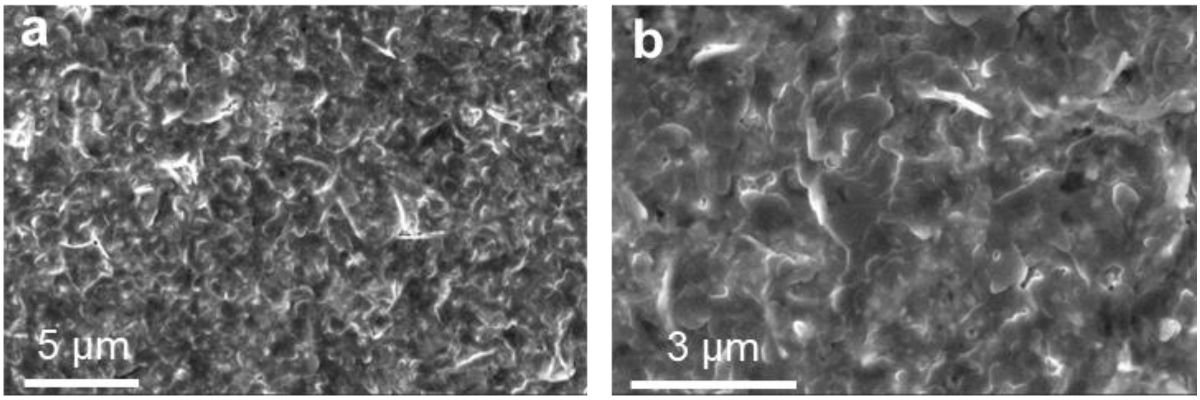

Figure 4.11 Top-view SEM images of **(a)**, $FA_{0.9}Cs_{0.1}PbI_3$ perovskite film treated with 10 mg/mL PEABr. **(b),** Magnified SEM images of $FA_{0.9}Cs_{0.1}PbBr_3$ perovskite film treated with 10 mg/mL PEABr.

The HAADF-STEM image in Figure 4.12a demonstrates that 3D $FA_{0.9}Cs_{0.1}PbI_3$ formed 2D layers with varying orientation and disparate thickness, ranging from 50 to 200 nm, after treatment with 10 mg/mL PEABr. Figure 4.12b illustrates that the ion exchange of PEABr and $FA_{0.9}Cs_{0.1}PbI_3$ results in the formation of several layers of 2D perovskite $n = 2$ on the surface first. Then, these layers subsequently stack on top of each other along with multiple layers of 2D perovskite $n = 1$ and $n = 2$. As depicted in Figure 4.12c, the 2D perovskite can be observed not only on the surface of 3D grains but also within the bulk phase of 3D grains, following the direction of 2D growth. The rapid ion exchange results in the formation of numerous 2D perovskites with diverse orientations on the surface of the 3D grain. These 2D perovskites intersect with each other, hindering their expansion in the present direction (Figure 4.12d). Thus, this approach may not be effective in producing 2D perovskite layers with uniform thickness and orientation, resulting in insufficient covering of 3D grains.

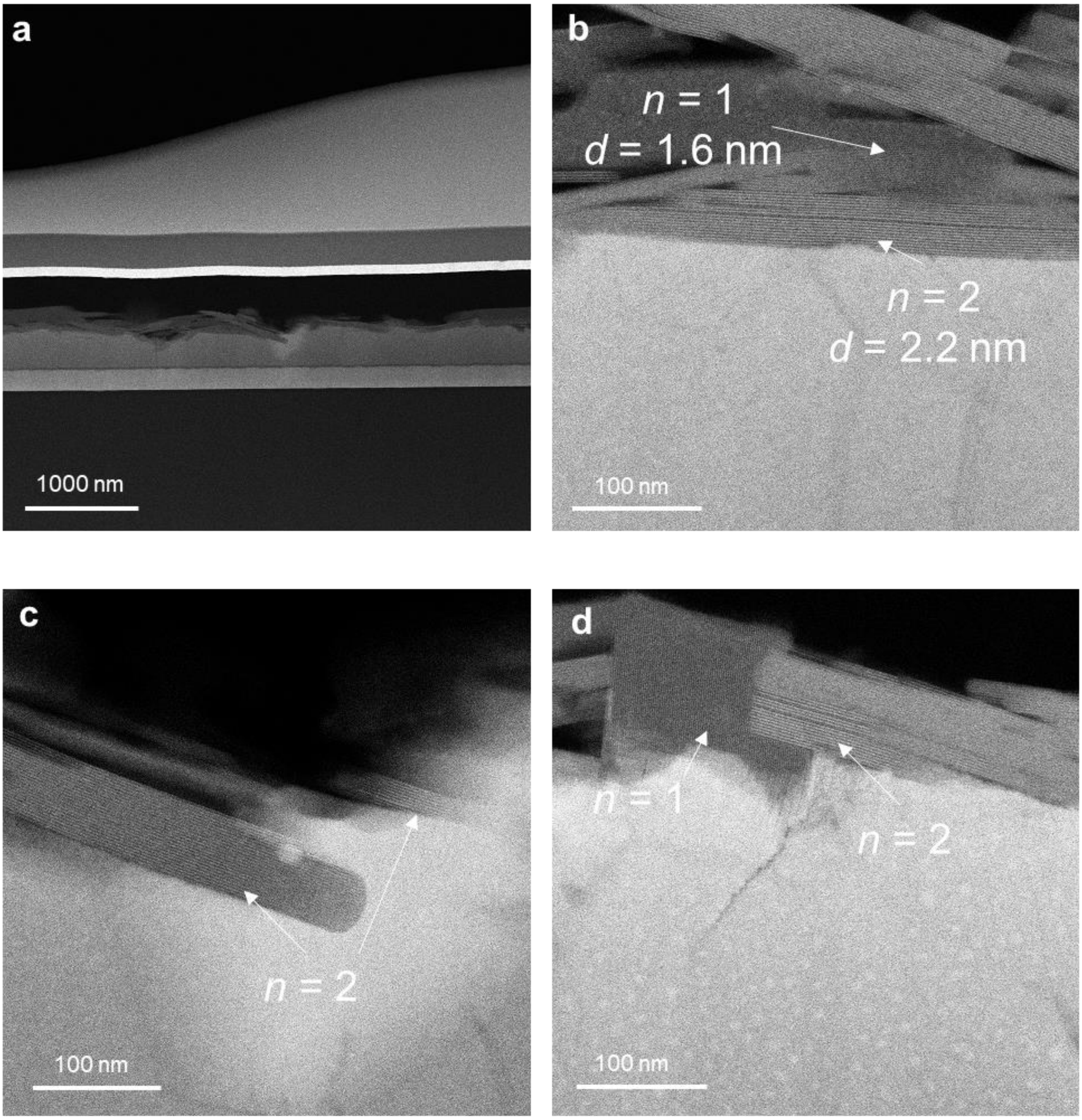

Figure 4.12 HAADF-STEM image of **(a-d)** $FA_{0.9}Cs_{0.1}PbI_3$ PSC treated with 10 mg/mL PEABr.

4.5 Conclusions

In this study, we explored the impact of different halide ions and treatments on the structural and optoelectronic properties of 2D/3D perovskite heterojunctions. By incorporating FACl into PEAI solutions, we observed a significant improvement in the uniformity and coverage of 2D perovskite layers over 3D perovskite grains. This adjustment led to enhanced device performance, as evidenced by increased V_{OC} and overall efficiency. The use of $\mathrm{FA_{0.9}Cs_{0.1}PbBr_3}$ with PEAI demonstrated that bromide-containing perovskites possess larger grain sizes, providing a promising avenue for stable optoelectronic applications. However, uneven 2D layer formation remained a challenge. Substituting PEAI with PEABr highlighted the potential of $\mathrm{Br^-}$ ions to influence ion exchange processes, resulting in diverse 2D perovskite orientations but also presenting challenges in achieving uniform coverage. Overall, this research underscores the importance of halide ion selection and treatment conditions in tailoring the microstructure and enhancing the performance of perovskite-based devices, paving the way for more durable and efficient photovoltaic applications.

Chapter 5 Synthesis of Lattice-Resolved Laminate-Structured Perovskite Heterointerface

5.1 Introduction

PSCs have emerged as a future photovoltaic (PV) technology due to their potential for combining very low cost and minimal carbon footprint in industrial manufacturing[3,180,181]. According to the sequence of depositing the device layers, PSCs are categorized into two types, regular (*n*-*i*-*p*) and inverted (*p*-*i*-*n*) PSCs. While significant advancements have been made in both types, regular PSCs have faced greater challenges regarding stability in real-world applications, primarily to the use of the lithium-doped Spiro-OMeTAD as the HTL. Consequently, inverted PSCs have garnered substantial attention in recent years and have achieved the highest PCEs[12,182]. In state-of-the-art inverted PSCs, self-assembled monolayers are used as the HTLs on the *p* side, creating intimate interfacial contacts and passivation, which result in superior PCEs and stability compared to regular PSCs. However, in inverted devices, the perovskite heterointerface on the *n* side remains relatively less ideal because of the limited molecular interaction of the fullerene-based ETL with the perovskite top surface[183-185]. In this regard, 2D perovskites or their relevant organic molecules have been incorporated as a type of effective top-surface passivators that can not only reduce the non-radiative recombination centers but also serve as a structurally capping layer to protect the film from environmental influences such as moisture ingression[19-22,185]. Numerous efforts have been made to tailor the molecular structures of 2D perovskite passivators with various organic cations, which have proven useful in achieving improved PCEs and stabilities in PSCs[186-188]. However, to date, detailed investigations into the heterointerface microstructures of 2D perovskite passivators remain rare, which may unlock new opportunities bringing up the level of device performance as well as contributing to revealing the passivation mechanisms.

In this work, by leveraging the lattice-resolved analysis capability of STEM, we observed nontrivial microstructural and phase heterogeneities in the 2D surface passivation layer deposited using the conventional method, featuring a discontinuous capping-layer microstructure and a random mixing of 2D perovskite phases with different octahedral-layer numbers (n = 2-5). We attributed this phenomenon to the uncontrolled interfacial reaction of the used 2D molecular salts with the 3D perovskite top surface, which also resulted in a detrimental morphological etching of grain boundaries due to their relatively high chemical reactivity. To mitigate these microstructural demerits, we demonstrated an unconventional route of surface passivation, in which the reaction of 2D molecular salts with 3D perovskite top surface is mediated via a "molecular sieve" layer of [6,6]-phenyl-C61-butyric acid methyl ester (PCBM). This route creates a laminate-structured surface (LSS) successively stacked by a 2D molecule layer, a PBCM interlayer, and a 2D perovskite layer of only n = 1 and 2 phases. The resultant LSS-based inverted PSCs show PCEs up to 26%, together with highly improved damp-heat and operational stabilities. Importantly, based on further STEM studies, we found LSS microstructure and phase have been well retained in the aged PSCs even after long-term stability tests, which can be attributed to the ion-blocking effects of the PCBM interlayer. This contrasts with the substantial microstructure and phase changes seen in control devices. This contrasts with the substantial microstructure and phase changes seen in control devices. This work highlights the importance of synthesizing uniform, stable passivator microstructures for perovskite photovoltaics and beyond.

5.2 Synthesis and lattice-resolved STEM analysis

For synthesizing the LSS sample, we first spin-coated an ultrathin interlayer of PCBM molecules (5 mg/mL solution in chlorobenzene (CB)) onto the surface of 3D $FA_{0.9}Cs_{0.1}PbI_3$ perovskite thin film and then spin-coated a 2D molecular salt-PEAI based solution in isopropanol (IPA; 10 mg/mL), followed by a mild thermal annealing at 100 ºC. As schematically illustrated in Figure 5.1, the sandwiched, ultrathin PCBM interlayer serves as an inert molecular sieve, which allows controlled ion penetration and exchange between the 3D perovskite and top surface sides. The PCBM-mediated interfacial reaction exhibits a much reduced rate and enables the formation of the uniform LSS microstructure. We also prepared a control PEAI-treated film sample without the involvement of the PCBM interlayer. We first compared the surface morphologies of the LSS and control samples using SEM. As seen in Figure 5.2, when a PCBM interlayer is applied, the perovskite film after the PEAI deposition exhibits a uniform contrast in SEM, indicating a uniform 2D perovskite coverage that preserves the original 3D perovskite topography (Figure 5.2a, b). In contrast, the control sample exhibits an irregular distribution of 2D perovskite phases (Figure 5.2c, d).

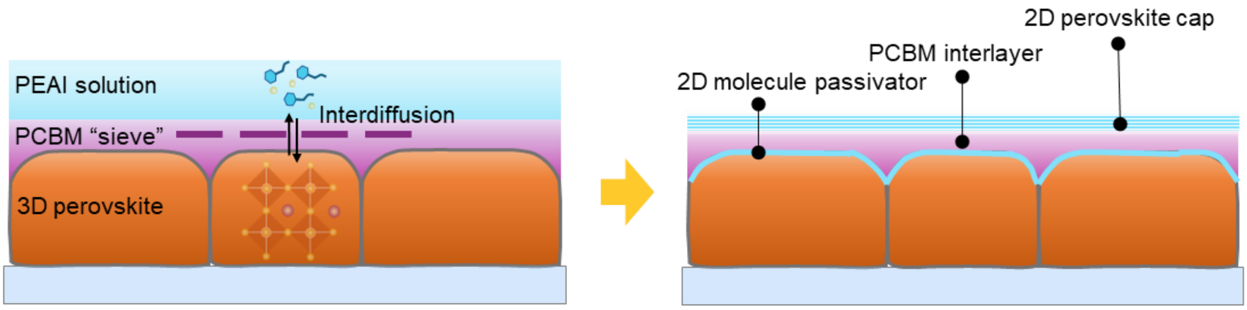

Figure 5.1 Schematic illustration of 2D perovskite growth and distribution of LSS sample.

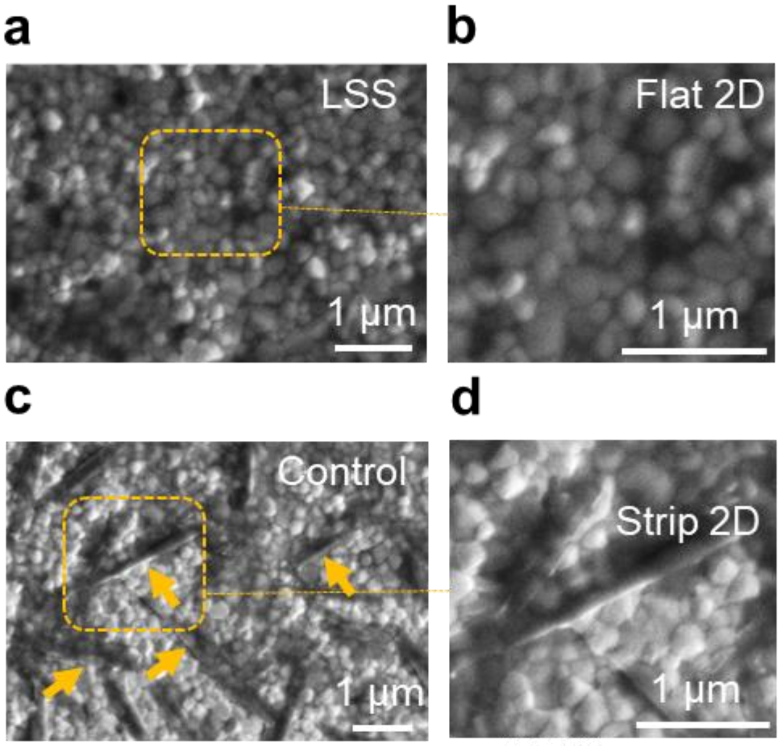

Figure 5.2 SEM images of $FA_{0.9}Cs_{0.1}PbI_3$ treated with PEAI with and without 5 mg/mL PCBM interlayer. **(a), (c),** SEM images of $FA_{0.9}Cs_{0.1}PbI_3$ treated with 10 mg/mL PEAI in IPA solution with and without 5 mg/mL PCBM interlayer. **(b), (d),** Magnified SEM images of the selected area as marked by the orange square in (**a**) and (**c**). Scale bar, 1 μm.

To gain an in-depth understanding of the perovskite heterointerface, we employed low-dose STEM to study the film cross-sectional microstructures. The capability of cross-sectional STEM observations to acquire lattice-resolved interface microstructural information has been demonstrated by several research works[20,23,189-191]. Figure 5.3a-b show the lower-magnification STEM images of both LSS and control films, acquired in high-angle annular dark field (HAADF) mode. Figure 5.3a reveals that the LSS sample maintains an intact surface of 3D perovskite grains compared with the control sample under the same PEAI treatment condition. The PCBM interlayer (the dark contrast sandwiched layer) has a characteristic thickness of ~10 nm measured from the HAADF-STEM image, on top of which is a continuous, uniform layer of 2D perovskite (~10 nm, typically 5-15 nm thick). In contrast, as seen in Figure 5.3b, in the control film, the 3D perovskite grains do not maintain their original surface microstructure after the PEAI treatment. A discontinuous layer consisting of randomly distributed 2D perovskite crystals is formed on top of the 3D perovskite grains. The thickness of this layer can vary widely from 15 to 50 nm, and there is partial deterioration of the original 3D perovskite grain surfaces (Figure 5.3b). This surface irregularity is attributed to the uneven and vigorous cation-exchange reaction between the 3D perovskite surface and the 2D organic spacer cation PEA^+. Notably, an increase in the PEAI concentration leads to a rise in the thickness and coverage of the 2D perovskite, and the surface deterioration becomes more evident when the PEAI concentration is increased to 15 mg/mL (Figure 5.4 and Figure 5.5). Even when the PEAI is diluted to 3 or 5 mg/mL, the formation of 2D perovskite will lead to evident erosion of the 3D grain surface (Figure 5.6). However, in the LSS sample, the ultrathin PCBM interlayer is formed with closely packed molecules, inherently containing nanochannels that allow a steady interlayer transport of PEA^+ and $FA^+/Cs^+/I^-$ upon thermal annealing. This slows down the reaction process. What is also important is that the chemically inert PCBM interlayer geometrically constrains the growth of as-formed 2D perovskite and molecular passivation layers. These factors contribute to the lateral homogeneity of the reaction front, which is essential to the control over the interfacial morphologies and the minimized impact on the 3D perovskite grain surface microstructure (Figure 5.7).

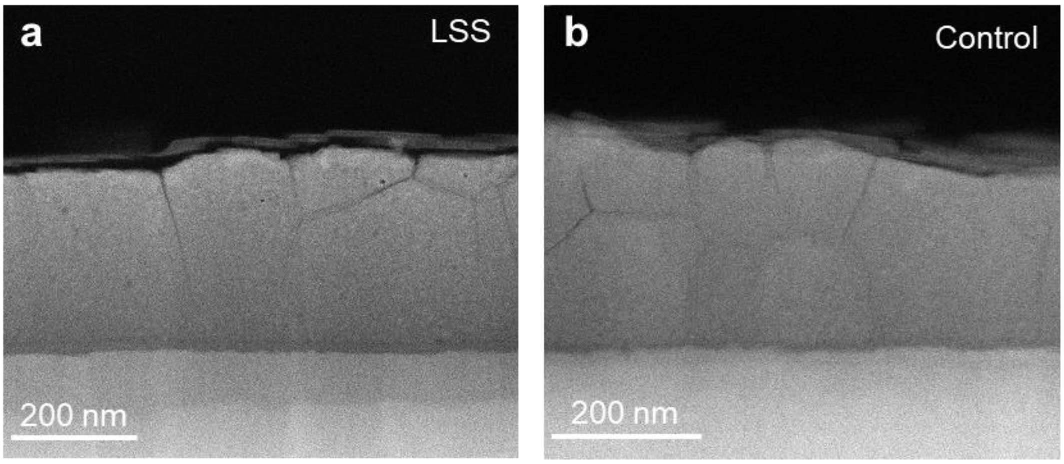

Figure 5.3 HAADF-STEM images of the **(a)** LSS sample and **(b)** control sample.

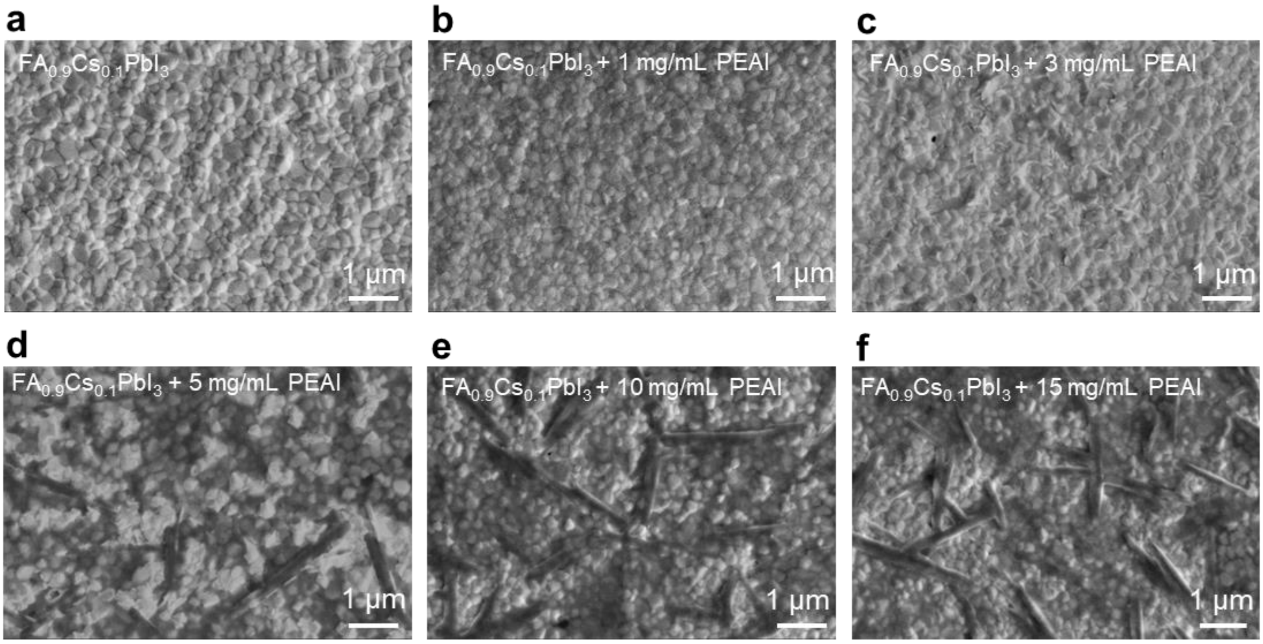

Figure 5.4 SEM images of $FA_{0.9}Cs_{0.1}PbI_3$ treated with concentrations of (**a-f**) 0,1,3,5,10,15 mg/mL PEAI in IPA solution.

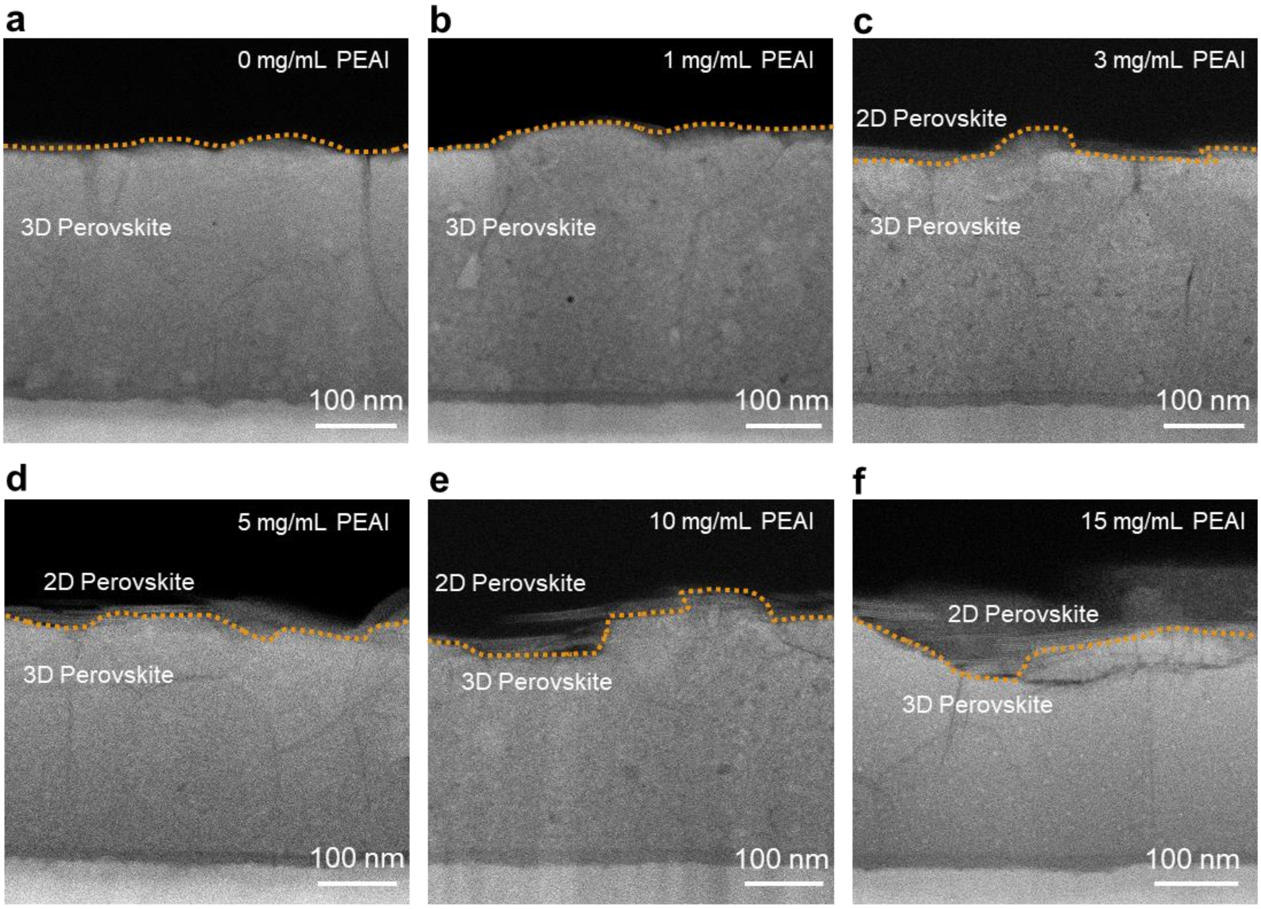

Figure 5.5 HAADF-STEM images of 3D $FA_{0.9}Cs_{0.1}PbI_3$ films treated with concentrations of (**a-f**) 0,1,3,5,10,15 mg/mL PEAI in IPA solution.

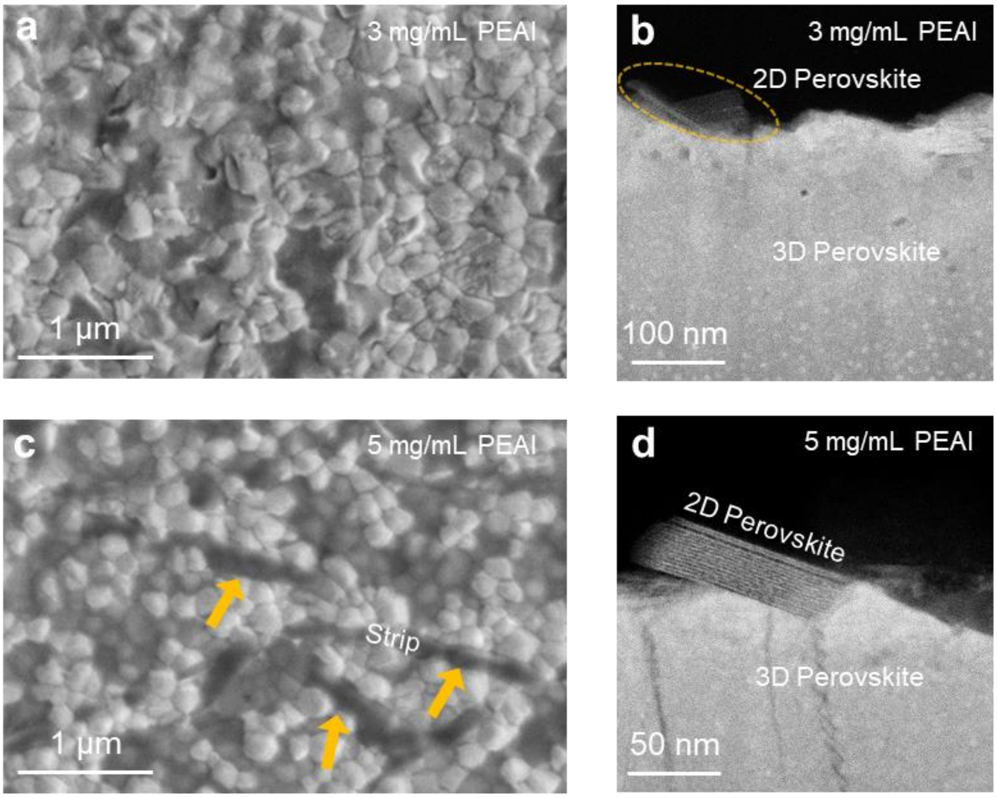

Figure 5.6 The morphology of 2D perovskite layers on 3D perovskite films prepared using dilute PEAI solutions and without the PCBM interlayer. **(a), (b),** SEM and cross-sectional STEM-HAADF image of the 2D perovskite layer (on top of the 3D perovskite film) prepared using 3 mg/mL PEAI, respectively. **(c), (d),** Top-view SEM and cross-sectional STEM-HAADF image of the 2D perovskite layer (on top of the 3D perovskite film) prepared using 5 mg/mL PEAI, respectively.

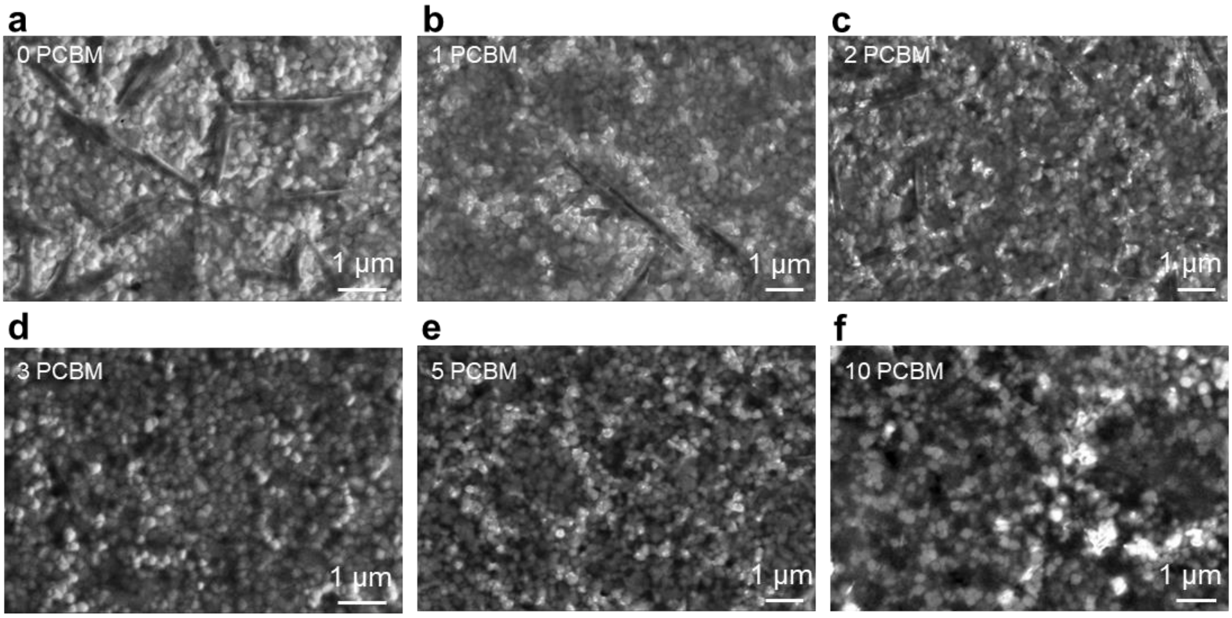

Figure 5.7 SEM images of $FA_{0.9}Cs_{0.1}PbI_3$ with concentrations of (**a-f**) 0,1,2,3,5,10 mg/mL PCBM interlayer and treated with 10 mg/mL PEAI in IPA solution.

To confirm the ion exchange through the ultrathin PCBM interlayer, we prepared another LSS sample by applying the same PCBM and PEAI treatments to a 3D $FA_{0.9}Cs_{0.1}PbBr_3$ perovskite film to track the transport of interfacial halide anions. The use of bromide instead of an iodide sample can facilitate the differentiation of halide anions supplied by the PEAI or the surface region of 3D perovskite grains in this reaction process. Using the STEM EELS analysis, we observed a co-existence of I^- and Br^- on the 3D grain surface and 2D capping layer, confirming the ion exchange between the PEAI salt and 3D grain surface through the PCBM molecular sieve (Figure 5.8). To examine the distribution of the PEA^+ within the LSS structure, the energy-loss near-edge structures (ELNES) of the nitrogen (N) K-edge was analyzed (Figure 5.9). ELNES in EELS enables atomic-scale fingerprinting of chemical bonding states, local coordination environments, and electronic structure characteristics through the fine oscillatory features within 50 eV of elemental ionization edges. The distinct electronic signatures of FA containing both C-N σ (binding energy 285.3 eV) and π* (286.7 eV) bonds, versus PEA with only σ bonding, enable their spatial distribution mapping within the LSS structure through energy-filtered ELNES analysis of the N-K edge (energy window 395-435 eV) with 0.38 eV spectral resolution. Within the 2D perovskite layer and the PCBM interlayer (regions I-IV in Figure 5.8b), the N K-edge structure features a main peak at 408.5 eV and a small pre-peak at 400.5 eV, consistent with the dominant C-N σ bond characteristics (π bond at around 400 eV, σ bond at around 408 eV) and confirms the presence of PEA^+ (Figure 5.9c)[192]. Additionally, the increased N K-edge signal intensity beneath the PCBM interlayer (region IV in Figure 5.9b) indicates a concentration of PEA^+ on the surface of the 3D grains. This concentration of PEA^+ on the 3D grain surface is evident in various LSS regions (Figure 5.10). As a result, 2D monolayers can be found on the 3D grain surface (Figure 5.11), suggesting the residual PEA^+ tends to form a 2D molecule passivator covering the 3D grains.

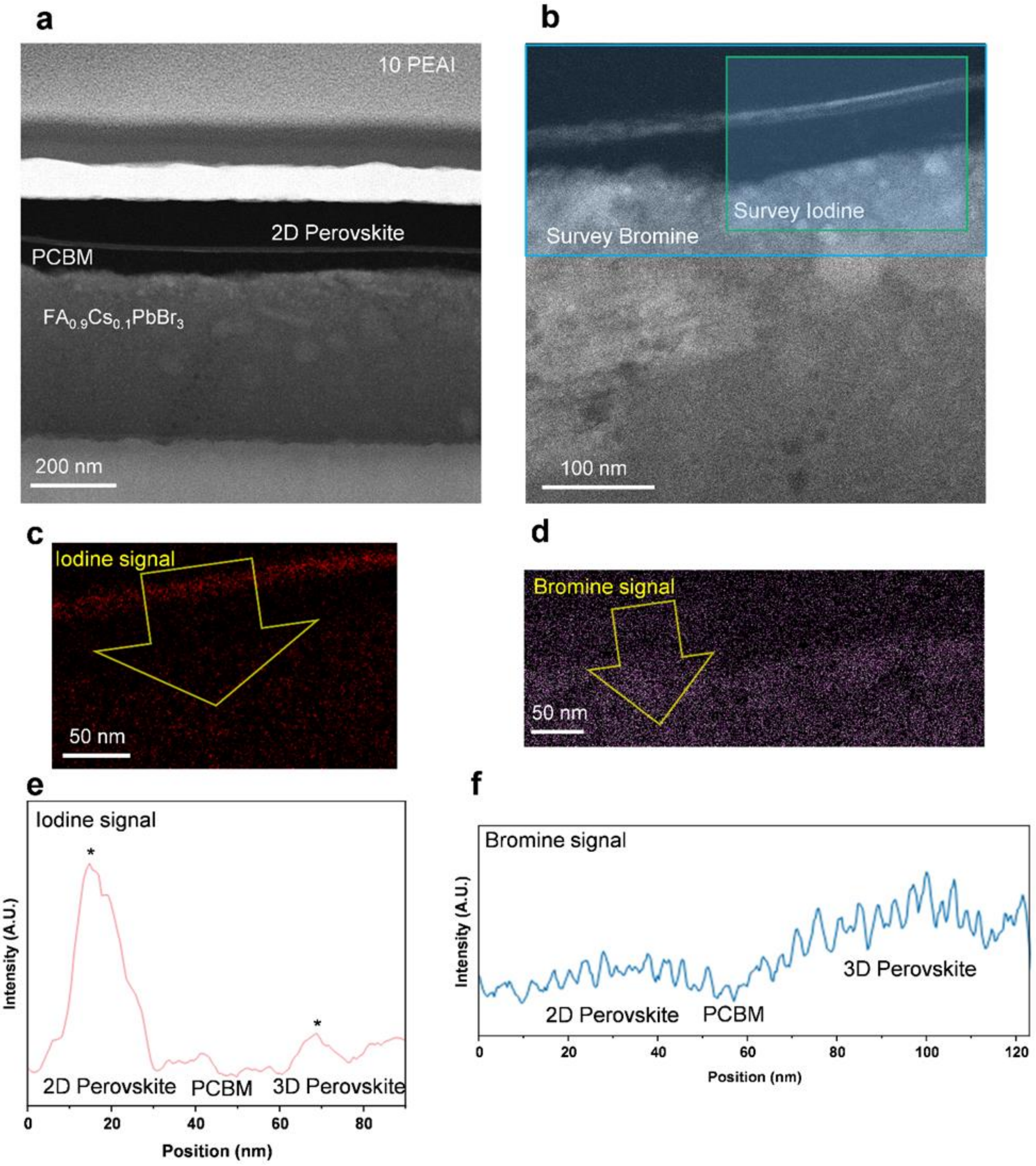

Figure 5.8 EELS STEM analysis. **(a), (b),** HAADF-STEM images of $FA_{0.9}Cs_{0.1}PbBr_3$ PSCs with 10 mg/mL PCBM interlayer and treated with 10 mg/mL PEAI in IPA solution. Green rectangle area in **(b)** is the survey region of EELS edge signal of I($M_{4,5}$) and blue rectangle area in **(b)** is the survey region of EELS edge signal of Br($L_{2,3}$). **(c), (d),** Corresponding EELS mapping images of iodine signal and

bromine signal. **(e), (f),** Line profile of the signal intensity marked by yellow orange arrows in **(c)** and **(d).**

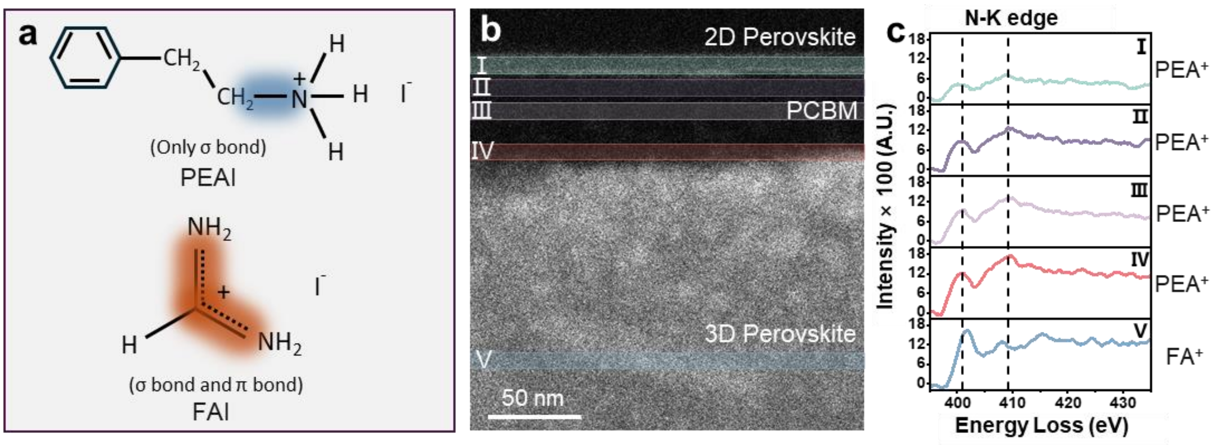

Figure 5.9 (a), PEA$^+$ only contains C-N σ bond, while FA$^+$ contains both C-N σ bond and π bond. **(b),** N K-edge was signal extracted from regions I-V of the LSS structure. **(c),** Non-normalized N K-edge profiles of regions I-V in **(b)**, demonstrating evident σ bond dominant (PEA$^+$) characteristics in regions I-IV and π bond characteristics (FA$^+$) in region V. The N K-edge signal intensity in Region IV is higher than in Region I-III. Region I-V successively refer to the 2D perovskite layer, the top region of the PCBM interlayer, the middle region of the PCBM interlayer, the PCBM/3D perovskite interfacial region, and the 3D perovskite film bulk region.

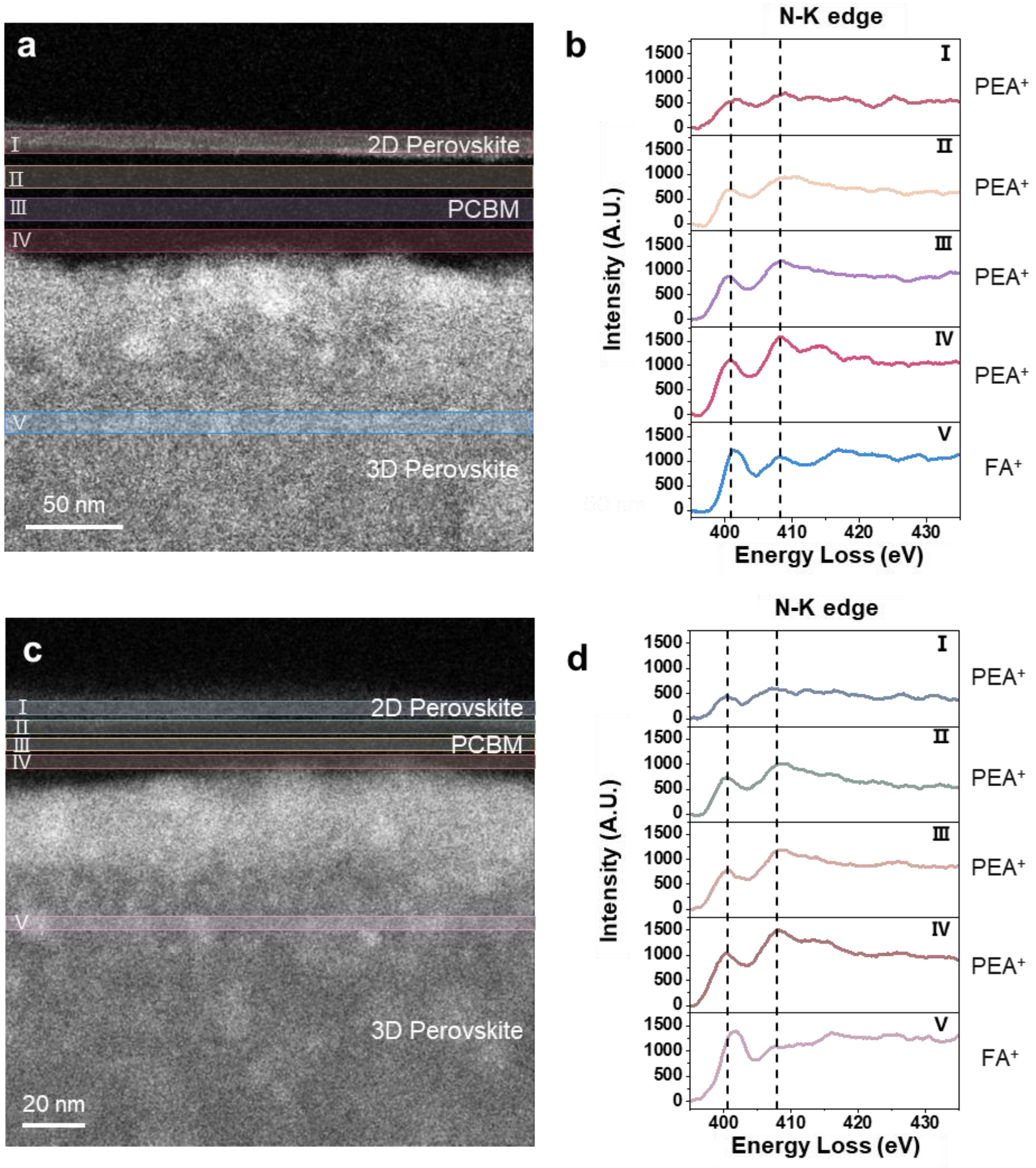

Figure 5.10 EELS ELNES analysis of the LSS structure. **(a), (c),** N K-edge signal extracted from regions I-V of two different regions of the LSS structure. **(b), (d),** Non-normalized N K-edge profiles of regions I-V in **a**, **c**, respectively, demonstrating clear σ bond dominant (PEA^+) characteristics in regions I-IV and π bond characteristics (FA^+) in region V.

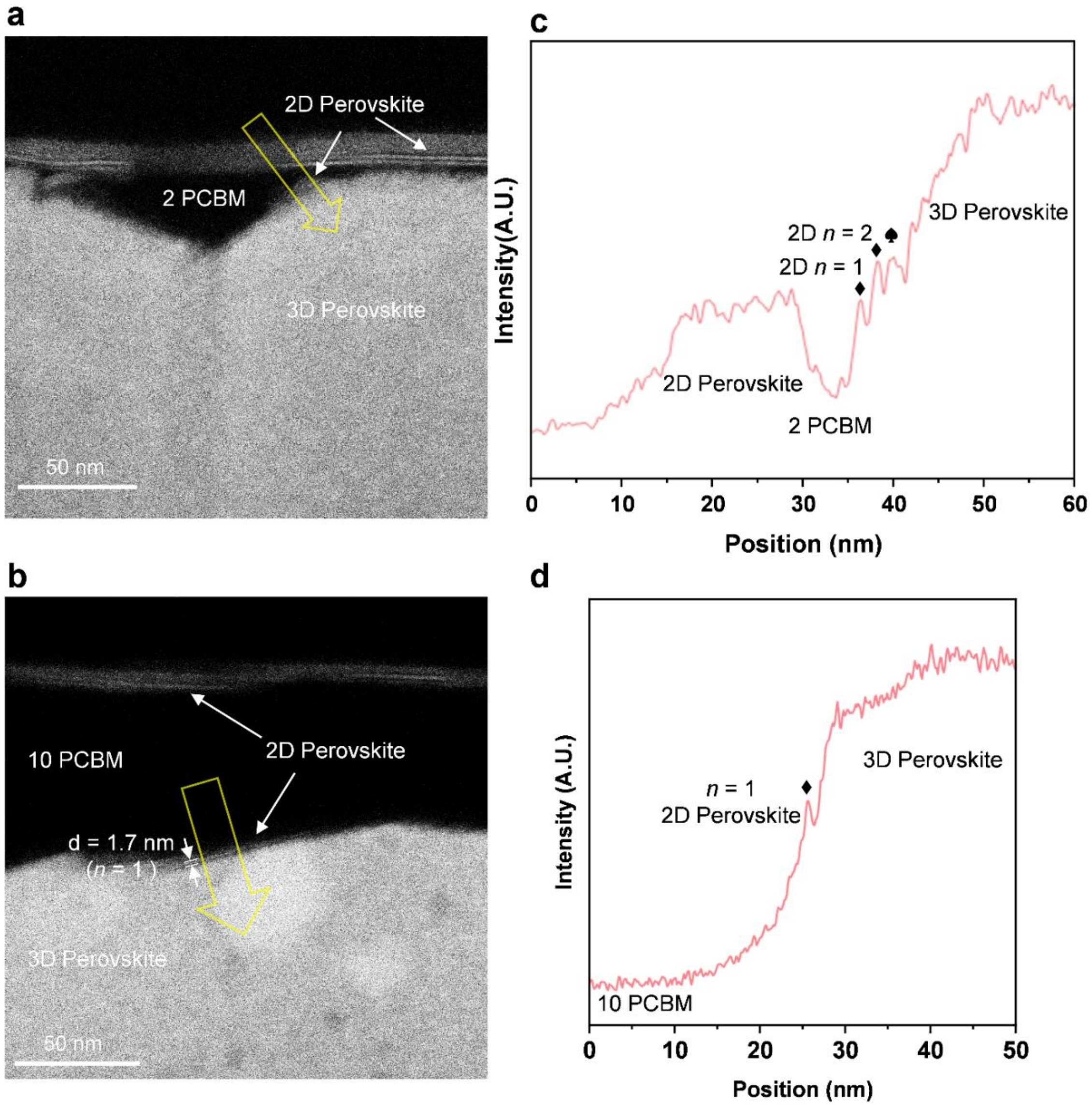

Figure 5.11 2D perovskite monolayers on 3D perovskite grains. **(a), (b),** HAADF-STEM images of $FA_{0.9}Cs_{0.1}PbI_3$ PSCs with 2 and 10 mg/mL PCBM interlayer and both treated with 10 mg/mL PEAI in IPA solution. **(c), (d),** Line profiles of the row of signal intensity marked by yellow arrows in **(a)** and **(b)**.

Based on this mechanism, we found that the thickness of the PCBM interlayer significantly affects the microstructure and phase of the 2D perovskite capping layer. We prepared PCBM interlayers of varying thicknesses from 0 to 60 nm by spin-coating a PCBM solution with concentrations of 1, 2, 3, 5, and 10 mg/mL. The 2D perovskite capping layer tends to be smoother and more continuous with an increase of the PCBM thickness, as shown in Figure 5.12. However, once the concentration of PCBM reaches 10 mg/mL, the interlayer can get as thick as 60 nm. The thick PCBM interlayer causes difficulties with ion exchange, inhibits the 2D layer from remaining continuous, and drastically reduces its thickness. The dependence of the PCBM interlayer thickness on the interfacial reaction kinetics is consistent with our earlier proposed PCBM-mediation mechanisms.

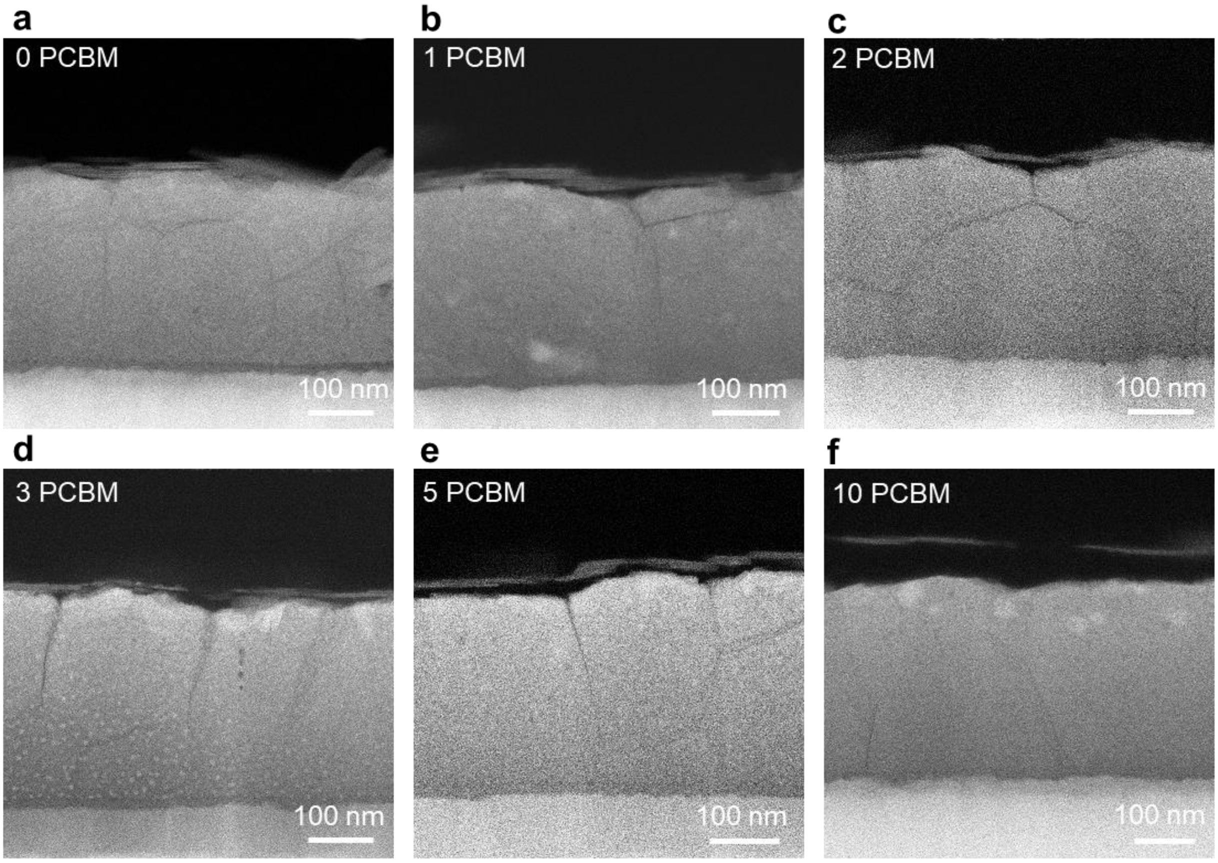

Figure 5.12 HAADF-STEM images of $FA_{0.9}Cs_{0.1}PbI_3$ films with different concentration of PCBM interlayer and treated with 10 mg/mL PEAI. HAADF-STEM images of samples with concentrations of **(a-f)** 0,1,2,3,5,10 mg/mL PCBM interlayer and treated with 10 mg/mL PEAI in IPA solution.

The *n*-value distribution and orientation of 2D perovskites, which are significant for managing band gaps and transporting carriers, are subjects that are under more research. For the control samples without interlayer, as the magnified HAADF-STEM image of the chosen area in Figure 5.3b, Figure 5.13a shows multiple layers of 2D perovskite with varying thickness are formed on top of the visibly rough 3D grain surface. Figure 5.13b is an enlarged image with the direction and region indicated by the arrow in Figure 5.10a, and Figure 13c shows the signal intensity line profile of Figure 5.13a. The 2D perovskite structure in Figure 5.13b is well-correlated with the layer distance measured in Figure 5.13c. The line profile study reveals that in the control sample, the *n*-value arrangement of 2D perovskites is disorderly, with $n = 2$ ($d = 2.20$ nm) being the primary component, as well as 2D perovskites with $n = 3$ ($d = 2.94$ nm) and $n = 5$ ($d = 4.18$ nm). In addition, we also noticed that control samples have 2D perovskite with varied orientations while having the same *n* value on flat 3D grain surfaces (Figure 5.14), whereas 2D perovskites with a high *n* value doped with a low *n* value are commonly found at undulating grain boundaries (Figure 5.15 and Figure 5.16). This should be attributed to the rapid formation of 2D perovskite during the contact between PEAI solution and the 3D grain surface. The interaction between PEA^+ and the remaining PbI_2 (Figure 5.17) as well as the considerable amount of free FA^+/Cs^+/I^- (Figure 5.18) on the 3D grain surface increases the possibility that some 2D perovskite with an uneven *n* value may not develop in a surface-parallel orientation and cause more damage on 3D grains (Figure 5.19).

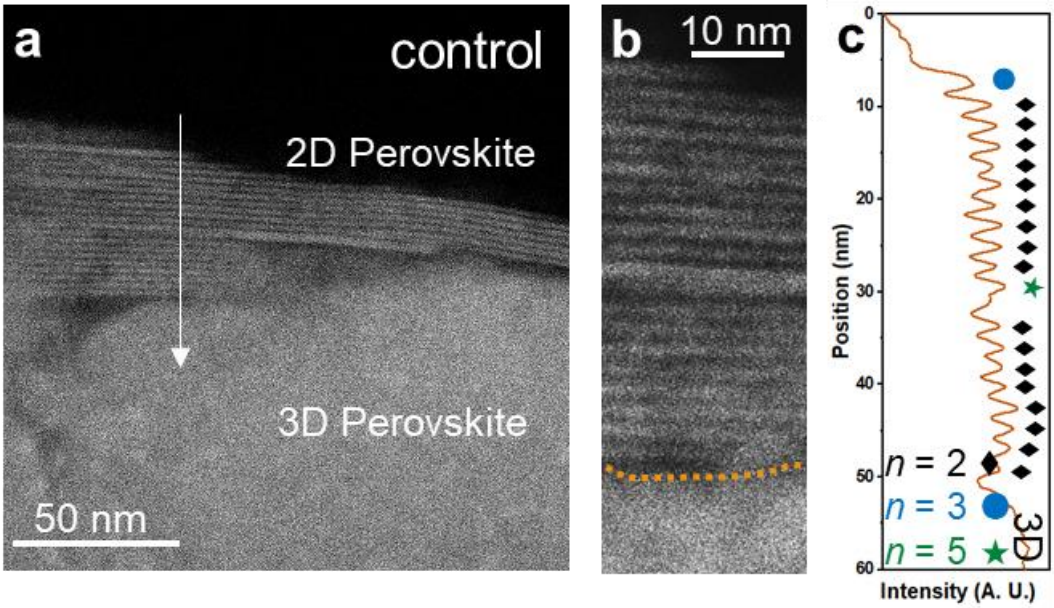

Figure 5.13 (a), (b), Magnified HAADF-STEM images of the control sample. (**c**)**,** Signal intensity line profile of the row marked in (**a**).

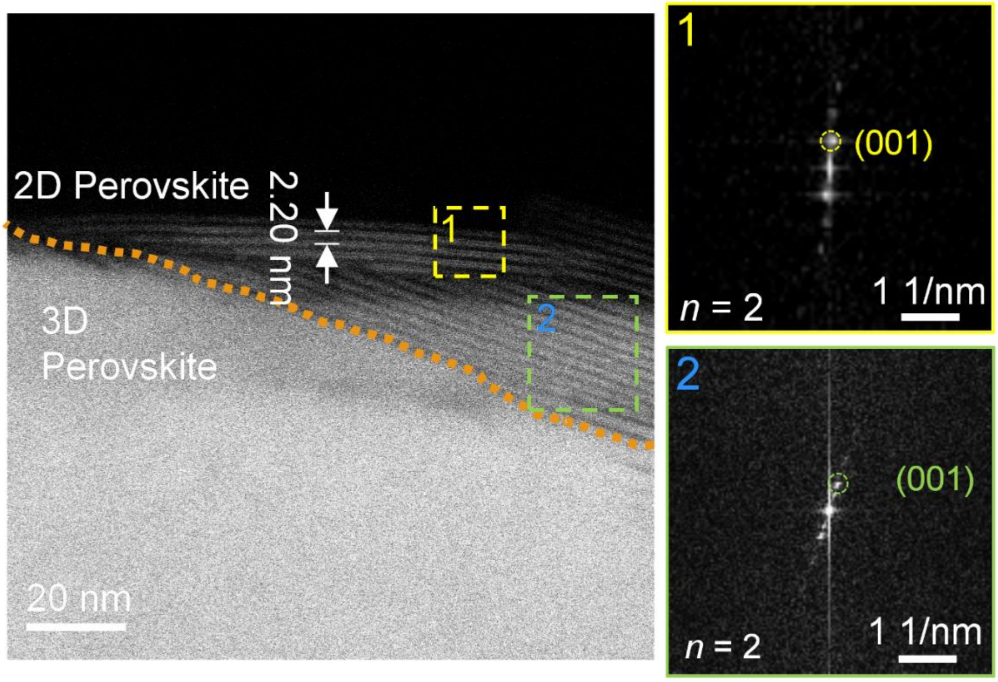

Figure 5.14 2D perovskite with varied orientations in the control sample. HAADF-STEM image of the control sample, treated with 10 mg/mL PEAI. Area 1 and area 2 Fast Fourier transform (FFT) shows the 2D *n* = 2 perovskite on 3D perovskite surface have different orientation.

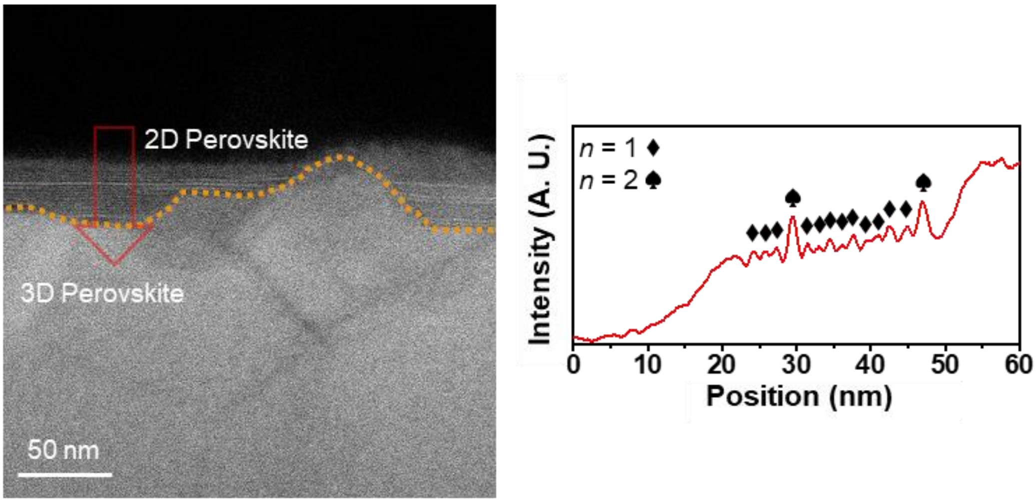

Figure 5.15 The *n*-value arrangement of 2D perovskite in control sample. HAADF-STEM image and corresponding line profile of red arrow area in left image of control sample, treated with 10 mg/mL PEAI.

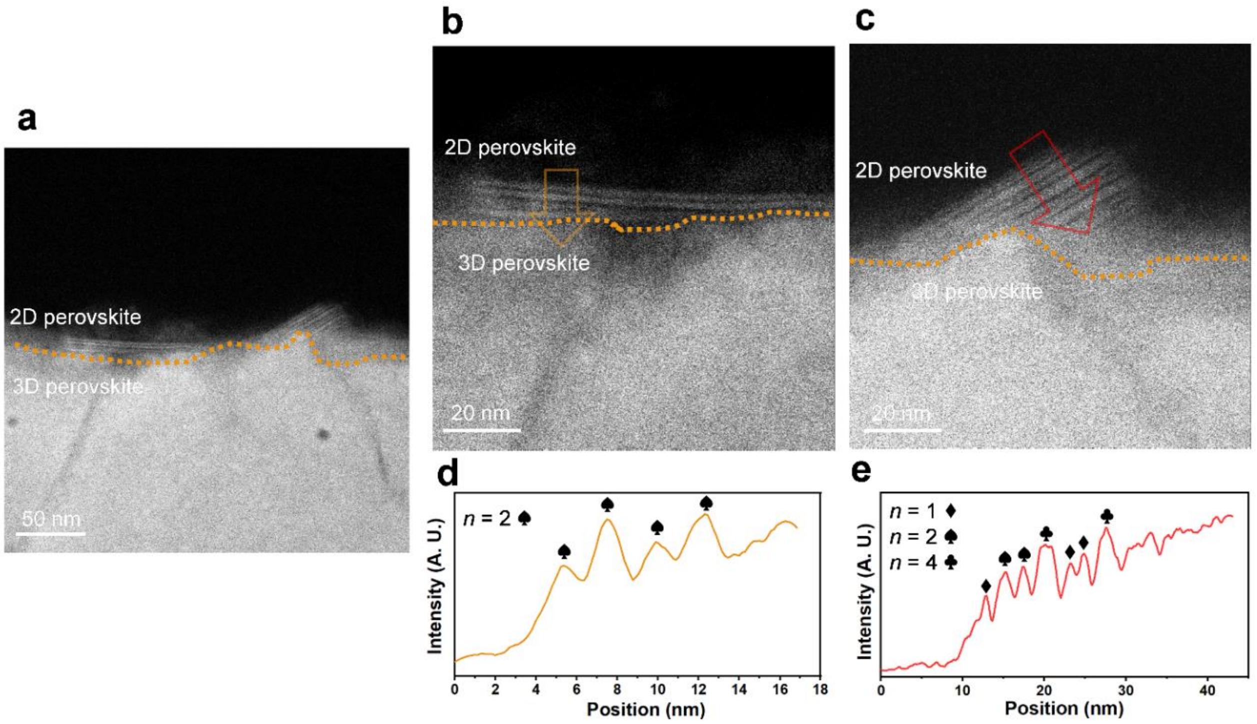

Figure 5.16 2D perovskites distribution on 3D perovskite grains surface and grain boundaries in control sample. (**a),** HAADF-STEM image of the control sample, treated with 5 mg/mL PEAI. (**b), (c),** Magnified HAADF-STEM images of the selected area in **(a)**. (**d), (e),** Corresponding line profiles of the row of signal intensity marked by yellow arrows in **(b)** and **(c)**.

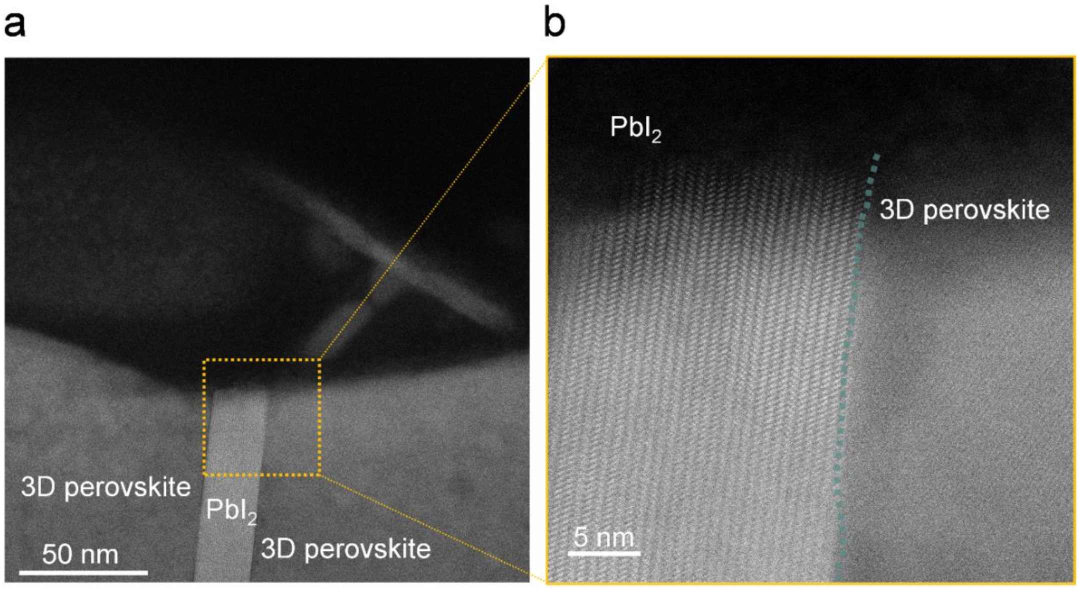

Figure 5.17 The remaining PbI_2 in 3D perovskite of control device. HAADF-STEM image of the control sample, treated with 10 mg/mL PEAI. **(a),** PbI_2 in 3D perovskite grains. **(b),** Magnification image of selected area in **(a)**.

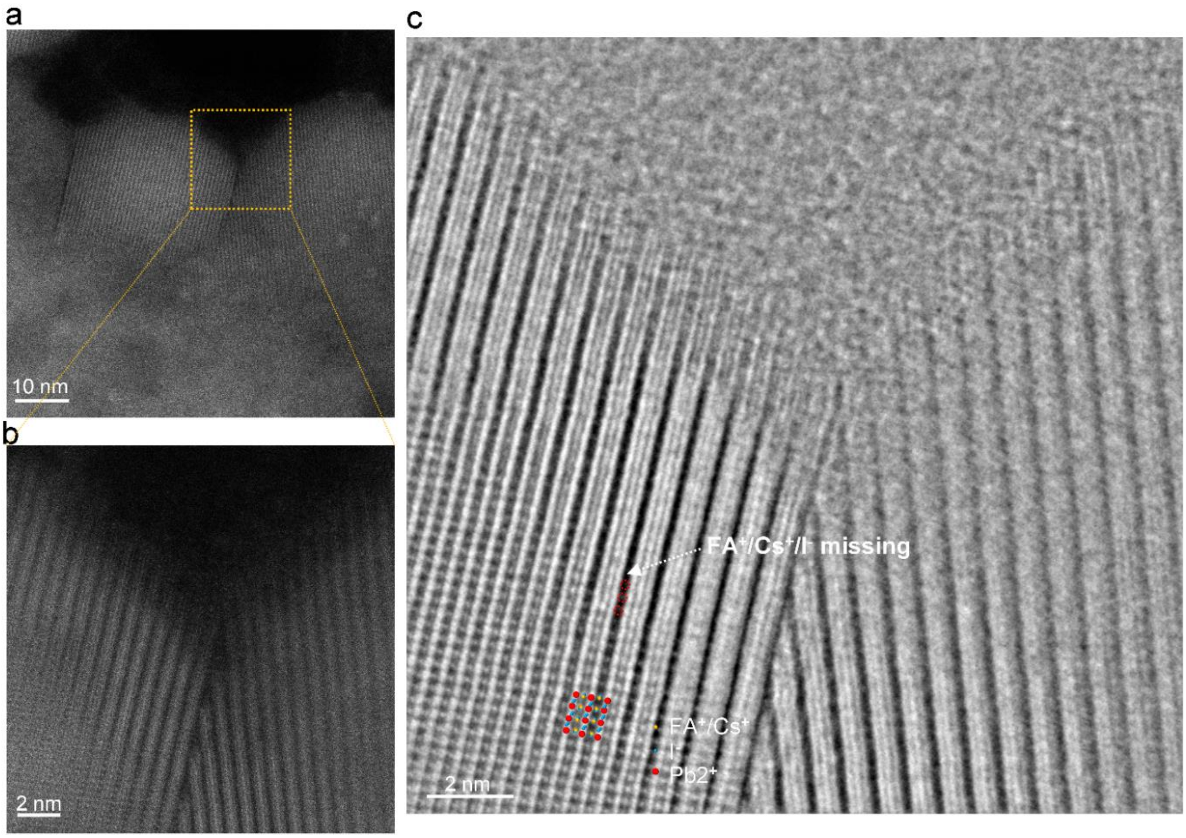

Figure 5.18 $FA^+/Cs^+/I^-$ lost on the 3D perovskite surface in control sample. Cross-sectional STEM image of 3D-2D device, treated with 10 mg/mL PEAI. **(a),** HAADF-STEM image of 3D perovskite grains. (**b**)**,** Magnification image of selected area in **(a)**. (**c**)**,** Atomic-resolution integrated differential phase contrast (iDPC)-STEM image of area in **(a)**. After PEAI solution treatment, some of the $FA^+/Cs^+/I^-$ will be lost on the surface of 3D grains.

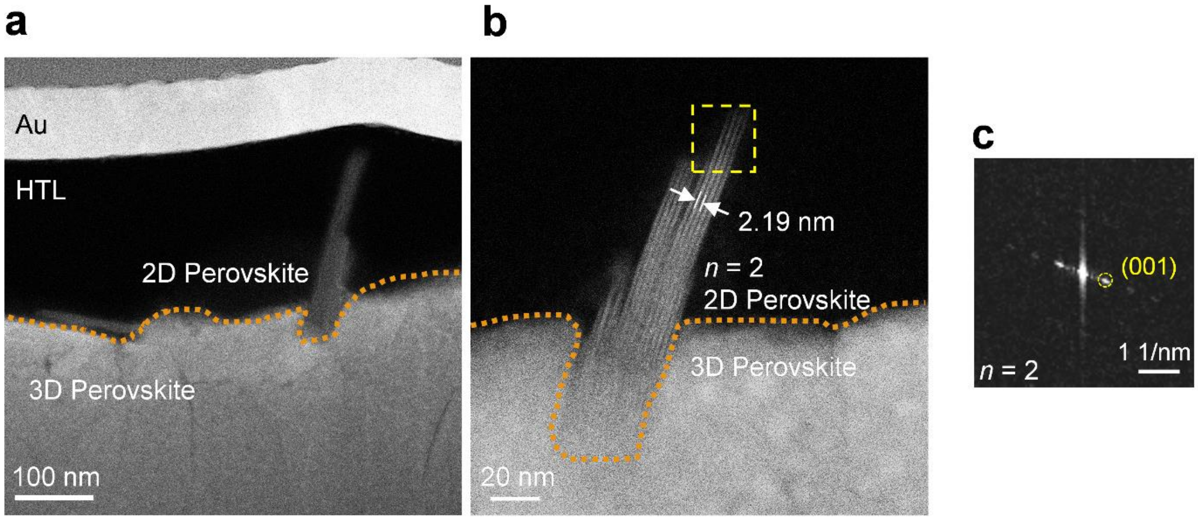

Figure 5.19 2D perovskites parallel and non-parallel to 3D grain surfaces in control sample. HAADF-STEM images of the control device, treated with 10 mg/mL PEAI. (**a**)**,** Horizontal and non-horizontal 2D perovskites simultaneously grow on the surface of 3D grains. (**b**)**,** High-resolution image of non-horizontal 2D perovskite. **(c),** FFT of selected area in (**b**).

When it comes to the LSS sample, a magnified image of the region in Figure 5.3a can be found in Figure 5.20a. Spinning the PEAI solution on the interlayer instead of directly on the 3D grains results in an ultra-thin 2D perovskite layer, like the two layers of $n = 2$ 2D perovskite seen in Figure 20b and Figure 5.20c, which are enlarged images of the arrowed region in Figure 5.20a and its corresponding intensity line profile. Due to the protective effect of PCBM, PEA^+ struggles to bind enough A-site ions and $[PbI_4]^{2-}$ in LSS samples, making it difficult for 2D perovskites with $n > 2$ to crystallize. Furthermore, the generation of high n-value 2D perovskite becomes increasingly challenging as the distance from the 3D grain surface increases. This allows 2D perovskite in LSS to be arranged from $n = 2$ to $n = 1$ (Figure 5.21), which is helpful to enhance carrier transport efficiency in *p-i-n* devices[20,22]. Additionally, the fraction of PbI_2 in 3D perovskite may also influence the n phases of 2D perovskite in the LSS sample. As shown in Figure 5.22, a deficiency of PbI_2 may hinder the formation of the $n = 1$ phase 2D perovskite, whereas the proportion of the $n = 1$ phase tends to increase with excess PbI_2 (Figure 5.22a, b). STEM observations also show more $n = 1$ phase 2D perovskite in the LSS sample prepared with $(FAI)_{0.9}(CsI)_{0.1}(PbI_2)_{1.15}$ 3D perovskite (Figure 5.22f).

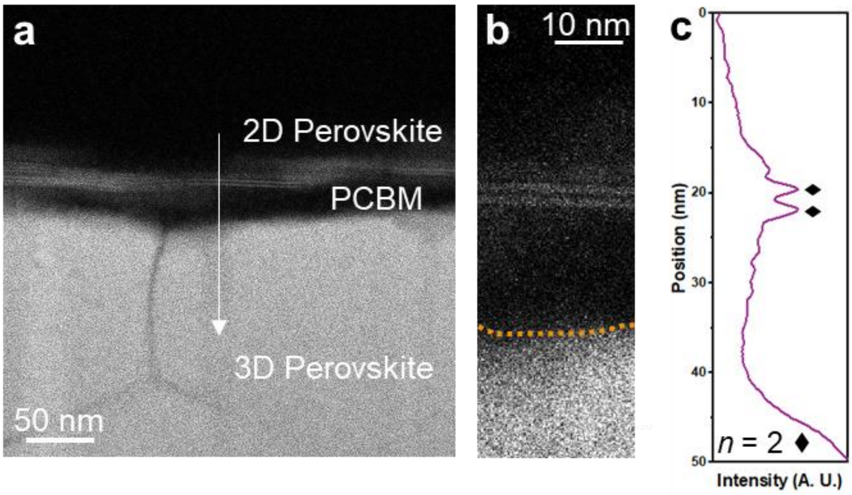

Figure 5.20 (a), (b), Magnified HAADF-STEM images of the LSS sample. **(c),** Signal intensity line profile of the row marked in (**a**).

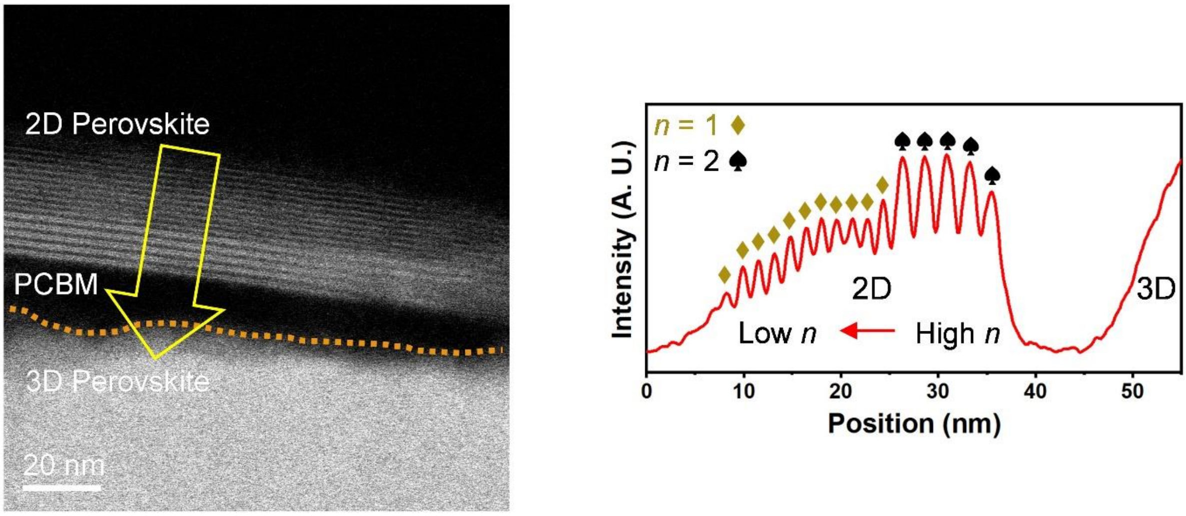

Figure 5.21 The *n*-value arrangement of 2D perovskite in LSS sample. HAADF-STEM image (left) and line profile image (right) of yellow arrow area in the LSS device (with 5 mg/mL PCBM interlayer), treated with 10 mg/mL PEAI.

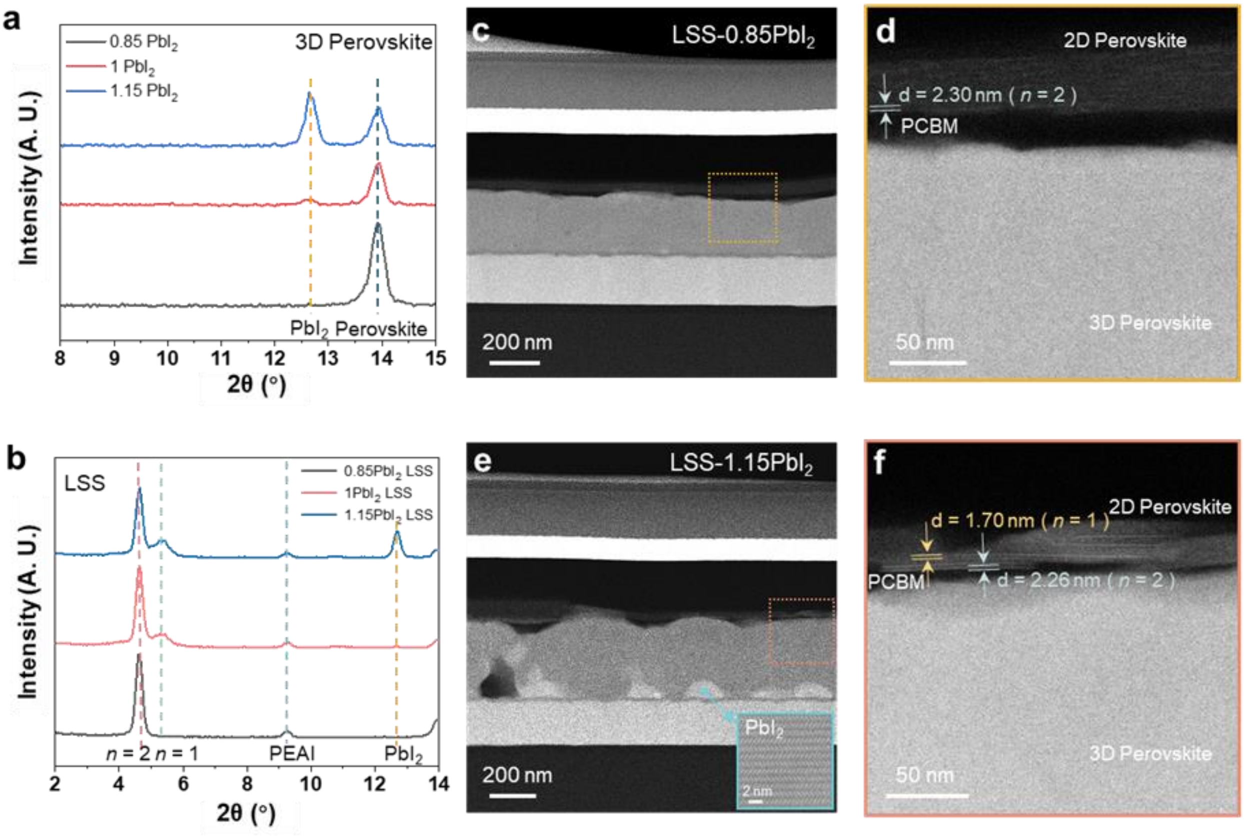

Figure 5.22 The LSS samples prepared on the 3D perovskite with different [PbI_2] fractions. **(a), (b),** XRD results of 3D perovskites with different PbI_2 fraction ($(FAI)_{0.9}\cdot(CsI)_{0.1}\cdot(PbI_2)_{0.85}$, $(FAI)_{0.9}\cdot(CsI)_{0.1}\cdot(PbI_2)_1$ and $(FAI)_{0.9}\cdot(CsI)_{0.1}\cdot(PbI_2)_{1.15}$) and corresponding LSS samples prepared by 3D perovskites, respectively. **(c),** STEM-HAADF image of the LSS-0.85PbI_2 sample. **(d),** Magnified image of the squared region in c shows the $n = 2$ phase 2D perovskite. **(e),** STEM-HAADF image of the LSS-1.15PbI_2 sample. **(f),** Magnified image of the squared region in e shows the 2D perovskite with $n = 1$ and $n = 2$ phases.

5.3 4D STEM of near-surface grain boundaries

The interaction between the PEAI salt and 3D perovskite may also influence the integrity of near-surface grain boundaries (GBs), which are critical to the performance of resultant PSC devices[182,193-197]. As conventional STEM imaging falls short of revealing the underlying crystalline structure, we employ a combination of four-dimensional STEM (4D-STEM) and nano-beam electron diffraction (NBED) techniques[198-201] to probe the microstructure and lattice orientation distributions in both the control and LSS samples. In the control film without the ultrathin PCBM interlayer, HAADF-STEM identifies a dark-contrast region beneath the 3D grain surface (Figure 5.23a), which is determined as $n = 2$ 2D perovskite by the corresponding NBED pattern (Figure 5.23a_1), nearly perpendicular to the 2D perovskite above the 3D grain (Figure 5.23a_2). The NBED patterns of the 3D grains (Figure 5.23a_3 and Figure 5.23a_4) demonstrate a typical orthogonal structure (space group *Pbnm*, $a = 0.8646$ nm, $b = 0.8818$ nm, $c = 1.2520$ nm), with the left and right segments exhibiting different orientations. To accurately represent the deformation of 3D grains, a virtual dark-field (DF) STEM image was reconstructed from the 4D diffraction dataset, as presented in Figure 5.23b and Figure 5.24. This image clearly shows that the grain boundary and adjacent regions of the 3D grains are significantly eroded by the 2D perovskite growing parallel to the grain boundary. In contrast, when it comes to the LSS sample, the HAADF-STEM image displays a distinct separation between the 3D grains and 2D perovskite by a thin PCBM interlayer (Figure 5.23c). The NBED pattern of the 2D perovskite, as depicted in NBED Figure 5.23c_1, indicates that the orientation of the 2D perovskite layer is approximately parallel to the surface of the 3D grains. Within this context, three distinct 3D perovskite grains, each with a unique orientation, are discernible from the 4D diffraction dataset (NBED Figure 5.23c_2-c_4 and Figure 5.25). The reconstructed DF-STEM image (Figure 5.23d) confirms that the surfaces and grain boundaries of the 3D grains are well-preserved, with no evidence of GB etching by the 2D perovskite, underscoring the protective role of the PCBM interlayer.

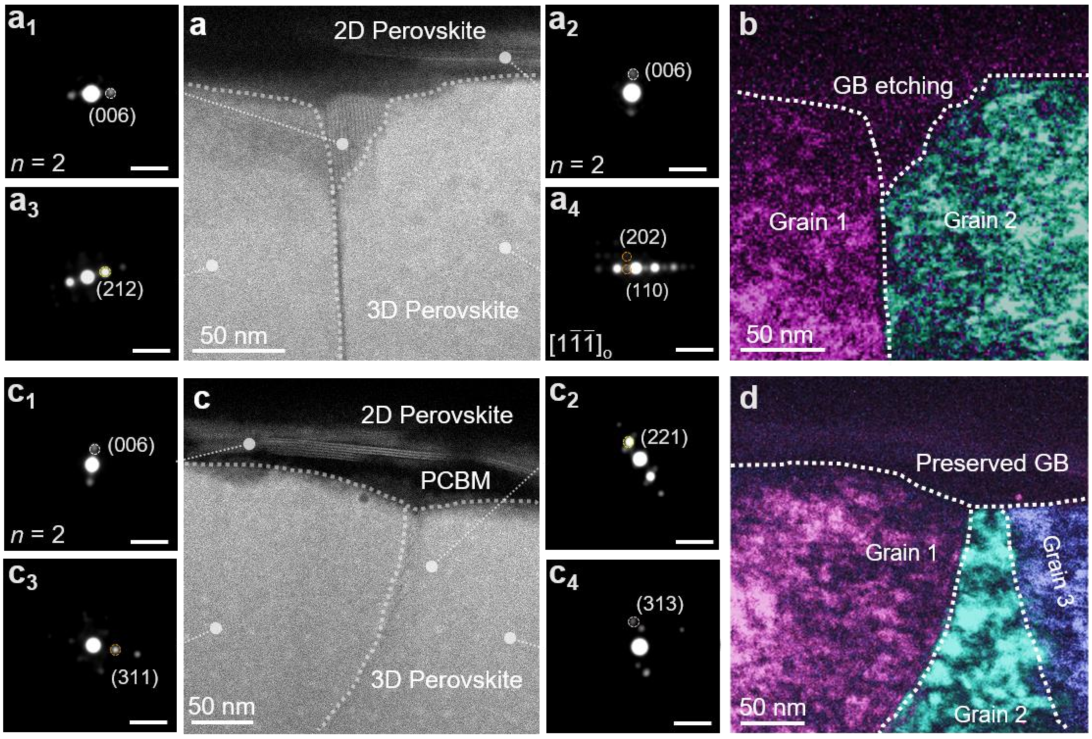

Figure 5.23 Near-surface grain boundary microstructures. **(a),** HAADF-STEM image of 3D-2D device. **(a$_1$)-(a$_4$),** The NBED images of the corresponding region on the control device. The scale bar is 5 nm^{-1}. **(b),** Virtual DF-STEM image reconstructed from NBED signals of **(a$_3$)** and **(a$_4$)**. **(c),** HAADF-STEM image of the LSS sample. **(c$_1$)-(c$_4$)**, The NBED images of the corresponding region on the LSS sample. The scale bar is 5 nm^{-1}. **(d),** Virtual DF-STEM image reconstructed from NBED signals of **(c$_2$)**, **(c$_3$)** and **(c$_4$)**.

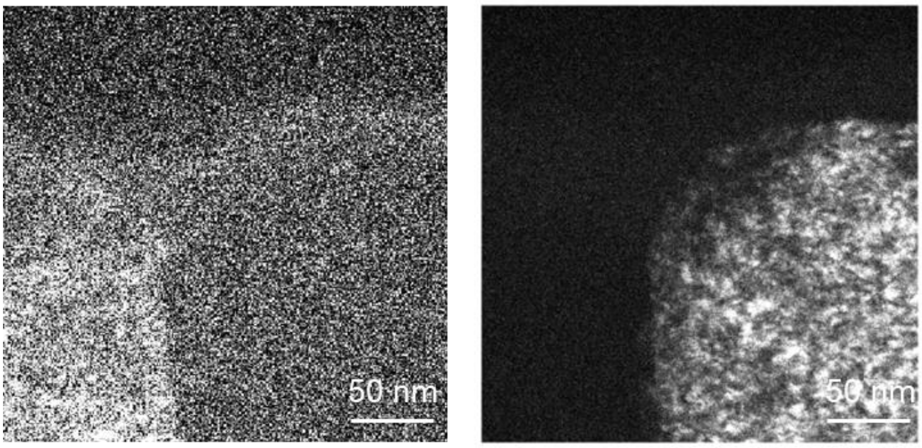

Figure 5.24 Dark-field STEM images reconstructed from selected nano-beam diffraction signal of 3D-2D sample.

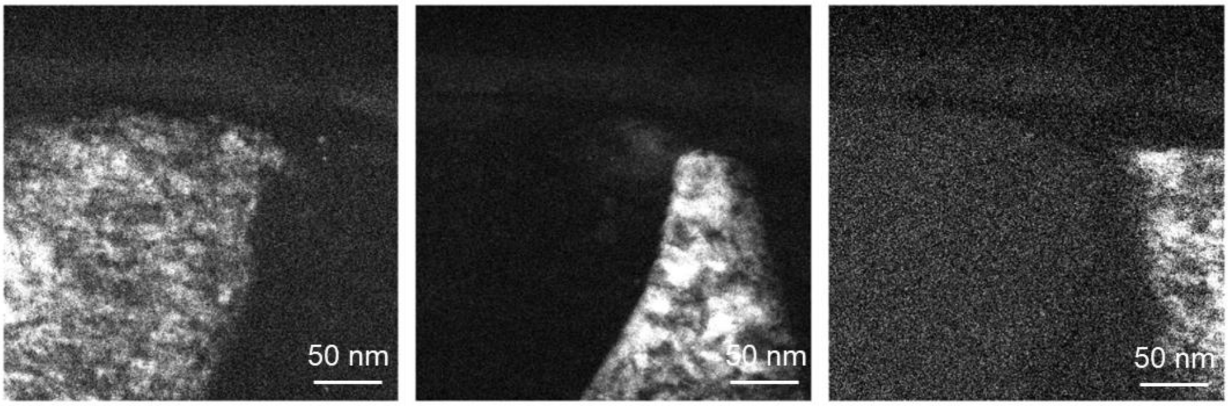

Figure 5.25 Dark-field STEM images reconstructed from selected nano-beam diffraction signal of the LSS sample.

5.4 Optoelectronic properties and chemical stability

We further performed X-ray diffraction (XRD) on the LSS and control films. In both cases, the passivation does not notably change the crystallinity and grain orientation of the pristine 3D perovskite films (Figure 5.26). Nevertheless, the use of the PCBM interlayer has a significant influence on the overall phase distribution and orientation of the as-formed 2D perovskite capping layer, as evidenced by the grazing-incidence wide-angle X-ray diffraction (GIWAXS) results shown in Figure 5.27a. Moreover, we did not observe any change in the bandgap (E_g) of the underlying 3D perovskite according to the normalized photoluminescence (PL) spectra (Figure 5.27b), further attesting to the preservation of bulk 3D perovskite phase in both LSS and control films. Interestingly, the PL spectra of the LSS sample show dominant emission peaks corresponding to $n = 1$ and 2, whereas PL emissions associated with a higher dimensionality of $n \geq 3$ phases become more pronounced in the control sample (Figure 5.27b), in accordance with the STEM observation. Herein, we elaborate in detail on the XRD and PL results shown in Figure 5.27. As seen in Figure 5.27a, in the LSS sample, both the $n = 1$ and $n = 2$ phases show notable XRD diffraction peaks. In Fig. 3b, the LSS sample mainly shows PL emission peaks for the $n = 1$ and $n = 2$ phases. These results are fully consistent with our STEM observations (Figure 5.20 and Figure 5.21). However, in the control sample, the characteristic diffraction peak of the $n =2$ phase dominates, while only a trace amount of diffraction appears for the $n = 1$ phase. Interestingly, the PL spectrum of the control sample shows remarkable emission peaks for the $n = 1$, 2, 3, and 4 phases. This is probably because the contained $n =1$, 3, and 4 phases in the control sample are nanoconfined in the dominating $n =2$ phase (Figure 5.13 and Figure 5.16), which makes them undetectable by XRD and still prominent in PL emission. In the LSS sample, the microstructure of the 2D layer is much more ordered, with mostly the octahedral layer stacked perpendicular to the film plane, according to the STEM observations (Figure 5.12). Therefore, the $n = 1$ phase remains visible in the XRD pattern of the LSS sample.

More importantly, the 2D perovskite (n = 1 and 2) capping layer formed uniformly on top of 3D perovskite surfaces in the LSS samples, as shown in the PL images in Figure 5.27c, indicating that the PCBM interlayer can induce uniform growth and distribution of 2D perovskites. We further monitored the PL emission centered at the 3D peak (~780 nm). We observed a uniform emission over a large area of 15 μm by 15 μm from the underlying 3D perovskite layer, confirming uniform 2D passivation for 3D perovskite films with the PCBM interlayer. Then, we employed steady-state and time-resolved PL spectra to investigate the effects of the PCBM interlayer on carrier dynamics at the perovskite heterointerface (Figure 5.27d-g). The detailed fitting parameters of our PL results are summarized in Table 5.1. The LSS and control samples were deposited on glass substrates. When the laser is incident from the glass side (bottom direction), the control sample exhibits stronger PL emission with a longer decay lifetime than pristine 3D perovskite films because of the suppression of nonradiative recombination associated with trap states at the surface (Figure 5.27d). After incorporating the PCBM interlayer, the LSS sample shows much stronger PL emission and further increases the average PL lifetime from 427 ns (control sample) to 925 ns (Figure 5.27f), indicating that the unique laminate structure can further enhance the optoelectronic quality of 3D perovskite films. Interestingly, when the laser is incident from the perovskite side (top direction), a more effective PL quenching occurs in the LSS films compared to pristine 3D and control samples (Figure 5.27e and Figure 5.27g). Such quenching is due to charge extraction at the 3D-2D interface, suggesting that the PCBM interlayer could help achieve better charge separation. The average carrier lifetime of LSS films is nearly threefold shorter than control films.

The quantum tunneling effect, a unique phenomenon in quantum mechanics, describes the process where microscopic particles (such as electrons) probabilistically penetrate potential energy barriers deemed insurmountable in classical physics. In our LSS samples, although the 2D perovskite alignment parallels 3D perovskite grains, the precisely controlled ultrathin architecture maintains electron transport efficiency through optimized quantum confinement engineering. The PCBM interlayer enabled uniform 2D perovskite (n = 1-2) capping on 3D surfaces, evidenced by large-area PL uniformity (15×15 μm²) and prolonged carrier lifetimes (925 ns vs. control's 427 ns). Top-side illumination revealed enhanced interfacial charge extraction in LSS films, exhibiting threefold faster PL quenching versus controls, confirming optimized 3D-2D heterojunction charge separation dynamics.

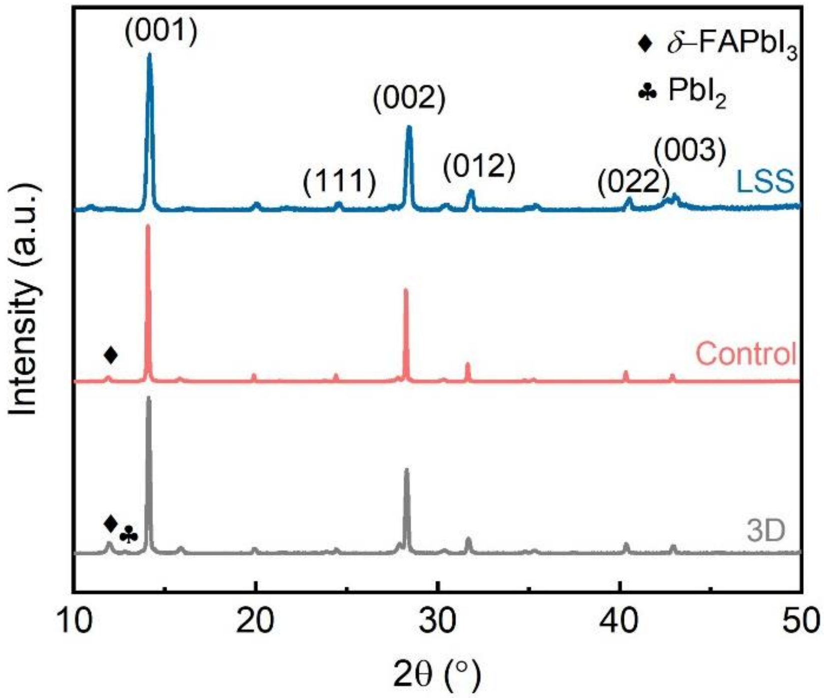

Figure 5.26 XRD patterns of the neat 3D, control, and LSS films.

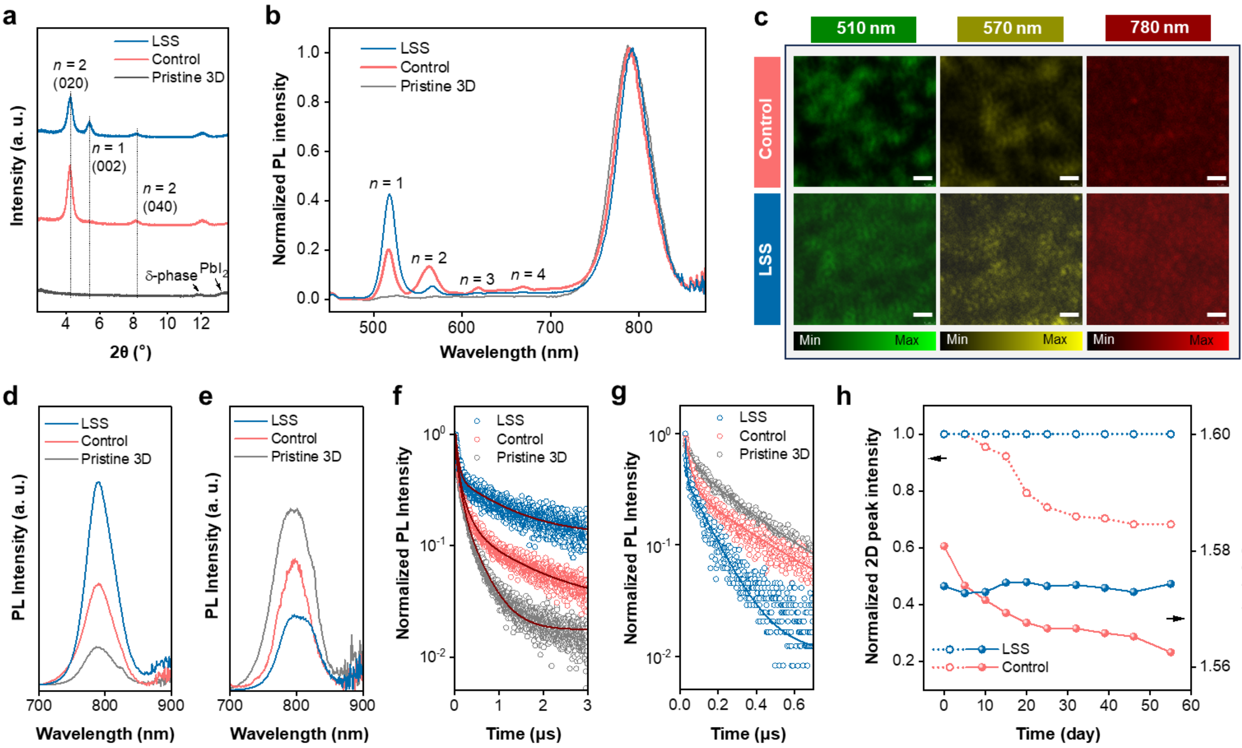

Figure 5.27 Optoelectronic properties and stability of perovskite films. **(a),** XRD patterns of pristine 3D, control, and LSS films. **(b),** Normalized PL spectra of pristine 3D, control, and LSS films. **(c),** PL images of control and LSS films at wavelength ~510 nm, ~570 nm, and ~780 nm correspond to *n* = 1 and 2 layers and 3D layers, respectively. The scale bar is 1 μm. Steady-state PL spectra of pristine 3D, control, and LSS films deposited on bare glass with excitation from glass (**d**) and perovskite (**e**) sides. Time-resolved PL spectra of pristine 3D, control, and LSS films deposited on bare glass with excitation from glass (**f**) and perovskite (**g**) sides. The solid lines in **(f), (g)** are the corresponding fit curves for the PL decays of LSS, control, and pristine 3D perovskite samples. **(h),** Evolution of 2D peak and 3D bandgap of control and LSS films by tracking UV-vis spectra under RH of 40%. (LSS: 3D perovskite sample with the PCBM-mediated 2D surface passivation treatment; Control: 3D perovskite sample with conventional 2D surface passivation treatment; Pristine 3D: 3D perovskite sample with no 2D surface passivation treatment.)

Table 5.1 Summaries of fitting parameters in TRPL spectra for different samples under different detection directions.

	Samples	A_1	τ_1 (ns)	A_2	τ_2 ((ns)	τ_{ave} (ns)
Bottom	LSS	0.71	64	0.29	1053	925
	Control	0.74	65	0.26	549	427
	Pure 3D	0.57	43	0.43	280	239
Top	LSS	0.40	6	0.60	131	127
	Control	0.70	31	0.30	372	316
	Pure 3D	0.52	67	0.48	416	364

The stability of LSS and control films was subsequently explored in a relative humidity (RH) of 75 ± 10%. To quantify the film degradation, we recorded the normalized absorbance decay of the 2D peak at ~560 nm corresponding to $n = 2$ and the bandgap evolution of the 3D perovskite for both the control and LSS samples during the aging test (Figure 5.28). As shown in Figure 5.27h, the control films exhibited gradual decreases in both the intensity of the 2D peak and the bandgap of the 3D perovskite after 55 days, indicating further interaction between the 2D and 3D structures during humidity aging. In contrast, the LSS films retained their integrity, with no degradation of their 2D and 3D structures, demonstrating outstanding chemical stability with improved resistance to water invasion.

The stability of 3D-2D perovskite films with or without the PCBM interlayer was subsequently explored in a relative humidity (RH) of 75 ± 10%. To quantify the film degradation, we recorded the normalized absorbance decay of the 2D peak at ~560 nm corresponding to $n = 2$ and the bandgap evolution of 3D perovskite for both the control and LSS samples during the aging test (Figure 5.28)[22]. As shown in Figure 5.27h, the control samples exhibited gradual decreases in both the intensity of the

2D peak and the bandgap of the 3D perovskite after 55 days, indicating further interaction between the 2D and 3D structures during humidity aging. In contrast, the LSS samples retained their integrity, with no destruction of their 2D and 3D structures, demonstrating outstanding protection from water invasion.

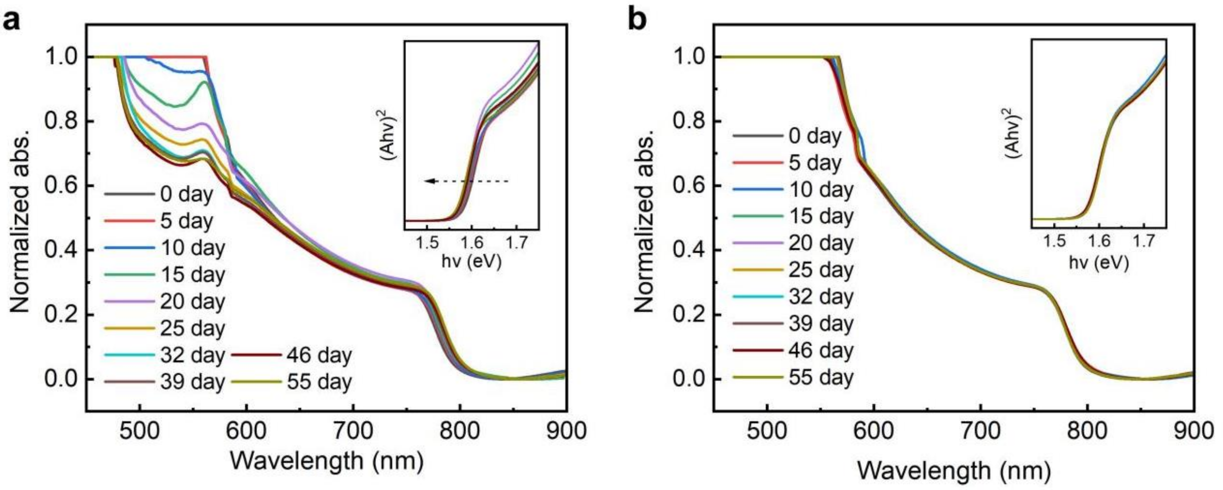

Figure 5.28 Humidity stability of different films. UV-vis spectra of control **(a)** and LSS **(b)** films exposed under RH of 75 ± 10% for 55 days. The insets show the evolution of the 3D bandgap during the aging time.

5.5 Photovoltaic performance and device stability

We evaluated the effects of laminate-structured perovskite heterointerface on the photovoltaic performance of inverted PSCs with the configuration of FTO/MeO-2PACz/3D-PCBM-2D/C_{60}/BCP (bathocuproine)/Ag (Figure 5.29a), where the perovskite film with the composition of $Cs_{0.05}(MA_{0.05}FA_{0.95})_{0.95}Pb(I_{0.95}Br_{0.05})_3$ was used as the active layer of PSCs (CsFAMA, bandgap of 1.57 eV, Figure 5.30). The effects of the concentrations of the PCBM and PEAI on photovoltaic performance were systematically studied, and the optimal concentration for both PEAI and PCBM was 5 mg ml^{-1} (Figure 5.31, Table 5.2, Table 5.3).

Concentration optimization of PEAI and PCBM for perovskite photovoltaic performance. We first optimized the PEAI concentrations for an ideal 3D-2D (control) PSC. Exemplified by a set of data (Figure 5.31a), upon increasing the PEAI concentrations (C_{PEAI}, mg/mL) in the anti-solvent of isopropanol, the PCE first augmented and subsequently decreased with a peak at $C_{\text{PEAI}} = 5$ (See detailed photovoltaic parameters in Table 5.2). Upon increasing the C_{PEAI} from 0 to 5, all photovoltaic parameters have been improved, where the PCE raised from 19.46 to 24.07, the V_{OC} from 1.100 V to 1.178 V, the J_{SC} from 23.40 mA/cm^2 to 24.34 mA/cm^2, and the FF from 75.62% to 83.98%. Then, we proceeded to optimize the PCBM concentrations for high efficient LSS PSCs. With the increase of PCBM concentrations (C_{PCBM}, mg/ml) in chlorobenzene from 0 to 5, the PCE increased from 23.71% to 25.25% (Exemplified by a set of data, Figure 5.31b), the V_{OC} from 1.176 V to 1.205 V, the J_{SC} from 24.02 mA/cm2 to 24.80 mA/cm2, and the FF from 82.79% to 84.48%. Upon further increasing the C_{PCBM}, all photovoltaic parameters exhibited successive decreases (Table 5.3). These results suggest that the optimal concentration of PCBM is 5 mg/ml.

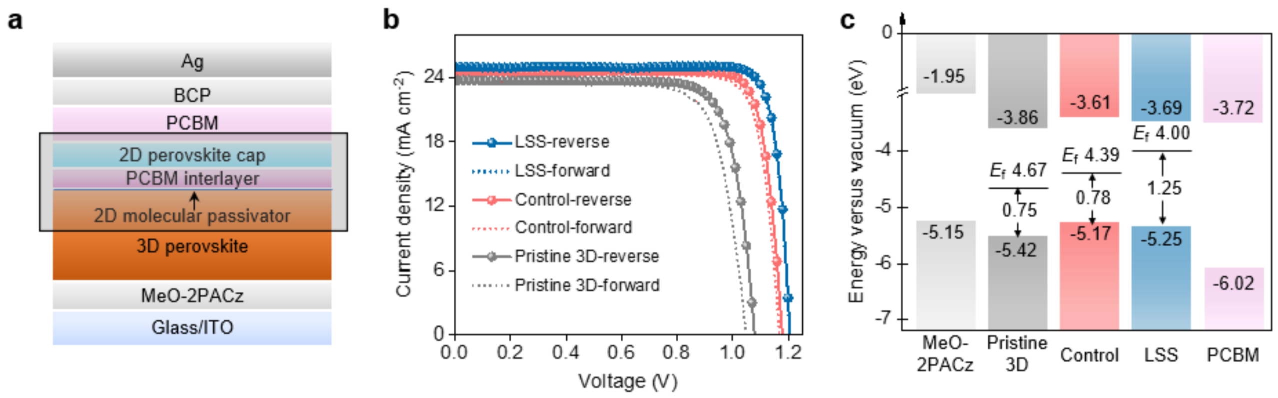

Figure 5.29 (a), Schematic illustration of device configuration for LSS-based inverted PSCs. **(b),** *J-V* curves of the best-performing pristine-3D, control, and LSS PSCs (at both reverse and forward scans). **(c),** Energy level scheme for pristine-3D, control, and LSS PSCs extracted from UPS data ([2-(3,6-Dimethoxy-9H-carbazol-9-yl)ethyl]phosphonic acid, MeO-2PACz; bathocuproine, BCP).

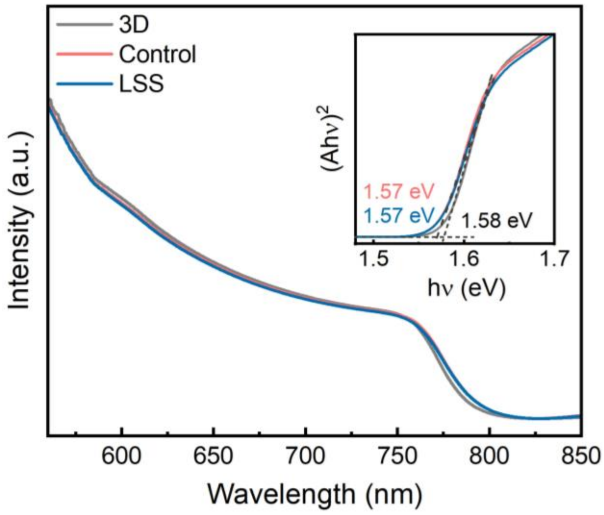

Figure 5.30 UV-vis absorption spectra of pristine-3D, control, and LSS films with the 3D perovskite composition of $Cs_{0.05}(MA_{0.05}FA_{0.95})_{0.95}Pb(I_{0.95}Br_{0.05})_3$.

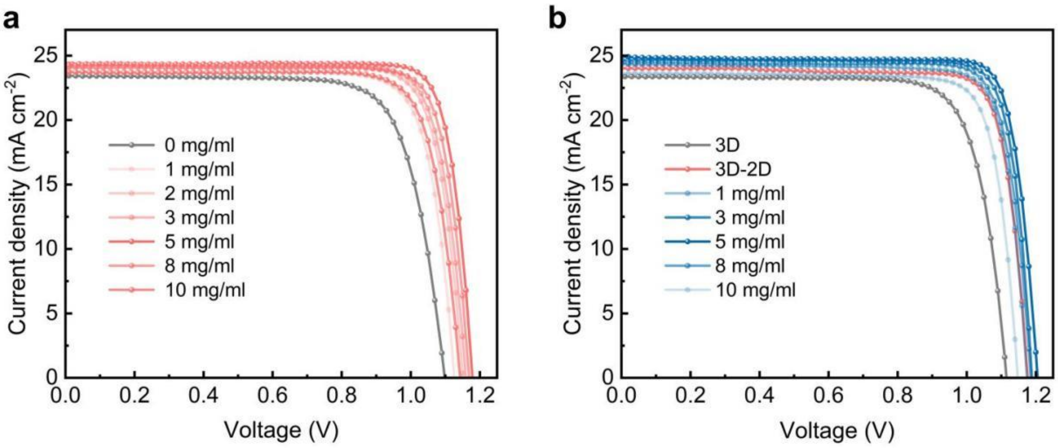

Figure 5.31 Concentration optimization of PEAI and PCBM for *p-i-n* PSCs. *J-V* curves of 3D-2D PSCs with different concentrations of PEAI (**a**) and PCBM (**b**). The pure 3D device is used as a reference.

Table 5.2 The photovoltaic parameters of 3D *n-i-p* devices with different concentrations of PEAI under reverse scanning.

PEAI concentrations	V_{OC} (V)	J_{SC} (mA/cm^2)	FF (%)	PCE (%)
3D (0 mg/ml)	1.100	23.40	75.62	19.46
3D-2D (1mg/ml)	1.126	23.67	80.60	21.49
3D-2D (2 mg/ml)	1.151	24.28	81.04	22.65
3D-2D (3 mg/ml)	1.169	24.32	82.57	23.47
3D-2D (5 mg/ml)	1.178	24.34	83.98	24.07
3D-2D (8 mg/ml)	1.170	24.09	82.94	23.38
3D-2D (10 mg/ml)	1.143	23.72	80.39	21.80

Table 5.3 The photovoltaic parameters of 3D-2D *n-i-p* devices with different concentrations of PCBM under reverse scanning.

PCBM concentrations	V_{OC} (V)	J_{SC} (mA/cm^2)	FF (%)	PCE (%)
3D-2D (0 mg/ml)	1.176	24.02	82.79	23.39
3D-PCBM-2D (1mg/ml)	1.176	24.33	82.86	23.71
3D-PCBM-2D (3 mg/ml)	1.194	24.64	83.66	24.61
3D-PCBM-2D (5 mg/ml)	1.205	24.80	84.48	25.25
3D-PCBM-2D (8 mg/ml)	1.185	24.46	83.51	24.21
3D-PCBM-2D (10 mg/ml)	1.145	23.63	80.91	21.89

As shown in current density-voltage (*J-V*) curves in Figure 5.29b, the champion control devices exhibited a decent PCE of 24.42% under reverse scanning, higher than that of pristine 3D devices (without 2D surface treatment, 20.30%) owing to the general passivation effect of 2D perovskite[117,202-206], whereas the champion efficiency of the LSS-based devices is further increased up to 25.97%, ascribed to the enhancement of all photovoltaic parameters with open-circuit voltage (V_{OC}) from 1.179 V to 1.206 V, short-circuit current density (J_{SC}) from 24.57 mA/cm^2 to 25.02 mA/cm^2, and fill factor (FF) from 84.31% to 86.08%. More importantly, the LSS devices exhibited a negligible hysteresis (hysteresis index (HI), 0.81%) when measured in both reverse and forward scanning (Table 5.4), which is significantly smaller than that of the pristine 3D (6.75%) and control (3.40%) devices. Further hysteresis analyses of *J-V* curves for different PSCs are provided in Figure 5.32 and summarized in next part. Additionally, the resultant LSS-based devices exhibit a better reproducibility compared with those of the 3D and control devices, as indicated by the statistics of 50 individual devices under each condition in Figure 5.33. The average PCEs rise increasingly from 17.27% for 3D to 22.98% for control, and to 24.69% for LSS, attributed to enhancements in all photovoltaic parameters.

Hysteresis analyses of J-V curves for different *p-i-n* PSCs. To verify the effect of PCBM interlayer on the *J-V* hysteresis of *p-i-n* devices, we tested a series of devices with different PCBM concentrations, and obtained corresponding *J-V* curves under forward and reverse scanning (FS and RS, Figure 5.32a-g). The PCEs of different devices in FS and RS are as follows: 18.63% and 16.73% for pure 3D, 23.71% and 21.90% for control, 24.07% and 22.99% for LSS (1 mg/ml), 23.71% and 21.90% for LSS (3 mg/ml), 25.20% and 24.92% for LSS (5 mg/ml), 23.84% and 23.14% for LSS (8 mg/ml), and 22.59% and 21.40% for LSS (10 mg/ml). Detailed photovoltaic parameters are listed in the insets of Figure 5.32a-g. Such hysteresis phenomena can be quantitatively described using the hysteresis index (HI), which is defined by the following formula:

$$\mathrm{HI} = (\mathrm{PCE_{RS}} - \mathrm{PCE_{FS}})/\mathrm{PCE_{RS}} \qquad (1)$$

where PCE_{FS} and PCE_{RS} are the power conversion efficiencies of forward and reverse scanning of *p-i-n* PSCs, respectively. We thus plotted the HI with different PCBM concentrations, as summarized in Figure 5.32h. Upon increasing the C_{PCBM}, the HI first augments and subsequently decreases with a peak at $C_{PCBM} = 5$. The HI value of LSS PSCs is calculated to be 0.011 upon the optimal concentration, which is far lower than those of pure (0.102) and control (0.076) PSCs, demonstrating a negligible hysteresis.

Table 5.4 The photovoltaic parameters of champion *p-i-n* 3D-2D devices with or without the PCBM interlayer under forward and reverse scanning.

Sample	V_{OC} (V)	J_{SC} (mA/cm^2)	FF (%)	PCE (%)
3D reverse	1.079	23.78	79.11	20.30
3D forward	1.048	23.76	76.01	18.93
Control reverse	1.179	24.57	84.31	24.42
Control forward	1.168	24.52	82.39	23.59
LSS reverse	1.206	25.17	86.08	26.13
LSS forward	1.205	25.19	85.37	25.91

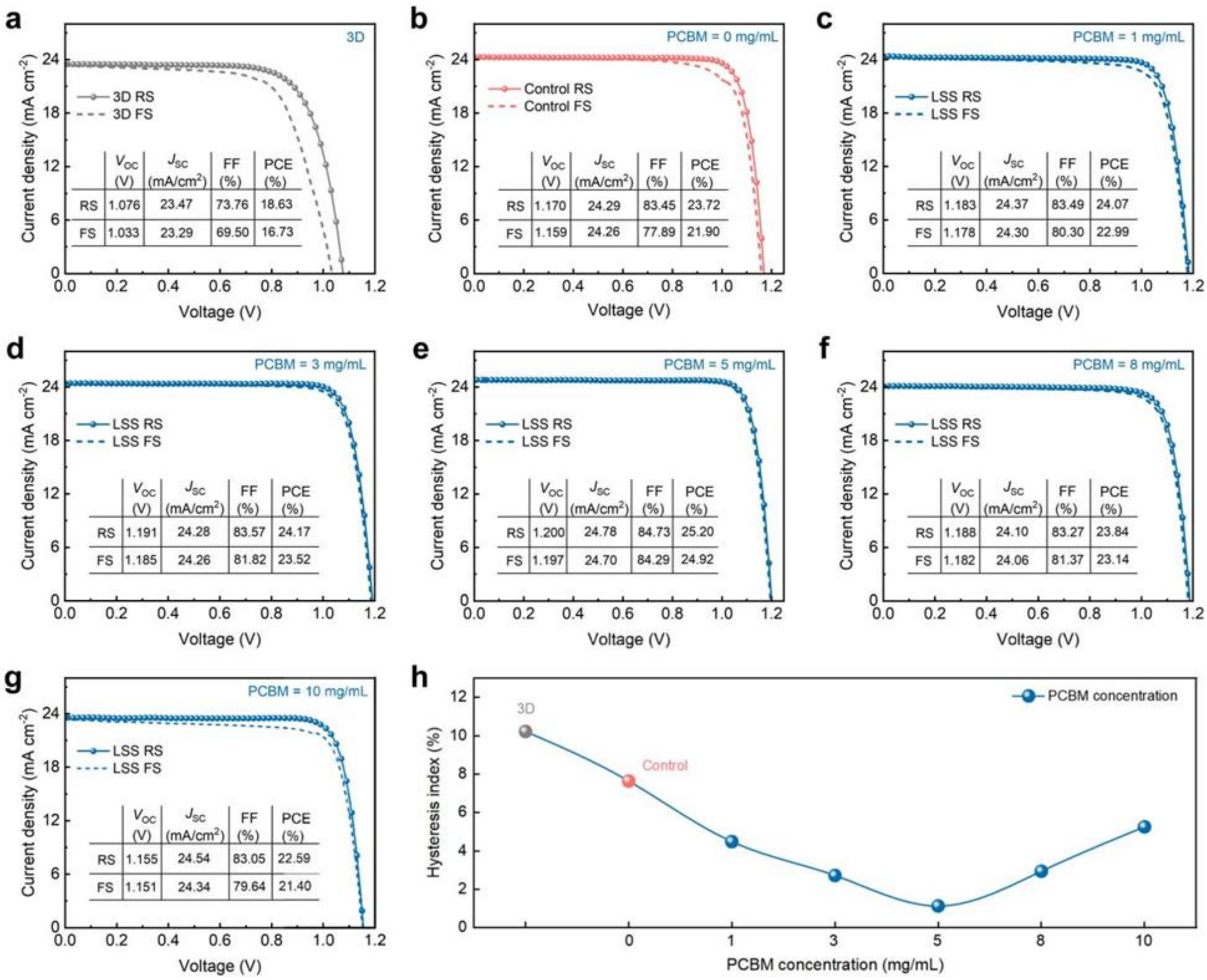

(a)

	V_{OC} (V)	J_{SC} (mA/cm^2)	FF (%)	PCE (%)
RS	1.076	23.47	73.76	18.63
FS	1.033	23.29	69.50	16.73

(b)

	V_{OC} (V)	J_{SC} (mA/cm^2)	FF (%)	PCE (%)
RS	1.170	24.29	83.45	23.72
FS	1.159	24.26	77.89	21.90

(c)

	V_{OC} (V)	J_{SC} (mA/cm^2)	FF (%)	PCE (%)
RS	1.183	24.37	83.49	24.07
FS	1.178	24.30	80.30	22.99

(d)

	V_{OC} (V)	J_{SC} (mA/cm^2)	FF (%)	PCE (%)
RS	1.191	24.28	83.57	24.17
FS	1.185	24.26	81.82	23.52

(e)

	V_{OC} (V)	J_{SC} (mA/cm^2)	FF (%)	PCE (%)
RS	1.200	24.78	84.73	25.20
FS	1.197	24.70	84.29	24.92

(f)

	V_{OC} (V)	J_{SC} (mA/cm^2)	FF (%)	PCE (%)
RS	1.188	24.10	83.27	23.84
FS	1.182	24.06	81.37	23.14

(g)

	V_{OC} (V)	J_{SC} (mA/cm^2)	FF (%)	PCE (%)
RS	1.155	24.54	83.05	22.59
FS	1.151	24.34	79.64	21.40

Figure 5.32 Hysteresis analyses of *J*-*V* curves for different *p*-*i*-*n* PSCs. *J*-*V* curves of PSCs for pure 3D **(a)**, control **(b)**, and LSS (**c-g**) with different concentrations of PCBM under forward and reverse scanning. **(h)**, The evolution of HI with the PCBM concentration increases.

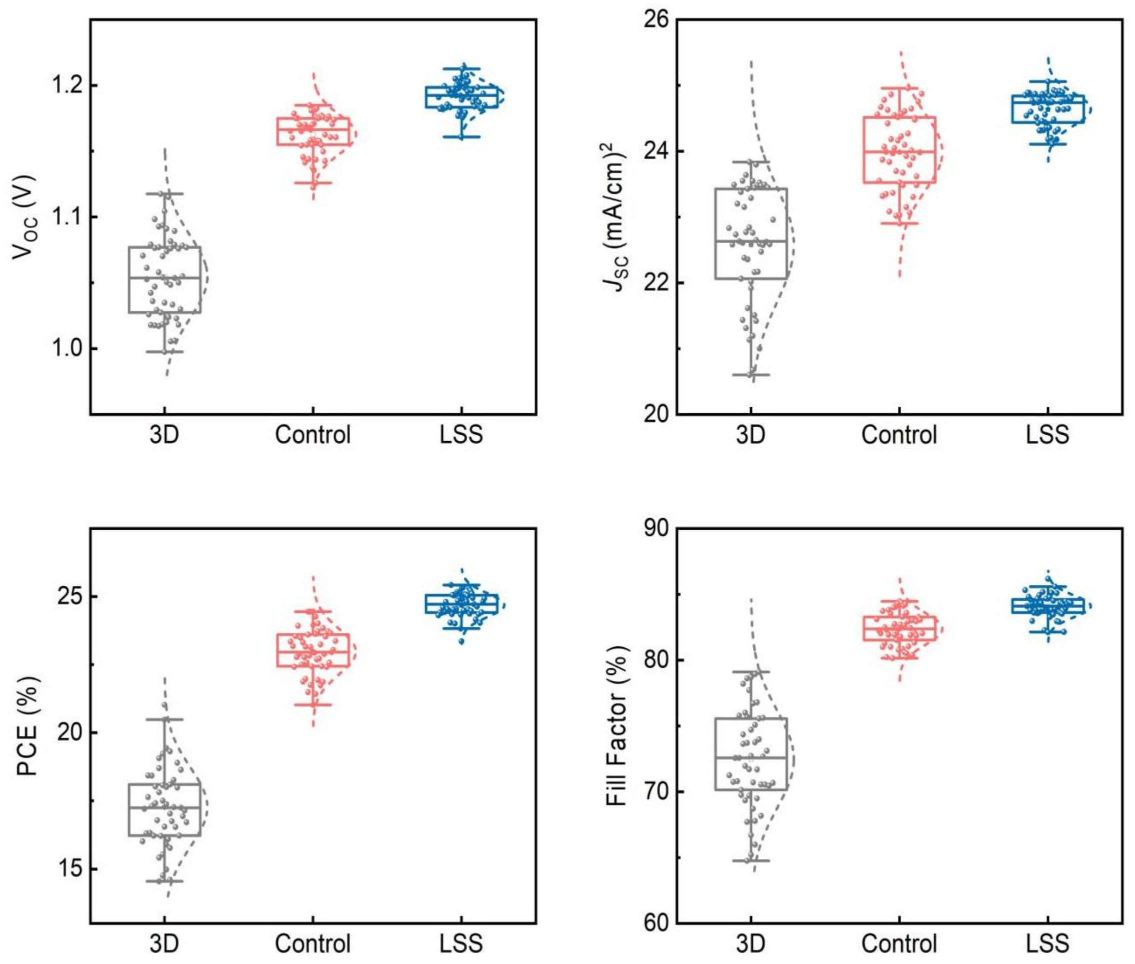

Figure 5.33 Statistical distributions of the photovoltaic parameters (V_{OC}, J_{SC}, FF, and PCE) for 50 individual *n-i-p* 3D-2D devices with or without PCBM interlayer. The 3D device is utilized as a reference. Both the concentrations of PEAI and PCBM are 5 mg/mL.

Additionally, the devices based on the construction of LSS exhibited better reproducibility compared with those of the 3D and control devices, as indicated by the statistics of 50 individual devices under each condition in Figure 5.33. As shown in Figure 5.33, there is a noticeable improvement in the average PCE from 17.27% (pure 3D) to 22.98% (control) and further to 24.69% (LSS). This improvement is due to the increase in Voc from 1.054 V to 1.163 V and 1.192 V, the Jsc from 22.58 mA/cm^2 to 23.99 mA/cm^2 and 24.64 mA/cm^2, and the FF from 72.47% to 82.38% and 84.10%. Moreover, it is worth noting that the LSS devices exhibit a narrower distribution compared to the pure 3D and control devices across all photovoltaic parameters, demonstrating excellent reproducibility of the present LSS strategy. The bandgap of the LSS device was determined to be 1.57 eV by differentiating its EQE spectrum, which exhibited an inflection point at 792 nm (Figure 5.34). The integrated J_{SC} from the EQE matched well with the value extracted from the *J-V* curve (Figure 5.34). The enhanced EQE in the long wavelength range of 650 to 780 nm is mainly attributed to the optimized energy-level arrangement at the interface between 3D perovskite and electron transport layer. The V_{OC} deficit (E_g -qV_{OC}) of the LSS device was calculated to be 0.364 V, which is among the lowest values reported so far for PSCs with an E_g of ~1.57 eV (Figure 5.35).

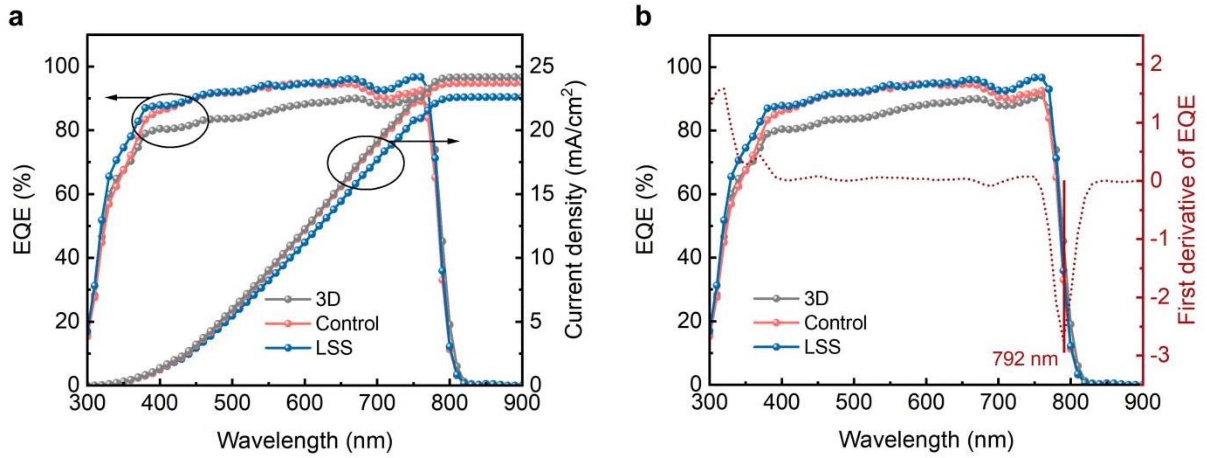

Figure 5.34 (a), EQE and integrated current density curves for the champion 3D (22.60 mA/cm^2), control (23.71 mA/cm^2), and LSS (24.18 mA/cm^2) CsFAMA devices. **(b),** EQE curves with determination of the bandgap for the LSS PSCs.

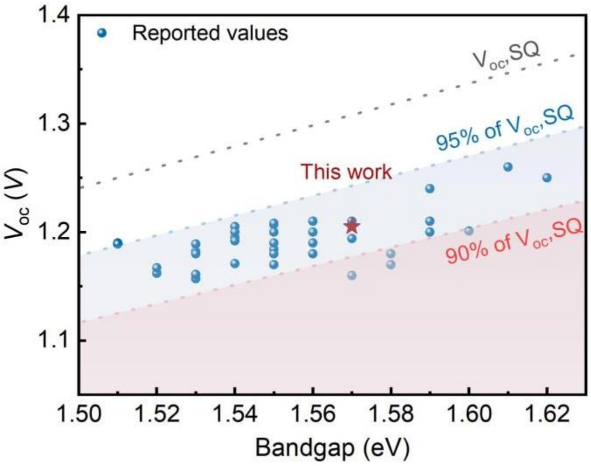

Figure 5.35 Summary of the reported V_{OC} values for the representative PSCs with different bandgaps.

To assess the effect of the PCBM interlayer on the interfacial energy-level alignments, we conducted the UPS tests for different perovskite films (Figure 5.36). Figure 5.29c shows the energy-level diagrams of [2-(3,6-Dimethoxy-9H-carbazol-9-yl)ethyl]phosphonic Acid (MeO-2PACz) anchored on FTO substrate[207-209], perovskites, and PCBM. The corresponding data was extracted from the UPS data. It is clearly found that the secondary electron cut-off ($E_{\text{cut-off}}$) shifted to a higher binding energy after PEAI post-treatment regardless of the PCBM interlayer, indicating that the ion exchange-induced 3D to 2D perovskite phase transition could lower the Fermi level (E_F) of perovskite films. Notably, the energetic gap between EF and the VBM of the LSS sample was wider than that of control, indicating the enhanced *n*-type character of 3D perovskite films[210-212]. Also, the CBM of LSS films was closer to the CBM of PCBM at the *n*-type contact, which resulted in more efficient charge transfer at the interface between the 3D-2D perovskite and the PCBM ETL. In contrast, the CBM of control films was much higher than the CBM of PCBM ETL with less n-type character, resulting in less efficient charge transfer of this 2D/3D perovskite interface at the electron-selective contact. Such an energy-level arrangement of LSS is conducive to the increase in build-in electric field of their PSC devices and have less charge accumulation at the electron-selective contact interface, contributing thus to the high V_{OC} and FF of PSCs, as evidenced by the Mott-Schottky (*M-S*) analyses (Figure 5.37).

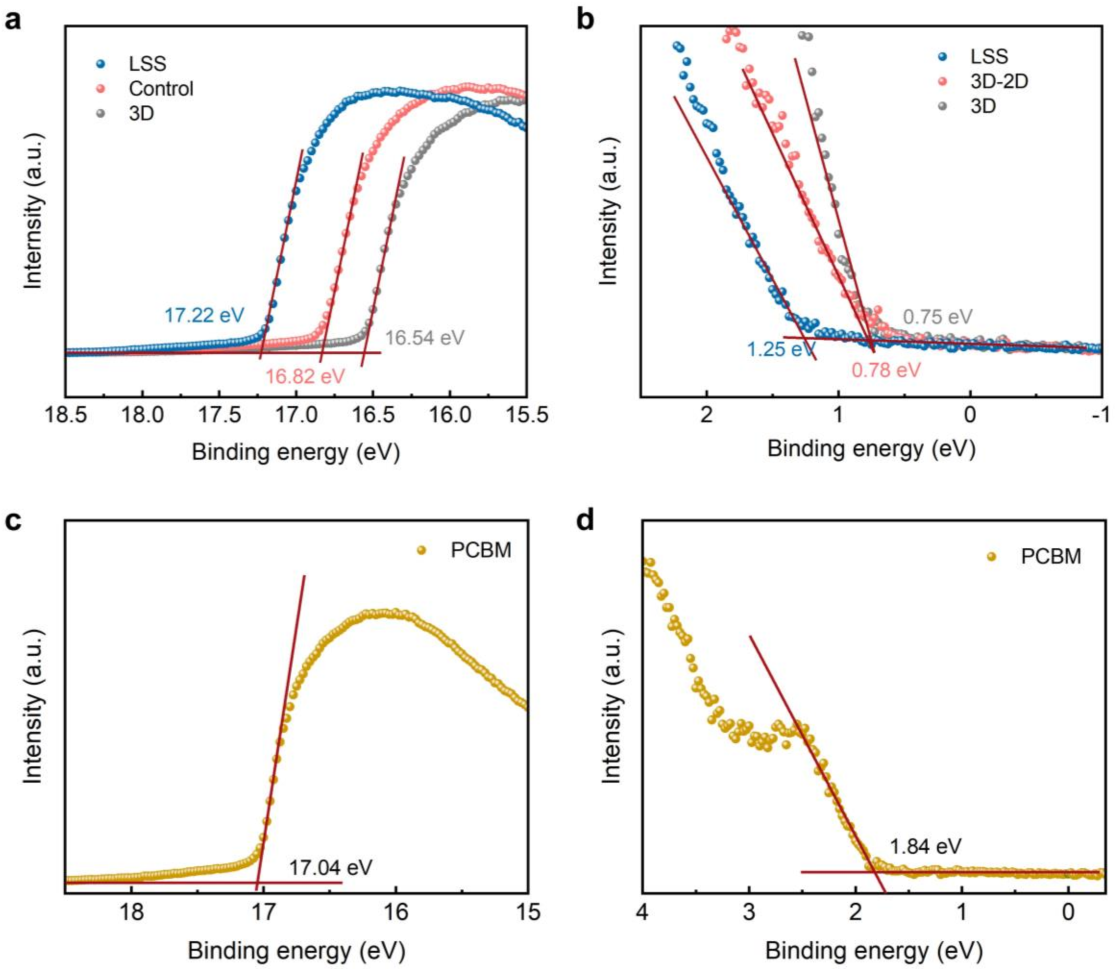

Figure 5.36 Helium La (21.22 eV) spectra of secondary electron cutoff (**a**) and valence band (**b**) for different films. Helium La (21.22 eV) spectra of secondary electron cutoff (**c**) and valence band (**d**) for PCBM ETL.

The Fermi level (E_F) was calculated by the equation: $E_F = E_{\text{cut-off}}$ - 21.22 eV, where $E_{\text{cut-off}}$ represents cut-off binding energy, 21.22 eV is the photon energy of excitation light. The $E_{\text{cut-off}}$ values were extracted to be 16.55 eV, 16.83 eV, and 17.22 eV for pure 3D, control, and LSS films, respectively. The E_F values were calculated to be -4.67 eV, -4.39 eV, and -4.00 eV for pure 3D, control, and LSS films, respectively. Then the valence band maximum (E_{VBM}) was calculated to be -5.42 eV, -5.17 eV, and -5.25 eV for pure 3D, control, and LSS films using the equation: $E_{\text{VBM}} = E_F - E_{\text{onset}}$ (E_{onset} is the onset potential in valence band spectra). The band gap (E_g) values of three perovskite films were obtained from the absorption and EQE spectra, which was calculated to be 1.57 eV. Thus, the conduction band minimum (E_{CBM}) was calculated to be -3.86 eV, -3.61 eV, and -3.69 eV for pure 3D, control, and LSS films, respectively. Similarly, the E_{CBM} and E_{VBM} of the PCBM ETL were calculated to be -3.72 eV and -6.02 eV, respectively.

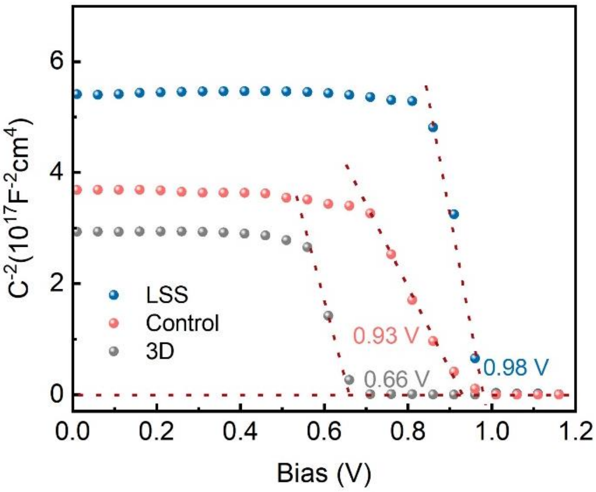

Figure 5.37 Mott-Schottky (*M-S*) plots of pure 3D, control, and LSS devices.

By applying the M-S relation, the capacitance-voltage (*C-V*) characteristics can reflect interfacial charge density, which is inversely proportional to the straight-line slope of the *M-S* plot. The slope of the LSS device (5.7×10^{17}) was larger than those of pure 3D (3.5×10^{17}) and control (0.4×10^{16}) devices, suggesting less charge accumulation at the interface between perovskite and PCBM. We attributed the fast charge transfer at interface to the optimized interface band-alignment induced by the PCBM interlayer. In addition, the LSS device demonstrated an increased build-in potential (V_{bi}) of 0.98 V compared with those of pure 3D (0.66 V) and control (0.93 V) devices.

To establish the stability of our improved *p-i-n* 3D-2D PSCs, we carried out a series of investigations under various test conditions. It should be noted that the C_{60} was used to replace PCBM as the ETL to fabricate devices with the configuration of FTO/MeO-2PACz/3D-perovskite/2D-perovskite with or without PCBM interlayer/C_{60}/BCP/Ag for stability study. We initially monitored the PCE evolution under continuous one-sun illumination in a nitrogen atmosphere (Figure 5.38). After further analyzing the evolution of photovoltaic parameters (V_{OC}, J_{SC}, and FF) for both control and LSS PSCs in N_2 under continuous one-sun illumination (Figure 5.38), it has been observed that as the aging time increases, the V_{OC} of control devices gradually increases and then gradually decreases with a peak at 168 h, while both the J_{SC} and FF exhibit a gradual decrease over time. In contrast, the LSS devices can retain their original FF and J_{SC} in addition to a slight decrease of V_{OC} after 1000 h of light soaking, demonstrating the excellent light stability of *p-i-n* PSCs after inserting the PCBM layer.

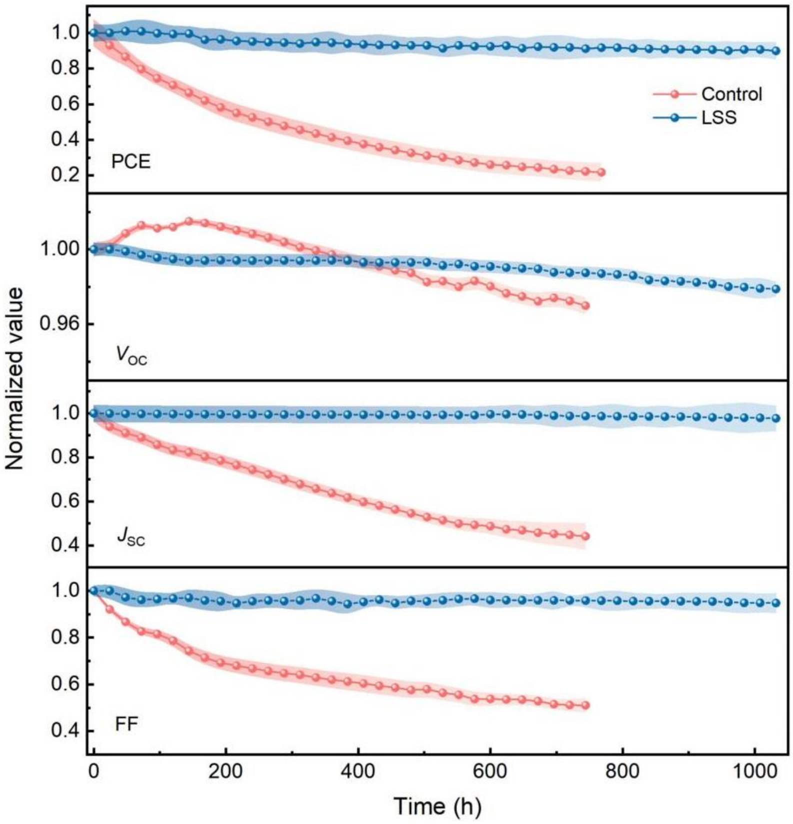

Figure 5.38 Evolution of normalized photovoltaic parameters (PCE, V_{OC}, J_{SC}, and FF) for control and LSS PSCs in N_2 under continuous one-sun illumination. The error bars represent the standard deviation for five devices.

The photo-stability of LSS devices is superior to that of the control devices, maintaining 90% (T_{90}) of their original PCE after 1,000 hours of illumination. While the control devices retained only 22% of their initial PCE after 768 hours. The remarkable enhancement observed is attributed to the block of ionic exchanges between 3D and 2D perovskites when inserting the PCBM layer, evidenced by the electronic analysis. Given that V_{OC} depends both on the active layer bandgap and the rate of nonradiative recombination. The emergence of the inflection point in V_{OC} in control devices is attributed to further ionic exchange between 2D and 3D perovskites that enables the formation of thicker 2D layer during aging, contributing to the wider bandgap and the worse film quality, thereby a trade-off between them. Thus, the J_{SC} of control devices gradually decrease with the aging time due to the thick 2D perovskite layer. In addition, the evolution of FF of control devices is relative to parasitic resistive losses (shunt and series). In general, achieving a high FF requires low recombination losses (high V_{OC}); smooth, uniform, and dense active layers (high shunt resistance, R_{sh}); and efficient charge extraction and transport (low series resistance, R_s). As shown in Figure 5.39, the gradual decreased R_{sh} and the gradual increased Rs with the aging time, demonstrating that the decrease of FF in control devices is determined by resistive losses. After inserting the PCBM layer, both the R_{sh} and Rs show negligible change during the light aging, suggesting the well retaining of all photovoltaic parameters in LSS PSCs.

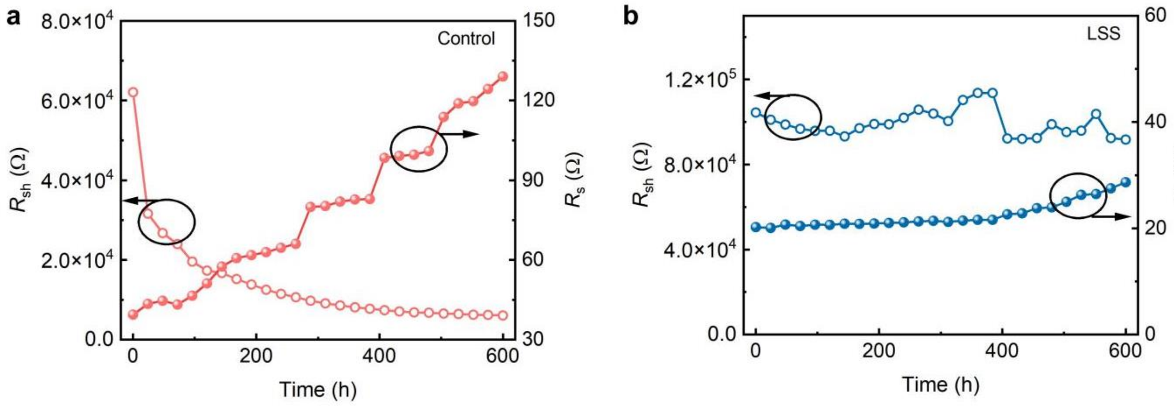

Figure 5.39 Evolution of the series resistance (R_s) and shunt resistance (R_{sh}) for control and LSS PSCs in N_2 under continuous one-sun illumination.

We then performed maximum power point (MPP) tracking tests under continuous light (100 mW cm^{-2}) following the ISOS-L-11 protocol. Typically, after 1,100 h, the LSS-based device still maintained 95% (T_{95}) of its initial PCE (Figure 5.40a), whereas for the control device, the PCE had dropped to 40% of its initial value after only 450 h. Furthermore, we placed encapsulated devices in a chamber to conduct the damp heat test (85°C and 85% RH) following the International Summit on Organic Photovoltaic Stability (ISOS) ISOS-D-3 protocol. As shown in Figure 5.40b, the LSS devices maintained 90.7% of their initial PCEs (23.02 ± 0.53%, Figure 5.41) over 1,000 hours under damp heat aging, whereas the control devices retained only 24.6% of their initial PCEs (21.08 ± 1.19%) within 500 hours. It is worth noting that the well-retained heterointerface microstructure after aging contributes to the better damp-heat durability of the LSS film, while for the control film without the PCBM interlayer, both the 2D and 3D components fail to maintain structural integrity, especially at the grain boundary region (Figure 5.40c-d).

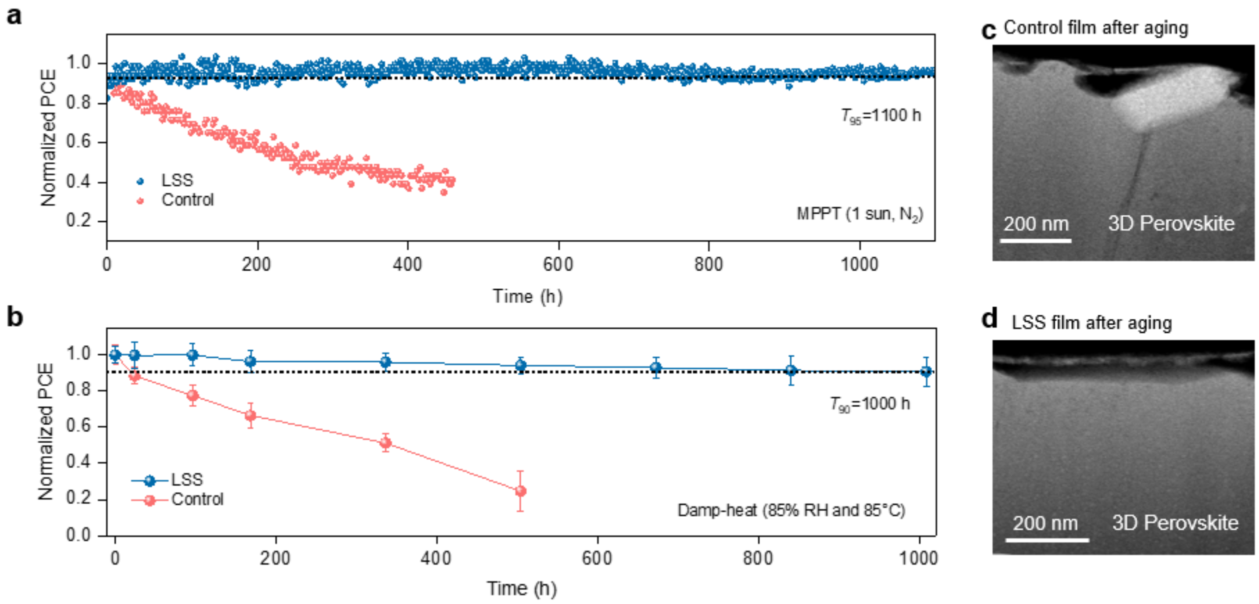

Figure 5.40 (a), Operational stability measured at maximum-power-point tracking in N_2 under continuous one-sun illumination for control and LSS PSCs. The initial PCEs of devices with and without LSS in (**a**) were typically 21.69% and 23.72%, respectively. **(b),** Evolution of PCEs of control

and LSS PSCs under 85% RH and 85°C. The error bars represent the standard deviation for 13 devices. **(c), (d),** HAADF-STEM images of control and LSS films after the identical damp-heat aging. (LSS: 3D perovskite sample with the PCBM-mediated 2D surface passivation treatment; Control: 3D perovskite sample with conventional 2D surface passivation treatment; Pristine 3D: 3D perovskite sample with no 2D surface passivation treatment.)

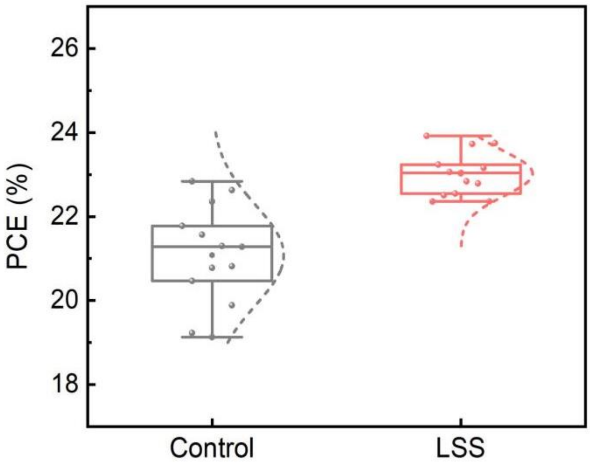

Figure 5.41 Initial PCEs of control and LSS PSCs.

To gain a more profound understanding, we compared the degradation behaviors of the LSS and control devices in the maximum power point (MPP) operational and ambient conditions. As illustrated in Figure 5.42, the 3D and 2D perovskite layers are seen in both the fresh control and LSS devices. After 15 days of the MPP operation, the control device shows substantial microstructural degradation and the formation of PbI_2, particularly at the grain boundaries (Figure 5.43a, b). Conversely, the LSS device exhibits only minor damage, primarily at the buried interface, while the LSS structure remains mostly intact (Figure 5.43c, d). Thus, it is deduced that the degradation in the control device in MPP conditions is primarily attributed to the ion migration, which is known to occur preferably along grain boundaries, triggering the observed microstructural change and phase degradation. In the LSS devices, ion migration is effectively blocked by the unique combination of the uniform 2D layer, the PCBM interlayer, and the

2D molecular layer. The degradation behaviors of the control and LSS samples in the ambient conditions are also very different. After being stored in a 50-60% relative humidity (RH) atmosphere for 10 days, the control sample's surface morphology changes dramatically, with the emergence of numerous pinholes (Figure 5.44a, b). In contrast, the LSS sample shows minimal surface changes (Figure 5.44c, d). STEM observations reveal that a large amount of PbI_2 forms in the 3D grains of the control sample (Figure 5.45a, b). Meanwhile, the LSS sample experiences little change with almost no PbI_2 formation (Figure 5.45c, d). We attribute the stability improvement under operational and ambient conditions mainly to the ion and moisture blocking effects of the PCBM interlayer and passivators within the LSS structure, in which the well-retained LSS microstructure and phase within the PSC devices reinforce the interface reliability and chemical stability of 3D perovskites.

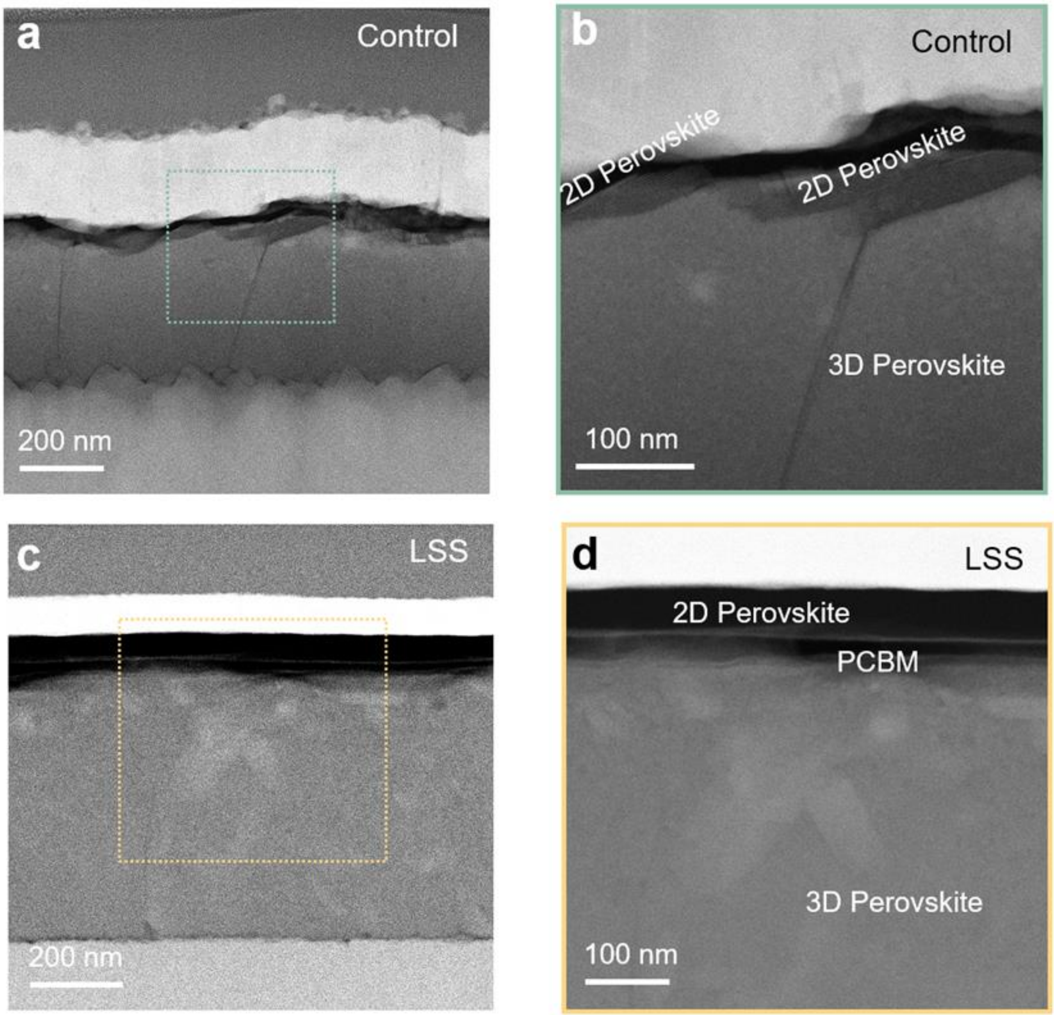

Figure 5.42 STEM-HAADF characterization of the control and LSS device samples before the MPP stability tests. **(a),** STEM-HAADF image of pristine control devices without PCBM interlayer. (**b**), Magnified STEM-HAADF image of the squared region in (**a**) shows the 2D and 3D perovskite structure. (**c**), STEM-HAADF image of pristine LSS devices. (**d**), Magnified STEM-HAADF image of the squared region in **c** shows the LSS structure.

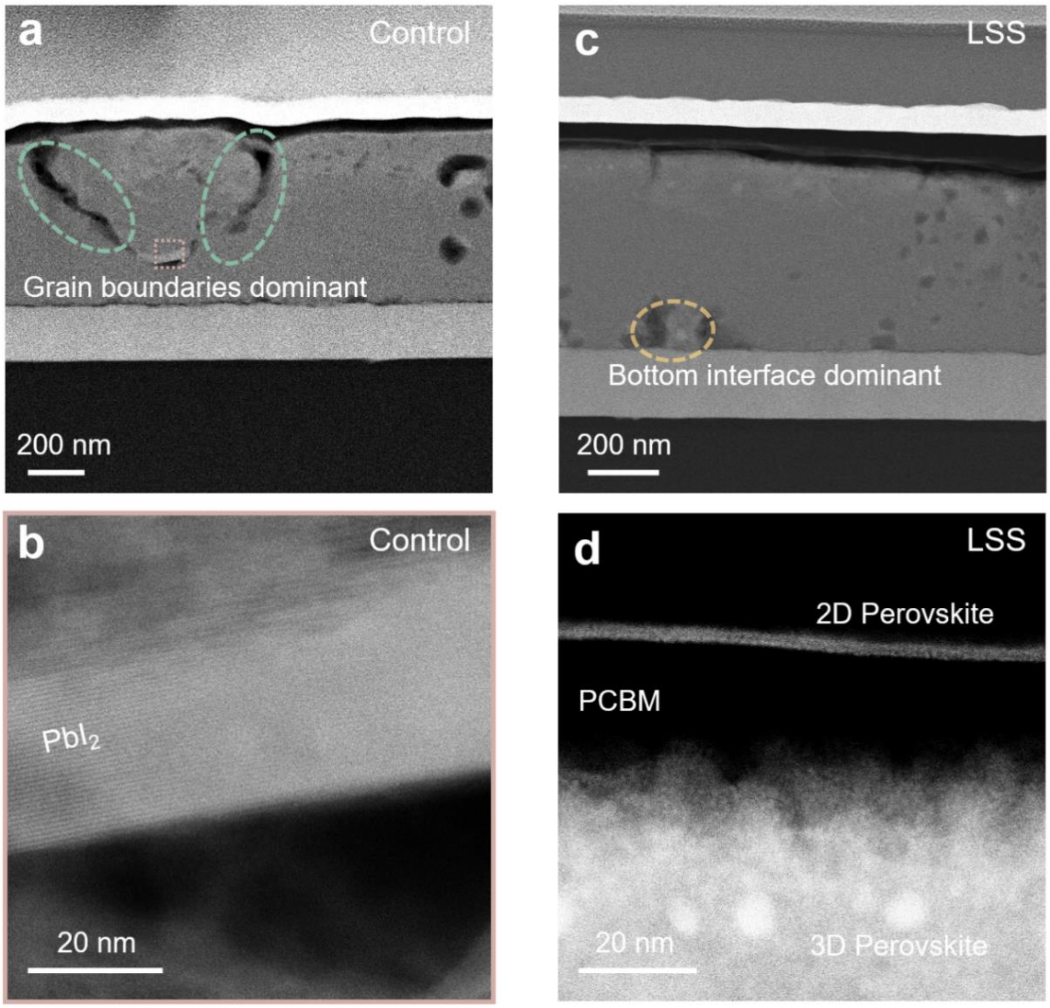

Figure 5.43 STEM-HAADF characterization of control and LSS devices after 15 days of MPP operation. **(a),** The grain-boundary regions of the control device exhibit serious damage. (**b**), Magnified STEM-HAADF image of the squared region in (**a**) showing the existence of PbI_2. (**c**), Only minor damage occurs in the LSS device, mainly at the buried interface. (**d**), The LSS structure remains intact.

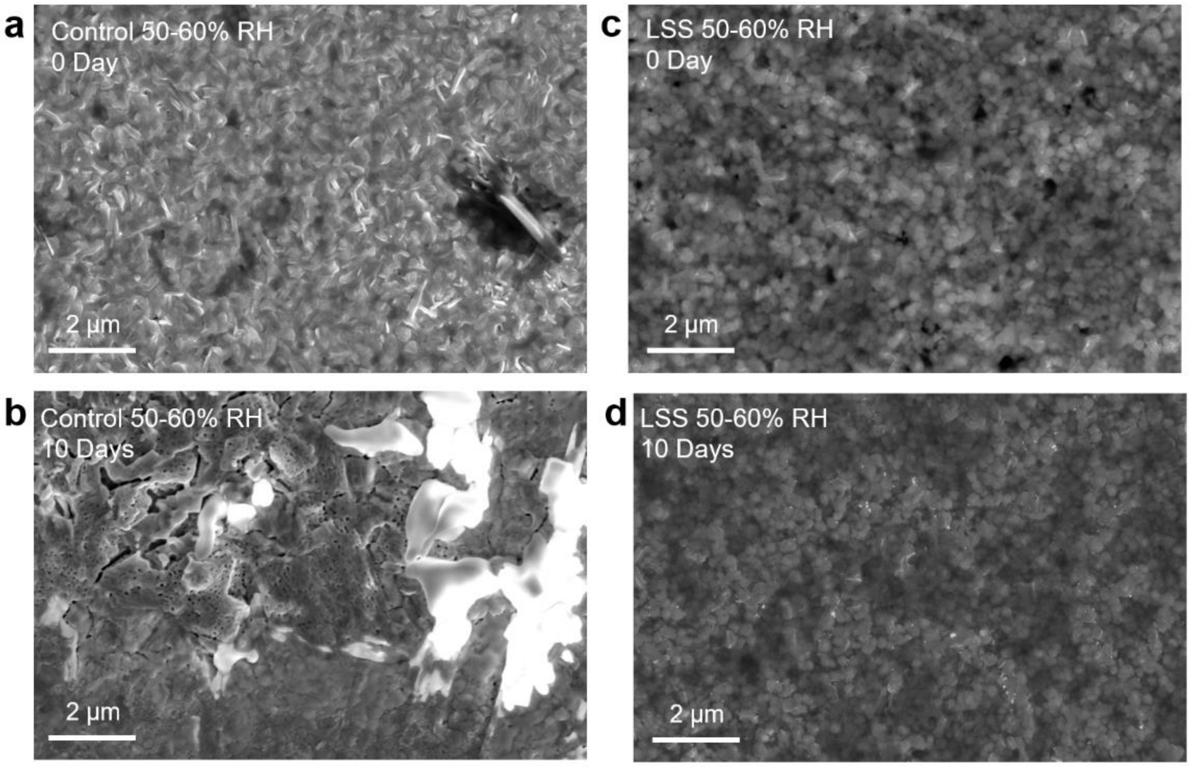

Figure 5.44 SEM characterization for the ambient degradation of control and LSS samples. **(a), (b),** SEM images of the control sample stored at 50-60% relative humidity for 0 and 15 days, respectively. **(c), (d),** SEM images of the LSS sample stored at 50-60% relative humidity for 0 and 15 days, respectively.

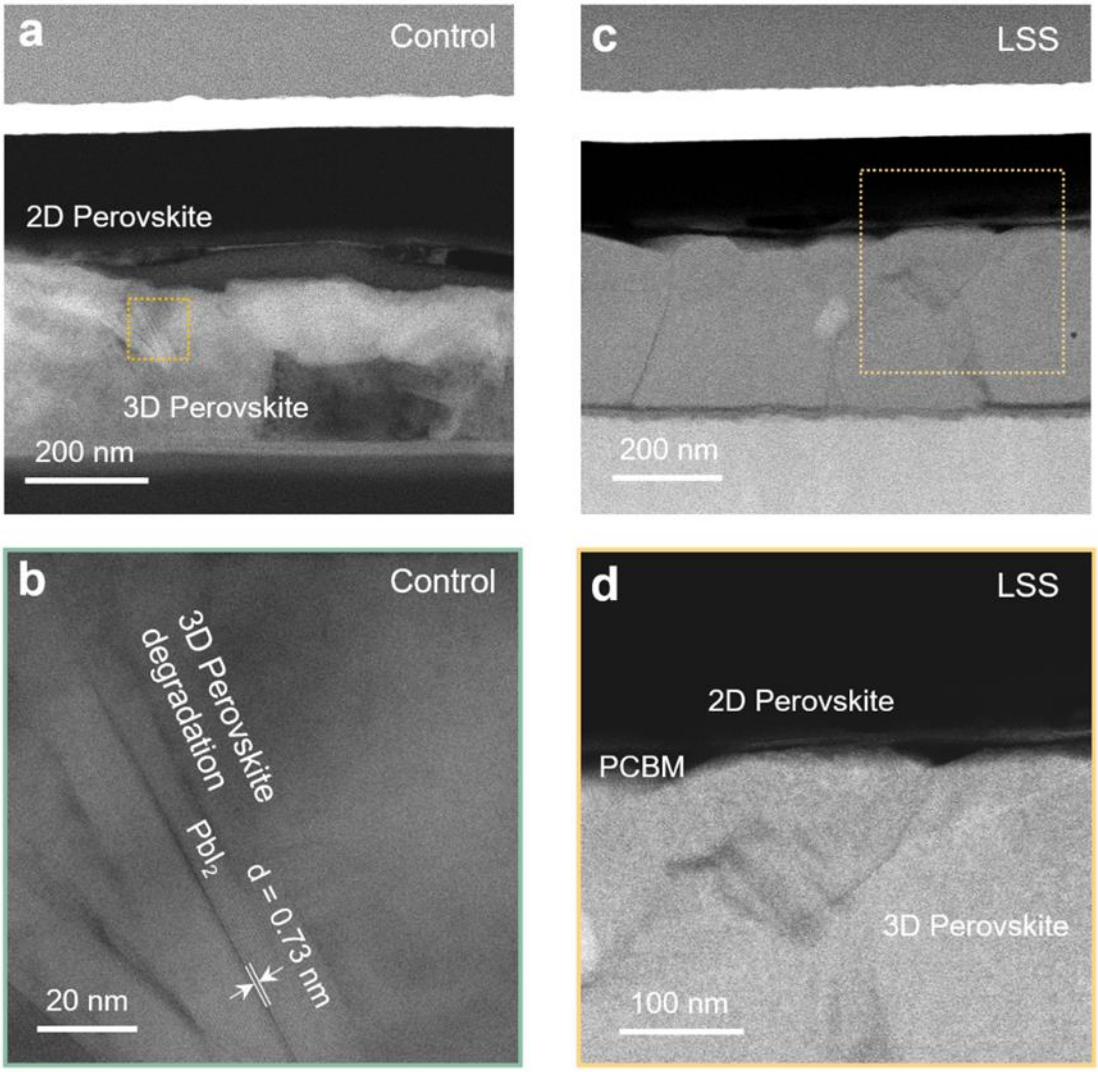

Figure 5.45 STEM-HAADF characterization for the ambient degradation of control and LSS devices. **(a),** STEM-HAADF image of the control device stored at 50-60% relative humidity for 15 days. **(b),** Magnified image of the squared region showing the prominent existence of PbI_2. **(c),** STEM-HAADF image of the LSS device exhibiting little change after the ambient storage. **(d),** Magnified image of the squared region in (**c**) showing the retention of the complete LSS structure.

5.6 Conclusion

In closing, our study demonstrates the use of a PCBM molecular interlayer in synthesizing a laminate-structured surface (LSS) for stabilizing PSCs. By mediating the reaction between 2D perovskite passivators and the underlying 3D perovskite layer, the PCBM interlayer promotes the formation of a uniform, phase pure 2D perovskite capping layer and a molecular passivation layer on the 3D perovskite surface. Detrimental grain boundary etching generally encountered in the conventional passivation approach is also alleviated. The unprecedented LSS is found beneficial to interfacial carrier transport and stability, leading to highly efficient and stable inverted PSCs. This study leverages cross-sectional high-resolution low-dose STEM methodology to investigate the interfacial morphology of the 2D passivation microstructure, and 4D-STEM NBED analysis to determine the structural integrity of grain boundaries in 3D perovskite layer. These lattice-resolved analyses underscore the critical role of fundamental surface microstructures in optimizing device performance and stability. The PCBM molecular interlayer approach can be expanded to form LSS types with various tailored characteristics by adopting other passivation-mediating molecules, creating a new path for advancing perovskite solar cell and module technologies.

Chapter 6 Conclusion and Outlook

6.1 Summary of Results

This thesis comprises two parts of work. The first part investigates the impact of halide ion on the distribution of 2D perovskite in 2D/3D perovskite heterojunctions. The second part focuses on the synthesis of lattice-resolved laminate-structured perovskite heterointerface.

In the first study, we explored the role of halide ions in influencing the structure and performance of 2D/3D perovskite heterojunctions. By incorporating halide ions such as chloride and bromide into perovskite films, we demonstrated significant improvements in the distribution and stability of 2D perovskite layers. The addition of FACl to PEAI solutions resulted in a smoother, more uniform 2D layer, enhancing the overall stability and efficiency of the PSCs. Similarly, the use of PEABr instead of PEAI showed potential in modifying ion exchange at the 2D/3D interface, though challenges remain in achieving uniform layer orientation and thickness. These findings underscore the critical impact of halide ion selection on the microstructural properties and optoelectronic performance of perovskite materials. By fine-tuning halide composition, we can optimize device performance, demonstrating the vast potential of tailored halide incorporation in advancing perovskite solar cell technologies. This research paves the way for further innovations in achieving high-efficiency and stable perovskite-based devices.

In the next study, we have successfully demonstrated the synthesis of a laminate-structured perovskite heterointerface mediated by a PCBM molecular interlayer. This novel approach addresses the significant challenge of uncontrolled surface reactions in the synthesis of 2D perovskite passivators, enabling the formation of a uniform, single-phase 2D perovskite capping layer. The incorporation of a

PCBM interlayer not only mitigates the detrimental grain-boundary etching observed in conventional methods but also facilitates the creation of a molecular passivation directly onto the perovskite surface. This results in improved charge energetics and film stability due to regulated band transitions and unique laminate-layer protection. The inverted PSCs fabricated using this method exhibit power conversion efficiencies up to 26% and enhanced device stabilities, as evidenced by T_{90} lifetimes exceeding 1,000 hours under ISOS-standardized protocols. Through lattice-resolved analyses, we provide insights into the relationship between microstructure and device performance, highlighting the critical importance of passivator-microstructure uniformity. These findings underscore the potential of our approach to significantly advance the performance and stability of perovskite optoelectronics, paving the way for more practical applications in photovoltaic technologies.

6.2 Prospects of Future Work

In recent years, researchers have succeeded in developing 2D/3D heterojunctions by combining 2D perovskite layers with conventional 3D perovskite structures. These heterojunctions have a tunable bandgap and demonstrate exceptional stability. However, based on lots of electron microscopy experiments, it remains evident that 2D/3D PSCs present certain noteworthy issues. These include the need to effectively control the distribution of 2D perovskite and optimize the combination with 3D perovskite in order to fully exploit the superior stability advantages offered by the 2D component. The last goal of this thesis is to present distinctive viewpoints that shed light on prospective subjects for future research.

Preparation of a 2D perovskite layer with non-ionic diffusion. Organic spacer cations have strong interactions with ions located at the A, B, and X sites on the 3D perovskite surface, resulting in the formation of 2D layers. However, controlling this process is challenging. This high-intensity imbalanced ion exchange causes severe damage to the 3D perovskite surface, resulting in a plethora of defects, especially at the surface and grain boundaries. This process also leads to the irregular assignment of *N* values inside the 2D perovskite layer, along with notable disparities in orientation and thickness. Physical transfer, thermal evaporation, or in-situ preparation techniques may efficiently minimize defects at the interface between 2D perovskite layers and 3D grain surfaces.

Interlayer between 3D and 2D perovskite. The 2D layer contacting the 3D perovskite presents several obstacles due to the insulation properties of the organic layers, which hinder efficient charge transport. The interlayer acts as a bridge, combining the advantages of both 2D and 3D perovskites. In order to facilitate efficient movement of charge carriers, the interlayer needs to have properties that enable it to energetically match both the 2D and 3D materials, hence providing an effortless passage of electrons and holes. Optimally, this layer should enhance the extraction of charges from the 3D perovskite while preserving it from environmental deterioration, and at the same time, enable the transfer of charges into the 2D perovskite without substantial loss. The interlayer in 2D/3D PSCs must achieve a delicate balance between boosting the environmental durability provided by the 2D perovskite and preserving the high mobility of the 3D perovskite to transport electric charges. The continuous improvement of interlayer materials and deposition techniques is anticipated to play a vital role in achieving highly efficient and stable 2D/3D PSCs.

References

1 Khan, I., Zakari, A., Dagar, V. & Singh, S. World energy trilemma and transformative energy developments as determinants of economic growth amid environmental sustainability. *Energy Economics* **108** (2022).

2 Kober, T., Schiffer, H. W., Densing, M. & Panos, E. Global energy perspectives to 2060 – WEC's World Energy Scenarios 2019. *Energy Strategy Reviews* **31** (2020).

3 Yoo, J. J., Seo, G., Chua, M. R., Park, T. G., Lu, Y., Rotermund, F., Kim, Y.-K., Moon, C. S., Jeon, N. J., Correa-Baena, J.-P., Bulović, V., Shin, S. S., Bawendi, M. G. & Seo, J. Efficient perovskite solar cells via improved carrier management. *Nature* **590**, 587-593 (2021).

4 Rode, A., Carleton, T., Delgado, M., Greenstone, M., Houser, T., Hsiang, S., Hultgren, A., Jina, A., Kopp, R. E., McCusker, K. E., Nath, I., Rising, J. & Yuan, J. Estimating a social cost of carbon for global energy consumption. *Nature* **598**, 308-314 (2021).

5 Ahmad, T. & Zhang, D. A critical review of comparative global historical energy consumption and future demand: The story told so far. *Energy Reports* **6**, 1973-1991 (2020).

6 Maka, A. O. M. & Alabid, J. M. Solar energy technology and its roles in sustainable development. *Clean Energy* **6**, 476-483 (2022).

7 Rabaia, M. K. H., Abdelkareem, M. A., Sayed, E. T., Elsaid, K., Chae, K.-J., Wilberforce, T. & Olabi, A. G. Environmental impacts of solar energy systems: A review. *Science of The Total Environment* **754** (2021).

8 Nijsse, F. J. M. M., Mercure, J.-F., Ameli, N., Larosa, F., Kothari, S., Rickman, J., Vercoulen, P. & Pollitt, H. The momentum of the solar energy transition. *Nature Communications* **14** (2023).

9 Kruitwagen, L., Story, K. T., Friedrich, J., Byers, L., Skillman, S. & Hepburn, C. A global inventory of photovoltaic solar energy generating units. *Nature* **598**, 604-610 (2021).

10 America's National Renewable Energy Laboratory. *Best Research-Cell Efficiencies*, https://www.nrel.gov/pv/cell-efficiency.html.

11 Kojima, A., Teshima, K., Shirai, Y. & Miyasaka, T. J. J. o. t. a. c. s. Organometal halide perovskites as visible-light sensitizers for photovoltaic cells. *Journal of the american chemical society* **131**, 6050-6051 (2009).

12 Chen, H., Liu, C., Xu, J., Maxwell, A., Zhou, W., Yang, Y., Zhou, Q., Bati, A. S., Wan, H. & Wang, Z. J. S. Improved charge extraction in inverted perovskite solar cells with dual-site-binding ligands. *Science* **384**, 189-193 (2024).

13 Park, S. M., Wei, M., Xu, J., Atapattu, H. R., Eickemeyer, F. T., Darabi, K., Grater, L., Yang, Y., Liu, C. & Teale, S. J. S. Engineering ligand reactivity enables high-temperature operation of stable perovskite solar cells. *Science* **381**, 209-215 (2023).

14 Nazir, G., Lee, S. Y., Lee, J. H., Rehman, A., Lee, J. K., Seok, S. I. & Park, S. J. Stabilization of Perovskite Solar Cells: Recent Developments and Future Perspectives. *Advanced Materials* **34** (2022).

15 Bati, A. S. R., Zhong, Y. L., Burn, P. L., Nazeeruddin, M. K., Shaw, P. E. & Batmunkh, M. Next-generation applications for integrated perovskite solar cells. *Communications Materials* **4** (2023).

16 Lee, J. W., Seol, D. J., Cho, A. N. & Park, N. G. J. A. m. High‐efficiency perovskite solar cells based on the black polymorph of HC (NH2) 2PbI3. *Advanced materials* **26**, 4991-4998 (2014).

17 Turren-Cruz, S.-H., Hagfeldt, A. & Saliba, M. J. S. Methylammonium-free, high-performance, and stable perovskite solar cells on a planar architecture. *Science* **362**, 449-453 (2018).

18 Smith, I. C., Hoke, E. T., Solis‐Ibarra, D., McGehee, M. D. & Karunadasa, H. I. J. A. C. I. E. A layered hybrid perovskite solar‐cell absorber with enhanced moisture stability. *Angewandte Chemie International Edition* **53**, 11232-11235 (2014).

19 Azmi, R., Utomo, D. S., Vishal, B., Zhumagali, S., Dally, P., Risqi, A. M., Prasetio, A., Ugur, E., Cao, F., Imran, I. F., Said, A. A., Pininti, A. R., Subbiah, A. S., Aydin, E., Xiao, C., Seok, S. I. & De Wolf, S. Double-side 2D/3D heterojunctions for inverted perovskite solar cells. *Nature* **628**, 93-98 (2024).

20 Azmi, R., Ugur, E., Seitkhan, A., Aljamaan, F., Subbiah, A. S., Liu, J., Harrison, G. T., Nugraha, M. I., Eswaran, M. K., Babics, M., Chen, Y., Xu, F., Allen, T. G., Rehman, A. u., Wang, C.-L., Anthopoulos, T. D., Schwingenschlögl, U., De Bastiani, M., Aydin, E. & De Wolf, S. Damp heat–stable perovskite solar cells with tailored-dimensionality 2D/3D heterojunctions. *Science* **376**, 73-77 (2022).

21 Jang, Y.-W., Lee, S., Yeom, K. M., Jeong, K., Choi, K., Choi, M. & Noh, J. H. Intact 2D/3D halide junction perovskite solar cells via solid-phase in-plane growth. *Nature Energy* **6**, 63-71 (2021).

22 Sidhik, S., Wang, Y., De Siena, M., Asadpour, R., Torma, A. J., Terlier, T., Ho, K., Li, W., Puthirath, A. B., Shuai, X., Agrawal, A., Traore, B., Jones, M., Giridharagopal, R., Ajayan, P. M., Strzalka, J., Ginger, D. S., Katan, C., Alam, M. A., Even, J., Kanatzidis, M. G. & Mohite, A. D. Deterministic fabrication of 3D/2D perovskite bilayer stacks for durable and efficient solar cells. *Science* **377**, 1425-1430 (2022).

23 Cai, S., Dai, J., Shao, Z., Rothmann, M. U., Jia, Y., Gao, C., Hao, M., Pang, S., Wang, P., Lau, S. P., Zhu, K., Berry, J. J., Herz, L. M., Zeng, X. C. & Zhou, Y. Atomically Resolved Electrically Active Intragrain Interfaces in Perovskite Semiconductors. *Journal of the American Chemical Society* **144**, 1910-1920 (2022).

24 Cai, S., Li, Z., Zhang, Y., Liu, T., Wang, P., Ju, M.-G., Pang, S., Lau, S. P., Zeng, X. C. & Zhou, Y. Intragrain impurity annihilation for highly efficient and stable perovskite solar cells. *Nature Communications* **15** (2024).

25 Kojima, A., Teshima, K., Shirai, Y. & Miyasaka, T. J. J. o. t. a. c. s. Organometal halide perovskites as visible-light sensitizers for photovoltaic cells. *Journal of the american chemical society* **131**, 6050-6051 (2009).

26 De Wolf, S., Holovsky, J., Moon, S.-J., Loper, P., Niesen, B., Ledinsky, M., Haug, F.-J., Yum, J.-H. & Ballif, C. J. T. j. o. p. c. l. Organometallic halide perovskites: sharp optical absorption edge and its relation to photovoltaic performance. *The journal of physical chemistry letters* **5**, 1035-1039 (2014).

27 Unger, E., Kegelmann, L., Suchan, K., Sörell, D., Korte, L. & Albrecht, S. J. J. o. M. C. A. Correction: Roadmap and roadblocks for the band gap tunability of metal halide perovskites. *Journal of Materials Chemistry A* **5**, 15983-15983 (2017).

28 Sutton, R. J., Eperon, G. E., Miranda, L., Parrott, E. S., Kamino, B. A., Patel, J. B., Hörantner, M. T., Johnston, M. B., Haghighirad, A. A. & Moore, D. T. J. A. E. M. Bandgap‐tunable cesium lead halide perovskites with high thermal stability for efficient solar cells. *Advanced Energy Materials* **6**, 1502458 (2016).

29 Snaith, H. J. J. T. j. o. p. c. l. Perovskites: the emergence of a new era for low-cost, high-efficiency solar cells. *The journal of physical chemistry letters* **4**, 3623-3630 (2013).

30 Stranks, S. D., Eperon, G. E., Grancini, G., Menelaou, C., Alcocer, M. J., Leijtens, T., Herz, L. M., Petrozza, A. & Snaith, H. J. J. S. Electron-hole diffusion lengths exceeding 1 micrometer in an organometal trihalide perovskite absorber. *Science* **342**, 341-344 (2013).

31 Duan, L., Liu, S., Wang, X., Zhang, Z. & Luo, J. J. A. S. Interfacial Crosslinking for Efficient and Stable Planar TiO2 Perovskite Solar Cells. *Advanced Science*, 2402796 (2024).

32 Wang, W., Li, X., Huang, P., Yang, L., Gao, L., Jiang, Y., Hu, J., Gao, Y., Che, Y. & Deng, J. J. A. M. In situ Blending For Co‐Deposition of Electron Transport and Perovskite Layers

Enables Over 24% Efficiency Stable Inverted Solar Cells. *Advanced Materials*, 2407349 (2024).

33 Zhao, Q., Zhang, B., Hui, W., Su, Z., Wang, H., Zhang, Q., Gao, K., Zhang, X., Li, B.-h. & Gao, X. J. J. o. t. A. C. S. Oxygen Vacancy Mediation in SnO2 Electron Transport Layers Enables Efficient, Stable, and Scalable Perovskite Solar Cells. *Journal of the American Chemical Society* (2024).

34 Song, J. W., Shin, Y. S., Kim, M., Lee, J., Lee, D., Seo, J., Lee, Y., Lee, W., Kim, H. B. & Mo, S. I. J. A. E. M. Post‐Treated Polycrystalline SnO2 in Perovskite Solar Cells for High Efficiency and Quasi‐Steady‐State‐IV Stability. *Advanced Energy Materials*, 2401753 (2024).

35 Zhu, H., Xu, Z., Zhang, Z., Lian, S., Wu, Y., Zhang, D., Zhan, H., Wang, L., Han, L. & Qin, C. J. A. M. Improved Hole‐Selective Contact Enables Highly Efficient and Stable FAPbBr3 Perovskite Solar Cells and Semitransparent Modules. *Advanced Materials*, 2406872 (2024).

36 He, L., Zhang, Y., Zhang, B., Li, T., Cai, Y., Ren, M., Zhang, J., Wang, P., Yuan, Y. J. E. & Science, E. Hole-transporting alternating copolymers for perovskite solar cells: thia [5] helicene comonomer outperforms planar perylothiophene analog. *Energy Environmental Science* **17**, 3937-3946 (2024).

37 Gong, S., Qu, G., Qiao, Y., Wen, Y., Huang, Y., Cai, S., Zhang, L., Jiang, K., Liu, S., Lin, M. J. E. & Science, E. A hot carrier perovskite solar cell with efficiency exceeding 27% enabled by ultrafast hot hole transfer with phthalocyanine derivatives. *Energy Environmental Science* **17**, 5080-5090 (2024).

38 Grotevent, M. J., Lu, Y., Šverko, T., Shih, M. C., Tan, S., Zhu, H., Dang, T., Mwaura, J. K., Swartwout, R. & Beiglböck, F. J. A. E. M. Additive‐Free Oxidized Spiro‐MeOTAD Hole Transport Layer Significantly Improves Thermal Solar Cell Stability. *Advanced Energy Materials*, 2400456 (2024).

39 Zhao, Y., Heumueller, T., Zhang, J., Luo, J., Kasian, O., Langner, S., Kupfer, C., Liu, B., Zhong, Y. & Elia, J. J. N. e. A bilayer conducting polymer structure for planar perovskite solar cells with over 1,400 hours operational stability at elevated temperatures. *Nature energy* **7**, 144-152 (2022).

40 An, Y., Perini, C. A. R., Hidalgo, J., Castro-Méndez, A.-F., Vagott, J. N., Li, R., Saidi, W. A., Wang, S., Li, X., Correa-Baena, J.-P. J. E. & Science, E. Identifying high-performance and durable methylammonium-free lead halide perovskites via high-throughput synthesis and characterization. *Energy Environmental Science* **14**, 6638-6654 (2021).

41 Baumeler, T., Arora, N., Hinderhofer, A., Akin, S., Greco, A., Abdi-Jalebi, M., Shivanna, R., Uchida, R., Liu, Y. & Schreiber, F. J. T. j. o. p. c. l. Minimizing the trade-off between photocurrent and photovoltage in triple-cation mixed-halide perovskite solar cells. *The journal of physical chemistry letters* **11**, 10188-10195 (2020).

42 Daboczi, M., Ratnasingham, S. R., Mohan, L., Pu, C., Hamilton, I., Chin, Y.-C., McLachlan, M. A. & Kim, J.-S. J. A. E. L. Optimal interfacial band bending achieved by fine energy level tuning in mixed-halide perovskite solar cells. *ACS Energy Letters* **6**, 3970-3981 (2021).

43 Lou, Q., Han, Y., Liu, C., Zheng, K., Zhang, J., Chen, X., Du, Q., Chen, C. & Ge, Z. J. A. E. M. π‐Conjugated Small Molecules Modified SnO2 Layer for Perovskite Solar Cells with over 23% Efficiency. *Advanced Energy Materials* **11**, 2101416 (2021).

44 Dai, Z., Yadavalli, S. K., Chen, M., Abbaspourtamijani, A., Qi, Y. & Padture, N. P. J. S. Interfacial toughening with self-assembled monolayers enhances perovskite solar cell reliability. *Science* **372**, 618-622 (2021).

45 Xu, T., Xiang, W., Yang, J., Kubicki, D. J., Tress, W., Chen, T., Fang, Z., Liu, Y. & Liu, S. J. A. M. Interface modification for efficient and stable inverted inorganic perovskite solar cells. *Advanced Materials* **35**, 2303346 (2023).

46 Yang, Q., Liu, X., Yu, S., Feng, Z., Liang, L., Qin, W., Wang, Y., Hu, X., Chen, S., Feng, Z. J. E. & Science, E. Hydroxylated non-fullerene acceptor for highly efficient inverted perovskite solar cells. *Energy Environmental Science* **14**, 6536-6545 (2021).
47 Chen, P., He, D., Huang, X., Zhang, C. & Wang, L. J. A. n. Bilayer 2D-3D Perovskite Heterostructures for Efficient and Stable Solar Cells. *ACS nano* **18**, 67-88 (2023).
48 Kim, E.-B., Akhtar, M. S., Shin, H.-S., Ameen, S., Nazeeruddin, M. K. J. J. o. P. & Reviews, P. C. P. A review on two-dimensional (2D) and 2D-3D multidimensional perovskite solar cells: Perovskites structures, stability, and photovoltaic performances. *Journal of Photochemistry Photobiology C: Photochemistry Reviews* **48**, 100405 (2021).
49 Li, X., Aftab, S., Abbas, A., Hussain, S., Aslam, M., Kabir, F., Abd-Rabboh, H. S., Hegazy, H., Xu, F. & Ansari, M. Z. J. N. E. Advances in mixed 2D and 3D perovskite heterostructure solar cells: a comprehensive review. *Nano Energy*, 108979 (2023).
50 Mahmud, M. A., Duong, T., Peng, J., Wu, Y., Shen, H., Walter, D., Nguyen, H. T., Mozaffari, N., Tabi, G. D. & Catchpole, K. R. J. A. F. M. Origin of efficiency and stability enhancement in high‐performing mixed dimensional 2D‐3D perovskite solar cells: a review. *Advanced Materials* **32**, 2009164 (2022).
51 Metcalf, I., Sidhik, S., Zhang, H., Agrawal, A., Persaud, J., Hou, J., Even, J. & Mohite, A. D. J. C. R. Synergy of 3D and 2D perovskites for durable, efficient solar cells and beyond. *Chemical Reviews* **123**, 9565-9652 (2023).
52 Wu, G., Liang, R., Ge, M., Sun, G., Zhang, Y. & Xing, G. J. A. M. Surface passivation using 2D perovskites toward efficient and stable perovskite solar cells. *Advanced Materials* **34**, 2105635 (2022).
53 Yu, D., Cao, F., Su, C. & Xing, G. J. A. o. C. R. Exploring, identifying, and removing the efficiency-limiting factor of mixed-dimensional 2D/3D perovskite solar cells. *Accounts of Chemical Research* **56**, 959-970 (2023).
54 Zhou, Q., Liu, B., Shai, X., Li, Y., He, P., Yu, H., Chen, C., Xu, Z.-X., Wei, D. & Chen, J. J. C. C. Precise modulation strategies of 2D/3D perovskite heterojunctions in efficient and stable solar cells. *Chemical Communications* **59**, 4128-4141 (2023).
55 Nazir, G., Lee, S. Y., Lee, J. H., Rehman, A., Lee, J. K., Seok, S. I. & Park, S. J. J. A. M. Stabilization of perovskite solar cells: recent developments and future perspectives. *Advanced Materials* **34**, 2204380 (2022).
56 Sharma, R., Sharma, A., Agarwal, S. & Dhaka, M. S. Stability and efficiency issues, solutions and advancements in perovskite solar cells: A review. *Solar Energy* **244**, 516-535 (2022).
57 Liang, Z., Zhang, Y., Xu, H., Chen, W., Liu, B., Zhang, J., Zhang, H., Wang, Z., Kang, D.-H., Zeng, J., Gao, X., Wang, Q., Hu, H., Zhou, H., Cai, X., Tian, X., Reiss, P., Xu, B., Kirchartz, T., Xiao, Z., Dai, S., Park, N.-G., Ye, J. & Pan, X. Homogenizing out-of-plane cation composition in perovskite solar cells. *Nature* **624**, 557-563 (2023).
58 Yang, G., Ren, Z., Liu, K., Qin, M., Deng, W., Zhang, H., Wang, H., Liang, J., Ye, F., Liang, Q., Yin, H., Chen, Y., Zhuang, Y., Li, S., Gao, B., Wang, J., Shi, T., Wang, X., Lu, X., Wu, H., Hou, J., Lei, D., So, S. K., Yang, Y., Fang, G. & Li, G. Stable and low-photovoltage-loss perovskite solar cells by multifunctional passivation. *Nature Photonics* **15**, 681-689 (2021).
59 Wang, S., Sakurai, T., Wen, W. & Qi, Y. Energy Level Alignment at Interfaces in Metal Halide Perovskite Solar Cells. *Advanced Materials Interfaces* **5**, 1800260 (2018).
60 Dong, L., Qiu, S., Cerrillo, J. G., Wagner, M., Kasian, O., Feroze, S., Jang, D., Li, C., Le Corre, V. M., Zhang, K. J. E. & Science, E. Fully printed flexible perovskite solar modules with improved energy alignment by tin oxide surface modification. *Energy Environmental Science* (2024).
61 Sun, Q., Meng, X., Liu, G., Duan, S., Hu, D., Shen, B., Kang, B. & Silva, S. R. P. J. A. F. M. SnO2 Surface Modification and Perovskite Buried Interface Passivation by 2, 5‐

Furandicarboxylic Acid for Flexible Perovskite Solar Cells. *Advanced Functional Materials*, 2404686 (2024).

62 Tong, X., Xie, L., Li, J., Pu, Z., Du, S., Yang, M., Gao, Y., He, M., Wu, S. & Mai, Y. J. A. M. Large Orientation Angle Buried Substrate Enables Efficient Flexible Perovskite Solar Cells and Modules. *Advanced Materials*, 2407032 (2024).

63 Chen, X., Cai, W., Niu, T., Wang, H., Liu, C., Zhang, Z., Du, Y., Cao, Y., Liu, P., Huang, W. J. E. & Science, E. Crystallization control via ligand-perovskite coordination for high-performance flexible perovskite solar cells. *Energy Environmental Science* (2024).

64 Tu, Y., Wu, J., Xu, G., Yang, X., Cai, R., Gong, Q., Zhu, R. & Huang, W. Perovskite Solar Cells for Space Applications: Progress and Challenges. *Advanced Materials* **33** (2021).

65 Bati, A. S., Zhong, Y. L., Burn, P. L., Nazeeruddin, M. K., Shaw, P. E. & Batmunkh, M. J. C. M. Next-generation applications for integrated perovskite solar cells. *Communications Materials* **4**, 2 (2023).

66 Chowdhury, T. A., Bin Zafar, M. A., Sajjad-Ul Islam, M., Shahinuzzaman, M., Islam, M. A. & Khandaker, M. U. Stability of perovskite solar cells: issues and prospects. *RSC Advances* **13**, 1787-1810 (2023).

67 Cheng, Y., Ding, L. J. E. & Science, E. Pushing commercialization of perovskite solar cells by improving their intrinsic stability. *Energy Environmental Science* **14**, 3233-3255 (2021).

68 Yang, Y., Liu, C., Mahata, A., Li, M., Roldán-Carmona, C., Ding, Y., Arain, Z., Xu, W., Yang, Y., Schouwink, P. A. J. E. & Science, E. Universal approach toward high-efficiency two-dimensional perovskite solar cells via a vertical-rotation process. *Energy Environmental Science* **13**, 3093-3101 (2020).

69 Lin, Y., Bai, Y., Fang, Y., Wang, Q., Deng, Y. & Huang, J. J. A. E. L. Suppressed ion migration in low-dimensional perovskites. *ACS Energy Letters* **2**, 1571-1572 (2017).

70 Mahmud, M. A., Duong, T., Peng, J., Wu, Y., Shen, H., Walter, D., Nguyen, H. T., Mozaffari, N., Tabi, G. D. & Catchpole, K. R. J. A. F. M. Origin of efficiency and stability enhancement in high‐performing mixed dimensional 2D‐3D perovskite solar cells: a review. *Advanced Functional Materials* **32**, 2009164 (2022).

71 Gharibzadeh, S., Abdollahi Nejand, B., Jakoby, M., Abzieher, T., Hauschild, D., Moghadamzadeh, S., Schwenzer, J. A., Brenner, P., Schmager, R. & Haghighirad, A. A. J. A. E. M. Record open‐circuit voltage wide‐bandgap perovskite solar cells utilizing 2D/3D perovskite heterostructure. *Advanced Energy Materials* **9**, 1803699 (2019).

72 Li, P., Zhang, Y., Liang, C., Xing, G., Liu, X., Li, F., Liu, X., Hu, X., Shao, G. & Song, Y. J. A. m. Phase pure 2D perovskite for high‐performance 2D–3D heterostructured perovskite solar cells. *Advanced materials* **30**, 1805323 (2018).

73 Grancini, G., Roldán-Carmona, C., Zimmermann, I., Mosconi, E., Lee, X., Martineau, D., Narbey, S., Oswald, F., De Angelis, F. & Graetzel, M. J. N. c. One-Year stable perovskite solar cells by 2D/3D interface engineering. *Nature communications* **8**, 15684 (2017).

74 Krishna, A., Gottis, S., Nazeeruddin, M. K. & Sauvage, F. J. A. F. M. Mixed dimensional 2D/3D hybrid perovskite absorbers: the future of perovskite solar cells? *Advanced Functional Materials* **29**, 1806482 (2019).

75 Dehghanipour, M., Behjat, A. & Bioki, H. A. J. J. o. M. C. C. Fabrication of stable and efficient 2D/3D perovskite solar cells through post-treatment with TBABF 4. *Journal of Materials Chemistry C* **9**, 957-966 (2021).

76 La-Placa, M.-G., Gil-Escrig, L., Guo, D., Palazon, F., Savenije, T. J., Sessolo, M. & Bolink, H. J. J. A. E. L. Vacuum-deposited 2D/3D perovskite heterojunctions. *ACS Energy Letters* **4**, 2893-2901 (2019).

77 Ma, C., Leng, C., Ji, Y., Wei, X., Sun, K., Tang, L., Yang, J., Luo, W., Li, C. & Deng, Y. J. N. 2D/3D perovskite hybrids as moisture-tolerant and efficient light absorbers for solar cells. *Nanoscale* **8**, 18309-18314 (2016).

78 Sutanto, A. A., Szostak, R., Drigo, N., Queloz, V. I., Marchezi, P., Germino, J., Tolentino, H. C., Nazeeruddin, M. K., Nogueira, A. F. & Grancini, G. J. N. l. In situ analysis reveals the role of 2D perovskite in preventing thermal-induced degradation in 2D/3D perovskite interfaces. *Nano letters* **20**, 3992-3998 (2020).

79 Yu, B. B., Chen, Z., Zhu, Y., Wang, Y., Han, B., Chen, G., Zhang, X., Du, Z. & He, Z. J. A. M. Heterogeneous 2D/3D tin - halides perovskite solar cells with certified conversion efficiency breaking 14%. *Advanced Materials* **33**, 2102055 (2021).

80 Zang, X., Xiong, S., Jiang, S., Li, D., Wu, H., Ren, H., Cao, A., Li, B., Ma, Z. & Chen, J. J. A. M. Passivating Dipole Layer Bridged 3D/2D Perovskite Heterojunction for Highly Efficient and Stable p - i - n Solar Cells. *Advanced Materials* **36**, 2309991 (2024).

81 Ding, S., Wang, Q., Gu, W., Tang, Z., Zhang, B., Wu, C., Zhang, X., Chen, H., Zhang, X. & Cao, R. J. N. P. Phase dimensions resolving of efficient and stable perovskite light-emitting diodes at high brightness. *Nature Photonics* **18**, 363-370 (2024).

82 Shi, E., Yuan, B., Shiring, S. B., Gao, Y., Akriti, Guo, Y., Su, C., Lai, M., Yang, P. & Kong, J. J. N. Two-dimensional halide perovskite lateral epitaxial heterostructures. *Nature* **580**, 614-620 (2020).

83 Blancon, J.-C., Even, J., Stoumpos, C. C., Kanatzidis, M. G. & Mohite, A. D. J. N. n. Semiconductor physics of organic–inorganic 2D halide perovskites. *Nature nanotechnology* **15**, 969-985 (2020).

84 Katan, C., Mercier, N. & Even, J. J. C. r. Quantum and dielectric confinement effects in lower-dimensional hybrid perovskite semiconductors. *Chemical reviews* **119**, 3140-3192 (2019).

85 Tanaka, K., Takahashi, T., Kondo, T., Umeda, K., Ema, K., Umebayashi, T., Asai, K., Uchida, K. & Miura, N. J. J. j. o. a. p. Electronic and excitonic structures of inorganic–organic perovskite-type quantum-well crystal (C4H9NH3) 2PbBr4. *Japanese journal of applied physics* **44**, 5923 (2005).

86 Blancon, J.-C., Stier, A. V., Tsai, H., Nie, W., Stoumpos, C. C., Traore, B., Pedesseau, L., Kepenekian, M., Katsutani, F. & Noe, G. J. N. c. Scaling law for excitons in 2D perovskite quantum wells. *Nature communications* **9**, 2254 (2018).

87 Filip, M. R., Eperon, G. E., Snaith, H. J. & Giustino, F. J. N. c. Steric engineering of metal-halide perovskites with tunable optical band gaps. *Nature communications* **5**, 5757 (2014).

88 Galkowski, K., Mitioglu, A., Miyata, A., Plochocka, P., Portugall, O., Eperon, G. E., Wang, J. T.-W., Stergiopoulos, T., Stranks, S. D., Snaith, H. J. J. E. & Science, E. Determination of the exciton binding energy and effective masses for methylammonium and formamidinium lead tri-halide perovskite semiconductors. *Energy Environmental Science* **9**, 962-970 (2016).

89 Spanopoulos, I., Hadar, I., Ke, W., Tu, Q., Chen, M., Tsai, H., He, Y., Shekhawat, G., Dravid, V. P. & Wasielewski, M. R. J. J. o. t. A. C. S. Uniaxial expansion of the 2D Ruddlesden–Popper perovskite family for improved environmental stability. *Journal of the American Chemical Society* **141**, 5518-5534 (2019).

90 Kinigstein, E. D., Tsai, H., Nie, W., Blancon, J.-C., Yager, K. G., Appavoo, K., Even, J., Kanatzidis, M. G., Mohite, A. D. & Sfeir, M. Y. J. A. M. L. Edge states drive exciton dissociation in ruddlesden–popper lead halide perovskite thin films. *ACS Materials Letters* **2**, 1360-1367 (2020).

91 Seitz, M., Magdaleno, A. J., Alcázar-Cano, N., Meléndez, M., Lubbers, T. J., Walraven, S. W., Pakdel, S., Prada, E., Delgado-Buscalioni, R. & Prins, F. J. N. c. Exciton diffusion in two-dimensional metal-halide perovskites. *Nature communications* **11**, 2035 (2020).

92 Wang, X., Rakstys, K., Jack, K., Jin, H., Lai, J., Li, H., Ranasinghe, C. S. K., Saghaei, J., Zhang, G. & Burn, P. L. J. N. c. Engineering fluorinated-cation containing inverted perovskite solar cells with an efficiency of> 21% and improved stability towards humidity. *Nature communications* **12**, 52 (2021).

93 Xing, J., Zhao, Y., Askerka, M., Quan, L. N., Gong, X., Zhao, W., Zhao, J., Tan, H., Long, G. & Gao, L. J. N. c. Color-stable highly luminescent sky-blue perovskite light-emitting diodes. *Nature communications* **9**, 3541 (2018).

94 Hu, Y., Schlipf, J., Wussler, M., Petrus, M. L., Jaegermann, W., Bein, T., Müller-Buschbaum, P. & Docampo, P. J. A. n. Hybrid perovskite/perovskite heterojunction solar cells. *ACS nano* **10**, 5999-6007 (2016).

95 Teale, S., Proppe, A. H., Jung, E. H., Johnston, A., Parmar, D. H., Chen, B., Hou, Y., Kelley, S. O. & Sargent, E. H. J. T. J. o. P. C. L. Dimensional mixing increases the efficiency of 2D/3D perovskite solar cells. *The Journal of Physical Chemistry Letters* **11**, 5115-5119 (2020).

96 Proppe, A. H., Johnston, A., Teale, S., Mahata, A., Quintero-Bermudez, R., Jung, E. H., Grater, L., Cui, T., Filleter, T. & Kim, C.-Y. J. N. c. Multication perovskite 2D/3D interfaces form via progressive dimensional reduction. *Nature communications* **12**, 3472 (2021).

97 Zhang, T., Long, M., Qin, M., Lu, X., Chen, S., Xie, F., Gong, L., Chen, J., Chu, M. & Miao, Q. J. J. Stable and efficient 3D-2D perovskite-perovskite planar heterojunction solar cell without organic hole transport layer. *Joule* **2**, 2706-2721 (2018).

98 Yoo, J. J., Wieghold, S., Sponseller, M. C., Chua, M. R., Bertram, S. N., Hartono, N. T. P., Tresback, J. S., Hansen, E. C., Correa-Baena, J.-P., Bulović, V. J. E. & Science, E. An interface stabilized perovskite solar cell with high stabilized efficiency and low voltage loss. *Energy Environmental Science* **12**, 2192-2199 (2019).

99 Mahmud, M. A., Duong, T., Yin, Y., Pham, H. T., Walter, D., Peng, J., Wu, Y., Li, L., Shen, H. & Wu, N. J. A. F. M. Double‑sided surface passivation of 3D perovskite film for high‑efficiency mixed‑dimensional perovskite solar cells. *Advanced Functional Materials* **30**, 1907962 (2020).

100 Chen, H., Teale, S., Chen, B., Hou, Y., Grater, L., Zhu, T., Bertens, K., Park, S. M., Atapattu, H. R. & Gao, Y. J. N. P. Quantum-size-tuned heterostructures enable efficient and stable inverted perovskite solar cells. *Nature Photonics* **16**, 352-358 (2022).

101 Wang, Z., Wang, F., Sun, W., Ni, R., Hu, S., Liu, J., Zhang, B., Alsaed, A., Hayat, T. & Tan, Z. a. J. A. F. M. Manipulating the trade‑off between quantum yield and electrical conductivity for high‑brightness quasi‑2D perovskite light‑emitting diodes. *Advanced Functional Materials* **28**, 1804187 (2018).

102 Ortiz‑Cervantes, C., Román‑Román, P. I., Vazquez‑Chavez, J., Hernández‑Rodríguez, M. & Solis‑Ibarra, D. J. A. C. Thousand‑fold Conductivity Increase in 2D Perovskites by Polydiacetylene Incorporation and Doping. *Angewandte Chemie* **130**, 14078-14082 (2018).

103 Lin, D., Zhang, T., Wang, J., Long, M., Xie, F., Chen, J., Wu, B., Shi, T., Yan, K. & Xie, W. J. N. E. Stable and scalable 3D-2D planar heterojunction perovskite solar cells via vapor deposition. *Nano Energy* **59**, 619-625 (2019).

104 Gong, C., Chen, X., Zeng, J., Wang, H., Li, H., Qian, Q., Zhang, C., Zhuang, Q., Yu, X. & Gong, S. J. A. M. Functional‑Group‑Induced Single Quantum Well Dion–Jacobson 2D Perovskite for Efficient and Stable Inverted Perovskite Solar Cells. *Advanced Materials* **36**, 2307422 (2024).

105 La-Placa, M.-G., Gil-Escrig, L., Guo, D., Palazon, F., Savenije, T. J., Sessolo, M. & Bolink, H. J. J. A. E. L. Vacuum-deposited 2D/3D perovskite heterojunctions. *ACS Energy Letters* **4**, 2893-2901 (2019).

106 Jung, E. H., Jeon, N. J., Park, E. Y., Moon, C. S., Shin, T. J., Yang, T.-Y., Noh, J. H. & Seo, J. J. N. Efficient, stable and scalable perovskite solar cells using poly (3-hexylthiophene). *Nature* **567**, 511-515 (2019).

107 Song, Z., Gao, Y., Zou, Y., Zhang, H., Wang, R., Chen, Y., Chen, Y. & Liu, Y. J. J. o. t. A. C. S. Single-Crystal-Assisted In Situ Phase Reconstruction Enables Efficient and Stable 2D/3D Perovskite Solar Cells. *Journal of the American Chemical Society* **146**, 1657-1666 (2024).

108 Almora, O., Aranda, C., Mas-Marzá, E. & Garcia-Belmonte, G. J. A. P. L. On Mott-Schottky analysis interpretation of capacitance measurements in organometal perovskite solar cells. *Applied Physics Letters* **109** (2016).

109 Zhang, X., Ren, X., Liu, B., Munir, R., Zhu, X., Yang, D., Li, J., Liu, Y., Smilgies, D.-M., Li, R. J. E. & Science, E. Stable high efficiency two-dimensional perovskite solar cells via cesium doping. *Energy Environmental Science* **10**, 2095-2102 (2017).

110 Shi, D., Adinolfi, V., Comin, R., Yuan, M., Alarousu, E., Buin, A., Chen, Y., Hoogland, S., Rothenberger, A. & Katsiev, K. J. S. Low trap-state density and long carrier diffusion in organolead trihalide perovskite single crystals. *Science* **347**, 519-522 (2015).

111 Chen, J., Kim, S. G. & Park, N. G. J. A. M. FA0. 88Cs0. 12PbI3− x (PF6) x interlayer formed by ion exchange reaction between perovskite and hole transporting layer for improving photovoltaic performance and stability. *Advanced Materials* **30**, 1801948 (2018).

112 Liu, Y., Akin, S., Pan, L., Uchida, R., Arora, N., Milić, J. V., Hinderhofer, A., Schreiber, F., Uhl, A. R. & Zakeeruddin, S. M. J. S. a. Ultrahydrophobic 3D/2D fluoroarene bilayer-based water-resistant perovskite solar cells with efficiencies exceeding 22%. *Science advances* **5**, eaaw2543 (2019).

113 Zhao, R., Sabatini, R. P., Zhu, T., Wang, S., Morteza Najjarian, A., Johnston, A., Lough, A. J., Hoogland, S., Sargent, E. H. & Seferos, D. S. J. J. o. t. A. c. s. Rigid conjugated diamine templates for stable Dion–Jacobson-type two-dimensional perovskites. *Journal of the American chemical society* **143**, 19901-19908 (2021).

114 Wang, S., Zhu, Y., Wang, C. & Ma, R. J. J. o. M. C. A. Interface modification by a multifunctional ammonium salt for high performance and stable planar perovskite solar cells. *Journal of Materials Chemistry A* **7**, 11867-11876 (2019).

115 Zhu, H., Liu, Y., Eickemeyer, F. T., Pan, L., Ren, D., Ruiz ‐ Preciado, M. A., Carlsen, B., Yang, B., Dong, X. & Wang, Z. J. A. M. Tailored amphiphilic molecular mitigators for stable perovskite solar cells with 23.5% efficiency. *Advanced Materials* **32**, 1907757 (2020).

116 Akin, S., Dong, B., Pfeifer, L., Liu, Y., Graetzel, M. & Hagfeldt, A. J. A. S. Organic ammonium halide modulators as effective strategy for enhanced perovskite photovoltaic performance. *Advanced Science* **8**, 2004593 (2021).

117 Min, H., Kim, M., Lee, S.-U., Kim, H., Kim, G., Choi, K., Lee, J. H. & Seok, S. I. J. S. Efficient, stable solar cells by using inherent bandgap of α-phase formamidinium lead iodide. *Science* **366**, 749-753 (2019).

118 Wang, R., Xue, J., Wang, K.-L., Wang, Z.-K., Luo, Y., Fenning, D., Xu, G., Nuryyeva, S., Huang, T. & Zhao, Y. J. S. Constructive molecular configurations for surface-defect passivation of perovskite photovoltaics. *Science* **366**, 1509-1513 (2019).

119 Quan, L. N., Yuan, M., Comin, R., Voznyy, O., Beauregard, E. M., Hoogland, S., Buin, A., Kirmani, A. R., Zhao, K. & Amassian, A. J. J. o. t. A. C. S. Ligand-stabilized reduced-dimensionality perovskites. *Journal of the American Chemical Society* **138**, 2649-2655 (2016).

120 Dong, Q., Fang, Y., Shao, Y., Mulligan, P., Qiu, J., Cao, L. & Huang, J. J. S. Electron-hole diffusion lengths> 175 μm in solution-grown CH3NH3PbI3 single crystals. *Science* **347**, 967-970 (2015).

121 Zhu, W., Wang, S., Zhang, X., Wang, A., Wu, C. & Hao, F. J. S. Ion migration in organic–inorganic hybrid perovskite solar cells: current understanding and perspectives. *Small* **18**, 2105783 (2022).

122 Li, Z., Xiao, C., Yang, Y., Harvey, S. P., Kim, D. H., Christians, J. A., Yang, M., Schulz, P., Nanayakkara, S. U., Jiang, C.-S. J. E. & Science, E. Extrinsic ion migration in perovskite solar cells. *Energy Environmental Science* **10**, 1234-1242 (2017).

123 Horn, J., Scholz, M., Oum, K., Lenzer, T. & Schlettwein, D. J. A. M. Influence of phenylethylammonium iodide as additive in the formamidinium tin iodide perovskite on interfacial characteristics and charge carrier dynamics. *APL Materials* **7** (2019).

124 Kang, Y., Li, R., Shen, X., Jin, B., Zhan, Y., Wang, A., Li, B., Song, Y., Xiao, G. & Dong, Q. J. N. E. Stability-enhanced perovskite heterointerfaces and solar cells via strongly anchored and sterically hindered ligands. *Nano Energy* **120**, 109178 (2024).

125 Jiang, N., Zhang, H.-W., Liu, Y.-F., Wang, Y.-F., Yin, D. & Feng, J. J. N. L. Transfer-imprinting-assisted growth of 2D/3D perovskite heterojunction for efficient and stable flexible inverted perovskite solar cells. *Nano Letters* **23**, 6116-6123 (2023).

126 Chang, X., Zhong, J. X., Li, S., Yao, Q., Fang, Y., Yang, G., Tan, Y., Xue, Q., Qiu, L. & Wang, Q. J. A. C. I. E. Two - Second - Annealed 2D/3D Perovskite Films with Graded Energy Funnels and Toughened Heterointerfaces for Efficient and Durable Solar Cells. *Angewandte Chemie International Edition* **62**, e202309292 (2023).

127 Chen, X., Deng, C., Wu, J., Chen, Q., Du, Y., Xu, Y., Li, R., Tan, L., Wei, Y. & Huang, Y. J. A. F. M. Supramolecular Aza Crown Ether Modulator for Efficient and Stable Perovskite Solar Cells. *Advanced Functional Materials* **34**, 2311527 (2024).

128 Wu, L., Li, G., Prashanthan, K., Musiienko, A., Li, J., Gries, T. W., Zhang, H., Köbler, H., Janasik, P. & Appiah, A. N. J. A. M. Stabilization of Inorganic Perovskite Solar Cells with a 2D Dion–Jacobson Passivating Layer. *Advanced Materials* **35**, 2304150 (2023).

129 Hou, Y., Wu, H., Yoon, J., Zheng, L., Yang, D., Ye, T., Wang, K., Wang, K. & Priya, S. J. A. E. M. Self - Assembly of 0D/3D Perovskite Bi - Layer from a Micro - Emulsion Ink. *Advanced Energy Materials* **13**, 2300570 (2023).

130 Yang, B., Dyck, O., Ming, W., Du, M.-H., Das, S., Rouleau, C. M., Duscher, G., Geohegan, D. B., Xiao, K. J. A. a. m. & interfaces. Observation of nanoscale morphological and structural degradation in perovskite solar cells by in situ TEM. *ACS applied materials* **8**, 32333-32340 (2016).

131 Li, G., Zhang, H. & Han, Y. J. C. R. Applications of Transmission Electron Microscopy in Phase Engineering of Nanomaterials. *Chemical Reviews* **123**, 10728-10749 (2023).

132 Guo, S., Zhang, X., Hao, M., Duan, T., Wang, W., Li, Z., Liu, G., Cai, S. & Zhou, Y. Liquid - Phase Transfer of Organic - Inorganic Halide Perovskite Films for TEM Investigation and Planar Heterojunction Fabrication. *Advanced Optical Materials* **12** (2023).

133 Bustillo, K. C., Zeltmann, S. E., Chen, M., Donohue, J., Ciston, J., Ophus, C. & Minor, A. M. J. A. o. c. r. 4D-STEM of beam-sensitive materials. *Accounts of chemical research* **54**, 2543-2551 (2021).

134 Ophus, C., Ercius, P., Sarahan, M., Czarnik, C., Ciston, J. J. M. & Microanalysis. Recording and using 4D-STEM datasets in materials science. *Microscopy Microanalysis* **20**, 62-63 (2014).

135 Ophus, C. J. M. & Microanalysis. Four-dimensional scanning transmission electron microscopy (4D-STEM): From scanning nanodiffraction to ptychography and beyond. *Microscopy Microanalysis* **25**, 563-582 (2019).

136 Ciston, J., Johnson, I. J., Draney, B. R., Ercius, P., Fong, E., Goldschmidt, A., Joseph, J. M., Lee, J. R., Mueller, A., Ophus, C. J. M. & Microanalysis. The 4D camera: Very high speed electron counting for 4D-STEM. *Microscopy Microanalysis* **25**, 1930-1931 (2019).

137 Roccapriore, K. M., Dyck, O., Oxley, M. P., Ziatdinov, M. & Kalinin, S. V. J. A. n. Automated experiment in 4D-STEM: exploring emergent physics and structural behaviors. *ACS nano* **16**, 7605-7614 (2022).

138 Yang, H., Jones, L., Ryll, H., Simson, M., Soltau, H., Kondo, Y., Sagawa, R., Banba, H., MacLaren, I. & Nellist, P. in *Journal of Physics: Conference Series.* 012032 (IOP Publishing).

139 Zeltmann, S. E., Müller, A., Bustillo, K. C., Savitzky, B., Hughes, L., Minor, A. M. & Ophus, C. J. U. Patterned probes for high precision 4D-STEM bragg measurements. *Ultramicroscopy* **209**, 112890 (2020).

140 Mu, X., Mazilkin, A., Sprau, C., Colsmann, A. & Kübel, C. J. M. Mapping structure and morphology of amorphous organic thin films by 4D-STEM pair distribution function analysis. *Microscopy* **68**, 301-309 (2019).

141 Rothmann, M. U., Kim, J. S., Borchert, J., Lohmann, K. B., O'Leary, C. M., Sheader, A. A., Clark, L., Snaith, H. J., Johnston, M. B. & Nellist, P. D. J. S. Atomic-scale microstructure of metal halide perovskite. *Science* **370**, eabb5940 (2020).

142 Yang, C. Q., Zhi, R., Rothmann, M. U., Xu, Y. Y., Li, L. Q., Hu, Z. Y., Pang, S., Cheng, Y. B., Van Tendeloo, G. & Li, W. J. A. M. Unveiling the intrinsic structure and intragrain defects of organic–inorganic hybrid perovskites by ultralow dose transmission electron microscopy. *Advanced Materials* **35**, 2211207 (2023).

143 Li, Y., Lu, Y., Huo, X., Wei, D., Meng, J., Dong, J., Qiao, B., Zhao, S., Xu, Z. & Song, D. J. R. a. Bandgap tuning strategy by cations and halide ions of lead halide perovskites learned from machine learning. *RSC advances* **11**, 15688-15694 (2021).

144 Unger, E., Kegelmann, L., Suchan, K., Sörell, D., Korte, L. & Albrecht, S. J. J. o. M. C. A. Roadmap and roadblocks for the band gap tunability of metal halide perovskites. *Journal of Materials Chemistry A* **5**, 11401-11409 (2017).

145 Al-Qaisi, S., Mahmood, Q., Kattan, N. A., Alhassan, S., Alshahrani, T., Sfina, N., Brini, S., Hakamy, A., Mera, A., Amin, M. A. J. J. o. P. & Solids, C. o. Tuning of band gap by variation of halide ions in K2CuSbX6 (X= Cl, Br, I) for solar cells and thermoelectric applications. *Journal of Physics Chemistry of Solids* **174**, 111184 (2023).

146 Kulkarni, S. A., Baikie, T., Boix, P. P., Yantara, N., Mathews, N. & Mhaisalkar, S. J. J. o. M. C. A. Band-gap tuning of lead halide perovskites using a sequential deposition process. *Journal of Materials Chemistry A* **2**, 9221-9225 (2014).

147 Choe, H., Jeon, D., Lee, S. J. & Cho, J. J. A. o. Mixed or segregated: Toward efficient and stable mixed halide perovskite-based devices. *ACS omega* **6**, 24304-24315 (2021).

148 Dasog, M. & Scott, R. W. J. L. Understanding the oxidative stability of gold monolayer-protected clusters in the presence of halide ions under ambient conditions. *Langmuir* **23**, 3381-3387 (2007).

149 Yang, J.-N., Wang, J.-J., Yin, Y.-C. & Yao, H.-B. J. C. S. R. Mitigating halide ion migration by resurfacing lead halide perovskite nanocrystals for stable light-emitting diodes. *Chemical Society Reviews* (2023).

150 Yuan, Y. & Huang, J. J. A. o. c. r. Ion migration in organometal trihalide perovskite and its impact on photovoltaic efficiency and stability. *Accounts of chemical research* **49**, 286-293 (2016).

151 Yoon, S. J., Kuno, M. & Kamat, P. V. J. A. E. L. Shift happens. How halide ion defects influence photoinduced segregation in mixed halide perovskites. *ACS Energy Letters* **2**, 1507-1514 (2017).

152 Futscher, M. H. & Deibel, C. J. A. E. L. Defect spectroscopy in halide perovskites is dominated by ionic rather than electronic defects. *ACS Energy Letters* **7**, 140-144 (2021).

153 Yuan, C., He, M., Liao, X., Liu, M., Zhang, Q., Wan, Q., Qu, Z., Kong, L. & Li, L. J. C. S. Interface defects repair of core/shell quantum dots through halide ion penetration. *Chemical Science* **14**, 13119-13125 (2023).

154 Ono, L. K., Liu, S. & Qi, Y. J. A. C. I. E. Reducing detrimental defects for high‐performance metal halide perovskite solar cells. *Angewandte Chemie International Edition* **59**, 6676-6698 (2020).

155 Wang, J., Shen, H., Li, W., Wang, S., Li, J. & Li, D. J. A. S. The Role of Chloride Incorporation in Lead‐Free 2D Perovskite (BA) 2SnI4: Morphology, Photoluminescence, Phase Transition, and Charge Transport. *Advanced Science* **6**, 1802019 (2019).

156 Garcia-Fernandez, A., Bermúdez-García, J. M., Castro-Garcia, S., Llamas-Saiz, A. L., Artiaga, R., López-Beceiro, J. J., Sánchez-Andújar, M. & Señarís-Rodríguez, M. A. J. I. C. [(CH3) 2NH2] 7Pb4X15 (X= Cl–and Br–), 2D-perovskite related hybrids with dielectric transitions and broadband photoluminiscent emission. *Inorganic Chemistry* **57**, 3215-3222 (2018).

157 Yang, L., Jin, Y., Fang, Z., Zhang, J., Nan, Z., Zheng, L., Zhuang, H., Zeng, Q., Liu, K. & Deng, B. J. N.-M. L. Efficient semi-transparent wide-bandgap perovskite solar cells enabled by pure-chloride 2D-perovskite passivation. *Nano-Micro Letters* **15**, 111 (2023).

158 Mao, L., Wu, Y., Stoumpos, C. C., Traore, B., Katan, C., Even, J., Wasielewski, M. R. & Kanatzidis, M. G. J. J. o. t. A. C. S. Tunable White-Light Emission in Single-Cation-Templated Three-Layered 2D Perovskites (CH3CH2NH3) 4Pb3Br10–x Cl x. *Journal of the American Chemical Society* **139**, 11956-11963 (2017).

159 Li, X., Guo, P., Kepenekian, M., Hadar, I., Katan, C., Even, J., Stoumpos, C. C., Schaller, R. D. & Kanatzidis, M. G. J. C. o. M. Small cyclic diammonium cation templated (110)-oriented 2D halide (X= I, Br, Cl) perovskites with white-light emission. *Chemistry of Materials* **31**, 3582-3590 (2019).

160 Chen, B., Liu, Z., Meng, K., Qiao, Z., Zhai, Y., Yu, R., Wu, L., Xiao, M., Pan, L. & Zheng, L. J. N. L. In Situ Observing and Tuning the Crystal Orientation of Two-Dimensional Layered Perovskite via the Chlorine Additive. *Nano Letters* **22**, 7826-7833 (2022).

161 Kamat, P. V. & Kuno, M. J. A. o. C. R. Halide ion migration in perovskite nanocrystals and nanostructures. *Accounts of Chemical Research* **54**, 520-531 (2021).

162 Aamir, M., Shahiduzzaman, M., Taima, T., Akhtar, J. & Nunzi, J. M. J. A. O. M. It is an All‐Rounder! On the Development of Metal Halide Perovskite‐Based Fluorescent Sensors and Radiation Detectors. *Advanced Optical Materials* **9**, 2101276 (2021).

163 Chen, J., Shao, J., Sun, R., Zhang, W., Huang, Y., Zheng, J. & Chi, Y. J. A. C. Anion exchanges of water-stable perovskite nanocrystals in the pure water phase and applications in detecting halide ions via a smartphone-based sensing platform. *Analytical Chemistry* **95**, 11839-11848 (2023).

164 Zhao, J., Pan, G., Zhu, Y., Liu, K., You, W., Chen, X., Song, H., Mao, Y. J. A. A. M. & Interfaces. High-efficiency and wavelength-tunable near-infrared emission of lanthanide ions doped lead-free halide double perovskite nanocrystals toward fluorescence imaging. *ACS Applied Materials Interfaces* **14**, 42215-42222 (2022).

165 Jiang, Y., Wei, K., Sun, C., Feng, Y., Zhang, L., Cui, M., Li, S., Li, W. D., Kim, J. T. & Qin, C. J. A. M. Unraveling Size‐Dependent Ion‐Migration for Stable Mixed‐Halide Perovskite Light‐Emitting Diodes. *Advanced Materials* **35**, 2304094 (2023).

166 Yue, X., Zhao, X., Fan, B., Yang, Y., Yan, L., Qu, S., Huang, H., Zhang, Q., Yan, H. & Cui, P. J. A. F. M. Surface regulation through dipolar molecule boosting the efficiency of mixed 2d/3d perovskite solar cell to 24%. *Advanced Functional Materials* **33**, 2209921 (2023).

167 Uzurano, G., Kuwahara, N., Saito, T., Fujii, A. & Ozaki, M. J. A. M. L. Orientation control of 2D perovskite in 2D/3D heterostructure by templated growth on 3D perovskite. *ACS Materials Letters* **4**, 378-384 (2022).

168 Chen, P., Bai, Y., Wang, S., Lyu, M., Yun, J. H. & Wang, L. J. A. F. M. In situ growth of 2D perovskite capping layer for stable and efficient perovskite solar cells. *Advanced Functional Materials* **28**, 1706923 (2018).

169 Zhang, C., Wang, S., Li, X., Yuan, M., Turyanska, L. & Yang, X. J. A. F. M. Core/shell perovskite nanocrystals: synthesis of highly efficient and environmentally stable FAPbBr3/CsPbBr3 for LED applications. *Advanced Functional Materials* **30**, 1910582 (2020).

170 Zhao, H., Chen, H., Bai, S., Kuang, C., Luo, X., Teng, P., Yin, C., Zeng, P., Hou, L. & Yang, Y. J. A. E. L. High-brightness perovskite light-emitting diodes based on FAPbBr3 nanocrystals with rationally designed aromatic ligands. *ACS Energy Letters* **6**, 2395-2403 (2021).

171 Han, D., Imran, M., Zhang, M., Chang, S., Wu, X.-g., Zhang, X., Tang, J., Wang, M., Ali, S. & Li, X. J. A. n. Efficient light-emitting diodes based on in situ fabricated FAPbBr3 nanocrystals: the enhancing role of the ligand-assisted reprecipitation process. *ACS nano* **12**, 8808-8816 (2018).

172 Kim, Y.-H., Lee, G.-H., Kim, Y.-T., Wolf, C., Yun, H. J., Kwon, W., Park, C. G. & Lee, T.-W. J. N. E. High efficiency perovskite light-emitting diodes of ligand-engineered colloidal formamidinium lead bromide nanoparticles. *Nano Energy* **38**, 51-58 (2017).

173 Zhao, L., Lee, K. M., Roh, K., Khan, S. U. Z. & Rand, B. P. J. A. M. Improved outcoupling efficiency and stability of perovskite light - emitting diodes using thin emitting layers. *Advanced Materials* **31**, 1805836 (2019).

174 Chen, H., Chen, Y., Zhang, T., Liu, X., Wang, X. & Zhao, Y. J. S. S. Advances to high - performance black - phase FAPbI3 perovskite for efficient and stable photovoltaics. *Small Structures* **2**, 2000130 (2021).

175 Pratheek, M., Sujith, P., Hameed, T. S. & Predeep, P. J. M. L. Effect of bromide doping on the phase stability and shelf life of the triple cation mixed halide perovskite single-crystals. *Materials Letters* **326**, 132903 (2022).

176 Li, G., Song, J., Wu, J., Song, Z., Wang, X., Sun, W., Fan, L., Lin, J., Huang, M. & Lan, Z. J. A. E. L. Efficient and stable 2D@ 3D/2D perovskite solar cells based on dual optimization of grain boundary and interface. *ACS Energy Letters* **6**, 3614-3623 (2021).

177 Kim, E.-B., Akhtar, M. S., Ameen, S., Umar, A., Qasem, H., Rubahn, H.-G., Shkir, M., Kaushik, A. & Mishra, Y. K. J. N. E. Improving the performance of 2D perovskite solar cells by carrier trappings and minifying the grain boundaries. *Nano Energy* **102**, 107673 (2022).

178 Yan, Y., Wang, R., Dong, Q., Yin, Y., Zhang, L., Su, Z., Wang, C., Feng, J., Wang, M., Liu, J. J. E. & Science, E. Polarity and moisture induced trans-grain-boundaries 2D/3D coupling structure for flexible perovskite solar cells with high mechanical reliability and efficiency. *Energy Environmental Science* **15**, 5168-5180 (2022).

179 Zhou, T., Xu, Z., Wang, R., Dong, X., Fu, Q. & Liu, Y. J. A. M. Crystal growth regulation of 2D/3D perovskite films for solar cells with both high efficiency and stability. *Advanced Materials* **34**, 2200705 (2022).

180 Chen, S., Deng, Y., Gu, H., Xu, S., Wang, S., Yu, Z., Blum, V. & Huang, J. Trapping lead in perovskite solar modules with abundant and low-cost cation-exchange resins. *Nature Energy* **5**, 1003-1011 (2020).

181 Čulík, P., Brooks, K., Momblona, C., Adams, M., Kinge, S., Maréchal, F., Dyson, P. J. & Nazeeruddin, M. K. Design and Cost Analysis of 100 MW Perovskite Solar Panel Manufacturing Process in Different Locations. *ACS Energy Letters* **7**, 3039-3044 (2022).

182 Tan, Q., Li, Z., Luo, G., Zhang, X., Che, B., Chen, G., Gao, H., He, D., Ma, G., Wang, J., Xiu, J., Yi, H., Chen, T. & He, Z. Inverted perovskite solar cells using dimethylacridine-based dopants. *Science* **620**, 545-551 (2023).

183 Ye, F., Zhang, S., Warby, J., Wu, J., Gutierrez-Partida, E., Lang, F., Shah, S., Saglamkaya, E., Sun, B. & Zu, F. J. N. C. Overcoming C60-induced interfacial recombination in inverted perovskite solar cells by electron-transporting carborane. *Nature Communications* **13**, 7454 (2022).

184 Chen, J., Luo, J., Hou, E., Song, P., Li, Y., Sun, C., Feng, W., Cheng, S., Zhang, H. & Xie, L. J. N. P. Efficient tin-based perovskite solar cells with trans-isomeric fulleropyrrolidine additives. *Nature Photonics* **18**, 464-470 (2024).

185 Li, Z., Sun, X., Zheng, X., Li, B., Gao, D., Zhang, S., Wu, X., Li, S., Gong, J., Luther, J. M., Li, Z. a. & Zhu, Z. Stabilized hole-selective layer for high-performance inverted p-i-n perovskite solar cells. *Science* **382**, 284-289 (2023).

186 Zhong, Y., Liu, G., Su, Y., Sheng, W., Gong, L., Zhang, J., Tan, L. & Chen, Y. Diammonium Molecular Configuration - Induced Regulation of Crystal Orientation and Carrier Dynamics for Highly Efficient and Stable 2D/3D Perovskite Solar Cells. *Angewandte Chemie International Edition* **61** (2021).

187 Yang, T., Ma, C., Cai, W., Wang, S., Wu, Y., Feng, J., Wu, N., Li, H., Huang, W., Ding, Z., Gao, L., Liu, S. & Zhao, K. Amidino-based Dion-Jacobson 2D perovskite for efficient and stable 2D/3D heterostructure perovskite solar cells. *Joule* **7**, 574-586 (2023).

188 Chen, H., Teale, S., Chen, B., Hou, Y., Grater, L., Zhu, T., Bertens, K., Park, S. M., Atapattu, H. R., Gao, Y., Wei, M., Johnston, A. K., Zhou, Q., Xu, K., Yu, D., Han, C., Cui, T., Jung, E. H., Zhou, C., Zhou, W., Proppe, A. H., Hoogland, S., Laquai, F., Filleter, T., Graham, K. R., Ning, Z. & Sargent, E. H. Quantum-size-tuned heterostructures enable efficient and stable inverted perovskite solar cells. *Nature Photonics* **16**, 352-358 (2022).

189 Cai, S., Li, Z., Zhang, Y., Liu, T., Wang, P., Ju, M.-G., Pang, S., Lau, S. P., Zeng, X. C. & Zhou, Y. Intragrain impurity annihilation for highly efficient and stable perovskite solar cells. *Nature Communications* **15**, 2329 (2024).

190 deQuilettes, D. W., Yoo, J. J., Brenes, R., Kosasih, F. U., Laitz, M., Dou, B. D., Graham, D. J., Ho, K., Shi, Y., Shin, S. S., Ducati, C., Bawendi, M. G. & Bulović, V. Reduced recombination via tunable surface fields in perovskite thin films. *Nature Energy* **9**, 457-466 (2024).

191 Li, H., Zhang, C., Gong, C., Zhang, D., Zhang, H., Zhuang, Q., Yu, X., Gong, S., Chen, X., Yang, J., Li, X., Li, R., Li, J., Zhou, J., Yang, H., Lin, Q., Chu, J., Grätzel, M., Chen, J. & Zang, Z. 2D/3D heterojunction engineering at the buried interface towards high-performance inverted methylammonium-free perovskite solar cells. *Nature Energy* **8**, 946-955 (2023).

192 Chen, J., Quan, X., Lu, M., Niu, Y. & Zhang, B. J. U. Quantitative Analysis Method for Nitrogen Electron Energy-Loss Near-Edge Structures in Nanocarbons Based on Density Functional Theory Calculations and Linear Regression. *Ultramicroscopy* **215**, 113006 (2020).

193 Yan, L., Huang, H., Cui, P., Du, S., Lan, Z., Yang, Y., Qu, S., Wang, X., Zhang, Q., Liu, B., Yue, X., Zhao, X., Li, Y., Li, H., Ji, J. & Li, M. Fabrication of perovskite solar cells in ambient air by blocking perovskite hydration with guanabenz acetate salt. *Nature Energy* **8**, 1158-1167 (2023).

194 Hao, M., Duan, T., Ma, Z., Ju, M. G., Bennett, J. A., Liu, T., Guo, P. & Zhou, Y. Flattening Grain ‐ Boundary Grooves for Perovskite Solar Cells with High Optomechanical Reliability. *Advanced Materials* **35**, 2211155 (2023).

195 Suo, J., Yang, B., Mosconi, E., Bogachuk, D., Doherty, T. A. S., Frohna, K., Kubicki, D. J., Fu, F., Kim, Y., Er-Raji, O., Zhang, T., Baldinelli, L., Wagner, L., Tiwari, A. N., Gao, F., Hinsch, A., Stranks, S. D., De Angelis, F. & Hagfeldt, A. Multifunctional sulfonium-based treatment for perovskite solar cells with less than 1% efficiency loss over 4,500-h operational stability tests. *Nature Energy* **9**, 172-183 (2024).

196 Ghasemi, M., Guo, B., Darabi, K., Wang, T., Wang, K., Huang, C.-W., Lefler, B. M., Taussig, L., Chauhan, M., Baucom, G., Kim, T., Gomez, E. D., Atkin, J. M., Priya, S. & Amassian, A. A multiscale ion diffusion framework sheds light on the diffusion–stability–hysteresis nexus in metal halide perovskites. *Nature Materials* **22**, 329-337 (2023).

197 You, S., Zeng, H., Liu, Y., Han, B., Li, M., Li, L., Zheng, X., Guo, R., Luo, L. & Li, Z. J. S. Radical polymeric p-doping and grain modulation for stable, efficient perovskite solar modules. *Science* **379**, 288-294 (2023).

198 Doherty, T. A., Nagane, S., Kubicki, D. J., Jung, Y.-K., Johnstone, D. N., Iqbal, A. N., Guo, D., Frohna, K., Danaie, M. & Tennyson, E. M. J. S. Stabilized tilted-octahedra halide perovskites inhibit local formation of performance-limiting phases. *Science* **374**, 1598-1605 (2021).

199 Macpherson, S., Doherty, T. A. S., Winchester, A. J., Kosar, S., Johnstone, D. N., Chiang, Y.-H., Galkowski, K., Anaya, M., Frohna, K., Iqbal, A. N., Nagane, S., Roose, B., Andaji-Garmaroudi, Z., Orr, K. W. P., Parker, J. E., Midgley, P. A., Dani, K. M. & Stranks, S. D. Local nanoscale phase impurities are degradation sites in halide perovskites. *Nature* **607**, 294-300 (2022).

200 Ophus, C. Four-Dimensional Scanning Transmission Electron Microscopy (4D-STEM): From Scanning Nanodiffraction to Ptychography and Beyond. *Microscopy and Microanalysis* **25**, 563-582 (2019).

201 Wang, D., Wang, P., Mondal, S., Hu, M., Wang, D., Wu, Y., Ma, T. & Mi, Z. Thickness scaling down to 5 nm of ferroelectric ScAlN on CMOS compatible molybdenum grown by molecular beam epitaxy. *Applied Physics Letters* **122** (2023).

202 Su, H., Zhang, L., Liu, Y., Hu, Y., Zhang, B., You, J., Du, X., Zhang, J., Ren, X. & Gou, J. J. N. E. Polarity regulation for stable 2D-perovskite-encapsulated high-efficiency 3D-perovskite solar cells. *Nano Energy* **95**, 106965 (2022).

203 Fan, W., Shen, Y., Deng, K., Chen, Q. & Bai, Y. J. J. o. M. C. A. A tailored spacer molecule in 2D/3D heterojunction for ultralow-voltage-loss and stable perovskite solar cells. *Journal of Materials Chemistry A* **9**, 26829-26838 (2021).

204 Li, M. H., Yeh, H. H., Chiang, Y. H., Jeng, U. S., Su, C. J., Shiu, H. W., Hsu, Y. J., Kosugi, N., Ohigashi, T. & Chen, Y. A. J. A. M. Highly efficient 2D/3D hybrid perovskite solar cells via low‐pressure vapor‐assisted solution process. *Advanced Materials* **30**, 1801401 (2018).

205 Lin, T., Dai, T. & Li, X. J. S. R. 2D/3D perovskite: a step toward commercialization of perovskite solar cells. *Solar RRL* **7**, 2201138 (2023).

206 Fiorentino, F., Albaqami, M. D., Poli, I., Petrozza, A. J. A. A. M. & Interfaces. Thermal-and light-induced evolution of the 2D/3D interface in lead-halide perovskite films. *ACS Applied Materials Interfaces* **14**, 34180-34188 (2021).

207 Lin, Y., Magomedov, A., Firdaus, Y., Kaltsas, D., El‐Labban, A., Faber, H., Naphade, D. R., Yengel, E., Zheng, X. & Yarali, E. J. C. 18.4% organic solar cells using a high ionization energy self‐assembled monolayer as hole‐extraction interlayer. *ChemSusChem* **14**, 3569-3578 (2021).

208 Zhang, H., Zhang, S., Ji, X., He, J., Guo, H., Wang, S., Wu, W., Zhu, W. H. & Wu, Y. J. A. C. Formamidinium Lead Iodide‐Based Inverted Perovskite Solar Cells with Efficiency over 25% Enabled by An Amphiphilic Molecular Hole‐Transporter. *Angewandte Chemie* **136**, e202401260 (2024).

209 Song, D., Ramakrishnan, S., Zhang, Y. & Yu, Q. J. A. E. L. Mixed Self-Assembled Monolayers for High-Photovoltage Tin Perovskite Solar Cells. *ACS Energy Letters* **9**, 1466-1472 (2024).

210 Noel, N. K., Habisreutinger, S. N., Wenger, B., Lin, Y. H., Zhang, F., Patel, J. B., Kahn, A., Johnston, M. B. & Snaith, H. J. J. A. E. M. Elucidating the Role of a Tetrafluoroborate‐Based Ionic Liquid at the n‐Type Oxide/Perovskite Interface. *Advanced Energy Materials* **10**, 1903231 (2020).

211 Xiong, S., Hou, Z., Zou, S., Lu, X., Yang, J., Hao, T., Zhou, Z., Xu, J., Zeng, Y. & Xiao, W. J. J. Direct observation on p-to n-type transformation of perovskite surface region during defect passivation driving high photovoltaic efficiency. *Joule* **5**, 467-480 (2021).

212 Ahmad, T., Wilk, B., Radicchi, E., Fuentes Pineda, R., Spinelli, P., Herterich, J., Castriotta, L. A., Dasgupta, S., Mosconi, E. & De Angelis, F. J. A. F. M. New fullerene derivative as an n‐type material for highly efficient, flexible perovskite solar cells of a *p*‐*i*‐*n* configuration. *Advanced Functional Materials* **30**, 2004357 (2020).